Mixing-Driven Abyssal Ocean Circulation over Sloping Topography

Thesis by

Henry G. Peterson

In Partial Fulfillment of the Requirements for the
Degree of
Doctor of Philosophy

CALIFORNIA INSTITUTE OF TECHNOLOGY
Pasadena, California

2025
Defended May 27, 2025

Henry G. Peterson
ORCID: 0000-0003-3491-7688

ACKNOWLEDGMENTS

This thesis work would not have been possible without the many important people in my life who have supported me over the years.

I consider myself particularly lucky to have had Jörn Callies as my Ph.D. advisor. His wisdom and patience as a mentor are inspiring, and I will forever be grateful for the unwavering trust he placed in me to develop a numerical model of the large-scale ocean circulation. There were times when I was certain the project would never succeed, but his infectious positivity always renewed my hope and motivation. I look forward to continuing our work together in the coming year.

I thank my thesis committee for their advice and encouragement. Andy Thompson's enthusiasm for this work always left me feeling like I could take on the world, and I appreciate all his mentorship in both science and life as well as all the work he does to better the department. It was a joy to have both Jess Adkins and Sarah Purkey on my committee, who challenged me to always consider how my idealistic theories apply to the real ocean. I also appreciated Tim Colonius' numerical and mathematical perspective and willingness to discuss the nitty-gritty details of the model.

I would also like to thank a recent addition to my mentor network, Donnie Pinkston, whose software advice was invaluable and will continue to be as we work to "productize" the model.

I am truly grateful to all of my previous mentors, who helped me work towards this milestone early on. Bill Boos, Burkhard Militzer, Inez Fung, and Felipe González-Cataldo each played a key role in introducing me to research in Earth science as an undergraduate. I would not have even made it to graduate school without their support. Tapio Schneider's excellent mentorship in my first years as a graduate student taught me how to ask the right science questions, and I am thankful for the continued support from him and the CliMA group as a whole.

I especially thank the staff at Caltech for making everything run smoothly, particularly Julie Lee, Nora Oshima, and Bronagh Glaser, whom I bothered most frequently. I would also like to thank Paul Wennberg and everyone at both Caltech's Center for Teaching, Learning, and Outreach and PCC's Science Success Center for helping me improve my teaching skills.

Graduate school would not have been the same without the many friends I have made along the way. Being a part of the Callies Group (Albion, Bucky, Charly, Haakon, Jack, Joe, Luna, Scott, Shane, Shirui, Shriya, and Xihan) has been a blast; I cherished our "GOSSIP" sessions, dumpling assembly lines, and group retreat and always felt welcome. I also could not have asked for a better cohort (Costa, Dave, Jordan, Polina, Ryan, and Shirui), who made first-year coursework palatable and continue to be close friends. A special shoutout to the Treatment Sanctuary (Costa, Jordan, Keefe, Matt, Mike, Molly, Nate, and Ryan); words will never describe how amazing that house was. As for the Lighthouse Crew (Emily and Jimmy), I just hope we see some more lighthouses together. Thank you to my longest-standing office buddy, Ruth, for all the great chats and work sessions. To Harrison, Lily, and Sara: thanks for believing in me and indoctrinating me into your cult. And Harrison, please go easy on Willy's Warriors (Jackie, Josh, Maciel, and, formerly, Reina) during the next battle. Yufeng, I am glad that our friendship has grown since those COVID Zoom calls, and I hope we get more boba soon. To everyone in the Caltech Orchestra, Turtle Club, and IM Soccer League (go SOPS!): thanks for all the good times. I would also like to thank all the friends I have met through the astronomy department for accepting me despite my work's focus on our little blue planet. Finally, thank you to my friends from Berkeley (GO BEARS) and Visalia for staying in touch and supporting me while I did this silly graduate school thing.

Most importantly, I thank my mom and dad for being there for me since day one, my brother and sisters for being amazing role models, and my nephews for being cute. Best family ever. And to Samantha Wu: thank you for sharing this time with me and always being by my side.

This work was financially supported by the National Science Foundation under Grant No. OCE-2149080 and by the Schmidt Academy for Software Engineering's graduate research fellowship.

ABSTRACT

The planetary-scale overturning circulation of the ocean is maintained by small-scale diapycnal mixing in the abyss. Recent theory and observations suggest that this turbulence is bottom-enhanced, confining the upwelling needed to close this circulation to thin bottom boundary layers (BLs) over sloping topography. Developing an understanding of how this mixing shapes the abyssal circulation, both locally and at the basin scale, is the unifying goal of this thesis.

The local response of a water column to mixing has previously been understood using a one-dimensional model of a rotating, stratified fluid over a sloping seafloor. Canonically, this model assumes no cross- or along-slope variations of the flow, pressure, and buoyancy anomalies. At steady state, it predicts a peculiar form of the net cross-slope transport, however, failing to consider its coupling to the global circulation. For symmetric bathymetry without along-slope variations, for instance, this large-scale context implies that all cross-slope BL transport must be exactly returned in the interior. This interior downwelling is then turned by the Coriolis acceleration, rapidly spinning up along-slope flow in balance with a cross-slope barotropic pressure gradient. With these added physics, the one-dimensional model better captures the local response to mixing over an idealized ridge, for example. Using BL theory, we explicitly describe how the BL and interior communicate in this model. The up-slope transport of dense water in the bottom BL contributes a net downward flux of buoyancy, creating an effective bottom boundary condition on the interior. The coupling goes both ways, with the interior stratification at the top of the BL setting the strength of the BL transport. Variations across the slope then allow for BL–interior exchange.

Ultimately, the net transport of the local response must conserve potential vorticity at the basin scale. To better understand this coupling for arbitrary topography, we develop a novel finite element model of the planetary geostrophic equations. Using a combination of simulations and BL theory, we then study the mixing-driven abyssal circulation in an idealized bowl-shaped basin. In the absence of wind forcing and the joint effect of baroclinicity and relief, the leading-order barotropic transport flows along f/H contours, where f is the Coriolis frequency and H is the depth. The local response to mixing is coupled to this barotropic circulation, simultaneously constrained by the barotropic circulation and forcing it via a bottom stress curl. For closed f/H contours, a strong along-contour barotropic circulation spins up, reminiscent of the local response described above. On the other hand, if these contours intersect the boundary, a case more typical in the real ocean, the barotropic transport is suppressed. This decouples the leading-order local response from the large-scale circulation and intensifies bottom BL upwelling. This work therefore suggests that the local abyssal stratification in the presence of bottom-enhanced mixing strongly depends on the large-scale context.

PUBLISHED CONTENT AND CONTRIBUTIONS

Peterson, H. G., and J. Callies, 2023: Coupling between abyssal boundary layers and the interior ocean in the absence of along-slope variations. *Journal of Physical Oceanography*, **53 (1)**, 307–322, doi:10.1175/JPO-D-22-0082.1.
Both authors conceived the study and wrote the paper. H.G.P. ran the simulations and carried out the analysis.

Peterson, H. G., and J. Callies, 2022: Rapid spinup and spindown of flow along slopes. *Journal of Physical Oceanography*, **52 (4)**, 579–596, doi:10.1175/JPO-D-21-0173.1.
Both authors conceived the study and wrote the paper. H.G.P. ran the simulations and carried out the analysis.

TABLE OF CONTENTS

Acknowledgments iii
Abstract v
Published Content and Contributions vi
Table of Contents vi
Chapter I: Introduction 1
Chapter II: Rapid Spin Up and Spin Down of Flow Along Slopes 8
2.1 Abstract 8
2.2 Introduction 8
2.3 Rapid Adjustment and Constrained Transport 12
2.4 Mixing-Generated Spin Up Over an Idealized Ridge 16
2.5 Spin Down and Ekman Arrest 20
2.6 Discussion 26
2.7 Conclusions 29
2.8 Appendix A: 1D Model in Coordinates Aligned with the Slope and Gravity . 30
2.9 Appendix B: Calculation of the Cross-Ridge Transport for General Topography 31
2.10 Appendix C: Spin Up with Rayleigh Drag 32
2.11 Appendix D: Comparison Between PG and Non-PG Transport-Constrained 1D Solutions 34
Chapter III: Coupling Between Abyssal Boundary Layers and the Interior Ocean in the Absence of Along-Slope Variations 36
3.1 Abstract 36
3.2 Introduction 36
3.3 One-dimensional boundary layer theory 39
3.4 Two-dimensional boundary layer theory 46
3.5 Asymptotic theory 53
3.6 Discussion 58
3.7 Conclusions 61
3.8 Appendix A: BL Theory when $U^\xi \neq 0$ 61
3.9 Appendix B: Axisymmetric Coordinates 63
Chapter IV: The νPGCM: A Flexible Finite Element Model of the Large-Scale Ocean Circulation 64
4.1 Introduction 64
4.2 Planetary geostrophic equations 66
4.3 Numerical method 69
4.4 Results 76
4.5 Conclusions and Future Directions 79
Chapter V: Connecting the Local Response to Abyssal Mixing to the Basin-scale Circulation 81
5.1 Abstract 81
5.2 Introduction 81
5.3 A model problem for an abyssal basin 84

5.4 Numerical inversions for the three-dimensional mixing-driven flow 88
5.5 Theory for the flow inversion 93
5.6 Discussion 100
5.7 Conclusions 102
5.8 Appendix A: The PG inversion with non-zero aspect ratio 102
5.9 Appendix B: BL solution to the frictional thermal wind equations 105
5.10 Appendix C: Models for the local response to mixing 110
Chapter VI: Conclusions and Future Directions 113
6.1 Conclusions 113
6.2 Future Directions 114
Bibliography 117

Chapter 1

INTRODUCTION

The long-term memory of Earth's climate is stored in the cold, dark depths of the abyssal ocean, waiting to be recalled as it travels back to the surface. There is water in the abyss that has not seen the surface in hundreds if not thousands of years. Although this can make these waters seem remote to humans, they are an integral part of our planet's climate. As a massive reservoir of heat, carbon, and other climate-relevant tracers, the abyss plays a crucial role in setting Earth's "heartbeat" as it cycles between glacial and inter-glacial states. Even the fate of anthropogenic climate change, though it will not be fully realized in our lifetimes, ultimately depends on how the abyss responds to a rapidly warming climate.

But how does this abyssal water begin its journey, and what allows it to finally return to the surface? By pulling up buckets of seawater, sailors have known that the deep ocean is cold since at least the mid-1700s. At first, it was hypothesized that this water came from the polar regions via hemispheric overturning cells that upwelled at the equator ("Lenz's Doctrine"; Carpenter, 1874). This picture was disproved by the Meteor expedition in the early 1900s, where oceanographers Alfred Merz and Georg Wüst discovered that the dense water formed in the North Atlantic spread at mid-depth beyond the equator, with the abyss being filled with southern-source water (Warren and Wunsch, 1981, dark blue arrows in Fig. 1.1a). Clearly, the deep ocean is not a stagnant tub filled with uniformly dense water.

This implies that, somehow, these abyssal waters must eventually return to the surface, enabling them to exert an influence on the climate. It has long been understood that this process cannot be entirely buoyancy driven—otherwise all motion would be confined to the upper ocean, where most of the heating/cooling occurs (Sandström, 1908; Jeffreys, 1925). Instead, some mechanical forcing is needed to explain the overturning we observe. It is now also understood that part of the overturning can be accomplished adiabatically: the wind forcing in the Southern Ocean tilts isopycnals enough to allow mid-depth northern-source water to resurface along isopycnals (e.g., Wolfe and Cessi, 2011; Marshall and Speer, 2012, shallower isopycnal in Fig. 1.1a).[1] The densest bottom waters, however, must cross isopycnals to resurface (deeper isopycnal in Fig. 1.1a); some form of turbulent mixing is vital for the overturning. Walter Munk described this process with his classic one-dimensional balance between diapycnal advection and diffusion in the vertical:

$$w\frac{\partial b}{\partial z} = \frac{\partial}{\partial z}\left(\kappa\frac{\partial b}{\partial z}\right), \tag{1.1}$$

[1] In reality, some diapycnal mixing of these waters does occur (e.g., Sloyan and Rintoul, 2001; Lumpkin and Speer, 2007; Ledwell et al., 2011), but it is not the leading order mechanism.

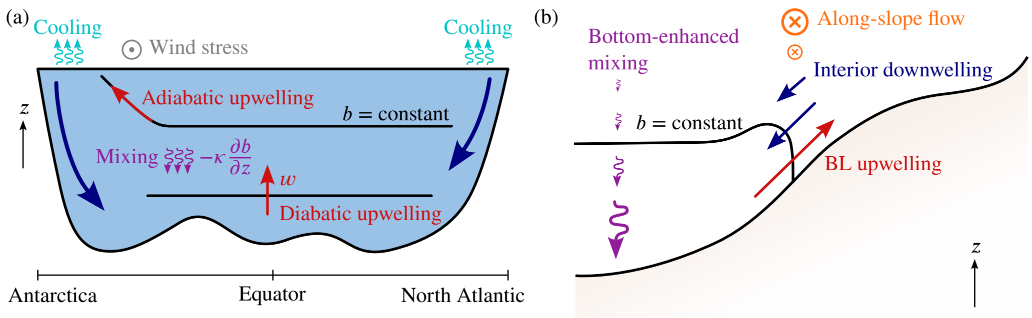

Figure 1.1: Sketches of (a) the meridional overturning circulation and (b) the effect of bottom-enhanced mixing over sloping bathymetry.

with the turbulent diffusivity κ parameterizing the mixing of buoyancy b through down-gradient diffusion (Munk, 1966). At the time, he assumed a constant diffusivity and inferred the vertical upwelling $w \sim O(10^{-7}\ \mathrm{m\,s^{-1}})$ from estimates of bottom water production. This leads to an exponential profile of buoyancy, and, fitting to an observed decay scale of $\kappa/w \sim O(1000\ \mathrm{m})$, a required diffusivity of $\kappa \sim O(10^{-4}\ \mathrm{m^2\,s^{-1}})$.

Since then, with the help of observations of dissipation rates from microstructure profilers and inferences of κ from tracer release experiments, the picture has become significantly more complicated. Initial estimates of interior diffusivities were found to be more than an order of magnitude smaller than Munk's initial estimate (e.g., Osborn and Cox, 1972; Gregg, 1989; Ledwell et al., 1993). Later, observational campaigns were able to uncover the "missing mixing" in the bottom few hundred meters of the ocean over rough topography, where κ can be strongly enhanced up to $O(10^{-3}\ \mathrm{m^2\,s^{-1}})$ (e.g., Polzin et al., 1997; Ledwell et al., 2000; Waterhouse et al., 2014, purple squiggles in Fig. 1.1b). Once again, Munk pioneered a shift in thinking, arguing that tidal dissipation plays a key role in generating this mixing (Munk and Wunsch, 1998). Of the approximately 2 TW of energy needed to mix bottom waters back to the surface, more than half is now thought to be generated by tidal forcing (Garrett and Kunze, 2007), with a sizeable chunk of the rest resulting from large-scale currents flowing over topographic features (Nikurashin and Ferrari, 2011). The observations and theory for how internal waves generated by tidal and geostrophic currents break over rough topography, generating small-scale turbulence, is still an active area of research (see Whalen et al., 2020, and references therein for a review). For the purposes of this thesis, we instead simply view this turbulence as a given forcing and ask the question:

How does near-bottom mixing

shape the abyssal circulation?

Even before observations revealed that mixing in the ocean is bottom-intensified, a number of studies recognized that the sloping bottom of the ocean is crucial in describing mixing-generated dynamics. Because buoyancy cannot be mixed through a solid boundary, the buoyancy flux $-\kappa\partial_z b$ must go to zero at the bottom[2]. This additional piece of the puzzle is key once we consider bottom-enhanced mixing: without it, Munk's simple one-dimensional balance would actually predict *downwelling* ($w < 0$) given observed near-exponential profiles of κ and b. The picture that then emerges consists of a net abyssal upwelling that is a small residual of weak subsidence throughout the interior and strong upwelling in thin bottom boundary layers (BLs; Garrett, 1990; Ferrari et al., 2016; de Lavergne et al., 2016; McDougall and Ferrari, 2017; Callies, 2018, red and blue arrows in Fig. 1.1b). Observations from a recent dye release experiment in a submarine canyon within the Rockall Trough appear to support this theory (Wynne-Cattanach et al., 2024).

The question now becomes: how does this local response to mixing couple to the global circulation? To answer this, we turn to the planetary geostrophic (PG) equations, which have been a cornerstone of our understanding of the large-scale ocean circulation (e.g., Robinson and Stommel, 1959; Welander, 1959; Colin de Verdière, 1988; Samelson and Vallis, 1997a; Salmon, 1998; Pedlosky, 1998). They are derived from the full Boussinesq system by assuming small Rossby numbers and large horizontal scales, filtering out fast-timescale dynamics while retaining nonlinear advection in the buoyancy equation. The PG inversion, which expresses the flow $\boldsymbol{u} = (u, v, w)$ and pressure p in terms of the buoyancy, reads

$$f\boldsymbol{z} \times \boldsymbol{u} = -\nabla p + b\boldsymbol{z} + \boldsymbol{F}, \tag{1.2}$$

$$\nabla \cdot \boldsymbol{u} = 0, \tag{1.3}$$

where f is the Coriolis parameter, $\boldsymbol{z}$ is the local vector opposite to gravity and $\boldsymbol{F}$ is a vector field representing friction. The buoyancy then evolves according to

$$\frac{\partial b}{\partial t} + \boldsymbol{u} \cdot \nabla b = \nabla \cdot (\kappa \nabla b), \tag{1.4}$$

the more general version of Munk's balance (1.1). In local Cartesian coordinates (x, y, z) and with a meridional gradient in the planetary vorticity such that $f = f_0 + \beta y$, the inviscid PG vorticity balance is then

$$\beta v = f\frac{\partial w}{\partial z}, \tag{1.5}$$

implying that meridional flow must be accompanied by stretching or squashing of the fluid column. The classic Stommel and Arons (1959a,b) theory uses this framework in the simple case of uniform diapycnal upwelling driven by constant mixing. In that case, integrating (1.5) over the depth of the abyss yields a weak poleward flow in the basin interior, implying that the dense water sourced at high latitudes is transported equatorward predominantly

[2]Technically, it should be equal to the geothermal heat flux, which I will neglect throughout this thesis work due to its relatively small magnitude in the modern climate (e.g., Emile-Geay and Madec, 2009; de Lavergne et al., 2016; McDougall and Ferrari, 2017).

within deep (frictional) western boundary currents. While the real abyssal circulation is much more complicated than this simple model, as we will see over the course of this thesis, western boundary currents are, in fact, a robust characteristic of the deep ocean.

Our understanding of the abyssal circulation beyond the Stommel and Arons theory has been shaped by a local one-dimensional form of the PG equations over a uniform slope (e.g., Phillips, 1970; Wunsch, 1970; Thorpe, 1987; Garrett et al., 1993; Callies, 2018).[3] In the canonical form of this model, variations in the flow, pressure, and buoyancy anomaly are neglected in planes parallel to the slope, allowing the local response to be directly computed. Intuition for the basin-scale circulation is then often derived from examining variations in the local response predicted by this model across a domain (e.g., Phillips et al., 1986; McDougall, 1989; Garrett, 1991; Dell and Pratt, 2015; Callies and Ferrari, 2018; Drake et al., 2020). The following phenomenology for the abyssal circulation then arises: bottom-enhanced mixing tilts isopycnals slightly upward before plunging them into the sloping seafloor (black line in Fig. 1.1b). The corresponding cross-slope[4] buoyancy gradients drive upslope flow in the bottom BL with downwelling aloft, accompanied by thermal wind shear in the along-slope flow (orange arrows in Fig. 1.1b). Under the canonical assumptions, the steady state of this local model demands that net cross-slope transport be $U = \kappa_\infty \cot\theta$, where κ_∞ is the far-field turbulent diffusivity and θ is the local slope angle (Thorpe, 1987; Garrett et al., 1993). This curious constraint on the interior flow, which clearly breaks down as $\theta \to 0$, is only achieved after the interior along-slope flow slowly diffuses to its steady state over thousands of years for typical abyssal parameters (MacCready and Rhines, 1991).

While it is possible for the local response to have an impact on the net transport of the global circulation, the opposite should also be true. Chapter 2 of this thesis, published as Peterson and Callies (2022), works toward this goal by adding a transport constraint to the local theory. In a symmetric domain with no along-slope variations, the net transport U should vanish to satisfy continuity (1.3). Adding this constraint to the local model implies that the net BL upwelling must be equal and opposite to the net downwelling in the interior. The local model must be modified to include a cross-slope barotropic pressure gradient $\partial_x P$ to support this added constraint. As the downwelling flow in the interior is turned in the along-slope direction by the Coriolis acceleration, it is put in geostrophic balance with this cross-slope pressure gradient. This allows the far-field flow to feel the effects of mixing within one inertial period, adjusting much more rapidly than the diffusion-limited canonical model. This transport-constrained model is able to fully capture mixing-generated dynamics in the absence of along-slope variations, such as the flow spun up by bottom-enhanced mixing over an idealized ridge (Ruan and Callies, 2020).

[3] The canonical one-dimensional dynamics are actually derived from the full Boussinesq equations (Chapter 2), but this is not necessary for the purpose of studying the salient abyssal dynamics.

[4] We use "cross-slope" for the horizontal direction pointing towards shallower depths and "along-slope" for the along-isobath direction perpendicular to this.

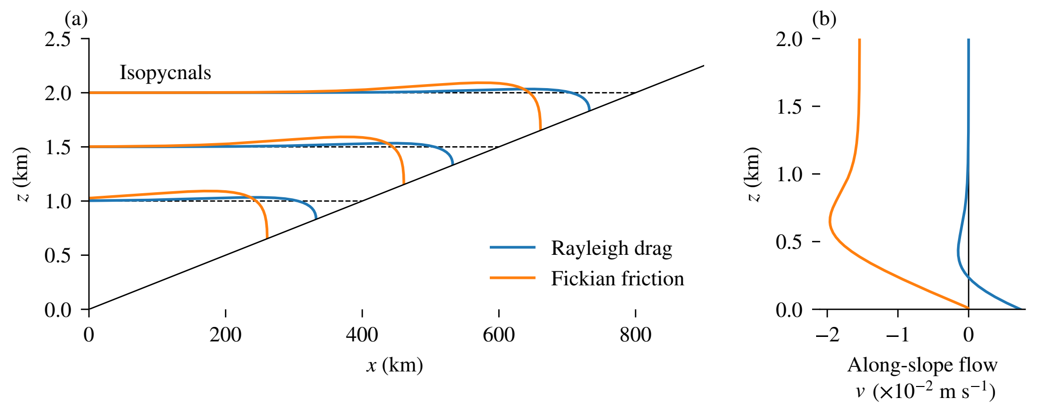

Figure 1.2: Comparison between the flow produced by bottom-intensified mixing in a one-dimensional model with Rayleigh drag versus Fickian friction. Shown are the (a) buoyancy fields remapped to the x–z plane and (b) along-slope flow after 10 years of spin up from rest using parameters typical of the Brazil Basin along the mid-Atlantic ridge. The isopycnals are qualitatively similar between the two models, but the resulting along-slope flow is critically different. A strong interior flow is generated when Fickian friction is used, while damping in the interior prevents such flow in the model with Rayleigh drag.

In Chapter 3, published as Peterson and Callies (2023), we make use of this more faithful model of the local response to mixing to pinpoint how abyssal BLs communicate with the interior. Using BL theory (e.g., Bender and Orszag, 1999; Chang, 2007), we make explicit the separation between interior and BL contributions to the flow and buoyancy. A classic application of this technique arises in the context of Stommel's (1948) gyre theory (Veronis, 1966), although there the coupling is one-way: the interior solution can be calculated in isolation, and the western BL is a passive element of the theory. For bottom BLs on slopes, however, the BL transport plays an active role in setting the structure of the interior solution. By moving dense water up the slope, the BL supplies a downward flux of buoyancy that the interior feels as an effective bottom boundary condition. This transport is itself dependent on the cross-slope interior stratification at the top of the BL, providing an avenue for exchange between the BL and interior.

The models in Chapters 2 and 3 rely on along-slope symmetry to be able to fully constrain the local response to mixing, a property that is broken if, for example, meridional variations in the Coriolis parameter f are allowed. To make progress in understanding the more general case, numerical solutions of the full PG equations (1.2)–(1.4) must be pursued. A number of PG circulation models (PGCMs) exist (e.g., Salmon, 1986; Samelson and Vallis, 1997b; Edwards et al., 1998; Callies and Ferrari, 2018), but they all employ Rayleigh drag in the momentum equations such that $\boldsymbol{F} = -r\boldsymbol{u}_\perp$ for some damping rate r. While this choice helps reduce the computational complexity of the problem, it leads to an excessive amount of drag on the interior flow, quashing the circulation (blue lines in Fig. 1.2). A more physical representation of the momentum fluxes filtered out by the PG approximation would be by a

Fickian friction term of the form

$$\boldsymbol{F} = \frac{\partial}{\partial z}\left(\nu \frac{\partial \boldsymbol{u}_\perp}{\partial z}\right), \tag{1.6}$$

with ν the turbulent viscosity (here we assume that fluxes in the local vertical direction z dominate). The PG flow can be thought of as the residual flow after a thickness-weighted average over transients, with this friction term parameterizing their effects on momentum by the divergence of an Eliassen–Palm flux (e.g., Young, 2012; Jansen et al., 2024). This turbulence closure leads to more physical flow in the interior (orange lines in Fig. 1.2), warranting the development of a νPGCM to revisit studies of the mixing-driven abyssal circulation.

Developing a numerical model of the PG equations with Fickian friction capable of resolving thin bottom BLs over complex topography is a challenging problem. Standard finite differencing schemes (Arakawa and Lamb, 1981) struggle to resolve the bathymetry adequately enough to faithfully represent BL upwelling. Terrain-following coordinate formulations solve this proble, but so-called "pressure gradient errors" (e.g., Haney, 1991) limit their ability to scale to global simulations. Our approach, described in Chapter 4, instead makes use of the geometrically flexible, high-order accurate finite element method on unstructured grids. This method is somewhat unconventional in the ocean modeling community, partly due to difficulties in simulating hydrostatic flows (e.g., Guillén-González and Rodríguez-Galván, 2015). The key innovation of the νPGCM is that it solves a form of the PG equations with an artificially increased aspect ratio (e.g., Kuang et al., 2005; Garner et al., 2007; Salmon, 2009), allowing it to leverage standard mixed finite element techniques for Stokes flow (e.g., Hughes, 1987; Elman et al., 2014). This method could even be extended to the full Boussinesq equations, potentially allowing for the use of finite elements in global ocean models without the need for ad hoc stabilization schemes.

In Chapter 5, we make use of the νPGCM to understand the physics of the mixing-driven abyssal circulation in an idealized bowl-shaped basin with no buoyancy advection, enabling us to isolate and study the connection between the local response to the basin-scale flow. While the local theory from Chapter 2 exploits along-slope symmetry to constrain U to zero, in general, the local response is coupled to a vorticity-conserving barotropic circulation. In particular, in the absence of wind forcing and the joint effect of baroclinicity and relief (JEBAR), the leading-order barotropic transport flows along f/H contours, where H is the depth. The local response to mixing is then simultaneously constrained by this circulation and a forcing to it via the bottom stress curl. If f/H contours are closed, a strong barotropic circulation spins up along them (e.g., Kawase, 1993; Thompson, 1995; Hallberg and Rhines, 1996), which can be understood using the theories built up in Chapters 2 and 3. On the other hand, when contours intersect the boundary, as is more typical in the real ocean, the barotropic transport is suppressed. This decouples the leading-order local response from the large-scale circulation and intensifies upwelling in the bottom BL.

Finally, in Chapter 6, we conclude and outline possible future directions of this research. The numerical and theoretical models presented in Chapters 4 and 5 open up many new opportunities for studying the phenomenology of the abyssal circulation within the new framework of mixing-driven upwelling in thin bottom BLs. In particular, one of the most exciting questions left to be pursued is how these dynamics connect to the global overturning and, ultimately, the climate system as a whole.

Chapter 2

RAPID SPIN UP AND SPIN DOWN OF FLOW ALONG SLOPES

This chapter is reproduced from the published article:

Peterson, H. G., and J. Callies, 2022: Rapid spinup and spindown of flow along slopes. *Journal of Physical Oceanography*, **52 (4)**, 579–596, doi:10.1175/JPO-D-21-0173.1.

As a self-contained work, some notation may differ from conventions used elsewhere in this thesis.

2.1 Abstract

The near-bottom mixing that allows abyssal waters to upwell tilts isopycnals and spins up flow over the flanks of mid-ocean ridges. Meso- and large-scale currents along sloping topography are subjected to a delicate balance of Ekman arrest and spin down. These two seemingly disparate oceanographic phenomena share a common theory, which is based on a one-dimensional model of rotating, stratified flow over a sloping, insulated boundary. This commonly used model, however, lacks rapid adjustment of interior flows, limiting its ability to capture the full physics of spin up and spin down of along-slope flow. Motivated by two-dimensional dynamics, the present work extends the one-dimensional model by constraining the vertically integrated cross-slope transport and allowing for a barotropic cross-slope pressure gradient. This produces a closed secondary circulation by forcing Ekman transport in the bottom boundary layer to return in the interior. The extended model can thus capture Ekman spin up and spin down physics: the interior return flow is turned by the Coriolis acceleration, leading to rapid rather than slow diffusive adjustment of the along-slope flow. This transport-constrained one-dimensional model accurately describes two-dimensional mixing-generated spin up over an idealized ridge and provides a unified framework for understanding the relative importance of Ekman arrest and spin down of flow along a slope.

2.2 Introduction

The ocean is a rotating, stratified shell of fluid with a geometrically complicated bottom boundary. The sloping seafloor affects a number of aspects of the ocean's circulation. It allows near-bottom diapycnal mixing to bend isopycnals and thus spin up a circulation in the abyss (e.g., Phillips, 1970; Wunsch, 1970; Garrett, 1990; Callies and Ferrari, 2018), and it allows for bottom Ekman layers to be arrested by buoyancy forces and thus for currents to slide along slopes without being spun down (Rhines and MacCready, 1989; MacCready and Rhines, 1991, 1993). These spin up and spin down processes have long been studied using the equations of motion in a coordinate frame that is rotated to align with the sloping bottom and simplified by considering variations in the slope-normal direction only (see Garrett et al., 1993, for a review). We here argue that new insight can be gained by enforcing a transport constraint in these one-dimensional dynamics and allowing for a time dependent cross-slope barotropic (vertically constant) pressure gradient. These modifications enable boundary mixing to spin up an interior flow much more rapidly than through "slow diffusion" (MacCready and Rhines, 1991), and they allow for Ekman spin down in addition to Ekman arrest, capturing the competition between the two processes.

Enhanced turbulent mixing near the seafloor is thought to be a crucial element of the overturning circulation of the abyssal ocean, and 1D dynamics have been a powerful tool for understanding the dynamical response to such mixing over a sloping bottom. Antarctic Bottom Water fills the abyss of the Atlantic and Pacific basins (e.g., Lumpkin and Speer, 2007; Talley, 2013). For these dense waters to return to the surface, they must cross isopycnals and thus require diapycnal mixing (e.g., Munk, 1966; Munk and Wunsch, 1998; Ferrari, 2014). Observations have revealed that this diapycnal mixing is strongly enhanced over rough topography (e.g., Polzin et al., 1997; Ledwell et al., 2000; Waterhouse et al., 2014), where tidal and geostrophic currents produce a field of vigorous internal waves that break and produce small-scale turbulence (e.g., Garrett and Kunze, 2007; Nikurashin and Ferrari, 2011). Our understanding of how the ocean responds to this mixing, both locally and globally, has been shaped by 1D theory for a stratified, rotating fluid overlying a sloping, insulated seafloor (e.g., Phillips, 1970; Wunsch, 1970; Thorpe, 1987; Garrett et al., 1993). This theory (and the thinking it inspires), suggests that bottom-intensified mixing spins up diabatic upslope flow in a thin bottom boundary layer and diabatic downslope flow in a stratified mixing layer above (Garrett, 1990; Ferrari et al., 2016; de Lavergne et al., 2016; McDougall and Ferrari, 2017; Callies, 2018). Variations in these locally produced flows give rise to exchange with the interior and produce a basin-scale circulation in the abyss (e.g., Phillips et al., 1986; McDougall, 1989; Garrett, 1991; Dell and Pratt, 2015; Callies and Ferrari, 2018; Drake et al., 2020).

It has recently become clear, however, that the canonical 1D theory falls short in capturing two- and three-dimensional abyssal spin up, even in highly idealized contexts. The cross-slope mean flow generated by the 1D system is too weak to keep abyssal mixing layers stratified and instead produces a configuration that is baroclinically unstable (Wenegrat et al., 2018; Callies, 2018). Even if the role of baroclinic eddies is set aside, as will be done in the remainder of this work, spin up in two dimensions is qualitatively different from that predicted by 1D theory. Ruan and Callies (2020), considering bottom-intensified mixing over an idealized mid-ocean ridge (cf., Fig. 2.1), found that an interior flow along the ridge spins up rapidly, in direct contrast to the slow diffusion predicted by the canonical 1D equations (MacCready and Rhines, 1991). We show below that this rapid adjustment can be captured in 1D dynamics if a constraint is imposed on the vertically integrated cross-slope transport.

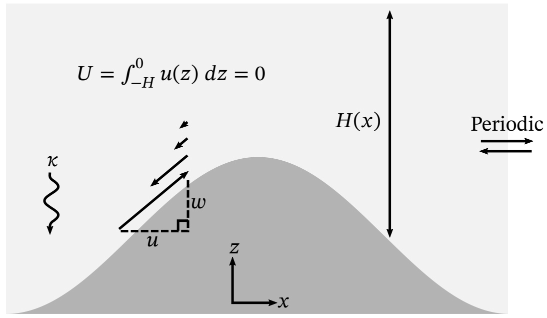

Figure 2.1: Sketch of idealized mid-ocean ridge geometry. By continuity and symmetry, the vertically integrated cross-ridge transport U must vanish.

The 1D dynamics have also been a cornerstone in our understanding of the spin down—or lack thereof—of meso- and large-scale geostrophic currents flowing along topographic slopes. Over a flat bottom boundary, a current induces Ekman transport in the bottom boundary layer. If the strength of the interior flow varies in the horizontal, so will the Ekman transport, leading to Ekman pumping and suction. By continuity, this generates a secondary circulation so that the boundary layer transport is returned in the interior. The Coriolis acceleration then turns the flow, spinning down the original current on a time scale of $\tau_S = f^{-1}\mathrm{Ek}^{-1/2}$ where f is the inertial frequency, $\mathrm{Ek} = \nu/fH^2$ is the Ekman number, ν is a turbulent viscosity scale, and H is a height scale (e.g., Pedlosky, 1979). The sloping boundary adds new physics to the problem: as fluid is moved up- or down-slope due to Ekman transport, it experiences a buoyancy force that opposes its motion (Rhines and MacCready, 1989; MacCready and Rhines, 1991). If a balance between the Coriolis and buoyancy forces is reached, the Ekman transport is "arrested." This shuts down the secondary circulation and halts further spin down, so that from then on the far-field current experiences an approximately free-slip bottom boundary condition. The timescale at which Ekman arrest occurs is roughly $\tau_A = (Sf)^{-1}$ where $S = N^2 \tan^2\theta/f^2$ is the slope Burger number for a fluid with buoyancy frequency N over a slope at an angle θ above the horizontal (MacCready and Rhines, 1991). The sloping topography thus enables the interior flow to persist if Ekman arrest is much faster than spin down, that is if $\tau_A/\tau_S = \mathrm{Ek}^{1/2}/S \ll 1$ (Garrett et al., 1993).

The canonical 1D model captures only the physics of Ekman arrest, not those of spin down. In that model, the cross-slope Ekman transport produced by the initial along-slope flow need not be returned in the interior, so the secondary circulation that can spin down the along-slope flow is lacking. While the physics of these two processes have now been known for decades, fully understanding their competition and interplay has been hampered by this disconnect. Chapman (2002) captured both processes in a simplified bulk model, but the connection to the more complete 1D dynamics remained opaque. We show below that a 1D

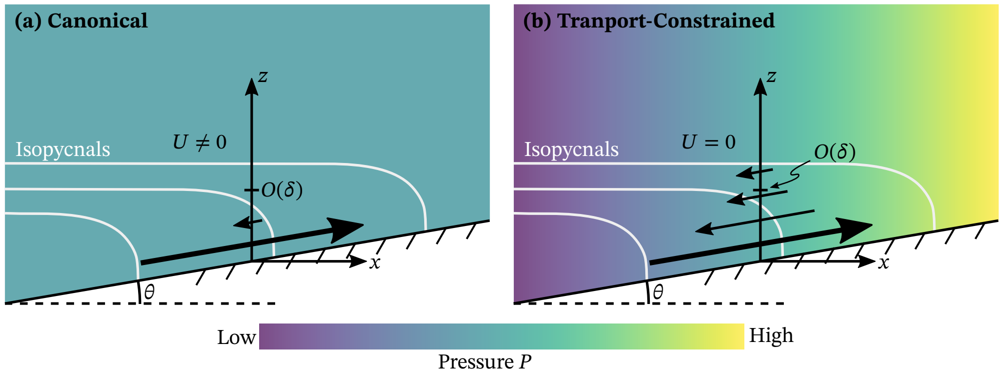

Figure 2.2: Difference between the canonical and transport-constrained 1D models. Sketched are typical isopycnals and cross-slope flow u as a function of z for spin-up with constant mixing coefficients. Colors represent the barotropic pressure gradient $\partial_x P$.

model derived directly from the full equations of motion can capture the physics of spin down and arrest if a transport constraint is imposed and a cross-slope pressure gradient is included, the same two modifications to the canonical 1D dynamics that allow for a rapid adjustment of the interior flow in spin up.

The key innovation of this work, introduced more fully in the next section, is thus a transport-constrained 1D model capable of representing rapid spin up and spin down. With the geometry sketched in Fig. 2.2 and using standard notation, the modified 1D dynamics are

$$\frac{\partial u}{\partial t} - fv = -\frac{\partial P}{\partial x} + b\tan\theta + \frac{\partial}{\partial z}\left(\nu\frac{\partial u}{\partial z}\right), \tag{2.1}$$

$$\frac{\partial v}{\partial t} + fu = \frac{\partial}{\partial z}\left(\nu\frac{\partial v}{\partial z}\right), \tag{2.2}$$

$$\frac{\partial b}{\partial t} + uN^2\tan\theta = \frac{\partial}{\partial z}\left[\kappa\left(N^2 + \frac{\partial b}{\partial z}\right)\right], \tag{2.3}$$

$$\int_0^H u \, \mathrm{d}z = U. \tag{2.4}$$

Crucially, U is an imposed cross-slope transport that we will typically set to zero, and P is a barotropic pressure perturbation from the background state of rest. The transport constraint enforces that any boundary layer transport must be returned outside the boundary layer, creating a secondary circulation and allowing for rapid adjustment of the along-slope flow. It is possible to impose this transport constraint because we allow for an implicitly determined time-varying barotropic cross-slope pressure gradient $\partial_x P$.

In canonical 1D dynamics, this cross-slope pressure gradient is absent from (2.1) or fixed in time to balance an initial along-slope flow. In that case, an anomalous geostrophic flow v must satisfy the balance $-fv = b\tan\theta$ (which by hydrostatic balance equals $\partial_z p \tan\theta$, the projection of the vertical perturbation pressure gradient onto the slope). A change in the geostrophically balanced along-slope flow thus requires a typically slow modification of the buoyancy anomaly b. The inclusion of a time-varying $\partial_x P$ in the modified equation (2.1) instead allows the balance $-fv = -\partial_x P$ and thus the rapid spin up or spin down of a (barotropic) geostrophic flow.

We derive this model in Section 2.3, where we motivate it by comparing the 1D and 2D equations in the planetary geostrophic (PG) limit. We then demonstrate the utility of the modified model by considering mixing-generated spin up over an idealized mid-ocean ridge in Section 2.4 and the spin down of an along-slope current in Section 2.5. We offer a discussion in Section 2.6 and conclude in Section 2.7.

2.3 Rapid Adjustment and Constrained Transport

In this section, we motivate the transport-constrained 1D model summarized above. We begin with a review of the canonical 1D theory, emphasizing the fact that it does not enforce any constraints on vertically integrated cross-slope transport. We then find that, when considering the 1D and 2D systems in the PG limit, the inversion statements take the same form and include an explicit transport term. In the 2D system, this term is constrained by the geometry of the domain. With this in mind, we modify the 1D model to allow for constrained transport by including a time-varying barotropic pressure gradient term.

2.3.1 Canonical one-dimensional dynamics

The canonical 1D model is typically derived by writing the Boussinesq equations in a rotated coordinate system aligned with a slope that is inclined at an angle θ above the horizontal (e.g., Garrett et al., 1993). We here deviate from this approach by remaining in the un-rotated coordinates, which is a slightly more natural choice if the horizontal components of the turbulent momentum and buoyancy fluxes are neglected but yields equivalent dynamics. Assuming no variations of the flow, pressure perturbation, or buoyancy perturbation in planes parallel to the slope (see Appendix A for a more detailed derivation), we obtain

$$\frac{\partial u}{\partial t} - fv = b\tan\theta + \frac{\partial}{\partial z}\left(\nu\frac{\partial u}{\partial z}\right), \tag{2.5}$$

$$\frac{\partial v}{\partial t} + fu = \frac{\partial}{\partial z}\left(\nu\frac{\partial v}{\partial z}\right), \tag{2.6}$$

$$\frac{\partial b}{\partial t} + uN^2\tan\theta = \frac{\partial}{\partial z}\left[\kappa\left(N^2 + \frac{\partial b}{\partial z}\right)\right], \tag{2.7}$$

where u is the cross-slope velocity, v is the along-slope velocity, and f is the (constant) inertial frequency. As explained in Appendix A, u is the horizontal projection of the cross-slope velocity as it would be defined in a fully rotated coordinate system, but we will still refer to it as the cross-slope velocity for simplicity. We have split the total buoyancy B into a constant background stratification and a perturbation so that $B = N^2 z + b$. Turbulent momentum and buoyancy transfer are represented by a diffusive closure with turbulent viscosity ν and turbulent diffusivity κ, related by the turbulent Prandtl number $\mu = \nu/\kappa$. We explore the consequences of using Rayleigh drag, a lower-order closure, in Appendix C (cf., Callies and Ferrari, 2018; Drake et al., 2020). The fluid satisfies no-slip and insulating boundary conditions at the bottom: $u = 0$, $v = 0$, and $\partial_z B = N^2 + \partial_z b = 0$ at $z = x \tan\theta = 0$, assuming (without loss of generality) that we apply these equations at $x = 0$. At the upper boundary, we impose no stress and a fixed buoyancy flux $-\kappa N^2$: $\partial_z u = 0$, $\partial_z v = 0$, and $\partial_z b = 0$ at $z = H + x\tan\theta = H$ at $x = 0$. The evolution is independent of H if H is large, in which case the domain can be considered semi-infinite. Importantly, the assumption that the pressure perturbation does not vary in the cross-slope direction leaves only the projection of the buoyancy force in (2.5).

Numerical, analytical, and approximate solutions to these equations for both constant and bottom-enhanced κ can be found in the literature (e.g., Garrett et al., 1993; Callies, 2018). The system has a steady state, in which the turbulent buoyancy flux convergence or divergence is balanced by cross-slope advection. This steady state is approached during both spin up and spin down first by rapid adjustment in the boundary layer, followed by a slow set up of a non-zero along-slope flow in the interior (Thorpe, 1987; MacCready and Rhines, 1991; Garrett et al., 1993). Outside the boundary layer, the dominant balance in (2.5) is $-fv = b\tan\theta$, so the along-slope flow and buoyancy perturbations evolve in lockstep. Combined with the other two equations, this yields

$$(1+S)\frac{\partial b}{\partial t} = \frac{\partial}{\partial z}\left(\kappa\left[N^2 + (1+\mu S)\frac{\partial b}{\partial z}\right]\right), \tag{2.8}$$

implying that the adjustment of the far field is diffusive and thus slow (MacCready and Rhines, 1991).

Throughout the evolution, the vertically integrated buoyancy budget is

$$\int_0^\infty \frac{\partial b}{\partial t}\,\mathrm{d}z + UN^2\tan\theta = \kappa_\infty N^2, \tag{2.9}$$

where κ_∞ is the far-field diffusivity. This implies that the steady state is achieved by balancing the turbulent buoyancy flux into the water column with a net upslope transport $U = \kappa_\infty \cot\theta$. During the transient, however, there is no explicit constraint on the cross-slope transport, and cross-slope transport in the boundary layer does not need to be returned above. This canonical 1D model thus lacks a closed secondary circulation that could produce a more rapid adjustment of the along-slope flow than through slow diffusion.

2.3.2 Canonical one-dimensional model in the planetary geostrophic framework

By considering both the 1D and 2D dynamics in the PG limit, we can directly compare their inversion statements and clarify the role of transport through an explicit term in the equations. The PG approximation assumes large horizontal scales and small Rossby numbers, rendering the tendency terms in the momentum equations negligible. This approximation is reasonable for mixing-generated spin up in the abyss, but the tendency terms are crucial in Ekman arrest and spin down. The simplified PG dynamics clearly illustrate the importance of constrained transport, however, which is ultimately key in both cases.

With the PG approximation applied, the canonical 1D equations (2.5) to (2.7) become

$$-fv = b\tan\theta + \frac{\partial}{\partial z}\left(\nu\frac{\partial u}{\partial z}\right), \tag{2.10}$$

$$fu = \frac{\partial}{\partial z}\left(\nu\frac{\partial v}{\partial z}\right), \tag{2.11}$$

$$\frac{\partial b}{\partial t} + uN^2\tan\theta = \frac{\partial}{\partial z}\left[\kappa\left(N^2 + \frac{\partial b}{\partial z}\right)\right]. \tag{2.12}$$

Given a buoyancy perturbation b, the momentum equations (2.10) and (2.11) allow us to invert for the flow (u, v), and the buoyancy is evolved in time through (2.12). We define a streamfunction $\chi(z)$ such that $u = \partial_z\chi$, allowing us to cast the inversion as a single streamfunction equation. Integrating (2.11) from some level to $z = H$ yields

$$\frac{\partial v}{\partial z} = \frac{f}{\nu}(\chi - U). \tag{2.13}$$

Differentiating (2.10) and substituting $\partial_z v$ from (2.13) yields the streamfunction inversion equation:

$$\frac{\partial^2}{\partial z^2}\left(\nu\frac{\partial^2\chi}{\partial z^2}\right) + \frac{f^2}{\nu}(\chi - U) = -\frac{\partial b}{\partial z}\tan\theta. \tag{2.14}$$

The boundary conditions are that $\chi = 0$ and $\partial_z\chi = 0$ at $z = 0$ and $\chi = U$ and $\partial_z^2\chi = 0$ at $z = H$. Although not needed for the evolution, the along-slope flow can also be inferred from χ by integrating (2.13) from the bottom up, using $v = 0$ at $z = 0$.

In these equations, the vertically integrated transport U must be treated as an unknown ($U = \kappa_\infty\cot\theta$ applies in steady state only). We must supplement (2.14) with an additional boundary condition. Enforcing $v = 0$ at $z = 0$ in (2.10) yields

$$\frac{\partial}{\partial z}\left(\nu\frac{\partial^2\chi}{\partial z^2}\right) = -b\tan\theta \quad \text{at} \quad z = 0, \tag{2.15}$$

which closes the system and allows us to determine U implicitly. As we will see in the next section, however, this vertically integrated transport is constrained by the non-local context in 2D and 3D geometries and cannot evolve as freely as in these canonical 1D equations.

2.3.3 Two-dimensional planetary geostrophic dynamics

Consider the mixing-generated spin up of PG flow over the idealized 2D ridge sketched in Fig. 2.1. If the 1D model is to serve its purpose, then we should expect it to provide an accurate description of the local flow on the flanks of the ridge. Continuity and symmetry imply that the vertically integrated cross-ridge transport within this domain must be zero, however, in contrast with the canonical model. This simple example of a non-local constraint on transport illustrates a key piece of physics missing from the canonical 1D theory.

To make this comparison explicit, we consider the 2D PG equations for a fluid with depth $H(x)$,

$$-fv = -\frac{\partial p}{\partial x} + \frac{\partial}{\partial z}\left(\nu\frac{\partial u}{\partial z}\right), \tag{2.16}$$

$$fu = \frac{\partial}{\partial z}\left(\nu\frac{\partial v}{\partial z}\right), \tag{2.17}$$

$$\frac{\partial p}{\partial z} = b, \tag{2.18}$$

$$\frac{\partial u}{\partial x} + \frac{\partial w}{\partial z} = 0, \tag{2.19}$$

$$\frac{\partial b}{\partial t} + u\frac{\partial b}{\partial x} + w\left(N^2 + \frac{\partial b}{\partial z}\right) = \frac{\partial}{\partial z}\left[\kappa\left(N^2 + \frac{\partial b}{\partial z}\right)\right], \tag{2.20}$$

where p is the pressure divided by a reference density and w is the vertical velocity. The boundary conditions are again an insulating and no-slip bottom, $N^2 + \partial_z b = 0$ and $u = v = 0$ at $z = -H$; a constant-flux and free-slip top $\partial_z b = 0$ and $\partial_z u = \partial_z v = 0$ at $z = 0$; and no normal flow across both boundaries, which together with $u = 0$ at $z = -H$ reduces to $w = 0$ at $z = -H$ and $z = 0$.

As before, we turn the momentum equations (2.16) to (2.19) into one streamfunction inversion. Defining $\chi(x, z)$ such that $u = \partial_z \chi$ and $w = -\partial_x \chi$, we have

$$\frac{\partial^2}{\partial z^2}\left(\nu\frac{\partial^2 \chi}{\partial z^2}\right) + \frac{f^2}{\nu}(\chi - U) = \frac{\partial b}{\partial x}, \tag{2.21}$$

where $U = \int_{-H}^{0} u \, \mathrm{d}z$ is the vertically integrated transport, a constant in x by continuity. The boundary conditions are similar to the 1D case: $\chi = 0$ and $\partial_z \chi = 0$ at $z = -H$ and $\chi = U$ and $\partial_z^2 \chi = 0$ at $z = 0$.

The inversion equations (2.14) and (2.21) have the same form in 1D and 2D. Under the assumption that b does not vary in planes parallel to the slope, $\partial_x b = -\partial_z b \tan\theta$. Continuity and symmetry over our 2D ridge (Fig. 2.1), however, set the transport term to zero—whereas the canonical 1D model generally produces a time-varying $U \neq 0$. This explicit difference between the two inversions causes qualitative differences between the 1D and 2D solutions, as seen in Ruan and Callies (2020) and further discussed below (Fig. 2.4). In general, the 1D dynamics are coupled to the barotropic vorticity equation via the vertically integrated transport terms. The sinusoidal ridge considered here is a simple incarnation of this coupling in which the transport is always zero. Although this choice of geometry is specific, it is not contrived; it should be possible to explain the dynamics over the ridge flanks with 1D theory. The same principles still hold for asymmetric 2D geometries, where U must be determined as part of the inversion but again is the result of a non-local constraint (see Appendix B).

2.3.4 Transport-constrained one-dimensional dynamics

The analysis of the PG inversions in the previous section suggests that a 1D model must include an additional constraint on U to faithfully reproduce local 2D dynamics. The canonical

1D model (2.5) to (2.7) must therefore be modified to include another degree of freedom, with a natural choice being a vertically constant, time-varying pressure gradient $\partial_x P$. This pressure gradient can accelerate a barotropic cross-slope flow u as needed to satisfy the transport constraint. The transport-constrained 1D dynamics are then

$$\frac{\partial u}{\partial t} - fv = -\frac{\partial P}{\partial x} + b\tan\theta + \frac{\partial}{\partial z}\left(\nu\frac{\partial u}{\partial z}\right), \tag{2.22}$$

$$\frac{\partial v}{\partial t} + fu = \frac{\partial}{\partial z}\left(\nu\frac{\partial v}{\partial z}\right), \tag{2.23}$$

$$\frac{\partial b}{\partial t} + uN^2\tan\theta = \frac{\partial}{\partial z}\left[\kappa\left(N^2 + \frac{\partial b}{\partial z}\right)\right], \tag{2.24}$$

$$\int_0^H u\,\mathrm{d}z = U, \tag{2.25}$$

with U prescribed. The tendency terms $\partial_t u$ and $\partial_t v$ are dropped if the PG approximation is applied.

As we will see in the solutions presented below, the transport constraint and barotropic pressure gradient are what allow the system to rapidly adjust in the interior. Physically, the requirement that $U = 0$ forces any boundary layer transport to be returned in the interior (Fig. 2.2). This secondary circulation is not the same as the dipole in the diabatic circulation generated by bottom-intensified mixing; it is present even in the case of constant κ and acts on the entire column. The interior cross-slope flow u is then turned by the Coriolis acceleration via (2.23), leading to rapid adjustment in the far-field along-slope flow v. This sets up geostrophic balance with the barotropic pressure gradient in the interior: $-fv = -\partial_x P$. Classic Ekman spin up and spin down dynamics are now captured.

It should be noted that this geostrophic adjustment occurs instantaneously if the PG approximation is applied. The secondary circulation that sets up the barotropic along-slope geostrophic flow is therefore only implicit in the PG model and not part of the explicit streamfunction χ.

2.4 Mixing-Generated Spin Up Over an Idealized Ridge

The modification to the 1D system described in the previous section enables it to capture the rapid spin up of interior flow encountered in 2D dynamics. The canonical 1D model fails to do so. To demonstrate this, we employ 1D and 2D numerical models to perform a mixing-generated spin-up experiment over the idealized symmetric ridge depicted in Fig. 2.1. For simplicity, we use the PG approximation for all models in this section, although subtle differences in spinup between PG and full models are noted in Appendix D.

2.4.1 Numerical models

We solve the 2D PG system given by the inversion equation (2.21) and evolution equation (2.20) using terrain-following coordinates and second-order finite differences (cf., Callies and Ferrari, 2018). Model parameters and geometry are taken from Ruan and Callies (2020)

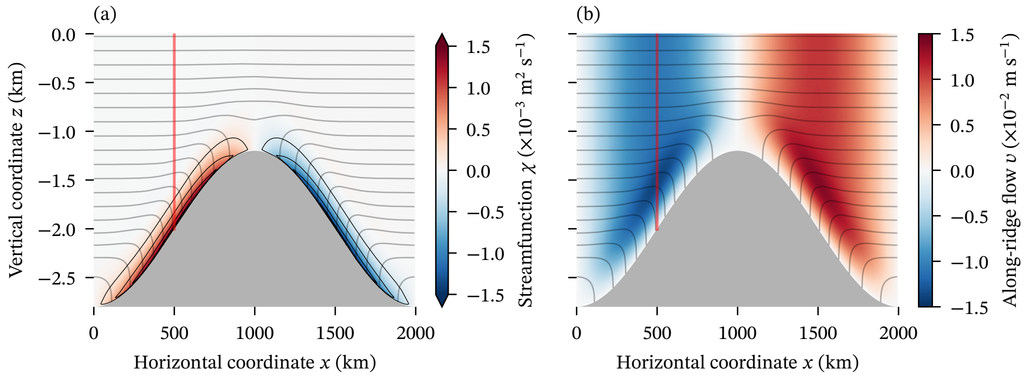

Figure 2.3: Flow fields in a 2D νPGCM simulation of mixing-generated spin up over the sinusoidal ridge sketched in Fig. 2.1. Shown are (a) the streamfunction χ (shading and black contours) with positive values indicating counter-clockwise and negative values indicating clockwise flow and (b) the along-ridge flow v (shading). The solution is shown after three years of spin up with bottom-intensified κ and $\mu = 1$. The gray curves show isopycnals, and the red vertical lines show where 1D profiles are examined in Figs. 2.4 and 2.5.

to roughly match those of the Brazil Basin (Table 2.1), except that we enlarge the ridge to a more realistic size because the computational constraints from Ruan and Callies (2020) do not apply here. Specifically, we take the domain height to be a sinusoid:

$$H(x) = H_0 + A \cos \frac{2\pi x}{L} \tag{2.26}$$

with $H_0 = 2$ km, $A = 800$ m, and $L = 2000$ km. Mixing is represented by a bottom-intensified profile of turbulent diffusivity,

$$\kappa = \kappa_0 + \kappa_1 e^{-(z+H)/h}, \tag{2.27}$$

with parameters obtained from a fit to Brazil Basin observations (Callies, 2018, Table 2.1). To reduce the impact of the upper boundary on the solution, we increase $H(x)$ uniformly by 1 km compared to Ruan and Callies (2020) and apply $\partial_z b = 0$ rather than $N^2 + \partial_z b = 0$ at $z = 0$. This ensures that isopycnals remain very nearly flat at the top of the domain, such that the PG evolution does not depend on the height of the domain. Horizontal grid spacing is uniform at about 7 km, whereas vertical grid spacing follows Chebyshev nodes with resolution on the order of 0.1 m at $z = -H$ to comfortably resolve the boundary layers.

Inertial frequency	f	-5.5×10^{-5} s^{-1}
Far-field buoyancy frequency	N	10^{-3} s^{-1}
Far-field diffusivity	κ_0	6×10^{-5} m^2 s^{-1}
Bottom-enhancement of diffusivity	κ_1	2×10^{-3} m^2 s^{-1}
Decay scale of diffusivity	h	200 m
Prandtl number	μ	1 or 200

Table 2.1: Parameters used in the spin-up calculations, taken from Ruan and Callies (2020) and roughly corresponding to the Mid-Atlantic Ridge flank in the Brazil Basin.

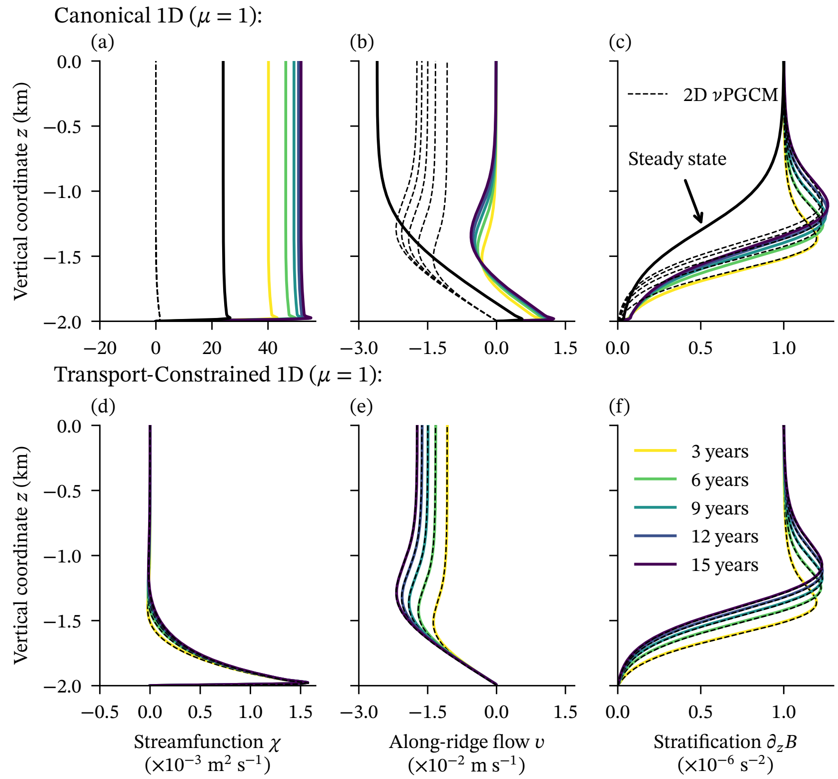

Figure 2.4: Comparison between the canonical and transport-constrained 1D solutions and their ability to capture the 2D simulation of mixing-generated spin up over a ridge. For all solutions, $\mu = 1$, and the profiles are taken at $x = 500$ km (red lines in Fig. 2.3). Shown are the (a), (d) streamfunction χ, (b), (e) along-ridge flow v, and (c), (f) stratification $\partial_z B$. The first row (a–c) shows the canonical 1D solution (steady state in black) while the second row (d–f) shows the transport-constrained 1D solution. All panels include the 2D νPGCM solution (dotted) for comparison.

We time step the full buoyancy B (rather than b) using a mixed implicit–explicit scheme and a time step of 10 days. We refer to this model as the 2D νPGCM.

We attempt to reproduce the 2D νPGCM solution locally with the two 1D theories, using the local slope angle ($\theta \approx 2.5 \times 10^{-3}$ radians) and fluid depth ($H = 2$ km) at the center of the ridge flank ($x = 500$ km, Fig. 2.3). The 1D models use the same numerical methods as the 2D νPGCM to solve the inversion equation (2.14) and evolution equation (2.12) over a single column. For the canonical case, the extra boundary condition given by (2.15) is employed, whereas for the transport-constrained case $U = 0$ is specified. The depth H is large enough that upper-boundary effects do not affect the solution. All models are initialized with $b = 0$, so that the total buoyancy is initially $B = N^2 z$.

2.4.2 Results

The insulating boundary condition at $z = -H$ leads to a buoyancy flux convergence and thus a positive buoyancy anomaly at the bottom, bending isopycnals into the ridge and spinning up a circulation (Fig. 2.3). Bottom-intensified mixing also produces buoyancy flux diver-

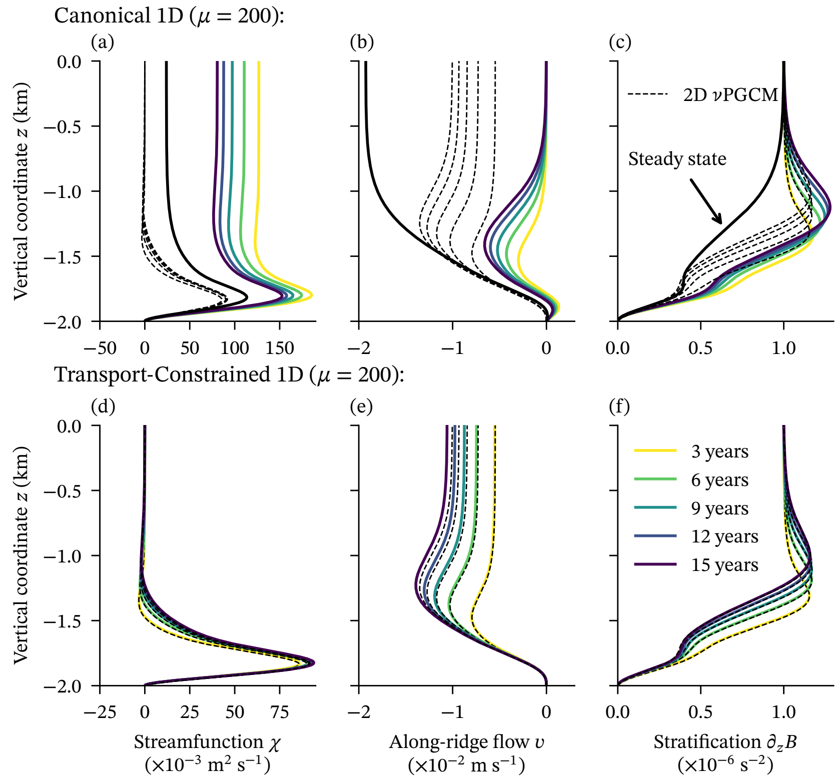

Figure 2.5: Comparison between the canonical and transport-constrained 1D solutions and their ability to capture the 2D simulation of mixing-generated spin up over a ridge. For all solutions, $\mu = 200$, and profiles are taken at $x = 500$ km (red lines in Fig. 2.3). Shown are the (a), (d) streamfunction χ, (b), (e) along-ridge flow v, and (c), (f) stratification $\partial_z B$. The first row (a–c) shows the canonical 1D solution (steady state in black) while the second row (d–f) shows the transport-constrained 1D solution. All panels include the 2D νPGCM solution (dotted) for comparison.

gence above, causing isopycnals to bend up before plunging towards the slope. Strong upwelling develops in a thin bottom boundary layer, broader and weaker downwelling occurs above, and a geostrophic along-slope flow emerges throughout the water column (Fig. 2.3). Our PG solutions are nearly identical to those of Ruan and Callies (2020), who simulated the full primitive equations using the MITgcm (Appendix D).

The canonical 1D theory fails to capture the evolution on the ridge flanks (Fig. 2.4a–c, Ruan and Callies, 2020). The canonical 1D theory predicts upslope flow in the bottom boundary layer that is an order of magnitude stronger than in the 2D system. The 2D streamfunction differs substantially from the canonical 1D theory, which produces substantial net cross-slope transport. The canonical 1D model predicts a diffusive progression of the along-slope flow into the interior, and substantial bottom stress induces the strong upslope Ekman transport. By contrast, the 2D simulation's transport constraint leads to zero bottom stress in the along-slope flow because (2.13) implies $\partial_z v = 0$ at $z = -H$ when $U = 0$. The buoyancy evolution is similar between the two models, except that the strong cross-slope flow in the canonical 1D solution maintains a stronger stratification in the bottom boundary layer.

In contrast with the canonical model, the transport-constrained 1D model matches the results from the 2D νPGCM very well (Fig. 2.4d–f). By enforcing the $U = 0$ constraint, we enable the streamfunction to match the 2D solution. Additionally, the secondary circulation sets up a barotropic pressure gradient that allows the far-field along-slope flow to rapidly adjust rather than grow diffusively as in the canonical theory. Finally, the two models yield nearly identical buoyancy profiles. In both models, advection is negligible, and the buoyancy evolution is dominated by diffusion. This is confirmed by separate simulations without the buoyancy advection terms, which yield very nearly identical solutions to those in Fig. 2.4 (not shown).

The transport-constrained 1D evolution equation only includes the cross-slope advection of the background buoyancy gradient $N^2 \tan\theta$, neglecting nonlinear transport terms. A system in which advection plays a more dominant role in the evolution of buoyancy would be a more challenging test of the transport-constrained 1D model. To achieve such a scenario, we increase the Prandtl number to $\mu = 200$ as a crude parameterization of baroclinic eddies (e.g., Rhines and Young, 1982; Greatbatch and Lamb, 1990; Callies, 2018; Holmes et al., 2019). The transport-constrained 1D model still accurately describes the 2D dynamics under these conditions (Fig. 2.5d–f). The increased Prandtl number thickens the boundary layer and strengthens the upwelling, which in turn maintains some of the stratification near the bottom boundary. The far-field along-slope flow still adjusts rapidly, although the transport-constrained 1D model slightly over-predicts this evolution, caused by minor differences in the buoyancy field arising from the 2D advection missing in the 1D model. The canonical 1D theory continues to fail miserably (Fig. 2.5a–c).

2.5 Spin Down and Ekman Arrest

As argued in the introduction, transport-constrained 1D dynamics can also elucidate the interplay between Ekman arrest and spin down on a slope. We ask how an initially barotropic along-slope flow V, which is in geostrophic balance with a cross-slope pressure gradient, $fV = \partial_x P$, adjusts to the presence of a sloping boundary. The current generates a cross-slope Ekman transport. This Ekman transport has two effects: it acts on the cross-slope buoyancy gradient to produce buoyancy anomalies that slow down this transport, and, through the transport constraint, it produces a secondary circulation in the interior that spins down the initial along-slope flow V. Depending on the relative timescales of arrest and spin down, either the secondary circulation spins down V, or the Ekman transport is arrested before V has been spun down, in which case the bottom becomes slippery and the flow persists.

This problem has been studied with the canonical 1D model by imposing a $\partial_x P$ that balances the initial flow and is held fixed in time (MacCready and Rhines, 1991; Garrett et al., 1993). Without a transport constraint, this model only contains the physics of Ekman arrest, with no mechanism for spinning down the interior flow other than slow diffusion. The transport-

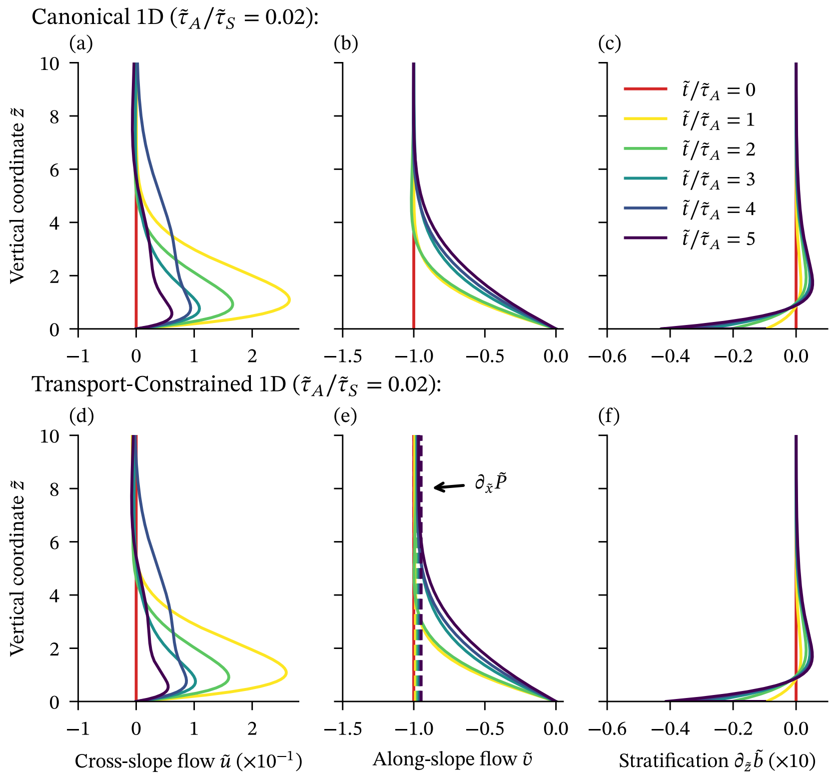

Figure 2.6: Comparison between the canonical and transport-constrained 1D simulations of spin down in a regime where Ekman arrest dominates. The Ekman number is $\mathrm{Ek} = 10^{-4}$, and the slope Burger number is $S = 0.5$, such that $\tilde{\tau}_A = 2$, $\tilde{\tau}_S = 10^2$, and $\tilde{\tau}_A/\tilde{\tau}_S = 2 \times 10^{-2}$. Shown are the (a), (d) cross-slope flow $\tilde{u}$, (b), (e) along-ridge flow $\tilde{v}$, and (c), (f) perturbation stratification $\partial_{\tilde{z}}\tilde{b}$ in increments of Ekman arrest times. The first row (a–c) shows the canonical 1D solution, while the second row (d–f) shows the transport-constrained 1D solution. The barotropic pressure gradient $\partial_{\tilde{x}}\tilde{P}$ is shown in dashed lines in (e) and held fixed at -1 in (b). For clarity, only the first 10 Ekman layer depths are shown, but the full domain height is $H/\delta = \mathrm{Ek}^{-1/2} = 100$.

constrained 1D model, in contrast, captures the secondary circulation and thus the physics of spin down. In this model, $\partial_x P$ is allowed to change with time, as needed to satisfy the transport constraint $U = 0$. In the following, we review the timescales for Ekman spin down and arrest and map out the parameter space using the transport-constrained 1D model.

2.5.1 Nondimensional one-dimensional equations

To distill the dynamics down to its fundamental parameters, we nondimensionalize the 1D equations by setting

$$t = T\tilde{t}, \quad z = \delta\tilde{z}, \quad u = V\tilde{u}, \quad v = V\tilde{v}, \quad b = \mathcal{B}\tilde{b}. \tag{2.28}$$

We assume a constant viscosity ν and set $\kappa = 0$ to focus on arrest and spin down without the effects of buoyancy diffusion (cf., MacCready and Rhines, 1991). We choose an inertial timescale, the Ekman layer height scale, and a buoyancy scale corresponding to the buoyancy anomaly produced by cross-slope Ekman advection persisting for one inertial timescale:

$$T = \frac{1}{f}, \quad \delta = \sqrt{\frac{\nu}{f}}, \quad \mathcal{B} = \frac{VN^2 \tan\theta}{f}. \tag{2.29}$$

With these scales, equations (2.22) to (2.25) become

$$\frac{\partial \tilde{u}}{\partial \tilde{t}} - \tilde{v} = -\frac{\partial \tilde{P}}{\partial \tilde{x}} + S\tilde{b} + \frac{\partial^2 \tilde{u}}{\partial \tilde{z}^2}, \tag{2.30}$$

$$\frac{\partial \tilde{v}}{\partial \tilde{t}} + \tilde{u} = \frac{\partial^2 \tilde{v}}{\partial \tilde{z}^2}, \tag{2.31}$$

$$\frac{\partial \tilde{b}}{\partial \tilde{t}} + \tilde{u} = 0, \tag{2.32}$$

$$\int_0^{H/\delta} \tilde{u}\, \mathrm{d}\tilde{z} = \tilde{U} = 0, \tag{2.33}$$

where we set $\tilde{U} = 0$. The nondimensional height of the domain may be written as $H/\delta = \mathrm{Ek}^{-1/2}$. The model is thus fully characterized by two nondimensional parameters: the slope Burger number $S = N^2 \tan^2\theta / f^2$ and the Ekman number $\mathrm{Ek} = \nu / f H^2$. It is worth noting that with these choices in the nondimensionalization, the total stratification becomes

$$\frac{\partial \tilde{B}}{\partial \tilde{z}} = \frac{f\delta \cot\theta}{V} + \frac{\partial \tilde{b}}{\partial \tilde{z}}, \tag{2.34}$$

introducing a third nondimensional number, $f\delta \cot\theta / V$, a measure of the background stratification. As a consequence of setting $\kappa = 0$, the flow's evolution is independent of this parameter.

2.5.2 Spin down and Ekman arrest timescales

Ekman spin down occurs when the geostrophic far-field along-slope flow $\tilde{v} = \pm 1$ is eroded by a secondary circulation. First, a cross-slope Ekman transport of order unity ($\tilde{u} \sim \mp 1$ over $0 < \tilde{z} \lesssim 1$) is generated. If the along-slope current had lateral structure, variations in this Ekman transport would produce convergences and divergences that would drive a secondary circulation. Despite not capturing such lateral variations in the current, the transport-constrained 1D model does produce this secondary circulation. The convergence and divergence of the Ekman transport is delegated to $\tilde{x} \to \pm\infty$ and the constraint $\tilde{U} = 0$ ensures that all cross-slope Ekman transport is returned in the interior. Being distributed uniformly over the domain of height H, this cross-slope return flow has a magnitude $\tilde{u} \sim \pm\delta/H = \pm\mathrm{Ek}^{1/2}$. With negligible friction in the interior, (2.31) implies that this return flow is turned into the along-slope direction by the Coriolis acceleration, $\partial_{\tilde{t}}\tilde{v} \approx -\tilde{u} \sim \mp\mathrm{Ek}^{1/2}$, spinning down the initial flow. This implies a spin-down timescale

$$\tilde{\tau}_S = \frac{1}{\sqrt{\mathrm{Ek}}}. \tag{2.35}$$

In dimensional terms, this is $\tau_S = f^{-1}\mathrm{Ek}^{-1/2}$ and a classical result (e.g., Pedlosky, 1979). It is worth noting that quasi-geostrophic dynamics suggest that, in a system with a characteristic lateral length scale L, the vertical height scale H in this scaling would be the minimum of

fL/N (the "Prandtl scale") and the fluid depth (e.g., Holton, 1965; MacCready and Rhines, 1991).

Ekman arrest, in contrast, involves the interaction of buoyancy forces with Ekman transport across a slope. As before, the initial along-slope flow $\tilde{v} = \partial_{\tilde{x}} \tilde{P} \sim \pm 1$ induces a cross-slope Ekman transport of order unity. The transport acts on the cross-slope buoyancy gradient through (2.32), generating a buoyancy anomaly of magnitude $\tilde{b} \sim \pm\tilde{\tau}$ over a timescale $\tilde{\tau}$. The buoyancy force opposes the transport, ultimately neutralizing it once $S\tilde{b} \sim \partial_{\tilde{x}} \tilde{P}$ in (2.30) and the near-bottom along-slope flow has been eliminated without requiring any change in $\partial_{\tilde{x}} \tilde{P}$. This yields an arrest timescale of

$$\tilde{\tau}_A = \frac{1}{S}, \tag{2.36}$$

or, in dimensional form, $\tau_A = (Sf)^{-1}$ (e.g., Rhines and MacCready, 1989). As pointed out by MacCready and Rhines (1991), this scaling needs modification if $S \gtrsim 1$, a regime in which the Ekman transport cannot be assumed to persist at its original magnitude for the full time $\tilde{\tau}$. We only straddle this parameter regime and ignore the correction proposed by MacCready and Rhines (1991) for simplicity. This makes our analysis of the above scaling relevant for abyssal ridges ($S \sim 10^{-3}$) and some continental slopes and seamounts ($S \sim 10^{-1}$).

Ekman spin down and arrest thus operate on different time scales. If the spin-down timescale is short compared to the arrest timescale, the along-slope current is spun down before the Ekman transport is arrested. Conversely, if the arrest timescale is short compared to the spin-down timescale, the Ekman transport is diminished before the current is spun down, and the arrested Ekman layer acts as an essentially slippery boundary condition for the persisting current. This competition between the two processes is characterized by the ratio of their timescales (Garrett et al., 1993):

$$\frac{\tilde{\tau}_A}{\tilde{\tau}_S} = \frac{\sqrt{\mathrm{Ek}}}{S}. \tag{2.37}$$

When this ratio is large, we expect spin down; when it is small, we expect arrest. These physics were identified by MacCready and Rhines (1991), but the canonical 1D model employed there did not capture spin down and thus could not elucidate this competition explicitly. As discussed in the introduction, the bulk model introduced in Chapman (2002) was capable of representing both processes but lacked a direct connection to the full equations of motion.

2.5.3 Numerical results

We now explore the competition between spin down and Ekman arrest across the parameter space (S, Ek), solving equations (2.30) to (2.33) numerically using second-order finite differences over a grid of 2^9 to 2^{11} Chebyshev nodes (depending on Ek) and a Crank–Nicolson timestepping scheme with a timestep of $\Delta\tilde{t} = \min\{\tilde{\tau}_A/100, \tilde{\tau}_S/100\}$. As mentioned above,

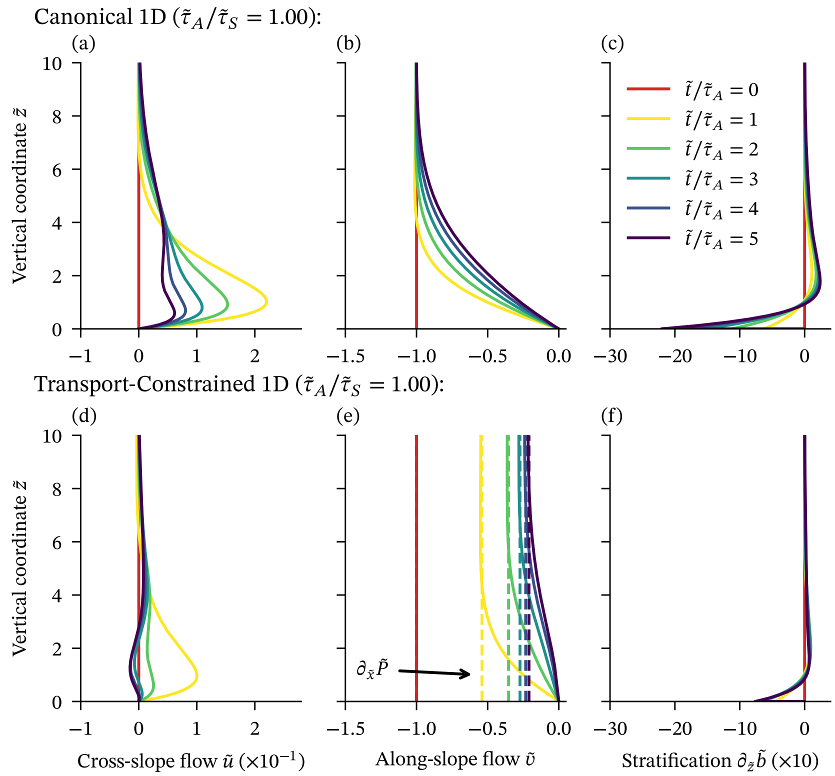

Figure 2.7: Comparison between the canonical and transport-constrained 1D simulations of spin down in a regime where spin down dominates. The Ekman number is $\text{Ek} = 10^{-4}$, and the slope Burger number is $S = 10^{-2}$, such that $\tilde{\tau}_A = 10^2$, $\tilde{\tau}_S = 10^2$, and $\tilde{\tau}_A/\tilde{\tau}_S = 1$. Shown are the (a), (d) cross-slope flow $\tilde{u}$, (b), (e) along-ridge flow $\tilde{v}$, and (c), (f) perturbation stratification $\partial_{\tilde{z}}\tilde{b}$ in increments of Ekman arrest times. The first row (a–c) shows the canonical 1D solution, while the second row (d–f) shows the transport-constrained 1D solution. The barotropic pressure gradient $\partial_{\tilde{x}}\tilde{P}$ is shown in dashed lines in (e) and held fixed at -1 in (b). For clarity, only the first 10 Ekman layer depths are shown, but the full domain height is $H/\delta = \text{Ek}^{-1/2} = 100$.

the depth of the domain depends on the Ekman number through $H/\delta = \text{Ek}^{-1/2}$, so more nodes are required for smaller Ek. We initialize all simulations with $\tilde{b} = 0$, $\tilde{u} = 0$, and a barotropic geostrophic flow $\tilde{v} = -1$, so as to induce upwelling in the Ekman layer. This choice is made without loss of generality: downwelling solutions induced by $\tilde{v} = 1$ are equivalent due to symmetry of the system with $\kappa = 0$. The along-slope flow must balance $\partial_{\tilde{x}}\tilde{P}$ so that, initially, we have $\partial_{\tilde{x}}\tilde{P} = \tilde{v} = -1$. To compare with the canonical 1D theory, we hold $\partial_{\tilde{x}}\tilde{P} = -1$ fixed and drop the transport constraint (2.33) as in MacCready and Rhines (1991). In the transport-constrained model, on the other hand, $\partial_{\tilde{x}}\tilde{P}$ is allowed to change in time, such that the extra constraint (2.33) can be satisfied.

We begin with a case in which Ekman arrest occurs before the interior flow is spun down. With $S = 0.5$ and $\text{Ek} = 10^{-4}$ ($H/\delta = 100$), the arrest and spin-down timescales are $\tilde{\tau}_A = 2$ and $\tilde{\tau}_S = 10^2$. Their ratio is $\tilde{\tau}_A/\tilde{\tau}_S = 0.02$, so Ekman arrest is about 50 times faster than spin down. This parameter regime might occur on the slopes of a typical seamount or on the

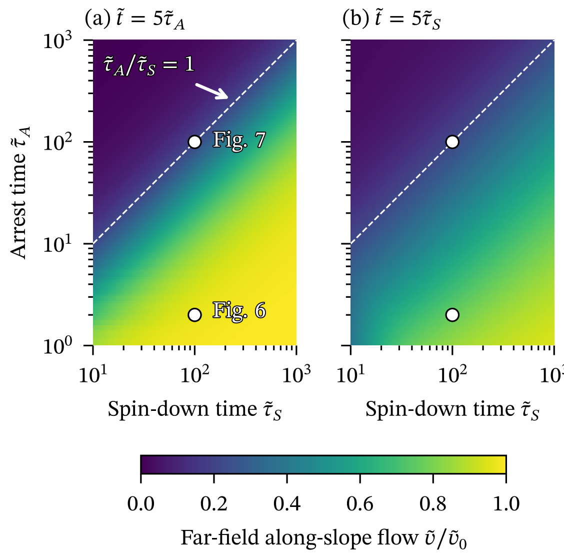

Figure 2.8: Competition between spin down and Ekman arrest in the transport-constrained 1D model. Colors show the fraction of the initial far-field along-slope flow $\tilde{v}$ remaining after (a) five arrest times and (b) five spin-down times for a wide range of spin-down timescales $\tilde{\tau}_S = \text{Ek}^{-1/2}$ and arrest timescales $\tilde{\tau}_A = 1/S$.

continental slope. Both the canonical and transport-constrained 1D models capture Ekman arrest, so they should produce similar results in this regime. Indeed, after five arrest times, the two model solutions show the same qualitative behavior (Fig. 2.6). In both models, the Ekman transport decays with time. The along-slope flow adjusts in the Ekman layer and shows a hint of diffusion into the interior in both cases, although the interior geostrophic flow is also spun down by a few percent in the transport-constrained 1D model. The stratification is enhanced by upwelling, although in the very bottom Ekman layer the models yield large negative perturbations to the stratification due to our choice of $\kappa = 0$. Depending on one's choice of nondimensional background stratification in (2.34), this could lead to gravitationally unstable solutions. This unphysical result was also encountered by MacCready and Rhines (1991), and subsequent studies used more sophisticated turbulence parameterizations to analyze the problem in the presence of convection (e.g., Trowbridge and Lentz, 1991; MacCready and Rhines, 1993; Brink and Lentz, 2010).

As we move into a parameter regime where spin down becomes important, the two models diverge (Fig. 2.7). With $S = 10^{-2}$ and $\text{Ek} = 10^{-4}$ ($H/\delta = 100$), the arrest and spin-down timescales are $\tilde{\tau}_A = \tilde{\tau}_S = 10^2$. Spin down is now as important as Ekman arrest. About 80% of the original geostrophic flow is eroded in the transport-constrained model after five Ekman arrest times, whereas the interior along-slope flow (by design) remains fixed at -1 in the canonical model. The rapid spin down of the geostrophic flow in the transport-constrained model also leads to much weaker Ekman transport and therefore smaller stratification changes in the boundary layer. These results are in contrast with Chapman's (2002) model, which suggested a more prominent role of Ekman arrest in this parameter regime. This quantitative difference might stem from differences in turbulence closures; Chapman (2002) used linear bottom drag, allowing his model to reach a non-trivial steady state. A more direct comparison between the two models can be achieved by employing the same turbulence closures in the transport-constrained 1D model, but that is beyond the scope of this paper. As the slope Burger number is further reduced to $S \sim 10^{-3}$ (and Ek held fixed), a value typical for abyssal ridge flanks such as in Fig. 2.1, spin down becomes strongly dominant over Ekman arrest.

To assess how accurately the ratio $\tilde{\tau}_A/\tilde{\tau}_S$ captures the competition between Ekman spin down and arrest in the transport-constrained model, we compute solutions with $\tilde{\tau}_A$ and $\tilde{\tau}_S$ varied over multiple orders of magnitude. The simple ratio of Ekman arrest time to spin down time captures the dynamics of the far-field along-slope flow remarkably well (Fig. 2.8). After five arrest times, $\tilde{t} = 5\tilde{\tau}_A$, simulations with a larger $\tilde{\tau}_A/\tilde{\tau}_S$ have smaller geostrophic flows than those with smaller ratios (Fig. 2.8a). If $\tilde{\tau}_A/\tilde{\tau}_S > 1$, the interior flow has been almost completely spun down at $\tilde{t} = 5\tilde{\tau}_A$, whereas for $\tilde{\tau}_A/\tilde{\tau}_S < 0.1$, the interior flow is almost entirely preserved at $\tilde{t} = 5\tilde{\tau}_A$ because Ekman arrest has prevented spin down. Spin down is not entirely prevented, however. After five spin-down times, $\tilde{t} = 5\tilde{\tau}_S$, the geostrophic current is substantially eroded, even when $\tilde{\tau}_A/\tilde{\tau}_S < 0.1$ (Fig. 2.8b).

2.6 Discussion

The transport-constrained model does not generally allow for a steady state. Part of the attraction of the canonical 1D model has been that it achieves a steady-state balance between buoyancy advection and diffusion. It has become apparent here, however, that this comes at the expense of implying a peculiar choice for the cross-slope mass transport: U is implicitly chosen such that the barotropic cross-slope pressure gradient is eliminated. This choice is clearly incorrect in our example of a simple 2D ridge. Our discussion therefore challenges the significance of the steady transport $U = \kappa_\infty \cot\theta$ of the canonical model. If the canonical steady state was for some reason desired, one could recover it by setting $U = \kappa_\infty \cot\theta$ in the transport-constrained 1D model, but it is not clear to us how that might be justified.[1] Instead, we argue that the transport U is the result of coupling with the non-local part of the dynamics and that achieving a steady state must also involve these non-local dynamics. The transport-constrained model thus encourages a reconsideration of the interaction between the boundary layer and interior dynamics. Boundary layer theory can be used to clarify the physics of this interaction, a topic we are planning to discuss in a separate manuscript.

The lack of a steady state also complicates discussions of the effectiveness of boundary mixing (Garrett, 1990; Garrett et al., 1993; Garrett, 2001). While advective restratification tends to be weaker with the transport constraint (cf., Ruan and Callies, 2020), a full discussion of

[1] Even if $\kappa_\infty = 0$, such that the canonical model has a steady state with $U = 0$, the evolution of the two models remains dramatically different because $U \neq 0$ in the canonical model before the steady state is reached.

this point must involve non-local effects that balance the net lightening in the 1D column, such that a steady state can be reached.

The dependence of the transport-constrained 1D model on the domain height H is worth clarifying. The spin-down physics discussed in Section 2.5 depend explicitly on H because the magnitude of the cross-slope return flow that develops in response to the Ekman transport depends on how deep a water column this return flow is distributed over. The spin-down timescale τ_S is thus proportional to H (or the Prandtl scale if the current has lateral structure on a scale similar to or smaller than the deformation radius). In contrast, the PG dynamics discussed in Section 2.4 are independent of H as long as isopycnals remain flat at the top of the domain. This is because the geostrophic adjustment of the along-slope current occurs instantaneously if the momentum tendencies are dropped. The actual rate of this adjustment, which does depend on H, becomes immaterial in the PG limit.

In general PG dynamics, the vertically integrated transport arises from the coupling between columnar baroclinic 1D inversions and the barotropic vorticity equation. The same is true in 2D, but the barotropic dynamics reduce to either $U = 0$ or an explicit formula for U (see Appendix B). Thinking of the dynamics in this way, in conjunction with boundary layer theory, is both conceptually and computationally advantageous. Extended to 3D in future work, this approach allows for new insight into the role of the bottom boundary layer in the dynamics of the abyssal circulation. The theory presented in this paper, however, does not lend itself to making claims about the large-scale context, and we do not make any effort to do so.

Throughout this work, we have relied on simple representations of turbulent momentum and buoyancy fluxes, certainly not giving justice to the complexity of turbulence in bottom boundary and stratified mixing layers. Even in idealized spin-down scenarios, turbulence can be generated by a mix of shear, gravitational, symmetric, and centrifugal instabilities (Wenegrat and Thomas, 2020). Furthermore, we have ignored the presence of small-scale topography, which excites the strong internal-wave field that produces bottom-intensified turbulence (e.g., Nikurashin and Legg, 2011), as well as baroclinic eddies, which might help restratify abyssal mixing layers (Callies, 2018). More sophisticated turbulence parameterizations can be added to the transport-constrained equations, or the transport constraint can be added to local three-dimensional calculations in slope-aligned coordinates that resolve the turbulence (e.g., Wenegrat et al., 2018; Callies, 2018; Ruan et al., 2019; Wenegrat and Thomas, 2020; Ruan et al., 2021). In spin-down calculations, for example, a more faithful description of the turbulent dynamics would reintroduce the asymmetry between downwelling- and upwelling-favorable currents. Despite this added complexity, however, the transport constraint and its consequences for rapid adjustment should remain important in many circumstances.

Under what circumstances does the canonical model remain accurate? One might hope that it does if $\mathrm{Ek}^{1/2} \gg S$, so that Ekman arrest quickly halts the spin down that is not captured by the canonical model. No matter how rapidly Ekman arrest occurs, however, we find that the transport-constrained 1D model still spins down the interior flow eventually (Fig. 2.8b). Conservatively, the canonical theory should thus be restricted to times $ft \ll \mathrm{Ek}^{-1/2}$, although the lifetime can be extended if Ekman arrest is fast enough to slow down the spin down process. In any case, this argument renders the canonical steady state meaningless and implies that the canonical 1D model is never valid under the PG approximation, in which spin down is instantaneous.

Equipped with the transport-constrained model, one should revisit previous results that were based on canonical 1D dynamics. In addition to the spin-down problem, in which slow diffusion is replaced by a rapid adjustment through a secondary circulation, several other topics might warrant reconsideration, for example:

1. Motivated by observations over the East Pacific Rise, Thompson and Johnson (1996) integrated the canonical equations starting from rest and with bottom-intensified mixing, very similar to the calculations presented in Section 2.4. They found bottom-intensified along-slope currents and inferred transports comparable to deep western boundary currents. Transport-constrained dynamics, however, produce flow that instead decays towards the bottom (compare Fig. 2.4b,e). While it remains unclear what happens in the presence of a planetary vorticity gradient, when interior meridional flow must be attended by vortex stretching, it is apparent that the canonical solutions should be considered less than definitive.

2. The mean flows discussed in Callies (2018) would similarly be altered by a transport constraint. Cross-slope transport in the bottom boundary layer is weaker when the integrated transport is constrained (e.g., Fig. 2.4a,d), implying that restratification by mean flows is even weaker than implied by the canonical model employed in Callies (2018). The conclusion that baroclinic eddies are crucial in enhancing the stratification in abyssal mixing layers is thus robust, as confirmed in Ruan and Callies (2020), where submesoscale eddies were found to dominate in a 3D model with constrained transport. The utility of the steady solutions to the canonical equations presented in Callies (2018), however, is called into question.

3. Benthuysen and Thomas (2012) examined the effects of boundary mixing on the potential vorticity (PV) of the fluid during the spin down of an initial along-slope current. In the canonical 1D model that they employed, the interior current is diffusively eroded until a non-trivial steady flow is reached, as described by MacCready and Rhines (1991). Benthuysen and Thomas (2012) found that the initial flow direction relative to the steady flow determines whether PV is injected or extracted from the fluid. If this study were revisited with the transport-constrained 1D model, the qual-

itative behaviour of the flow would be altered, at least if spin down dominates over Ekman arrest (as in Figs. 2.7). The conclusion that PV fluxes primarily depend on the direction of the initial current, however, relies only on Ekman buoyancy flux physics and is likely robust.

2.7 Conclusions

Recent work has highlighted the role that abyssal mixing layers play in the circulation of the abyssal ocean (Ferrari et al., 2016; de Lavergne et al., 2016; McDougall and Ferrari, 2017; Holmes et al., 2018; Callies and Ferrari, 2018; Drake et al., 2020). A starting point for understanding these dynamics of a stratified, rotating fluid overlying an inclined seafloor has been the canonical 1D theory first developed by Phillips (1970) and Wunsch (1970). We have shown here, however, that the choice to set the cross-slope pressure gradient to zero in these dynamics eliminates important physics. If instead a constraint is imposed on the vertically integrated cross-slope transport, which can be thought of as arising from the non-local context of the 1D column, and a barotropic cross-slope pressure gradient is allowed, rapid spin up and spin down of the interior along-slope flow can be captured. With this transport constraint, a secondary cross-slope circulation can develop in the 1D framework, even if there are no lateral variations in the flow, and act on the interior flow. These modified 1D dynamics accurately capture the mixing-generated spin up over an idealized 2D ridge, where the canonical 1D dynamics fail. It can be hoped that these transport-constrained 1D dynamics can serve as a more reliable cornerstone for building a theory of the abyssal circulation than the canonical 1D system.

Capturing the Ekman spin down of an interior current, the transport-constrained 1D model can also be used to study the competition between spin down and Ekman arrest in a unified framework. We have presented the simplest model of this competition, employing a constant viscosity and no buoyancy diffusion, in which previous expectations are exactly matched. For $S \ll 1$, the competition is described completely by the ratio of spin-down and arrest timescales $\tau_A/\tau_S = \mathrm{Ek}^{1/2}/S$ (MacCready and Rhines, 1991; Garrett et al., 1993). A more detailed exploration of these dynamics, with more realistic turbulence closures plugged into the transport-constrained model or with a transport constraint imposed on turbulence-resolving simulations, is left to future work.

Data availability statement. The numerical models for all the simulations presented here are hosted at `https://github.com/hgpeterson/nuPGCM`.

Acknowledgments. We thank Henri Drake, Xiaozhou Ruan, and Paola Cessi for useful discussions of this work. We also thank the two anonymous reviewers for their insightful comments on the manuscript.

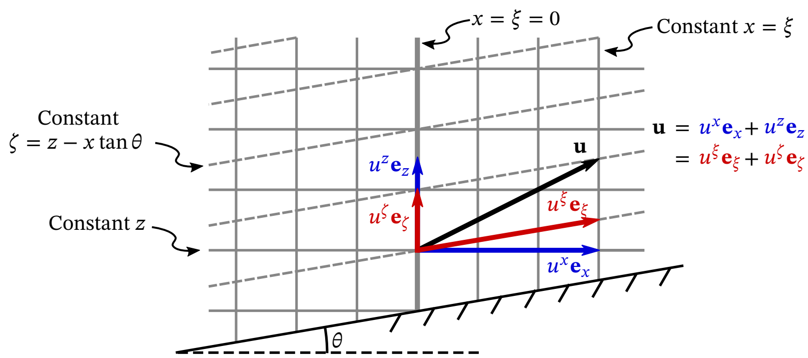

Figure 2.9: Sketch of the coordinates aligned with the slope and gravity as used in the 1D model. The covariant basis vector of coordinate j is denoted by $\boldsymbol{e}_j$, and the corresponding contravariant component of the velocity vector is denoted by u^j, such that $\boldsymbol{u} = u^j\boldsymbol{e}_j$ (summation implied).

2.8 Appendix A: 1D Model in Coordinates Aligned with the Slope and Gravity

Here we derive the 1D model by transforming into a coordinate system in which coordinate lines are aligned with the slope and with the direction of gravity (Fig. 2.9). This coordinate system is a more natural choice than the often-used fully rotated coordinate system if the horizontal components of the turbulent momentum and buoyancy fluxes are neglected from the outset. If the turbulence is roughly isotropic, this neglect is consistent with the assumption of a small aspect ratio made to drop inertial terms in the vertical momentum equation.

The hydrostatic Boussinesq equations in Cartesian coordinates (x, y, z), with z aligned with gravity, read

$$\frac{\partial u^x}{\partial t} + \boldsymbol{u}\cdot\nabla u^x - f u^y = -\frac{\partial p}{\partial x} + \frac{\partial}{\partial z}\left(\nu\frac{\partial u^x}{\partial z}\right), \tag{2.38}$$

$$\frac{\partial u^y}{\partial t} + \boldsymbol{u}\cdot\nabla u^y + f u^x = -\frac{\partial p}{\partial y} + \frac{\partial}{\partial z}\left(\nu\frac{\partial u^y}{\partial z}\right), \tag{2.39}$$

$$b = \frac{\partial p}{\partial z}, \tag{2.40}$$

$$\frac{\partial u^x}{\partial x} + \frac{\partial u^y}{\partial y} + \frac{\partial u^z}{\partial z} = 0, \tag{2.41}$$

$$\frac{\partial b}{\partial t} + \boldsymbol{u}\cdot\nabla b + u^z N^2 = \frac{\partial}{\partial z}\left[\kappa\left(N^2 + \frac{\partial b}{\partial z}\right)\right], \tag{2.42}$$

where the velocity components are written using superscripts rather than as u, v, and w as in the main text. The superscripts indicate contravariant components, and this tensor notation helps keep the notation clear as we transform into the non-Cartesian coordinates. We now define a new coordinate system (ξ, η, ζ) such that $\zeta = 0$ at the sloping boundary (Fig. 2.9):

$$\xi = x, \quad \eta = y, \quad \zeta = z - x\tan\theta. \tag{2.43}$$

This is analogous to terrain-following coordinates but for an infinite slope and no horizontal upper boundary (cf., Callies and Ferrari, 2018). The contravariant velocity components under this coordinate transformation are then

$$u^\xi = u^x, \quad u^\eta = u^y, \quad u^\zeta = u^z - u^x\tan\theta, \tag{2.44}$$

and the partial derivatives transform as

$$\frac{\partial}{\partial x} = \frac{\partial}{\partial \xi} - \tan\theta \frac{\partial}{\partial \zeta}, \quad \frac{\partial}{\partial y} = \frac{\partial}{\partial \eta}, \quad \frac{\partial}{\partial z} = \frac{\partial}{\partial \zeta}. \tag{2.45}$$

Hydrostatic balance thus implies that

$$-\frac{\partial p}{\partial x} = -\frac{\partial p}{\partial \xi} + \tan\theta \frac{\partial p}{\partial \zeta} = -\frac{\partial p}{\partial \xi} + b\tan\theta, \tag{2.46}$$

so that the hydrostatic Boussinesq equations in this new coordinate system read

$$\frac{\partial u^\xi}{\partial t} + \boldsymbol{u}\cdot\nabla u^\xi - f u^\eta = -\frac{\partial p}{\partial \xi} + b\tan\theta + \frac{\partial}{\partial \zeta}\left(\nu \frac{\partial u^\xi}{\partial \zeta}\right), \tag{2.47}$$

$$\frac{\partial u^\eta}{\partial t} + \boldsymbol{u}\cdot\nabla u^\eta + f u^\xi = -\frac{\partial p}{\partial \eta} + \frac{\partial}{\partial \zeta}\left(\nu \frac{\partial u^\eta}{\partial \zeta}\right), \tag{2.48}$$

$$b = \frac{\partial p}{\partial \zeta}, \tag{2.49}$$

$$\frac{\partial u^\xi}{\partial \xi} + \frac{\partial u^\eta}{\partial \eta} + \frac{\partial u^\zeta}{\partial \zeta} = 0, \tag{2.50}$$

$$\frac{\partial b}{\partial t} + \boldsymbol{u}\cdot\nabla b + u^\xi N^2\tan\theta + u^\zeta N^2 = \frac{\partial}{\partial \zeta}\left[\kappa\left(N^2 + \frac{\partial b}{\partial \zeta}\right)\right]. \tag{2.51}$$

Neglecting all variations in ξ and η, except for the barotropic pressure gradient $\partial_x P$ if desired, implies that $u^\zeta = 0$ by continuity, and the equations simplify to

$$\frac{\partial u^\xi}{\partial t} - f u^\eta = -\frac{\partial P}{\partial x} + b\tan\theta + \frac{\partial}{\partial \zeta}\left(\nu \frac{\partial u^\xi}{\partial \zeta}\right), \tag{2.52}$$

$$\frac{\partial u^\eta}{\partial t} + f u^\xi = \frac{\partial}{\partial \zeta}\left(\nu \frac{\partial u^\eta}{\partial \zeta}\right), \tag{2.53}$$

$$\frac{\partial b}{\partial t} + u^\xi N^2\tan\theta = \frac{\partial}{\partial \zeta}\left[\kappa\left(N^2 + \frac{\partial b}{\partial \zeta}\right)\right]. \tag{2.54}$$

Since $u^\xi = u^x$, $u^\eta = u^y$, and $\partial_\zeta = \partial_z$, these are equivalent to (2.5) to (2.7) (with $\partial_x P = 0$) and (2.22) to (2.24) in the main text. We note that $u^\xi = u^x$ is the horizontal projection of the cross-slope velocity as it would be defined in a fully rotated coordinate system. This is because the basis vector $\boldsymbol{e}_\xi = \boldsymbol{e}_x + \tan\theta\,\boldsymbol{e}_z$ does not have unit length (Fig. 2.9).

2.9 Appendix B: Calculation of the Cross-Ridge Transport for General Topography

For symmetric 2D bottom topography such as in Fig. 2.1, it is immediately clear by continuity and symmetry that the vertically integrated cross-ridge flow U must vanish. Similarly, if the depth H vanishes anywhere in the 2D domain, $U = 0$ everywhere follows by continuity. For general topography in a 2D periodic domain, however, we need to compute U along with the PG inversion (2.21). We here show how this can be done and illustrate the procedure with a solution for mixing-generated spin up over an asymmetric 2D ridge (Fig. 2.10).

First, it is useful to split the streamfunction χ into two components:

$$\chi = \chi^b + U\chi^U. \tag{2.55}$$

The buoyancy component χ^b is defined as solving

$$\frac{\partial^2}{\partial z^2}\left(\nu\frac{\partial^2\chi^b}{\partial z^2}\right)+\frac{f^2}{\nu}\chi^b=\frac{\partial b}{\partial x} \tag{2.56}$$

with the boundary conditions $\chi^b = 0$ at both $z = -H$ and $z = 0$. The transport component χ^U instead solves

$$\frac{\partial^2}{\partial z^2}\left(\nu\frac{\partial^2\chi^U}{\partial z^2}\right)+\frac{f^2}{\nu}\chi^U=\frac{f^2}{\nu}, \tag{2.57}$$

with the boundary conditions $\chi^U = 0$ at $z = -H$ and $\chi^U = 1$ at $z = 0$, such that (2.55) solves the inversion equation (2.21) and satisfies the boundary conditions $\chi = 0$ at $z = -H$ and $\chi = U$ at $z = 0$. Note that both χ^b and χ^U are independent of U and can be calculated without its knowledge.

To obtain a formula for U, we follow a similar approach as in the classic "Island Rule" (e.g., Pedlosky et al., 1997). We begin by taking the x-mean, denoted by $\langle\,\cdot\,\rangle$, of the x-momentum equation (2.16) at $z = 0$, which gives

$$-f\langle v\rangle-\left\langle\frac{\partial}{\partial z}\left(\nu\frac{\partial u}{\partial z}\right)\right\rangle=0 \quad \text{at} \quad z=0. \tag{2.58}$$

Applying the definition of the streamfunction and the relation (2.13), this can be written as

$$\left\langle\overline{\frac{f^2}{\nu}(\chi-U)}\right\rangle+\left\langle\frac{\partial}{\partial z}\left(\nu\frac{\partial^2\chi}{\partial z^2}\right)\right\rangle=0 \quad \text{at} \quad z=0, \tag{2.59}$$

where $\overline{(\cdot)}=\int_{-H}^{0}(\cdot)\,\mathrm{d}z$. Substituting (2.55) and solving for U yields

$$U=-\frac{\left\langle\frac{\partial}{\partial z}\left(\nu\frac{\partial^2\chi^b}{\partial z^2}\right)\right\rangle_{z=0}+\left\langle\overline{\frac{f^2}{\nu}\chi^b}\right\rangle}{\left\langle\frac{\partial}{\partial z}\left(\nu\frac{\partial^2\chi^U}{\partial z^2}\right)\right\rangle_{z=0}+\left\langle\overline{\frac{f^2}{\nu}(\chi^U-1)}\right\rangle}, \tag{2.60}$$

thus completing the solution to (2.14).

To showcase the calculation using (2.60), we perform a simulation of mixing-generated spin up over the asymmetric ridge in Fig. 2.10. We obtain $U \approx 1.7\times10^{-4}\ \mathrm{m^2\,s^{-1}}$ after three years of spin up.

2.10 Appendix C: Spin Up with Rayleigh Drag

In studies of mixing-generated spin up in the abyss, the turbulent transport of momentum has been parameterized using Rayleigh drag by Callies and Ferrari (2018) and Drake et al. (2020). Here we briefly show the consequences of such a closure in the context of the transport-constrained 1D theory.

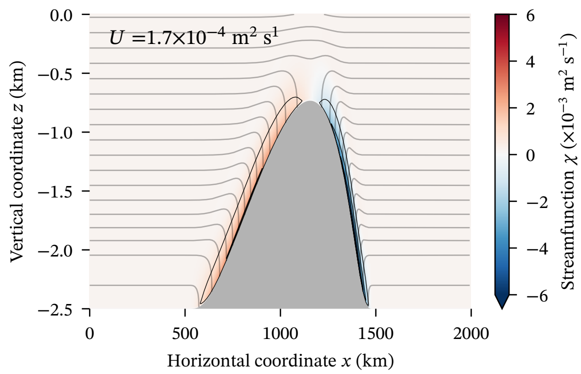

Figure 2.10: Mixing-generated spin up over an asymmetric ridge, showing net transport $U \approx 1.7 \times 10^{-4}$ m^2 s^{-1}. The streamfunction (shading and black contours) is shown at 3 years, with positive values indicating counter-clockwise flow and negative values clockwise flow. The gray curves show isopycnals.

The momentum and continuity equations for the 2D PG system with Rayleigh drag take the form

$$-fv = \frac{\partial p}{\partial x} - ru, \tag{2.61}$$

$$fu = -rv, \tag{2.62}$$

$$\frac{\partial p}{\partial z} = b, \tag{2.63}$$

$$\frac{\partial u}{\partial x} + \frac{\partial w}{\partial z} = 0, \tag{2.64}$$

where r is a friction parameter. The lower order of these equations compared with (2.16) to (2.19) reduces the number of boundary conditions that we may apply: we only require no-normal flow at the bottom and top boundaries. As above, we define a streamfunction such that $\partial_z \chi = u$, yielding the inversion equation

$$\frac{f^2 + r^2}{r} \frac{\partial^2 \chi}{\partial z^2} = -\frac{\partial b}{\partial x}, \tag{2.65}$$

with boundary conditions $\chi = 0$ at $z = -H$ and $\chi = U$ at $z = 0$. Notice that, in contrast to the case with Fickian momentum transfer, the streamfunction response to a buoyancy gradient is not localized in z. There is no height scale other than the domain height. As in Appendix B, the streamfunction can be split into buoyancy and transport components to obtain a formula for U:

$$U = -\left\langle \frac{\partial \chi^b}{\partial z} \right\rangle_{z=0} \Bigg/ \left\langle \frac{\partial \chi^U}{\partial z} \right\rangle_{z=0}. \tag{2.66}$$

Let us now compare this with the 1D system. In a slope-aligned coordinate system and with a barotropic cross-slope pressure gradient included, the PG momentum equations with

Rayleigh drag take the form

$$-fv = -\frac{\partial P}{\partial x} + b\tan\theta - ru, \tag{2.67}$$

$$fu = -rv, \tag{2.68}$$

or, as a streamfunction equation,

$$\frac{f^2 + r^2}{r}\frac{\partial^2 \chi}{\partial z^2} = \frac{\partial b}{\partial z}\tan\theta, \tag{2.69}$$

with boundary conditions $\chi = 0$ at $z = 0$ and $\chi = U$ at $z = H$. Again, the inversion is equations are equivalent in 2D and the transport-constrained 1D system. The lack of an additional height scale applies to the transport-constrained 1D model as well, which means that solutions depend strongly on the domain height H. This also means that the limit $H \to \infty$ is no attainable in the transport-constrained model with Rayleigh drag. This is clear from the vertical integral of the momentum equations, which yields

$$\frac{f^2 + r^2}{r}U = -H\frac{\partial P}{\partial x} + \int_0^H b\tan\theta \, \mathrm{d}z. \tag{2.70}$$

The limit $H \to \infty$ thus requires $\partial_x P \to 0$, but then the transport U cannot be specified separately.

As with Fickian diffusion, the transport-constrained 1D model better captures the 2D solution. Rayleigh friction applies throughout the whole water column, however, causing return flow to spread across the full domain. This leads to errors in both 1D models due to their slope-aligned coordinate system.

2.11 Appendix D: Comparison Between PG and Non-PG Transport-Constrained 1D Solutions

In the main text, we argue that the PG approximation is sufficient for describing the dynamics of mixing-generated spin up over an idealized ridge. Additionally, we claim that our PG solutions match those of Ruan and Callies (2020), who solved the 2D primitive equations. For full transparency, we here show a comparison between the transport-constrained 1D dynamics with and without momentum tendency terms included (Fig. 2.11).

To directly compare with the solutions in Ruan and Callies (2020), we use a domain height of $H = 1$ km and show the solutions in intervals of 1000 days. The slope-aligned coordinate system in the 1D theory makes it difficult to reproduce their results with boundary conditions applied on a horizontal upper boundary. To minimize boundary layer effects at the upper boundary, we therefore retain a constant buoyancy flux $-\kappa N^2$ as in the main text, which leads to slight differences in the upper 200 m from Ruan and Callies (2020).

Overall, the transport-constrained 1D PG model predicts mixing-generated spin up that is nearly identical to the 2D primitive equation solution shown in Ruan and Callies (2020)

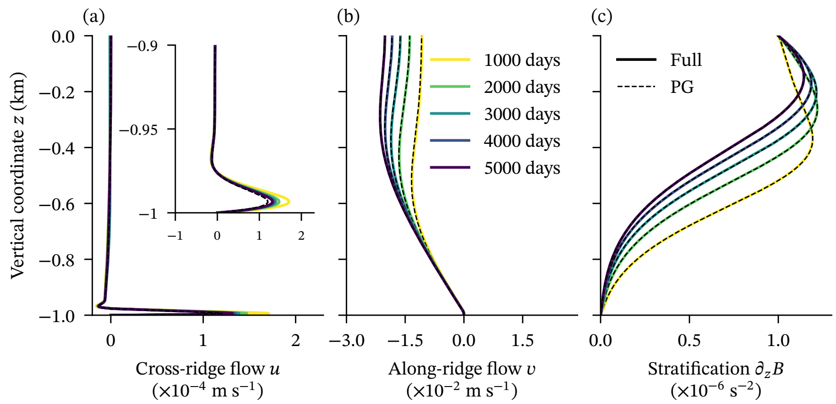

Figure 2.11: Comparison between PG and full transport-constrained 1D solutions for mixing-generated spin up. For all solutions, parameters are as in Ruan and Callies (2020) (i.e. Table 2.1 with $\mu = 1$, $\theta = 2.5 \times 10^{-3}$, and $H = 1$ km). Shown are the (a) cross-slope flow u, (b), along-slope flow v, and (c) stratification $\partial_z B$. Solid lines denote full solutions while dotted lines show PG solutions. The transport-constrained 1D PG model matches Ruan and Callies (2020) remarkably well (cf., their Fig. 4), with the full model capturing fast variations in Ekman transport [inset of panel (a)].

(cf., their Fig. 4). The only substantial difference is that the Ekman transport in the PG system instantaneously adjusts and remains roughly constant throughout the 5000 day spin up, whereas the full system produces initially larger and subsequently decreasing cross-slope flow (Fig. 2.11a). This arises because the initial buoyancy field does not satisfy the bottom boundary condition, so the initial adjustment is faster than the inertial timescale.

Chapter 3

COUPLING BETWEEN ABYSSAL BOUNDARY LAYERS AND THE INTERIOR OCEAN IN THE ABSENCE OF ALONG-SLOPE VARIATIONS

This chapter is reproduced from the published article:

Peterson, H. G., and J. Callies, 2023: Coupling between abyssal boundary layers and the interior ocean in the absence of along-slope variations. *Journal of Physical Oceanography*, **53 (1)**, 307–322, doi:10.1175/JPO-D-22-0082.1.

As a self-contained work, some notation may differ from conventions used elsewhere in this thesis.

3.1 Abstract

To close the overturning circulation, dense bottom water must upwell via turbulent mixing. Recent studies have identified thin bottom boundary layers (BLs) as locations of intense upwelling, yet it remains unclear how they interact with and shape the large-scale circulation of the abyssal ocean. The current understanding of this BL–interior coupling is shaped by 1D theory, suggesting that variations in locally produced BL transport generate exchange with the interior and thus a global circulation. Until now, however, this picture has been based on a 1D theory that fails to capture the local evolution in even highly idealized 2D geometries. The present work applies BL theory to revised 1D dynamics, which more naturally generalizes to two and three dimensions. The BL is assumed to be in quasi-equilibrium between the upwelling of dense water and the convergence of downward buoyancy fluxes. The BL transport, for which explicit formulae are presented, exerts an influence on the interior by modifying the bottom boundary condition. In 1D, this BL transport is independent of the interior evolution, but in 2D the BL and interior are fully coupled. Once interior variables and the bottom slope are allowed to vary in the horizontal, the resulting convergences and divergences in the BL transport exchange mass with the interior. This framework allows for the analysis of previously inaccessible problems such as the BL–interior coupling in the presence of an exponential interior stratification, laying the foundation for developing a full theory for the abyssal circulation.

3.2 Introduction

Thin boundary layers (BLs) at the ocean's bottom have recently come into focus as the primary locations in which small-scale turbulence lightens bottom waters, thus playing a crucial role in closing the overturning circulation of the abyss (Ferrari et al., 2016; de Lavergne et al., 2016). The connection between these BLs and the large-scale abyssal circulation, however, remains to be fully explained. The cornerstone of our present understanding of the mixing-generated abyssal circulation is a 1D model of a stratified, rotating fluid overlying a sloping, insulated seafloor (e.g., Phillips, 1970; Wunsch, 1970; Thorpe, 1987; Garrett et al., 1993). This 1D theory helped bring bottom BLs into center stage, predicting that the local response to bottom-intensified mixing is characterized by diabatic upslope flow in the thin BL compensated in part by diabatic downslope flow spread across the interior (Garrett, 1990; Ferrari et al., 2016; de Lavergne et al., 2016; McDougall and Ferrari, 2017; Callies, 2018). Our description of large-scale abyssal dynamics is shaped by this local theory: the natural conclusion is that variations in these locally produced flows generate exchange with the interior and producing a global circulation (e.g., Phillips et al., 1986; McDougall, 1989; Garrett, 1991; Dell and Pratt, 2015; Holmes et al., 2018). This picture fails to consider the potential feedback of the circulation produced in the interior back onto the BL, however, suggesting that this framework is incomplete.

In addition to this lack of two-way coupling, progress has also been hampered by the canonical 1D theory failing to reproduce the local evolution in simple 2D geometries. The canonical 1D model predicts slow diffusion of the interior along-slope flow (MacCready and Rhines, 1991), whereas simulations of bottom-intensified mixing over an idealized 2D mid-ocean ridge display rapid spin up of the interior (Ruan and Callies, 2020). In Peterson and Callies (2022, hereafter PC22), we remedied this shortcoming by including the physics of a secondary circulation and barotropic pressure gradient. The key is to constrain the vertically integrated cross-slope transport to force upwelling flow in the BL to return in the interior. This downwelling flow is then turned in the along-slope direction by the Coriolis acceleration and balanced by a barotropic pressure gradient, leading to rapid adjustment in the interior as seen in 2D. With this more faithful 1D model, we have a reliable foundation to describe the role of abyssal BLs in the large-scale circulation.

Callies and Ferrari (2018) and Drake et al. (2020) connected BL dynamics to the horizontal circulation in a 3D planetary-geostrophic (PG) model with idealized bathymetry and Rayleigh friction. Callies and Ferrari (2018) found that, for vertically constant interior stratification and on moderate slopes, local 1D theory accurately emulates the 3D model's dynamics. On the sloping sidewalls of the idealized bathymetry, upslope transport in thin bottom BLs is compensated by downwelling aloft. At the base of the slopes, however, 1D theory breaks down in favor of a basin-scale circulation that feeds the BLs on slopes. An integral of the local upslope 1D BL transport along the perimeter of the basin provides an accurate estimate of the overturning. These ideas fail, however, once the interior stratification is far from constant, because 1D theory can only consider perturbations to a constant background stratification (Drake et al., 2020). This is a severe limitation, given the real ocean's near-exponential stratification (e.g., Munk, 1966). For a more realistic stratification, downwelling in the interior is weakened and BL upwelling dominates, though the vertical extent and structure of the net transport remains to be explained. In this work, we provide a frame-

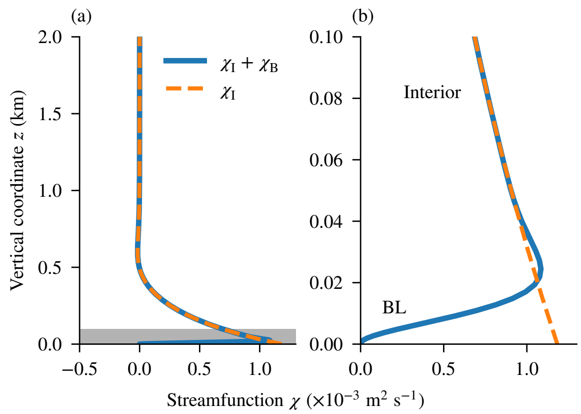

Figure 3.1: Illustration of the BL correction to interior solution. Shown is a typical streamfunction χ, defined such that $\partial_z \chi = u^x$ where u^x is the cross-slope flow, after three years of mixing-generated abyssal spin up at a slope Burger number $\varrho = 10^{-3}$ (see section 3.3). The solution is depicted over (a) the entire 2 km domain as well as (b) a zoom-in to the bottom 100 m, shown in (a) in gray shading. The interior solution χ_I varies slowly compared with the scale of the BL, and the BL correction χ_B ensures that boundary conditions are satisfied.

work for concretely understanding this interplay between the BL and interior.

Below, we derive self-contained equations for interior 1D and 2D PG dynamics on an f-plane with effective boundary conditions that capture the effects of BLs. We accomplish this using BL theory, splitting variables into their interior and BL contributions (e.g., Bender and Orszag, 1999; Chang, 2007, Fig. 3.1). This explicitly separates the interior and BL dynamics and allows for deep physical insight into their coupling. Famously, Stommel's (1948) gyre theory can be solved with BL methods (Veronis, 1966), although the coupling there is one-way: the interior solution can be calculated in isolation, and the western BL is a passive element of the theory. We find that this is different for bottom BLs on slopes. Their structure is shaped by the interior solution, but the buoyancy and mass fluxes carried in the BL feed back on the interior solution in the form of boundary conditions.

A central result of this paper is an explicit expression for the cross-slope BL transport (per unit along-slope distance) in terms of interior variables and flow parameters. In 1D, the BL transport takes the form $\kappa \cot\theta \, \mu\varrho/(1+\mu\varrho)$, where $\mu = \nu/\kappa$ is the turbulent Prandtl number with ν being the turbulent viscosity and κ the turbulent diffusivity, and $\varrho = N^2 \tan^2\theta / f^2$ is the slope Burger number with N being the background interior buoyancy frequency, f the inertial frequency, and θ the bottom slope angle. All variables are evaluated at the bottom (or, more generally, just above the BL). In the canonical 1D framework, a steady-state balance between cross-slope upwelling of dense water and turbulent mixing requires that the *total* transport tends towards $\kappa_\infty \cot\theta$, where κ_∞ is the far-field turbulent diffusivity (Thorpe, 1987; Garrett et al., 1993). Our revised result instead applies to the bottom BL transport and is valid throughout transient evolution, provided that the BL has adjusted to a quasi-steady state. Unlike the canonical result, this expression smoothly approaches zero as $\theta \to 0$, more harmoniously connecting the model over a slope with conventional flat-bottom Ekman theory (e.g., Pedlosky, 1979). The expression has the same form in 2D, but there the slope Burger number is a function of interior cross-isobath buoyancy gradients as well as the local topographic slope. Thus, in 2D, variations in interior buoyancy gradients and the topographic slope cause convergence in the BL transport, generating exchange with the interior. A similar process occurs in 3D with the added physics of along-isobath variations and a modified interior balance, but we leave the details of 3D dynamics to future work.

In section 3.3, we begin by reviewing the transport-constrained 1D model from PC22, followed by a derivation of the 1D BL theory. We derive the 2D BL theory in section 3.4, applying the framework to simulations of mixing-generated spin up under a vertically varying background stratification. In section 3.5, we re-derive the 1D and 2D BL equations in a more rigorous fashion, quantifying the accuracy of our claims in the previous sections and uncovering some subtleties in the dynamics. Finally, we provide discussion and conclusions in sections 3.6 and 3.7, respectively.

3.3 One-dimensional boundary layer theory

In this section, we apply BL theory to the revised 1D model from PC22 and present results from numerical integrations of both the full and BL equations. Here and throughout the paper, we employ PG scaling, thus focusing our attention on the slow and large-scale response to mixing. The PG flow should be interpreted as the residual flow after a thickness-weighted average over transients due to turbulence, waves, and baroclinic eddies, with the effect of these transients included as parameterized Eliassen–Palm and diapycnal fluxes (Young, 2012).

3.3.1 Transport-constrained one-dimensional dynamics

We first consider 1D PG dynamics along a uniform slope at an angle θ above the horizontal. The 1D model is typically derived by writing the Boussinesq equations in a rotated coordinate system aligned with the slope (e.g., Garrett et al., 1993). We slightly deviate from this approach by keeping the vertical coordinate aligned with gravity, which is a more natural choice if the horizontal components of the turbulent momentum and buoyancy fluxes are neglected, but it yields equivalent dynamics (PC22).[1] Specifically, we write the 1D model in (ξ, η, ζ) coordinates defined by

$$\xi = x, \quad \eta = y, \quad \zeta = z - x \tan\theta, \tag{3.1}$$

where (x, y, z) defines the usual Cartesian coordinate system with z aligned with gravity. These coordinates are analogous to terrain-following coordinates (used below) in 1D

[1] In the limit $\theta \ll 1$, the gravity-aligned coordinate system employed here and the previously used fully rotated coordinate system yield the same equations.

with $\zeta = 0$ at the bottom. Neglecting all variations in ξ and η, except for the barotropic pressure gradient $\partial_x P$ (equivalently, $\partial_\xi P$, since P is independent of z), and constraining the vertically integrated cross-slope transport to U^ξ (typically to zero), the PG equations become

$$-fu^\eta = -\frac{\partial P}{\partial x} + b' \tan\theta + \frac{\partial}{\partial \zeta}\left(\nu \frac{\partial u^\xi}{\partial \zeta}\right), \tag{3.2}$$

$$fu^\xi = \frac{\partial}{\partial \zeta}\left(\nu \frac{\partial u^\eta}{\partial \zeta}\right), \tag{3.3}$$

$$\frac{\partial b'}{\partial t} + u^\xi N^2 \tan\theta = \frac{\partial}{\partial \zeta}\left[\kappa\left(N^2 + \frac{\partial b'}{\partial \zeta}\right)\right], \tag{3.4}$$

$$\int_0^\infty u^\xi \, d\zeta = U^\xi. \tag{3.5}$$

Here, u^ξ is the cross-slope velocity[2] and u^η is the along-slope velocity. We have split the total buoyancy b into a constant background stratification and a perturbation so that $b = N^2 z + b'$. The fluid satisfies no-slip and insulating boundary conditions at the bottom: $u^\xi = 0$, $u^\eta = 0$, and $\partial_\zeta b = N^2 + \partial_\zeta b' = 0$ at $\zeta = 0$. In the far field, we impose decay conditions on the shear and anomalous buoyancy flux: $\partial_\zeta u^\xi \to 0$, $\partial_\zeta u^\eta \to 0$, and $\partial_\zeta b' \to 0$ as $\zeta \to \infty$. The extra degree of freedom supplied by $\partial_x P$ allows the transport constraint (3.5) to be satisfied at all times. Physically, this constraint forces cross-slope upwelling in the BL to return in the interior, where it is then turned into the along-slope direction by the Coriolis force. In the PG framework, this process is instantaneous, and the far-field along-slope flow satisfies the balance: $-fu^\eta = -\partial_x P$. This leads to rapid spin up of the along-slope flow throughout the water column, as seen in simulations of 2D spin up (Ruan and Callies, 2020, PC22).

We employ a simple down-gradient closure for the turbulent momentum and buoyancy fluxes generated by, e.g., breaking internal waves but allow for variations in the mixing coefficients ν and κ. We assume these variations to occur on a scale larger than the BL thickness. In our examples below, ν and κ are bottom-enhanced in abyssal mixing layers a few hundred meters thick, inspired by typical observations over rough mid-ocean ridges. Our main results, however, generalize to the case in which ν and κ vary rapidly within the BL, for example going to zero in a log-layer.

As in PC22, we cast equations (3.2) to (3.5) into an inversion equation for the flow, written in terms of a streamfunction $\chi(\zeta)$ defined such that $u^\xi = \partial_\zeta \chi$, and an evolution equation for the buoyancy perturbation:

$$\frac{\partial^2}{\partial \zeta^2}\left(\nu \frac{\partial^2 \chi}{\partial \zeta^2}\right) + \frac{f^2}{\nu}(\chi - U^\xi) = -\frac{\partial b'}{\partial \zeta}\tan\theta, \tag{3.6}$$

$$\frac{\partial b'}{\partial t} + \frac{\partial \chi}{\partial \zeta} N^2 \tan\theta = \frac{\partial}{\partial \zeta}\left[\kappa\left(N^2 + \frac{\partial b'}{\partial \zeta}\right)\right]. \tag{3.7}$$

[2]Due to our non-orthogonal coordinate system, u^ξ is technically the x-projection of the cross-slope velocity as it would be defined in a fully rotated coordinate system (PC22, appendix A). For simplicity, we refer to it as the "cross-slope velocity" throughout.

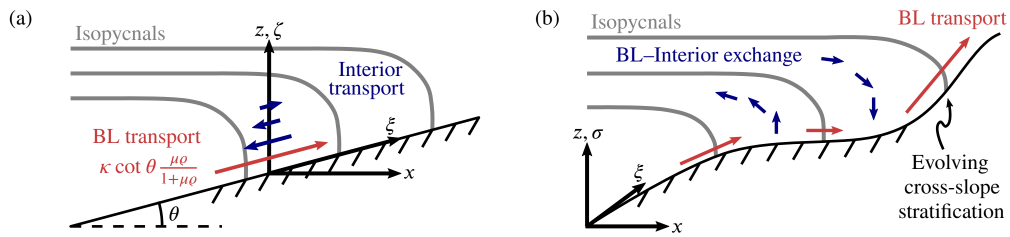

Figure 3.2: Sketch of BL theory framework for (a) 1D dynamics over a uniform slope and (b) 2D dynamics over more complicated topography.

The boundary conditions are that $\chi = 0$ and $\partial_\zeta \chi = 0$ at $\zeta = 0$ and $\chi \to U^\xi$ as $\zeta \to \infty$. If desired, one may infer the along-slope flow from χ by integrating

$$\frac{\partial u^\eta}{\partial \zeta} = \frac{f}{\nu}(\chi - U^\xi) \tag{3.8}$$

from the bottom up, using $u^\eta = 0$ at $\zeta = 0$. Equations (3.6) and (3.7) fully describe the 1D PG system and can readily be solved numerically. But insight into the BL–interior coupling is more easily gained using BL theory.

3.3.2 Boundary layer theory

Under steady conditions, equations (3.6) and (3.7) can be combined to form a single fourth-order ordinary differential equation for χ. The fourth- and zeroth-order terms in that equation balance if χ varies on a scale q^{-1} defined by

$$(\delta q)^4 = 1 + \mu\varrho, \tag{3.9}$$

where $\delta = \sqrt{2\nu/f}$ is the familiar flat-bottom Ekman layer thickness, and the mixing coefficients are evaluated at $\zeta = 0$. This defines the BL scale of a rotating fluid adjacent to a sloping bottom (e.g., Garrett et al., 1993). For typical abyssal parameters, $q^{-1} \sim 10$ m (Callies, 2018). This thinness of the BL compared to the scale of variations in the interior ocean is what allows us to apply BL theory.

We begin by splitting solutions into interior contributions χ_I and b'_I, which vary slowly in ζ, and BL corrections χ_B and b'_B, which ensure boundary conditions are satisfied and have appreciable magnitude in the thin BL only. A similar approach was taken in Callies (2018) with the canonical 1D model, but the analysis presented here is time-dependent and extensible to higher dimensions (section 3.4). If the mixing coefficients ν and κ vary on a scale much larger than q^{-1}, the fourth-order term in (3.6) can be neglected in the interior:

$$\frac{f^2}{\nu}\chi_\mathrm{I} = -\frac{\partial b'_\mathrm{I}}{\partial \zeta}\tan\theta, \tag{3.10}$$

assuming $U^\xi = 0$ (see appendix A for the $U^\xi \neq 0$ case). Substituted back into the buoyancy equation (3.7), this reduces the interior dynamics to a modified diffusion equation:

$$\frac{\partial b_{\mathrm{I}}'}{\partial t} = \frac{\partial}{\partial \zeta}\left(\kappa\left[N^2 + (1+\mu\varrho)\frac{\partial b_{\mathrm{I}}'}{\partial \zeta}\right]\right). \tag{3.11}$$

This is a result familiar from Gill (1981), Garrett and Loder (1981), and Garrett (1982): advection of the background stratification by the secondary circulation becomes a horizontal diffusion term, with diffusivity $\nu N^2/f^2$. The form here is the result of the sloping boundary: the vertical coordinate depends on the slope-parallel distance multiplied by $\tan\theta$, which explains the factor $\tan^2\theta$ in the additional diffusion term.

This interior evolution must be complemented by a representation of the bottom BL that supplies an effective boundary condition for the interior equation. The key assumption here is that the BL scale q^{-1} is thin compared to interior variations. This thinness of the BL also implies that it is quasi-steady on the time scales of the interior evolution. The BL correction thus satisfies the steady buoyancy equation

$$\frac{\partial \chi_{\mathrm{B}}}{\partial \zeta} N^2 \tan\theta = \frac{\partial}{\partial \zeta}\left(\kappa \frac{\partial b_{\mathrm{B}}'}{\partial \zeta}\right). \tag{3.12}$$

Since all BL variables decay into the interior, i.e., as $\zeta \to \infty$, this balance can be integrated to

$$\chi_{\mathrm{B}} N^2 \tan\theta = \kappa \frac{\partial b_{\mathrm{B}}'}{\partial \zeta}. \tag{3.13}$$

This relation is all that is needed to derive a boundary condition on the interior solution. At $\zeta = 0$, $\chi_{\mathrm{I}} + \chi_{\mathrm{B}} = 0$, such that the full $\chi = 0$ boundary condition is satisfied. So, using (3.10),

$$\frac{\partial b_{\mathrm{B}}'}{\partial \zeta} = -\frac{N^2\tan\theta}{\kappa}\chi_{\mathrm{I}} = \mu\varrho \frac{\partial b_{\mathrm{I}}'}{\partial \zeta} \quad \text{at} \quad \zeta = 0. \tag{3.14}$$

The insulating boundary condition then becomes

$$0 = N^2 + \frac{\partial b_{\mathrm{I}}'}{\partial \zeta} + \frac{\partial b_{\mathrm{B}}'}{\partial \zeta} = N^2 + (1+\mu\varrho)\frac{\partial b_{\mathrm{I}}'}{\partial \zeta} \quad \text{at} \quad \zeta = 0. \tag{3.15}$$

The BL correction thus contributes an additional term $\mu\varrho\partial_\zeta b_{\mathrm{I}}'$ to the boundary condition for the interior buoyancy evolution (3.11). The added term represents physics akin to an Ekman buoyancy flux (e.g., Marshall and Nurser, 1992; Thomas and Lee, 2005): the BL transport χ_{I} acts on the cross-slope buoyancy gradient $N^2\tan\theta$ and produces a buoyancy sink for the interior. This boundary condition on the interior problem implies a stratification at the top of the BL that is reduced from the background by a factor $\mu\varrho/(1+\mu\varrho)$ and a BL transport, from combining (3.15) and (3.10),

$$\chi_{\mathrm{I}} = \kappa\cot\theta \frac{\mu\varrho}{1+\mu\varrho} \quad \text{at} \quad \zeta = 0, \tag{3.16}$$

as claimed in the introduction (Fig. 3.2a). We note that the transport-constrained system, unlike the canonical one, has no steady state in a semi-infinite domain, yet previous work on the BL–interior interaction has often begun with the canonical result that the steady transport is $U^\xi = \kappa_\infty \cot\theta$ (e.g., Woods, 1991; Callies and Ferrari, 2018; Drake et al., 2020). The revised expression in (3.16) instead applies to the transport confined to the BL and more sensibly leaves the net transport (and steady-state dynamics) to be controlled by the large-scale context.

If desired, the BL correction can easily be determined from

$$\frac{\partial^4 \chi_\mathrm{B}}{\partial \zeta^4} + 4q^4 \chi_\mathrm{B} = 0, \tag{3.17}$$

with $\chi_\mathrm{B} = -\chi_\mathrm{I}$ and $\partial_\zeta \chi_\mathrm{B} = 0$ at $\zeta = 0$ (neglecting the much smaller interior contribution to $\partial_\zeta \chi$ at the bottom) and $\chi_\mathrm{B} \to 0$ as $\zeta \to \infty$. This has a similar form as the steady canonical 1D problem with constant mixing coefficients (e.g., Garrett et al., 1993), but the boundary conditions and right-hand side are different because the transport constraint is imposed and the interior solution has been subtracted out. The general solution takes the form of the familiar Ekman spiral:

$$\chi_\mathrm{B} = -\chi_\mathrm{I} e^{-q\zeta}(\cos q\zeta + \sin q\zeta), \tag{3.18}$$

where χ_I is evaluated at $\zeta = 0$ as in (3.16).

This analytical expression for the BL correction also allows us to directly diagnose how the far-field along-slope flow is influenced by the BL. From (3.8) and (3.10), the interior along-slope shear follows thermal wind balance,

$$\frac{\partial u_\mathrm{I}^\eta}{\partial \zeta} = -\frac{1}{f}\frac{\partial b_\mathrm{I}'}{\partial \zeta}\tan\theta, \tag{3.19}$$

which implies, upon integration in the vertical,

$$u_\mathrm{I}^\eta(\zeta) = u_\mathrm{I}^\eta(0) - \frac{1}{f}\left[b_\mathrm{I}'(\zeta) - b_\mathrm{I}'(0)\right]\tan\theta. \tag{3.20}$$

The integration constant $u_\mathrm{I}^\eta(0)$, the flow at the upper edge of the BL, can be determined from the BL solution (3.18) and (3.8): $u_\mathrm{I}^\eta(0) = -u_\mathrm{B}^\eta(0) = -f\chi_\mathrm{I}(0)/q\nu(0)$. This BL contribution to the interior along-slope flow has the same form as the steady-state canonical result with constant mixing coefficients (Thorpe, 1987; Garrett et al., 1993), but here it is rapidly spun up and accompanied by an additional interior thermal-wind component. We will see in section 3.5 that this BL contribution is typically of higher asymptotic order than the thermal-wind contribution.

It should be noted that the key results (3.15) and (3.16) also apply if there are variations in the mixing coefficients within the thin BL, as may be expected as the turbulence becomes suppressed very close to the bottom. The physics that lead to (3.15) and (3.16) are that the diffusive buoyancy flux into the BL is balanced by cross-slope advection within the BL and that the interior obeys (3.10). While the BL corrections are more complicated if ν and κ are not approximately constant across the BL, for example including a log-layer if the mixing coefficients go to zero near the bottom, the effective boundary condition for the interior is the same.

In summary, BL theory has enabled us to elucidate the connection between the BL and interior in 1D. The BL transport quickly adjusts to (3.16), regardless of the interior dynamics. This transport allows the BL to communicate with the interior by moving dense water up the slope, providing a buoyancy sink and modifying the interior bottom boundary condition (3.15) (Fig 3.2a). In 1D, the BL is thus independent of the evolution of the interior, yet the cross-slope advection by the BL transport affects the interior dynamics. As we will see in the next section, the BL–interior coupling in 2D are even richer, with the interior being able to feed back onto the BL. But first, we present some illustrative 1D examples.

3.3.3 Examples

The following experiments depict 1D PG spin up with and without BL theory. The simulations start in a state of rest: isopycnals are flat ($b' = 0$), and the flow is zero ($\chi = 0$). The turbulent mixing then generates a buoyancy perturbation, bending isopycnals into the slope and spinning up a circulation. The transport constraint ensures that BL transport is exactly returned in the interior, and without a source of dense bottom water, the initial stratification is mixed away with time.

To numerically solve the 1D PG equations, we use second-order finite differences as in PC22. The model can either solve for the full flow and density profiles using equations (3.6) and (3.7) or evolve the interior variables of the BL theory with equation (3.11). Model parameters are adapted from Callies (2018) and roughly match those of the Brazil Basin (Table 3.1). Mixing is represented by a bottom-intensified profile of turbulent diffusivity,

$$\kappa = \kappa_0 + \kappa_1 e^{-\zeta/h}, \tag{3.21}$$

with parameters obtained from a fit to Brazil Basin observations (Callies, 2018, Table 3.1). When solving the full 1D PG equations, grid spacing follows Chebyshev nodes with resolution on the order of 0.1 m at $\zeta = 0$ to comfortably resolve the boundary layers. The BL simulations need not resolve the thin bottom BL, and we therefore use a uniform grid

Inertial frequency	f	-5.5×10^{-5} s^{-1}
Far-field buoyancy frequency	N	10^{-3} s^{-1}
Far-field diffusivity	κ_0	6×10^{-5} m^2 s^{-1}
Bottom-enhancement of diffusivity	κ_1	2×10^{-3} m^2 s^{-1}
Decay scale of diffusivity	h	200 m
Prandtl number	μ	1

Table 3.1: Parameters used in simulations of spin up, adapted from Callies and Ferrari (2018) and roughly corresponding to the mid-Atlantic ridge flank in the Brazil Basin.

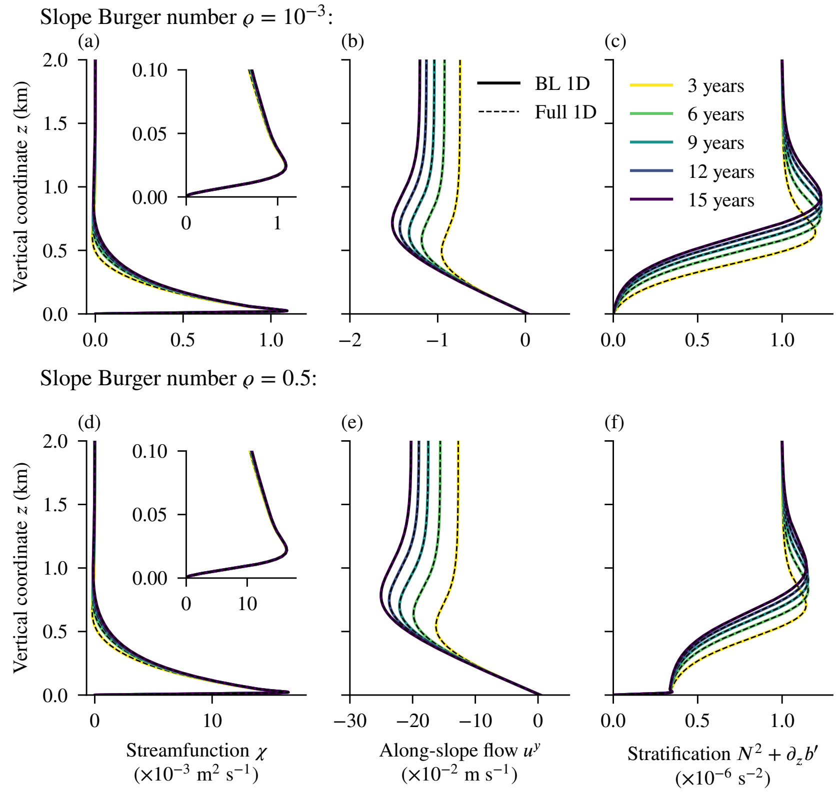

Figure 3.3: Comparison of the 1D BL solution with full 1D PG spin up over two different slope angles. Shown are the (a), (d) streamfunction χ, (b), (e) along-slope flow $u^y = u^\eta$, and (c), (f) stratification $N^2 + \partial_z b'$ as functions of $z = \zeta$ for separate simulations in which the slope Burger number is (a–c) $\varrho = 10^{-3}$, corresponding to a bottom slope of $\theta \approx 1.7 \times 10^{-3}$ rad, and (d–f) $\varrho = 0.5$ so that $\theta \approx 3.9 \times 10^{-2}$ rad. The insets of (a) and (d) show the streamfunction χ in the bottom 100 m, showcasing the accuracy of the BL correction. The 1D BL theory matches the 1D dynamics perfectly.

spacing of 8 m for these. The domain height of 2 km is large enough that upper-boundary effects do not affect the solution. The model is integrated forward in time using an implicit timestepping scheme with a timestep of one day.

The 1D BL model yields an excellent approximation of the full 1D PG solution (Fig. 3.3). The interior dynamics match the interior of the full solution, and although the BL model only explicitly computes the interior evolution, the BL correction computed offline from (3.18) is very accurate. The match is trivial when $\mu = 1$ and $\varrho = 10^{-3}$, because the shallow slope leads to a relatively weak BL transport, and thus the advective modification to the buoyancy flux in (3.11) and (3.15) is negligible. The interior system is then nearly identical to the full one, with diffusion dominating the dynamics. The case where $\varrho = 0.5$, in contrast, is a more trying test of the 1D BL theory. The BL transport in this case is an order of magnitude larger than before, leading to enhanced stratification in the BL. This is properly captured in the BL model, with the interior stratification reaching about 0.4×10^{-6} s^{-2} at the bottom and the BL correction bringing it smoothly to zero.

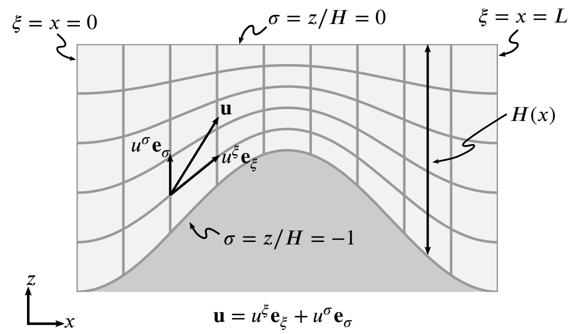

Figure 3.4: Sketch of terrain-following coordinates used in 2D BL theory. The covariant basis vector of coordinate j is denoted by $\boldsymbol{e}_j$, and the corresponding contravariant component of the velocity vector is denoted by u^j, such that $\boldsymbol{u} = u^j \boldsymbol{e}_j$ (summation implied).

The assumption of 1D dynamics breaks down as soon as lateral variations in the slope are allowed, but we can anticipate the upcoming 2D results using intuition derived from the above 1D theory. Equation (3.16) gives an explicit expression for the BL transport in 1D depending on the local slope angle θ and buoyancy gradient across the slope $N^2 \tan\theta$. In 2D, these inputs are spatially dependent, with horizontal buoyancy gradients also varying in time as part of the interior dynamics. Local 1D theory would thus predict convergences and divergences in BL transport, generating BL–interior mass exchange (Fig. 3.2b). This leads to a more complex picture in 2D, with interior dynamics feeding back onto the BL, as we will see in the following section.

3.4 Two-dimensional boundary layer theory

In this section, we extend the 1D BL theory to the 2D PG equations in terrain-following coordinates. We first derive the 2D BL equations and then apply them to idealized numerical simulations.

3.4.1 Boundary layer theory

In 2D, the interaction between the BL and interior is more interesting because, in addition to the BL advection imposing a buoyancy flux on the interior, variations in the BL transport produce mass exchange with the interior (e.g., Phillips et al., 1986; McDougall, 1989; Kunze et al., 2012; Dell and Pratt, 2015; Ledwell, 2018; Holmes et al., 2018). The BL theory generalizes from 1D to 2D and brings these physics into clearer focus.

Applying the BL theory to the 2D PG equations is most easily done in terrain-following coordinates:

$$\xi = x, \quad \eta = y, \quad \sigma = \frac{z}{H}, \tag{3.22}$$

where $H(x)$ is the fluid depth (Fig. 3.4). Under this transformation, derivatives in (x, z)

space become

$$\frac{\partial}{\partial x} = \frac{\partial}{\partial \xi} - \frac{\sigma \partial_x H}{H} \frac{\partial}{\partial \sigma} \quad \text{and} \quad \frac{\partial}{\partial z} = \frac{1}{H} \frac{\partial}{\partial \sigma}, \tag{3.23}$$

and the contravariant velocity components are

$$u^\xi = u^x, \quad u^\eta = u^y, \quad \text{and} \quad u^\sigma = \frac{1}{H}\left(u^z - \sigma \frac{\partial H}{\partial x} u^x\right), \tag{3.24}$$

assuming no variations in η (see appendix B of Callies and Ferrari (2018) for more details). The 2D PG equations in terrain-following coordinates are then

$$-f u^\eta = -\frac{\partial p}{\partial \xi} + \sigma \frac{\partial H}{\partial x} b + \frac{1}{H^2} \frac{\partial}{\partial \sigma}\left(\nu \frac{\partial u^\xi}{\partial \sigma}\right), \tag{3.25}$$

$$f u^\xi = \frac{1}{H^2} \frac{\partial}{\partial \sigma}\left(\nu \frac{\partial u^\eta}{\partial \sigma}\right), \tag{3.26}$$

$$\frac{1}{H} \frac{\partial p}{\partial \sigma} = b, \tag{3.27}$$

$$\frac{\partial}{\partial \xi}\left(H u^\xi\right) + \frac{\partial}{\partial \sigma}\left(H u^\sigma\right) = 0, \tag{3.28}$$

$$\frac{\partial b}{\partial t} + u^\xi \frac{\partial b}{\partial \xi} + u^\sigma \frac{\partial b}{\partial \sigma} = \frac{1}{H^2} \frac{\partial}{\partial \sigma}\left(\kappa \frac{\partial b}{\partial \sigma}\right), \tag{3.29}$$

where p is the pressure divided by a reference density. The boundary conditions are again an insulating and no-slip bottom, $\partial_\sigma b = 0$ and $u^\xi = u^\eta = 0$ at $\sigma = -1$; a constant-flux and free-slip top $H^{-1}\partial_\sigma b = N^2$ and $\partial_\sigma u^\xi = \partial_\sigma u^\eta = 0$ at $\sigma = 0$; and no normal flow across both boundaries, $u^\sigma = 0$ at $\sigma = -1$ and $\sigma = 0$. We neglect horizontal turbulent fluxes, consistent with the assumption of a small aspect ratio if the turbulence is close to isotropic. This is in contrast with some other PG models, which employed horizontal diffusion terms to satisfy the no-normal-flow condition at vertical side-walls (e.g., Colin de Verdière, 1986; Samelson and Vallis, 1997b).

As before, we express the momentum equations (3.25) to (3.28) as one streamfunction inversion. We define $\chi(\xi, \sigma)$ such that the continuity equation (3.28) is automatically satisfied:

$$H u^\xi = \frac{\partial \chi}{\partial \sigma} \quad \text{and} \quad H u^\sigma = -\frac{\partial \chi}{\partial \xi}. \tag{3.30}$$

Integrating (3.26) from some level to $\sigma = 0$, we obtain

$$\frac{1}{H} \frac{\partial u^\eta}{\partial \sigma} = \frac{f}{\nu}(\chi - U^\xi), \tag{3.31}$$

as in equation (3.8). Here, $U^\xi = \int_{-1}^{0} H u^\xi \, d\sigma$ is the vertically integrated transport, a constant in ξ by continuity. Combining $H^{-1}\partial_\sigma$ of (3.25) and ∂_ξ of (3.27) and substituting $H^{-1}\partial_\sigma u^\eta$ from (3.31) yields the streamfunction inversion equation similar to 1D:

$$\frac{1}{H^4} \frac{\partial^2}{\partial \sigma^2}\left(\nu \frac{\partial^2 \chi}{\partial \sigma^2}\right) + \frac{f^2}{\nu}(\chi - U^\xi) = \frac{\partial b}{\partial \xi} - \frac{\sigma}{H} \frac{\partial H}{\partial x} \frac{\partial b}{\partial \sigma}. \tag{3.32}$$

The boundary conditions are similar to the 1D case but for a finite domain: $\chi = 0$ and $\partial_\sigma \chi = 0$ at $\sigma = -1$ and $\chi = U^\xi$ and $\partial_\sigma^2 \chi = 0$ at $\sigma = 0$.

Splitting b and χ into BL and interior contributions and neglecting the fourth-order term in (3.32) in the interior as before, the interior inversion reads

$$\frac{f^2}{\nu}\chi_\mathrm{I} = \frac{\partial b_\mathrm{I}}{\partial \xi} - \frac{\sigma}{H}\frac{\partial H}{\partial x}\frac{\partial b_\mathrm{I}}{\partial \sigma} = \frac{\partial b_\mathrm{I}}{\partial x}, \tag{3.33}$$

setting $U^\xi = 0$ as implied by a configuration that is symmetric in x (see appendix A for the $U^\xi \neq 0$ case). The circulation in the x–z plane is simply proportional to the buoyancy gradient in x. The interior buoyancy evolution is given by

$$\frac{\partial b_\mathrm{I}}{\partial t} + \frac{1}{H}\left(\frac{\partial \chi_\mathrm{I}}{\partial \sigma}\frac{\partial b_\mathrm{I}}{\partial \xi} - \frac{\partial \chi_\mathrm{I}}{\partial \xi}\frac{\partial b_\mathrm{I}}{\partial \sigma}\right) = \frac{1}{H^2}\frac{\partial}{\partial \sigma}\left(\kappa \frac{\partial b_\mathrm{I}}{\partial \sigma}\right). \tag{3.34}$$

The BL physics appear in the boundary condition on the interior buoyancy field. The BL buoyancy budget, assuming a quasi-steady state and a slowly varying interior buoyancy field, is

$$\frac{1}{H}\frac{\partial \chi_\mathrm{B}}{\partial \sigma}\frac{\partial b_\mathrm{I}}{\partial \xi} = \frac{1}{H^2}\frac{\partial}{\partial \sigma}\left(\kappa \frac{\partial b_\mathrm{B}}{\partial \sigma}\right), \tag{3.35}$$

with $\partial_\xi b_\mathrm{I}$ evaluated at $\sigma = -1$. The neglected advection terms are smaller by a factor $(qH)^{-1} \ll 1$ than the terms retained in (3.35). This is because the boundary conditions enforce that $\chi_\mathrm{B} \sim \chi_\mathrm{I}$ and $\partial_\sigma b_\mathrm{B} \sim \partial_\sigma b_\mathrm{I}$, such that $\partial_\sigma \chi_\mathrm{B} \sim (qH)\partial_\sigma \chi_\mathrm{I}$ and $b_\mathrm{B} \sim (qH)^{-1} b_\mathrm{I}$ (see section 3.5 for more detail). Vertically integrating (3.35) across the BL and applying the boundary conditions $\chi_\mathrm{I} + \chi_\mathrm{B} = 0$ and $\partial_\sigma b_\mathrm{I} + \partial_\sigma b_\mathrm{B} = 0$ at $\sigma = -1$, as well as decay conditions for χ_B and $\partial_\sigma b_\mathrm{B}$, yields

$$\chi_\mathrm{I}\frac{\partial b_\mathrm{I}}{\partial \xi} = \frac{\kappa}{H}\frac{\partial b_\mathrm{I}}{\partial \sigma} \quad \text{at} \quad \sigma = -1. \tag{3.36}$$

Substituting this bottom boundary condition for the interior into the interior inversion (3.33), we again arrive at an explicit formula for this BL transport:

$$\chi_\mathrm{I} = \frac{\kappa}{\frac{\partial H}{\partial x}}\frac{\frac{\mu}{f^2}\frac{\partial H}{\partial x}\frac{\partial b_\mathrm{I}}{\partial \xi}}{1 - \frac{\mu}{f^2}\frac{\partial H}{\partial x}\frac{\partial b_\mathrm{I}}{\partial \xi}} = \frac{\frac{\nu}{f^2}\frac{\partial b_\mathrm{I}}{\partial \xi}}{1 - \frac{\mu}{f^2}\frac{\partial H}{\partial x}\frac{\partial b_\mathrm{I}}{\partial \xi}} \quad \text{at} \quad \sigma = -1. \tag{3.37}$$

This is the generalization of the 1D result (3.16): $-\partial_x H$ is analogous to the local slope $\tan\theta$ and $\partial_\xi b_\mathrm{I}$ now takes the place of the previously constant cross-slope buoyancy gradient $N^2 \tan\theta$. Note that this expression is again well-behaved in the limit of small slopes ($\partial_x H \to 0$) and thus gives a globally valid expression for the BL transport and of the mass exchange $H u_\mathrm{I}^\sigma = -\partial_\xi \chi_\mathrm{I}$ at $\sigma = -1$ between the BL and the interior.

As in 1D, we can now explicitly describe contributions to the interior along-slope flow from thermal wind in the interior and a contribution from shear in the BL. Combining (3.31) and (3.33) yields the thermal-wind balance

$$\frac{1}{H}\frac{\partial u_\mathrm{I}^\eta}{\partial \sigma} = \frac{1}{f}\frac{\partial b_\mathrm{I}}{\partial x}, \tag{3.38}$$

which, upon integration in the vertical, becomes

$$u_{\mathrm{I}}^{\eta}(\sigma) = -\frac{f\chi_{\mathrm{I}}(-1)}{\nu(-1)q} + \frac{H}{f}\int_{-1}^{\sigma}\frac{\partial b_{\mathrm{I}}}{\partial x}(\tilde{\sigma})\,d\tilde{\sigma}. \tag{3.39}$$

The first term again represents the BL contribution $u_{\mathrm{I}}^{\eta} = -u_{\mathrm{B}}^{\eta}$ at $\sigma = -1$, which may be computed directly from the BL solution

$$\chi_{\mathrm{B}} = -\chi_{\mathrm{I}}e^{-qH(\sigma+1)}[\cos qH(\sigma+1) + \sin qH(\sigma+1)], \tag{3.40}$$

similar to (3.18). Here q can still be written in the same form as in (3.9) but with a generalized slope Burger number $\varrho = -\partial_x H \partial_\xi b_{\mathrm{I}}(-1)/f^2$, which varies in the horizontal. Equation (3.39) has the same form as (3.20), except that cross-slope buoyancy gradients can now contribute to the thermal-wind term.

In 2D, we again find that the interior solution experiences a buoyancy flux due to the cross-slope advection by the BL transport. In contrast to the 1D case, however, both the BL transport given by (3.37) and the cross-slope buoyancy gradient $\partial_\xi b_{\mathrm{I}}$ may vary in time and space (Fig. 3.2b). Convergence in the BL transport then drives mass injection into the interior, further altering $\partial_\xi b_{\mathrm{I}}$ and continuing the feedback process.

It is worth noting that BL theory can also be applied to a passive tracer, not just buoyancy. The interior tracer concentration would have a similar effective boundary condition capturing transport by BL flow. The interior tracer equation should also include a representation of along-isopycnal stirring (Redi, 1982).

3.4.2 Examples

We now illustrate these theoretical results using numerical simulations over idealized topographies. We solve the full 2D PG system (3.29) and (3.32) and the 2D BL PG system (3.33) and (3.34) using numerical methods and model parameters similar to the 1D case described above. The mixing profile is now written as

$$\kappa = \kappa_0 + \kappa_1 e^{-(z+H)/h}, \tag{3.41}$$

following the bottom topography. First, we study spin up over an idealized azimuthally symmetric seamount with constant initial stratification. We then analyze spin up over an idealized mid-Atlantic ridge with both constant and exponentially varying initial stratification. As in the 1D spin up experiments, the simulations all start with flat isopycnals and no flow. The circulation that emerges is powered by the potential-energy source $\kappa\partial_z b$ integrated over the domain.

Idealized seamount

The topography of the abyssal ocean has a range of slopes. Seamounts, for instance, can reach slope Burger numbers of order 10 or more and have received some attention regarding

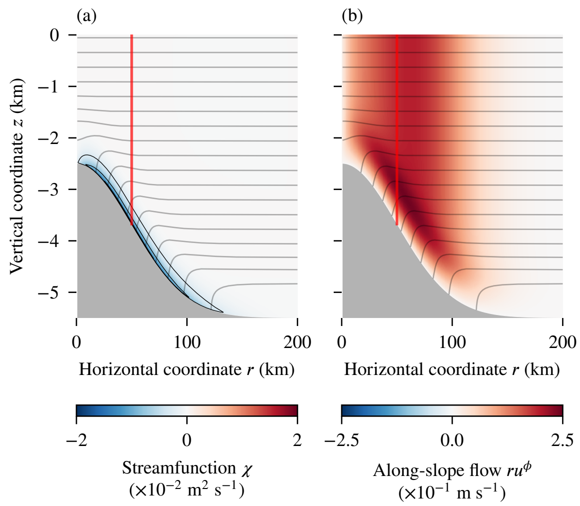

Figure 3.5: Flow fields in a simulation of mixing-generated PG spin up over an idealized 2D seamount. Shown are (a) the streamfunction χ (shading and black contours) with positive values indicating counter-clockwise and negative values indicating clockwise flow and (b) the along-slope flow $u^y = u^\eta$. The solution is shown after 20 years of spin up. The gray curves show isopycnals, and the red vertical lines show where 1D profiles are examined in Fig. 3.6.

their role in the abyssal overturning circulation (e.g., McDougall, 1989; McDougall and Ferrari, 2017; Ledwell, 2018; Holmes et al., 2018). The 1D BL theory [equation (3.11)] is sensitive to the slope Burger number, with a steeper slope leading to a larger modification of the diffusive buoyancy flux by advection. At the same time, the 2D BL theory shows that horizontal variations in this slope lead to gradients in BL transport that are not taken into account by the 1D theory. In this section, we therefore compare both 1D and 2D BL solutions to the full 2D PG flow over a seamount.

Similar to the analysis in Ledwell (2018), we consider an azimuthally symmetric Gaussian seamount in axisymmetric coordinates (Fig. 3.5). On an f-plane, the flow is invariant under rotation about the center of the seamount, allowing us to fully describe the flow using 2D theory (see appendix B). The depth of the seafloor as a function of distance r from the symmetry axis is given by

$$H(r) = H_0 - A \exp\left(-\frac{r^2}{2\ell^2}\right), \tag{3.42}$$

where the maximum depth is $H_0 = 5.5$ km, the height of the seamount is $A = 3$ km, the width of the seamount is $\ell = 50$ km, and the width of the domain is $L = 200$ km. We assume no flow at $r = 0$ and allow the flow to evolve freely at $r = L$, consistent with our assumption that horizontal diffusion may be neglected. In the horizontal, the grid has an even spacing of about 0.8 km. As in the 1D models, we use Chebyshev nodes in the vertical when solving the full 2D PG equations (with a near-bottom resolution of about 10^{-5} in σ-space) and uniform grid spacing for the 2D BL equations (with a resolution of about 10^{-3}

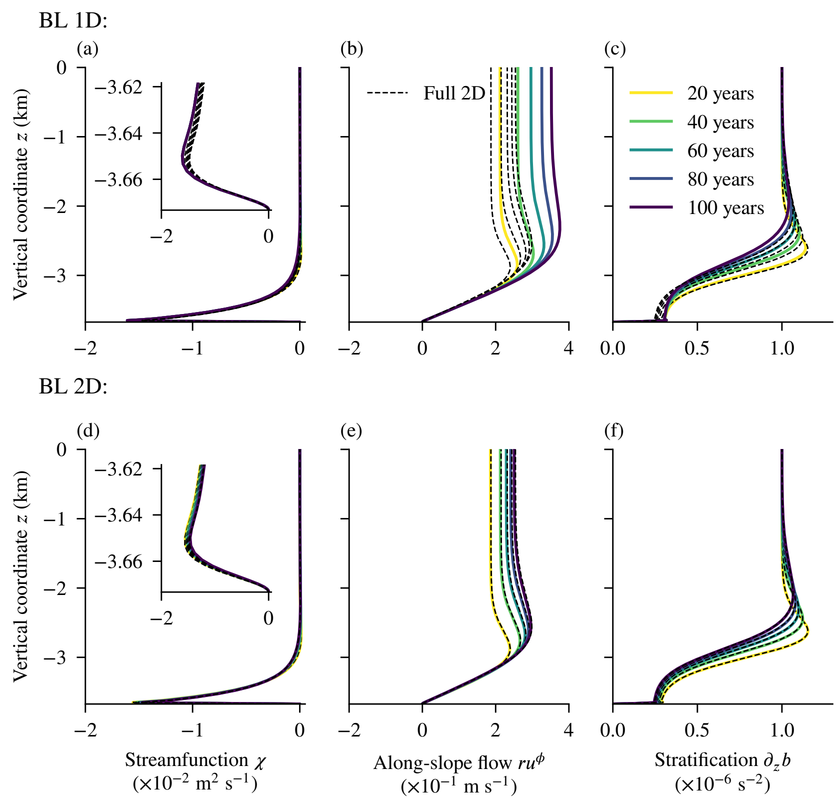

Figure 3.6: Comparison of the 1D and 2D BL solutions with full 2D PG mixing-generated spin up over a seamount. Profiles are taken at the steepest slope on the seamount (red lines in Fig. 3.5). Shown are the (a), (d) streamfunction χ, (b), (e) along-slope flow $u^y = u^\eta$, and (c), (f) stratification $\partial_z b$. The insets of (a) and (d) show the streamfunction χ in the bottom 50 m, showcasing the BL correction. The 1D BL solution is a decent approximation to the flow, but the cross-slope variations considered in the 2D BL theory allow it to better match the full 2D solution in this high slope Burger number regime.

in σ-space). We initialize the model at rest with a constant stratification $b = N^2 z$ and use a mixed implicit–explicit time integration scheme with a timestep of one day.

At the steepest point on the seamount ($r = 50$ km, red lines in Fig. 3.5), the slope Burger number ϱ is order unity. The 1D BL solution applied at this position over-predicts the stratification in the bottom 500 m and under-predicts it above (Fig. 3.6). This leads to errors in the predicted interior along-slope flow, which can be understood from (3.20) and (3.39): even subtle changes in the buoyancy field can lead to substantial impacts on u_I^η after being integrated throughout the column. The 1D BL solution's buoyancy field differs from that of the 2D solution because its secondary circulation, enforced simply by a transport constraint, is stronger. This is due to the lack of a two-way feedback in 1D; the BL cannot exchange mass with the interior and the induced changes in the interior do not reduce the BL transport. The 2D BL theory, in contrast, captures these physics and agrees well with the full 2D model. This confirms that the 2D BL equations are capable of fully capturing 2D PG spin up, even

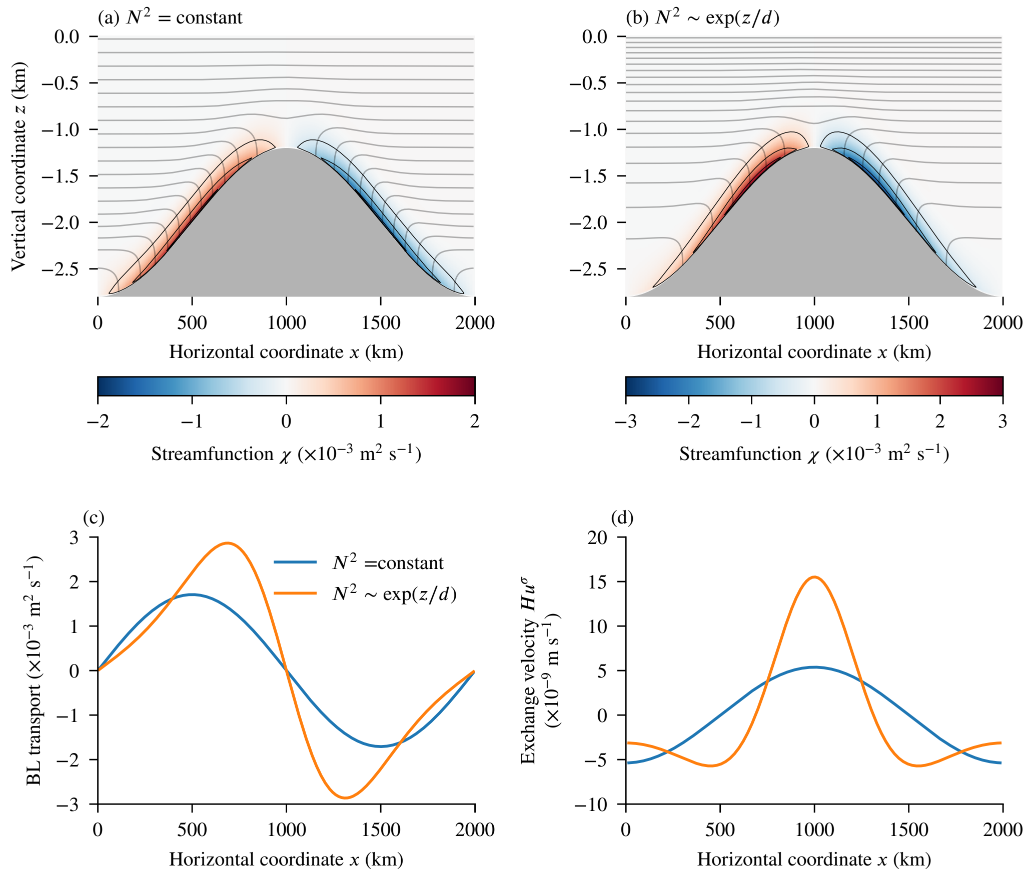

Figure 3.7: Simulations of mixing-generated PG spin up over an idealized 2D mid-ocean ridge with varying initial stratifications. Shown are the streamfunctions χ (shading and black contours) with positive values indicating counter-clockwise and negative values indicating clockwise flow for simulations with (a) constant initial stratification and (b) exponential initial stratification (isopycnals in gray). For each simulation, we show (c) the BL transport U_B^ξ computed from equation (3.37) and (d) the resulting exchange velocity $Hu^\sigma = -\partial_\xi U_\mathrm{B}^\xi$. The solutions are shown after three years of spin up. The gradient in stratification across the ridge facilitates larger exchange velocities at the peak and flanks.

in regimes with relatively large variations in local slope.

Exponential background stratification

The simulations presented so far were initialized with a constant background stratification. In the real ocean, the stratification varies significantly in the vertical, often decreasing close to exponentially with depth (e.g., Munk, 1966). A number of studies have attempted to discern how this may shape the abyssal circulation, often qualitatively arguing that variations in stratification across slopes must lead to gradients in BL transports, inducing BL–interior exchange (e.g., Phillips et al., 1986; Salmun et al., 1991). Quantitative explanations of this process, however, have remained complicated and opaque at best. A major benefit of the BL theory framework built up here is that it provides concise expressions for the BL transport in terms of interior variables, allowing us to reason about how varying background stratification might impact the abyss with minimal mathematical gymnastics.

Let us consider an idealized mid-Atlantic ridge, following previous studies of mixing-generated spin up in the abyss (e.g., Ruan and Callies, 2020; Drake et al., 2020, PC22). The depth of the 2D ridge is given by

$$H(x) = H_0 + A\cos\left(\frac{2\pi x}{L}\right), \tag{3.43}$$

where the mean depth is $H_0 = 2$ km, the amplitude is $A = 800$ m, and the width is $L = 2000$ km (Fig. 3.7). At the steepest point on the ridge, the slope Burger number ϱ is approximately 2×10^{-3} , typical of the mid-Atlantic ridge. We apply periodic boundary conditions at $x = 0$ and $x = L$ and use a constant horizontal grid spacing of about 8 km. The vertical grid spacing is as before. We run one simulation with constant initial stratification as before and one initialized with an exponential stratification: $\partial_z b \propto e^{z/d}$. We set the decay scale to $d = 1000$ m and choose the proportionality constant such that the bottom stratification at the center of the ridge flank matches that of the simulation with constant $N^2 = 10^{-6}$ s^{-2}. We again use a mixed implicit–explicit timestepping scheme, this time with a timestep of 10 days, enabled by the much weaker advective terms.

The circulation in the case with exponential initial stratification is stronger and more confined to the peak of the ridge compared to the case with constant initial stratification (Fig. 3.7a,b). This is better understood by the explicit formula for 2D BL transport derived in the previous subsection. Evaluating equation (3.37) for these simulations, we see that the BL transport is enhanced at the peak of the ridge with exponential background stratification (Fig. 3.7c). For the small slopes in this simulation, equation (3.37) reduces to

$$\chi_\mathrm{I} \approx \frac{\nu}{f^2}\frac{\partial b_\mathrm{I}}{\partial \xi} \quad \text{at} \quad \sigma = -1. \tag{3.44}$$

In the case with constant stratification, the initial cross-slope buoyancy gradient is proportional to $-\partial_x H$ and does not change appreciably with time, explaining the sinusoidal BL transport. For exponential stratification, in contrast, we have $\partial_\xi b_\mathrm{I} \propto -e^{-H/d}\partial_x H$, which is enhanced at shallower depths. As a result, the exchange velocity

$$Hu^\sigma = -\partial_\xi \chi_\mathrm{I} \approx -\frac{\nu}{f^2}\frac{\partial^2 b_\mathrm{I}}{\partial \xi^2} \quad \text{at} \quad \sigma = -1 \tag{3.45}$$

is also enhanced for the case with exponential stratification (Fig. 3.7d). In both cases, $\partial_\xi b_\mathrm{I}$ does not evolve much in the first three years, so the exchange does not either. The BL theory enables us to easily and quantitatively understand this behavior.

3.5 Asymptotic theory

In the previous sections, we derived the BL equations somewhat heuristically, glossing over some detail of the underlying asymptotics. In this section, we present a more rigorous derivation of the BL theory that justifies the claims in the previous sections and sheds light on the asymptotic orders of the various components of the flow. The casual reader should note that the contents of this section are not required to understand the main results of the paper.

We show below that, in both 1D and 2D, the cross-slope flow is of lower order than the along-slope flow in the interior, aligning with our intuition from the examples above. The interior flow evolves on a slow timescale driven by diffusion and second-order advection of the leading-order buoyancy in the interior. The BL flow is of first order, in between the orders of the interior along- and cross-slope flows. If the transport is constrained to zero, this implies that the leading-order interior flow vanishes at the bottom. These results do not generally hold in 3D, but we leave this generalization to future work.

3.5.1 One-dimensional asymptotics

To begin the formal derivation of the 1D BL equations, we first nondimensionalize the 1D equations (3.2)–(3.5) in order to isolate the key parameters in the problem. We define characteristic scales for the vertical coordinate, velocities, and mixing coefficients such that

$$\zeta \sim H_0, \quad u^\xi, u^\eta \sim U, \quad \nu \sim \nu_0, \quad \text{and} \quad \kappa \sim \kappa_0, \tag{3.46}$$

where ν_0 and κ_0 are characteristic values of ν and κ. We assume that the pressure and buoyancy terms in (3.2) scale with the Coriolis term and that the buoyancy perturbation scales with the background buoyancy scale:

$$\frac{\partial P}{\partial x} \sim fU \quad \text{and} \quad b' \sim \frac{fU}{\tan\theta} = N^2 H_0. \tag{3.47}$$

Assuming an advective timescale, so that

$$t \sim \frac{H_0}{U\tan\theta} = \frac{f}{N^2\tan^2\theta}, \tag{3.48}$$

then yields the nondimensional 1D equations

$$-u^\eta = -\frac{\partial P}{\partial x} + b' + \varepsilon^2 \frac{\partial}{\partial \zeta}\left(\nu \frac{\partial u^\xi}{\partial \zeta}\right), \tag{3.49}$$

$$u^\xi = \varepsilon^2 \frac{\partial}{\partial \zeta}\left(\nu \frac{\partial u^\eta}{\partial \zeta}\right), \tag{3.50}$$

$$\mu\varrho\left(\frac{\partial b'}{\partial t} + u^\xi\right) = \varepsilon^2 \frac{\partial}{\partial \zeta}\left[\kappa\left(1 + \frac{\partial b'}{\partial \zeta}\right)\right], \tag{3.51}$$

$$\int_0^\infty u^\xi \, d\zeta = U^\xi, \tag{3.52}$$

where all variables are redefined to their scaled versions. The nondimensional parameters for the 1D problem are thus the Ekman number $\varepsilon^2 = \nu_0/fH_0^2$, the Prandtl number $\mu = \nu_0/\kappa_0$, and the slope Burger number $\varrho = N^2\tan^2\theta/f^2$, although μ and ϱ only appear as a product, so $\mu\varrho$ can be considered a single parameter. The reason for defining the Ekman number as ε^2 will become clear in the BL analysis below.

To develop the asymptotic theory, we assume the scaling $\varepsilon \ll 1$ and $\mu\varrho \sim 1$. While the Burger number is typically small in the abyss, the turbulent Prandtl number may be large if momentum fluxes by baroclinic eddies are taken into account. If instead $\mu\varrho \ll 1$, buoyancy advection is negligible in the BL, and the theory developed with $\mu\varrho \sim 1$ remains accurate (Fig. 3.3a).

We begin with the interior and expand all variables in ε^2: $u^\xi_\mathrm{I} = u^\xi_{\mathrm{I}0} + \varepsilon^2 u^\xi_{\mathrm{I}2} + \dots$, etc. This expansion into even powers of ε is sufficient because ε only appears as ε^2 in the interior equations. The $O(1)$ interior flow then satisfies

$$-u^\eta_{\mathrm{I}0} = -\frac{\partial P_0}{\partial x} + b'_{\mathrm{I}0}, \tag{3.53}$$

$$u^\xi_{\mathrm{I}0} = 0, \tag{3.54}$$

$$\frac{\partial b'_{\mathrm{I}0}}{\partial t} = 0. \tag{3.55}$$

At this order, the interior along-slope flow is in balance with the barotropic pressure gradient and the projection of the buoyancy perturbation, and the interior cross-slope flow is zero. The $O(1)$ buoyancy equation is trivial, implying that the interior buoyancy evolution is slow compared to the advective timescale assumed in the scaling.

To obtain the evolution of the $O(1)$ interior buoyancy, we need to go to $O(\varepsilon^2)$ and also expand the time coordinate, $\partial_t = \partial_{t_0} + \varepsilon^2 \partial_{t_2} + \dots$ Higher-order buoyancy terms inherit the slow evolution from the low orders, so $\partial_{t_0} b'_{\mathrm{I}2} = 0$. The buoyancy equation (3.51) at $O(\varepsilon^2)$ is then

$$\mu\varrho \left(\frac{\partial b'_{\mathrm{I}0}}{\partial t_2} + u^\xi_{\mathrm{I}2} \right) = \frac{\partial}{\partial \zeta} \left[\kappa \left(1 + \frac{\partial b'_{\mathrm{I}0}}{\partial \zeta} \right) \right]. \tag{3.56}$$

This implies that advection and turbulent diffusion operate on a slow time t_2. Since the $O(1)$ and $O(\varepsilon)$ interior cross-slope flows are zero, the dominant buoyancy advection is by the second-order flow in the interior, given by (3.50) at $O(\varepsilon^2)$:

$$u^\xi_{\mathrm{I}2} = \frac{\partial}{\partial \zeta} \left(\nu \frac{\partial u^\eta_{\mathrm{I}0}}{\partial \zeta} \right). \tag{3.57}$$

Equations (3.53), (3.56), and (3.57) comprise the leading-order interior dynamics. They can be expressed in terms of the streamfunction χ_I, whose leading non-zero component is $\chi_{\mathrm{I}2}$, recovering (3.10) and (3.11) above (assuming $U^\xi = 0$). The interior along-slope flow can be obtained by integrating the thermal-wind balance $\partial_\zeta u^\eta_{\mathrm{I}0} = -\partial_\zeta b'_{\mathrm{I}0}$, which follows from a ζ-derivative of (3.53):

$$u^\eta_{\mathrm{I}0} = u^\eta_{\mathrm{I}0}(0) - \left[b'_{\mathrm{I}0} - b'_{\mathrm{I}0}(0) \right]. \tag{3.58}$$

The integration constant $u^\eta_{\mathrm{I}0}(0)$ must be determined from the BL correction. If the transport constraint is $U^\xi = 0$, one finds that $u^\eta_{\mathrm{I}0}(0) = 0$.

In the thin bottom BL, ζ-derivatives are enhanced, elevating the diffusion terms in (3.49)–(3.51) to $O(1)$. Given that the BL thickness scales with ε, we assume the BL variables to depend on the re-scaled vertical coordinate $\bar{\zeta} = \zeta/\varepsilon$, with which $\partial_\zeta = \varepsilon^{-1}\partial_{\bar{\zeta}}$. The nondimensional BL equations are then

$$-u_\mathrm{B}^\eta = b_\mathrm{B}' + \frac{\partial}{\partial\bar{\zeta}}\left(\nu\frac{\partial u_\mathrm{B}^\xi}{\partial\bar{\zeta}}\right), \tag{3.59}$$

$$u_\mathrm{B}^\xi = \frac{\partial}{\partial\bar{\zeta}}\left(\nu\frac{\partial u_\mathrm{B}^\eta}{\partial\bar{\zeta}}\right), \tag{3.60}$$

$$\mu\varrho\left(\frac{\partial b_\mathrm{B}'}{\partial t} + u_\mathrm{B}^\xi\right) = \frac{\partial}{\partial\bar{\zeta}}\left(\kappa\frac{\partial b_\mathrm{B}'}{\partial\bar{\zeta}}\right). \tag{3.61}$$

Crucially, the insulating bottom boundary condition picks up a factor of ε^{-1} after this re-scaling:

$$1 + \frac{\partial b_\mathrm{I}'}{\partial\zeta} = -\frac{1}{\varepsilon}\frac{\partial b_\mathrm{B}'}{\partial\bar{\zeta}} \quad \text{at} \quad \zeta = 0. \tag{3.62}$$

This factor of ε^{-1} means that we need an $O(\varepsilon)$ BL buoyancy to absorb the $O(1)$ interior buoyancy flux into the BL. We thus expand the BL variables in terms of ε rather than ε^2. We immediately find that the $O(1)$ BL buoyancy flux must vanish at the bottom: $\partial_{\bar{\zeta}} b_\mathrm{B0}' = 0$. In the case with zero net transport ($U^\xi = 0$), this condition, along with the boundary conditions on the flow $u_\mathrm{B0}^\xi = 0$ and $u_\mathrm{B0}^\eta = -u_\mathrm{I0}^\eta$ at $\bar{\zeta} = 0$, forces the $O(1)$ BL flow to vanish and the $O(1)$ interior along-slope flow to go to zero at the bottom, consistent with the examples shown in Fig. 3.3 (see appendix A for the $U^\xi \neq 0$ case). The BL flow instead comes in at $O(\varepsilon)$, in between the orders of the interior along- and cross-slope flows. This $O(\varepsilon)$ BL flow satisfies

$$-u_\mathrm{B1}^\eta = b_\mathrm{B1}' + \frac{\partial}{\partial\bar{\zeta}}\left(\nu\frac{\partial u_\mathrm{B1}^\xi}{\partial\bar{\zeta}}\right), \tag{3.63}$$

$$u_\mathrm{B1}^\xi = \frac{\partial}{\partial\bar{\zeta}}\left(\nu\frac{\partial u_\mathrm{B1}^\eta}{\partial\bar{\zeta}}\right), \tag{3.64}$$

$$\mu\varrho u_\mathrm{B1}^\xi = \frac{\partial}{\partial\bar{\zeta}}\left(\kappa\frac{\partial b_\mathrm{B1}'}{\partial\bar{\zeta}}\right), \tag{3.65}$$

with the bottom boundary conditions $\partial_{\bar{\zeta}} b_\mathrm{B1}' = -(1 + \partial_\zeta b_\mathrm{I0}')$, $u_\mathrm{B1}^\xi = 0$, and $u_\mathrm{B1}^\eta = 0$. The tendency term $\partial_{t_0} b_\mathrm{B1}'$ is dropped because the interior does not evolve on this timescale, so the BL will not either. These BL equations are equivalent to (3.12) and (3.17).

This more rigorous derivation of the 1D BL equations clarifies the asymptotic orders of the various components of the flow. The leading-order contributions are $O(\varepsilon^2)$ for the interior cross-slope flow, $O(1)$ for the interior along-slope flow, and $O(\varepsilon)$ for both components of the BL flow. Buoyancy does not have an $O(1)$ BL correction—only its derivative does.

3.5.2 Two-dimensional asymptotics

The 2D asymptotics follow in much the same way as in 1D. We again nondimensionalize the equations of motion (3.25)–(3.29), setting characteristic scales equivalent to (3.46)–(3.48):

$$\xi \sim L, \quad u^\xi, u^\eta \sim U, \quad u^\sigma \sim \frac{U}{L}, \quad H \sim H_0, \quad \nu \sim \nu_0, \quad \kappa \sim \kappa_0,$$
$$p \sim UfL, \quad b \sim \frac{fUL}{H_0} = N^2 H_0, \quad t \sim \frac{L}{U}. \tag{3.66}$$

We then arrive at the nondimensional 2D PG equations

$$-u^\eta = -\frac{\partial p}{\partial \xi} + \sigma \frac{\partial H}{\partial x} b + \frac{\varepsilon^2}{H^2} \frac{\partial}{\partial \sigma}\left(\nu \frac{\partial u^\xi}{\partial \sigma}\right), \tag{3.67}$$

$$u^\xi = \frac{\varepsilon^2}{H^2} \frac{\partial}{\partial \sigma}\left(\nu \frac{\partial u^\eta}{\partial \sigma}\right), \tag{3.68}$$

$$\frac{1}{H}\frac{\partial p}{\partial \sigma} = b, \tag{3.69}$$

$$\frac{\partial}{\partial \xi}\left(H u^\xi\right) + \frac{\partial}{\partial \sigma}\left(H u^\sigma\right) = 0, \tag{3.70}$$

$$\mu\varrho\left(\frac{\partial b}{\partial t} + u^\xi \frac{\partial b}{\partial \xi} + u^\sigma \frac{\partial b}{\partial \sigma}\right) = \frac{\varepsilon^2}{H^2}\frac{\partial}{\partial \sigma}\left(\kappa \frac{\partial b}{\partial \sigma}\right), \tag{3.71}$$

where $\varrho = N^2 H_0^2 / f^2 L^2$ is now the conventional Burger number. Again assuming the scaling $\varepsilon \ll 1$ and $\mu\varrho \sim 1$, expanding interior variables in ε^2, and matching orders as before, we arrive at the complete set of interior equations

$$-u^\eta_{\mathrm{I}0} = -\frac{\partial p_{\mathrm{I}0}}{\partial \xi} + \sigma \frac{\partial H}{\partial x} b_{\mathrm{I}0}, \tag{3.72}$$

$$u^\xi_{\mathrm{I}2} = \frac{1}{H^2}\frac{\partial}{\partial \sigma}\left(\nu \frac{\partial u^\eta_{\mathrm{I}0}}{\partial \sigma}\right), \tag{3.73}$$

$$\frac{1}{H}\frac{\partial p_{\mathrm{I}0}}{\partial \sigma} = b_{\mathrm{I}0}, \tag{3.74}$$

$$\frac{\partial}{\partial \xi}\left(H u^\xi_{\mathrm{I}2}\right) + \frac{\partial}{\partial \sigma}\left(H u^\sigma_{\mathrm{I}2}\right) = 0, \tag{3.75}$$

$$\mu\varrho\left(\frac{\partial b_{\mathrm{I}0}}{\partial t_2} + u^\xi_{\mathrm{I}2} \frac{\partial b_{\mathrm{I}0}}{\partial \xi} + u^\sigma_{\mathrm{I}2} \frac{\partial b_{\mathrm{I}0}}{\partial \sigma}\right) = \frac{1}{H^2}\frac{\partial}{\partial \sigma}\left(\kappa \frac{\partial b_{\mathrm{I}0}}{\partial \sigma}\right). \tag{3.76}$$

We again find that the interior along-slope flow is of lower order than the interior cross-slope flow, and the interior buoyancy evolution is again slow. In 2D, the interior slope-normal flow $u^\sigma_{\mathrm{I}2}$ comes in, contributing a second-order advective flux in the vertical, along with the cross-slope advection. Formulated using the streamfunction $\chi_{\mathrm{I}2}$, this recovers the interior equations (3.33) and (3.34) derived above. The $O(1)$ interior along-slope flow can again be obtained by integrating thermal wind in the vertical, with the bottom correction $u^\eta_{\mathrm{I}0}(-1)$ dropping out for $U^\xi = 0$.

The BL contribution can again be assessed after a re-scaling of the vertical coordinate such that $\bar{\sigma} = \sigma/\varepsilon$. We again find that the $O(1)$ BL flow, along with the interior along-slope flow $u^\eta_{\mathrm{I}0}$ at the bottom, vanishes when $U^\xi = 0$. The BL flow is instead of $O(\varepsilon)$, satisfying

$$-u^\eta_{\mathrm{B}1} = -\frac{\partial H}{\partial x} b_{\mathrm{B}1} + \frac{1}{H^2}\frac{\partial}{\partial \bar{\sigma}}\left(\nu \frac{\partial u^\xi_{\mathrm{B}1}}{\partial \bar{\sigma}}\right), \tag{3.77}$$

$$u^\xi_{\mathrm{B}1} = \frac{1}{H^2}\frac{\partial}{\partial \bar{\sigma}}\left(\nu \frac{\partial u^\eta_{\mathrm{B}1}}{\partial \bar{\sigma}}\right), \tag{3.78}$$

$$\mu \varrho u^\xi_{\mathrm{B}1}\frac{\partial b_{\mathrm{I}0}}{\partial \xi} = \frac{1}{H^2}\frac{\partial}{\partial \bar{\sigma}}\left(\kappa \frac{\partial b_{\mathrm{B}1}}{\partial \bar{\sigma}}\right), \tag{3.79}$$

with hydrostatic balance and continuity implying that $p_{\mathrm{B}1} = 0$ and $u^\sigma_{\mathrm{B}1} = 0$, respectively. The BL is again characterized by a balance between cross-slope advection and down-gradient diffusion of buoyancy, with the BL buoyancy flux due to $b_{\mathrm{B}1}$ balancing the interior buoyancy flux due to $b_{\mathrm{I}0}$ at the bottom as before: $1 + \partial_\sigma b_{\mathrm{I}0} = -\partial_{\bar{\sigma}} b_{\mathrm{B}1}$ at $\sigma = -1$. The tendency term in (3.79) is again dropped because the interior evolution is slow, so the BL evolution must be slow as well. Expressing $H u^\xi_{\mathrm{B}1} = \partial_{\bar{\sigma}} \chi_{\mathrm{B}2}$, vertically integrating (3.79), and enforcing $\chi_{\mathrm{I}2} + \chi_{\mathrm{B}2} = 0$ at $\sigma = -1$ yields an effective boundary condition on the interior. The BL-interior exchange velocity $u^\sigma_{\mathrm{I}2} = -u^\sigma_{\mathrm{B}2}$ at $\sigma = -1$ may be obtained by vertically integrating

$$\frac{\partial}{\partial \xi}\left(H u^\xi_{\mathrm{B}1}\right) + \frac{\partial}{\partial \bar{\sigma}}\left(H u^\sigma_{\mathrm{B}2}\right) = 0. \tag{3.80}$$

The leading-order equations obtained using this more rigorous approach again match the expressions derived heuristically above. The asymptotic orders revealed by this approach are the same as in the 1D case.

3.6 Discussion

Callies and Ferrari (2018) studied the mixing-generated abyssal circulation in an idealized global basin using PG dynamics, but their model employed Rayleigh drag rather than a Fickian friction. The models and theory presented here make use of a down-gradient turbulence closure of the momentum fluxes, allowing them to produce more realistic BLs and avoid unphysical interior momentum sinks. Still, the results presented here provide some insight into the conclusions from this previous study. With Rayleigh drag, Callies and Ferrari (2018) found that the canonical 1D model was a reasonably accurate emulator for the full dynamics over slopes with a constant initial stratification. This may have been somewhat of a coincidence, as in their case the steady state canonical transport $\kappa_\infty \cot\theta$ was zero everywhere, adding a transport constraint to the canonical 1D model. With Fickian friction, setting $\kappa_\infty = 0$ does not immediately make the canonical 1D model equivalent to the transport-constrained 1D model because it still evolves diffusively and with nonzero transport, taking thousands of years to equilibrate (PC22). Rayleigh drag, in contrast, damps flow in the interior, allowing for fast adjustment (in a matter of years, not shown) to the $U^\xi = 0$ steady state. The combination of $\kappa_\infty = 0$ and Rayleigh drag thus conspired to let Callies and Ferrari (2018) get the right answer from the canonical model, but modifying either of these choices would have made the argument fall apart.

Furthermore, Callies and Ferrari's (2018) application of BL theory was somewhat *ad hoc*. For slopes steep enough for the canonical BL theory to apply, the steady-state transport was exactly zero, meaning that all upslope transport was exactly balanced by downslope transport above. The BL theory broke down at the base of the slopes, allowing the BLs to be fed by dense water from the south and the less dense downwelled water to return south, forming a basin-wide circulation that constituted an overturning. The overturning transport could thus be estimated with an isobath integral of the upslope transport in BLs on the slopes. As Drake et al. (2020) pointed out, however, this approach is not successful if the interior stratification is far from constant and canonical BL theory does not apply. The theory presented here supplies a globally valid expression for the BL transport that allows for variations in the interior stratification. At this point, this expression is only a diagnostic tool, itself depending on the interior dynamics, but it unambiguously describes how the interior can exert control on the BL, and vice versa, ultimately generating a basin-wide circulation that involves both BL and interior pathways—and mass exchange between them. This sharpens our view of the abyssal overturning, with no confusion about the roles of the BL and interior.

The framework presented here can also help understand the results from Drake et al. (2020) regarding how water mass transformations are affected by changes in the interior stratification. Using the same 3D PG model with Rayleigh friction as in Callies and Ferrari (2018), they found that the degree of compensation between BL upwelling and interior downwelling is strongly dependent on vertical variations in the initial stratification. With only the canonical 1D theory as a starting point, they were unable to explain the vertical extent and structure of water mass transformations. The BL theory presented here would enable us to understand these physics more clearly, because it explicitly separates the BL and interior components of the flow. This allows us to describe the abyssal circulation in terms of flows into and out of the BL, rather than simply bulk diapycnal motion throughout the water column. In section 3.4, we demonstrated the power of this framework in describing abyssal spin up in 2D with exponential initial stratification. Applied to 3D simulations such as those in Drake et al. (2020), this approach would undoubtedly shed light on what shapes the vertical structure of water mass transformations in the abyss.

Here, we have only presented results in 1D and 2D. We leave the 3D case to a future paper, but preliminary work indicates that much of the theory developed here carries over, although there are some key differences. In 3D, the interior dynamics satisfies geostrophic balance in both the ξ and η directions. Because of this, the asymptotics in 3D are qualitatively different from those presented in section 3.5 of this paper: instead of evolving on a slower timescale, the leading-order 3D interior buoyancy field is advected by the geostrophic velocities, with diffusion only playing a role at higher order. We anticipate that this qualitative difference between 2D and 3D may be crucial in explaining the full 3D abyssal circulation. In 3D, it is also no longer possible to write the PG inversion in terms of a scalar streamfunction. This makes the mathematics more complicated, but it is still possible to write down an expression for the 3D BL transport in terms of interior variables evaluated at the bottom. As in 2D, the 3D BL mass and buoyancy transports feed back on the interior, now with gradients in the η direction shaping the flow field. A future extension to 3D will allow us to explain the dynamics of abyssal circulations in more complicated and realistic geometries, including cases with variations in f.[3]

Our BL theory results are not only theoretically useful but could also lighten the computational demand of simulating the abyssal circulation. The interior solution can be computed without the need to resolve the thin BL, allowing numerical models to have coarser grids and larger timesteps. This is crucial when studying the 3D system over long abyssal timescales of thousands or tens of thousands of years (e.g., Wunsch and Heimbach, 2008; Liu et al., 2009; Jansen et al., 2018). This framework could even be used to analyze tracer transport without explicitly resolving the BL, allowing us to better understand carbon and heat storage (e.g., Sarmiento and Toggweiler, 1984) and Lagrangian pathways (e.g., Rousselet et al., 2021) in the abyss. If needed, the BL correction can be computed after the fact on a finer grid as was done for Figs. 3.3 and 3.6.

Although the results presented here are derived in the context of PG dynamics, they might also point the way towards a parameterization of the effects of BLs over a sloping seafloor in primitive-equation models. Applying effective boundary conditions on the interior evolution, following the BL framework, should most easily be accomplished in models with terrain-following coordinates But a translation to z-coordinates also appears feasible, which would alleviate not only the need to resolve thin boundary layers in the vertical but also the need to capture BL flow across the artificial steps in the topography in such models. An extension of the BL theory to 3D is needed, however, to produce expressions directly useful for such a parameterization effort.

The circulation in the examples presented in this paper depend on the particular, simple closure of turbulent momentum and buoyancy fluxes employed in all of them. Although Fickian friction is much more physical than Rayleigh drag, our use of it with a simple profile for ν still glosses over the true complexity of turbulence in the abyss. Without a more faithful representation of the internal-wave field and baroclinic eddies in abyssal mixing layers, we cannot claim to be accurately simulating the dynamics of the real ocean. The BL framework, however, is robust to the choice of turbulence parameterization—as long as the vertical scale of the turbulent mixing in the interior is larger than the thickness of the BL, our approach should require minimal modification. The results presented here are in terms of a particular choice of parameterization, but the general themes describing how the BL and interior communicate will carry over to more complex closures. This flexibility makes

[3] Variations in f will allow for vortex stretching in the absence of friction: $\beta u^y = f \partial_z u^z$, where $\beta = \partial_y f$. In the f-plane solutions considered here, a non-zero interior vertical velocity only appears at second order (see section 3.5).

BL theory an attractive tool for understanding the mixing-generated abyss over a hierarchy of complexities.

3.7 Conclusions

Motivated by observations of bottom-enhanced mixing, recent work on the abyssal circulation has focused on the role of thin bottom BLs (Ferrari et al., 2016; de Lavergne et al., 2016; McDougall and Ferrari, 2017; Holmes et al., 2018; Callies and Ferrari, 2018; Drake et al., 2020). Until now, the coupling between these BLs and the interior circulation remained opaque, with most of our understanding coming from somewhat heuristic arguments using 1D theory. The framework presented in this work uses BL theory to paint a clear picture of the interior–BL interaction of the mixing-generated abyssal circulation. By explicitly defining BL and interior contributions to the flow, we obtain expressions for the BL transport in 1D and 2D that are bounded for all bottom slopes, solving the old 1D conundrum of the steady total transport $\kappa_\infty \cot\theta$ being set by the far-field mixing and diverging for small slopes. In the revised theory, the BL transport is set by local flow parameters and interior variables evaluated at the bottom, with the total transport allowed to evolve according to the global context. The interior dynamics are themselves modified by this BL transport, which advects dense water up-slope and thus modifies the interior bottom boundary condition. This two-way coupling provides a complex yet transparent story of how BLs influence the abyssal circulation, and this framework makes previously unwieldy problems, such as determining the response to vertically varying initial stratification, comparatively simple. With these promising results, we anticipate that BL theory will play a crucial role in the development of a more complete understanding of the abyssal circulation in the real ocean.

Data availability statement. The numerical models for all the simulations presented here are hosted at `https://github.com/hgpeterson/nuPGCM`.

Acknowledgments. This material is based upon work supported by the National Science Foundation under Grant No. OCE-2149080. We thank David Marshall and an anonymous reviewer for their helpful feedback on our original manuscript.

3.8 Appendix A: BL Theory when $U^\xi \neq 0$

For completeness, we here show how the BL theory derivations in sections 3.3 and 3.4 are slightly altered when the transport U^ξ is non-zero. In both 1D and 2D, the interior inversion is modified to include the added transport term. The BL accounts for $1/(1+\mu\varrho)$ of the total transport, leading to a modified interior bottom boundary condition compared to before. The 2D case is special in that the total transport is itself a function of the flow and geometry of the domain (see appendix B of PC22), allowing us to derive an explicit equation for U^ξ in that case.

3.8.1 One-dimensional theory

The 1D interior inversion for general U^ξ is

$$\frac{f^2}{\nu}(\chi_\mathrm{I} - U^\xi) = -\frac{\partial b_\mathrm{I}'}{\partial \zeta}\tan\theta. \tag{3.81}$$

This does not affect $\partial_\zeta \chi_\mathrm{I}$, leaving the interior evolution equation (3.11) unchanged. This new interior balance results in a modified bottom boundary condition compared with equation (3.15):

$$\kappa\left[N^2 + (1+\mu\varrho)\frac{\partial b_\mathrm{I}'}{\partial\zeta}\right] = U^\xi N^2 \tan\theta \quad \text{at} \quad \zeta = 0. \tag{3.82}$$

The added flux on the right-hand side represents the integrated buoyancy supplied to the column by the net transport U^ξ. The BL transport (cf. 3.16) now takes the form

$$\chi_\mathrm{I} = \frac{U^\xi}{1+\mu\varrho} + \kappa\cot\theta\frac{\mu\varrho}{1+\mu\varrho} \quad \text{at} \quad \zeta = 0, \tag{3.83}$$

supplying a fraction of the total transport. For $\mu\varrho \ll 1$, the BL absorbs the majority of the added transport. Note that the bottom boundary condition may be written as $\kappa(N^2 + \partial_\zeta b_\mathrm{I}') = \chi_\mathrm{I} N^2 \tan\theta$ regardless of whether U^ξ is nonzero. The BL correction χ_B remains the same as in (3.18), with χ_I at $\zeta = 0$ now coming from (3.83).

The asymptotic order of U^ξ must match that of χ_I, so it must be restricted to be $O(\varepsilon^2)$. It is then simple to incorporate $U^\xi \neq 0$ into the theory presented in section 3.5.

3.8.2 Two-dimensional theory

In 2D, the general interior inversion is

$$\frac{f^2}{\nu}(\chi_\mathrm{I} - U^\xi) = \frac{\partial b_\mathrm{I}}{\partial \xi} - \frac{\sigma}{H}\frac{\partial H}{\partial x}\frac{\partial b_\mathrm{I}}{\partial \sigma}, \tag{3.84}$$

and again the BL absorbs a fraction of the added transport so that (3.37) becomes

$$\chi_\mathrm{I} = \frac{U^\xi}{1+\mu\varrho} + \frac{\kappa}{\partial_x H}\frac{\mu\varrho}{1+\mu\varrho} \quad \text{at} \quad \sigma = -1, \tag{3.85}$$

where $\varrho = -\partial_x H \partial_\xi b_\mathrm{I}/f^2$ at $\sigma = -1$. For symmetric topography, $U^\xi = 0$, but this is not the case in general. We can infer U^ξ for asymmetric geometries with knowledge of the interior buoyancy distribution. Evaluating (3.39) at $\sigma = 0$ and taking the mean in ξ, denoted by $\langle\cdot\rangle$, we have

$$\left\langle u_\mathrm{I}^\eta(0)\right\rangle = 0 = -\left\langle \frac{f}{q\nu}\chi_\mathrm{I}\right\rangle + \left\langle \frac{H}{f}\int_{-1}^{0}\frac{\partial b_\mathrm{I}}{\partial x}(\sigma)\,d\sigma\right\rangle, \tag{3.86}$$

where, crucially, the BL transport from equation (3.85) now depends on U^ξ . We have assumed that the domain is tall enough such that gradients in buoyancy at $\sigma = 0$ are small and therefore $\langle u_\mathrm{I}^\eta(0)\rangle = 0$. Solving for U^ξ yields

$$U^\xi = \frac{\left\langle H\int_{-1}^{0}\frac{\partial b_\mathrm{I}}{\partial x}(\sigma)\,d\sigma\right\rangle + \left\langle \frac{1}{q}\frac{\partial_\xi b_\mathrm{I}}{1+\mu\varrho}\right\rangle}{\left\langle \frac{f^2}{q\nu}\frac{1}{1+\mu\varrho}\right\rangle}, \tag{3.87}$$

where all variables are evaluated at $\sigma = -1$ unless otherwise noted. Simulations of an asymmetric ridge, similar to that in appendix B of PC22, confirm the accuracy of this formula (not shown).

Again, we restrict ourselves to cases where the non-dimensional U^ξ is $O(\varepsilon^2)$, the same order as χ_I. This is true when the second term on the right in equation (3.86) of lower order than the first. This is always the case after a fast initial adjustment.

3.9 Appendix B: Axisymmetric Coordinates

For simulations of an idealized seamount, we transform to axisymmetric coordinates, assuming rotational symmetry. The depth H is then a function of the radial distance r and invariant under rotation about the origin by some angle ϕ, leading to effectively 2D flow. Defining $\rho = r$ and $\sigma = z/H$, we have

$$-\rho f u^\phi = -\frac{\partial p}{\partial \rho} + \sigma \frac{\partial H}{\partial r} b + \frac{1}{H^2}\frac{\partial}{\partial \sigma}\left(\nu \frac{\partial u^\rho}{\partial \sigma}\right), \tag{3.88}$$

$$\rho f u^\rho = \frac{\rho^2}{H^2}\frac{\partial}{\partial \sigma}\left(\nu \frac{\partial u^\phi}{\partial \sigma}\right), \tag{3.89}$$

$$\frac{\partial p}{\partial \sigma} = bH, \tag{3.90}$$

$$\frac{\partial}{\partial \rho}(\rho H u^\rho) + \frac{\partial}{\partial \sigma}(\rho H u^\sigma) = 0, \tag{3.91}$$

$$\frac{\partial b}{\partial t} + u^\rho \frac{\partial b}{\partial \rho} + u^\sigma \frac{\partial b}{\partial \sigma} = \frac{1}{H^2}\frac{\partial}{\partial \sigma}\left(\kappa \frac{\partial b}{\partial \sigma}\right). \tag{3.92}$$

The streamfunction inversion takes the same form as in Cartesian coordinates,

$$\frac{1}{H^4}\frac{\partial^2}{\partial \sigma^2}\left(\nu \frac{\partial^2 \chi}{\partial \sigma^2}\right) + \frac{f^2}{\nu}(\chi - U) = \frac{\partial b}{\partial \rho} - \frac{\sigma}{H}\frac{\partial H}{\partial r}\frac{\partial b}{\partial \sigma}, \tag{3.93}$$

with a slight difference in the streamfunction definition due to the new form of the divergence operator:

$$u^\rho = \frac{1}{H}\frac{\partial \chi}{\partial \sigma} \quad \text{and} \quad u^\sigma = -\frac{1}{\rho H}\frac{\partial(\rho\chi)}{\partial \rho}. \tag{3.94}$$

Chapter 4

THE νPGCM: A FLEXIBLE FINITE ELEMENT MODEL OF THE LARGE-SCALE OCEAN CIRCULATION

4.1 Introduction

The ocean is a vast reservoir of heat, carbon, nutrients, and other tracers crucial to the evolution of Earth's climate (e.g. Sarmiento and Gruber, 2006). The dense abyssal waters formed due to buoyancy loss in the polar regions (e.g., Lumpkin and Speer, 2007; Talley, 2013) sequester these tracers away from the surface for hundreds to thousands of years, regulating the climate on long timescales (e.g., Sarmiento and Toggweiler, 1984). Alongside observational efforts, numerical ocean models are valuable tools for elucidating the key elements of this circulation. Historically, improvements in these models have gone hand-in-hand with developments in our oceanographical understanding and have shaped policy and planning (Fox-Kemper et al., 2021). In particular, the character of the modeled overturning circulation exherts a strong control on simulated past (e.g., Kageyama et al., 2009; Zhang et al., 2013), present, and future (e.g., Gregory et al., 2005; Winton et al., 2014; He et al., 2017; Weijer et al., 2020; Baker et al., 2023) climates.

Paradoxically, this slow, planetary-scale circulation is dependent on fast, small-scale turbulence that cannot be directly resolved in a numerical model of the global ocean. The densest bottom waters formed in the Southern Ocean must undergo diapycnal mixing to lighten and return to the surface (e.g., Munk, 1966; Munk and Wunsch, 1998; Ferrari, 2014). Typically, this small-scale mixing is parameterized in models by down-gradient diffusion of buoyancy with either a fixed profile of turbulent diffusivity κ or a time-dependent scheme calibrated to high-resolution simulations (e.g., Large et al., 1994). Microstructure observations of turbulence in the abyss show that mixing is strongly heterogeneous and most vigorous over rough topography (e.g. Polzin et al., 1997; Ledwell et al., 2000; Waterhouse et al., 2014), where internal waves break and become non-linear (e.g., Garrett and Kunze, 2007; Nikurashin and Ferrari, 2011). This spatial structure of turbulence suggests that the abyssal upwelling crucial for closing the overturning is confined to the bottom $O(10\text{ m})$ of the ocean and over topographic slopes (e.g., Ferrari et al., 2016; de Lavergne et al., 2016; McDougall and Ferrari, 2017).

These thin bottom boundary layers (BLs) present a unique challenge in simulating the large-scale ocean circulation. Due to computational demands, even state-of-the-art global ocean models have a resolution of $O(100\text{ m})$ near the bottom (e.g., ECCO Consortium et al., 2021), with yet coarser resolutions needed to simulate the coupled climate system over thousands of years (e.g., Rugenstein et al., 2019). When simulating the full Boussinesq system, the timestep is limited by fast-timescale dynamics such as small-scale turbulence, internal waves, and baroclinic eddies, most of which cannot be directly resolved at the coarse spatial resolution of global ocean models in the first place. A more natural approach would be to employ the planetary geostrophic (PG) approximation (e.g., Pedlosky, 1979; Vallis, 2017), filtering out the intertial terms in the momentum equations by assuming small Rossby numbers while retaining full buoyancy advection by assuming large horizontal scales. The PG equations have been a cornerstone of our understanding of the large-scale ocean circulation (e.g., Robinson and Stommel, 1959; Welander, 1959; Colin de Verdière, 1988; Samelson and Vallis, 1997a; Salmon, 1998; Pedlosky, 1998), with a number of PG circulation models (PGCMs) already in existence (e.g., Salmon, 1986; Samelson and Vallis, 1997b; Edwards et al., 1998; Callies and Ferrari, 2018). For computational simplicity, these models employ Rayleigh drag in the momentum equations, leading to excessive damping of interior flows and unphysical bottom BLs (Peterson and Callies, 2023). In our νPGCM, described below, we instead view the PG flow as the residual flow after a thickness-weighted average over transients, parameterizing their effects on momentum through an Eliassen–Palm flux with turbulent viscosity ν (e.g., Young, 2012; Jansen et al., 2024).

The complex land-sea boundary of the ocean poses another challenge for its numerical simulation. Not only is this geometry crucial in setting up the qualitative "figure-8" shape of the overturning (e.g., Ferrari et al., 2014), but in the context of abyssal upwelling, the sloping bottom is what allows bottom BL flows to upwell dense water against the stratified buoyancy field. Idealized "shoebox" models with a flat bottom are capable of generating seemingly Earth-like overturning circulations (e.g., Nikurashin and Vallis, 2011; Jansen and Nadeau, 2019), but the diapycnal upwelling of abyssal waters occurs within unrealistic BLs on vertical side-walls in these models. The majority of ocean models with realistic bathymetry use structured meshes and finite differencing (Arakawa and Lamb, 1981) due to their ease, efficiency, and familiarity (e.g., Griffies et al., 2009; Fox-Kemper et al., 2019). Although shaved-cell implementations exist to better resolve the bottom bathymetry (e.g., Adcroft et al., 1997), they are rarely used in practice and still lead to a "staircase" pattern that requires prohibitively high horizontal resolution to represent up-slope BL flows. Terrain-following vertical coordinates are an attractive solution, though errors associated with representing horizontal pressure gradients in these coordinates (e.g., Haney, 1991) and the singularity along the coastline are currently a barrier for their adoption in global models.

While less standard in models of the global ocean, the geometrical flexibility of unstructured grids and the high order accuracy of the finite element method combine to make a particularly desirable alternative. Part of the reason for the slow adoption of these methods in geophysical fluid dynamics problems is that they were initially designed for elliptic partial differential equations. The PG equations can be thought of separately as an advection–diffusion equation for buoyancy and an inversion statement for the flow and pressure. Finite element solutions to the advection–diffusion problem are now standard, though a stabilization scheme is sometimes necessary (e.g., Elman et al., 2014). The PG inversion, on the other hand, can be thought of as an incompressible Stokes problem with a body force due to rotation and the added physics of buoyancy forces. Textbook mixed finite element techniques (e.g., Hughes, 1987; Elman et al., 2014) are effective at solving the Stokes problem for isotropic diffusion, but they lose accuracy and even destabilize for hydrostatic problems (e.g., Guillén-González and Rodríguez-Galván, 2015). Following multiple other studies (e.g., Kuang et al., 2005; Garner et al., 2007; Salmon, 2009), we employ the "aspect ratio trick," artificially increasing the aspect ratio α while holding all other nondimensional parameters fixed. This re-introduces diffusion in the local-vertical momentum equation, guaranteeing numerical stability. Even for large aspect ratios ($\alpha \lesssim 1/2$) compared to the ocean ($\alpha = 10^{-3}$), the qualitative behavior of the flow remains the same.

In the next section, we introduce the PG equations that we use to describe the physics of the mixing-generated abyssal circulation. We will choose a particular nondimensionalization that makes the role of the aspect ratio explicit while also retaining isotropy in the friction terms. In section 4.3, we describe how the νPGCM solves these equations numerically using finite elements and an artificially enhanced aspect ratio. We briefly conclude with some example simulations in a parabolic bowl basin in section 4.4, showcasing some of the capabilities of this model.

4.2 Planetary geostrophic equations

As prefaced in the introduction, we aim to describe the large-scale ocean circulation using the PG equations, which are derived from the Boussinesq equations by assuming large horizontal scales and small Rossby numbers. In index notation, the dimensional PG equations in Cartesian space (x_1, x_2, x_3) read

$$2e_{ijk}\Omega_j u_k = -\frac{\partial p}{\partial x_i} + bz_i + \frac{\partial}{\partial x_j}\left(2\nu\sigma_{ij}\right), \tag{4.1}$$

$$\frac{\partial u_i}{\partial x_i} = 0, \tag{4.2}$$

$$\frac{\partial b}{\partial t} + u_i\frac{\partial b}{\partial x_i} = \frac{\partial}{\partial x_i}\left(\kappa\frac{\partial b}{\partial x_i}\right), \tag{4.3}$$

where $\boldsymbol{u} = (u_1, u_2, u_3)$ is the velocity vector, p is the pressure, and b is the buoyancy. The first term in (4.1) represents the Coriolis acceleration, with e_{ijk} the Levi–Civita symbol for the cross product and $\boldsymbol{\Omega}$ the rotation vector of the volume; we do not make the traditional approximation. The buoyancy force acts only in the direction opposite to gravity, defined by the unit vector $\boldsymbol{z}(\boldsymbol{x})$. We parameterize turbulent mixing of buoyancy by a down-gradient flux proportional to the turbulent diffusivity κ (Munk, 1966). The Eliassen–Palm fluxes parameterizing mixing due to eddies contribute a diffusion term in the momentum equations with eddy viscosity ν. To account for spatially varying ν, this friction term is written in terms of the rank-2 strain rate tensor,

$$\sigma_{ij} = \sigma(\boldsymbol{u})_{ij} = \frac{1}{2}\left(\frac{\partial u_i}{\partial x_j} + \frac{\partial u_j}{\partial x_i}\right). \tag{4.4}$$

For constant ν, this term is equivalent to the regular Laplacian of $\boldsymbol{u}$. We apply a no-slip condition on the flow at the bottom boundary of the domain Γ_B, and at the surface Γ_S we demand no normal flow and that the stress in the local horizontal direction is set by the wind stress:

$$\boldsymbol{u} = 0 \quad \text{on} \quad \Gamma_\text{B}, \tag{4.5}$$

$$u_i n_i = 0 \quad \text{and} \quad \nu\sigma_{ij}n_i = \tau_{ij}n_i \quad \text{on} \quad \Gamma_\text{S}, \tag{4.6}$$

where $\boldsymbol{n}$ is the normal vector to the boundary. The buoyancy flux through the bottom is set to $\mathcal{G}$ (typically zero unless accounting for geothermal heating effects), and either the buoyancy or the buoyancy flux can be set at the surface:

$$-\kappa\frac{\partial b}{\partial x_i}n_i = \mathcal{G} \quad \text{on} \quad \Gamma_\text{B}, \tag{4.7}$$

$$b = b_\text{S} \quad \text{or} \quad -\kappa\frac{\partial b}{\partial x_i}n_i = \mathcal{F} \quad \text{on} \quad \Gamma_\text{S}. \tag{4.8}$$

These PG dynamics can be viewed separately as an evolution equation for buoyancy (4.3) and an inversion statement for the flow (4.1). A single timestep in the numerical model, described below and illustrated in Fig. 4.4, makes use of this separation rather than simultaneously evolving the entire system. Although the code supports arbitrary initial conditions, for the purposes of understanding the basic phenomenology of the mixing-driven circulation, we here initialize all simulations with flat isopycnals aligned with gravity and constant stratification N^2 such that $\partial_z b = N^2$ at $t = 0$ (using the notation $\partial_z \equiv z_i\partial_{x_i}$).

4.2.1 Nondimensionalization and parameters

To isolate role of the aspect ratio in this problem, the νPGCM ultimately solves the nondimensional PG equations, derived below. We scale all spatial coordinates by the natural length scale of the domain L (e.g., the radius of the planet or the width of the basin) and all velocities by the same scale:

$$x_i = L\tilde{x}_i \quad \text{and} \quad u_i = U\tilde{u}_i, \tag{4.9}$$

for $i = 1, 2, 3$. Given the typical initial condition defined above, a natural scaling for buoyancy would be $b \sim N^2 H$ for some depth scale of the ocean H. Unlike in quasi-geostrophic theory, however, the PG equations do not explicitly impose a background stratification so that, in general, a representative scale for N^2 in the abyssal ocean will depend on the context of the problem. We additionally define characteristic scales for the rotation rate and mixing coefficients:

$$\Omega_i \sim \Omega, \quad \nu \sim \nu_0, \quad \kappa \sim \kappa_0. \tag{4.10}$$

Finally, we assume that the pressure gradient term in (4.1) scales with the Coriolis term, that the buoyancy also scales with the pressure scale divided by H from hydrostatic balance, and that time scales advectively:

$$p \sim \Omega U L, \quad b \sim \frac{\Omega U L}{H} = N^2 H, \quad t \sim \frac{L}{U}. \tag{4.11}$$

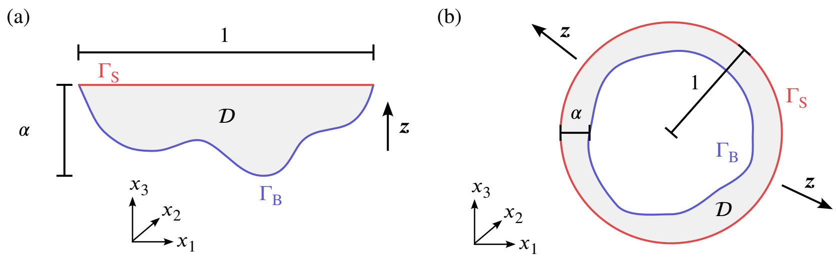

Figure 4.1: Sketches of a slice along x_1 of (a) an isolated basin with x_3 aligned with gravity and (b) the global ocean represented as a spherical shell embedded in Cartesian space.

Applying these scales to equations (4.1)–(4.3) yields the following nondimensional PG equations:

$$2e_{ijk}\tilde{\Omega}_j\tilde{u}_k = -\frac{\partial\tilde{p}}{\partial\tilde{x}_i} + \alpha^{-1}\tilde{b}z_i + \alpha^2\varepsilon^2\frac{\partial}{\partial\tilde{x}_j}\left(2\tilde{\nu}\tilde{\sigma}_{ij}\right), \tag{4.12}$$

$$\frac{\partial\tilde{u}_i}{\partial\tilde{x}_i} = 0, \tag{4.13}$$

$$\mu\varrho\left(\frac{\partial\tilde{b}}{\partial\tilde{t}} + \tilde{u}_i\frac{\partial\tilde{b}}{\partial\tilde{x}_i}\right) = \alpha^2\varepsilon^2\frac{\partial}{\partial\tilde{x}_i}\left(\tilde{\kappa}\frac{\partial\tilde{b}}{\partial\tilde{x}_i}\right), \tag{4.14}$$

where $\alpha = H/L$ is the aspect ratio, $\varepsilon^2 = \nu_0/\Omega H^2$ is the Ekman number, $\varrho = N^2H^2/\Omega^2L^2$ is the Burger number, and $\mu = \nu_0/\kappa_0$ is the turbulent Prandtl number. The wind stress boundary condition at the surface is now $\alpha^2\varepsilon^2\tilde{\nu}\tilde{\sigma}(\tilde{\boldsymbol{u}})_{ij}n_i^{\mathrm{S}} = \tilde{\tau}_{ij}n_i^{\mathrm{S}}$ and the buoyancy boundary conditions are $-\tilde{\kappa}\partial_{\tilde{x}_i}\tilde{b}n_i = \tilde{\mathcal{G}}$ at the bottom and either $\tilde{b} = \tilde{b}_{\mathrm{S}}$ or $-\tilde{\kappa}\partial_{\tilde{x}_i}\tilde{b}n_i = \tilde{\mathcal{F}}$ at the surface. Since we will work in nondimensional coordinates for the remainder of the paper, we will henceforth drop the $\tilde{}$ notation.

With all three spatial coordinates scaled by L, the effect of the aspect ratio α on the dynamics is made explicit and the domain $\mathcal{D}$ itself must have an aspect ratio of α. For an isolated basin with x_3 being the vertical coordinate aligned with gravity, this implies that $-\alpha \le x_3 \le 0$ (Fig. 4.1a). If instead $\mathcal{D}$ is the entire ocean, α naturally becomes the thickness of the shell relative to the radius of the sphere (Fig. 4.1b). This scaling guarantees that the viscous friction term in (4.12) is spatially isotropic, a desirable property for computing numerical solutions. More importantly, for $\alpha > 0$ hydrostatic balance is not exactly required, as can be seen by dotting (4.12) with the local vertical $\boldsymbol{z}$:

$$\frac{\partial p}{\partial z} = \alpha^{-1}b + \alpha^2\varepsilon^2\frac{\partial}{\partial x_j}\left(2\nu\sigma_{ij}\right)z_i, \tag{4.15}$$

where again $\partial_z \equiv z_i\partial_{x_i}$. For the ocean, typical order-of-magnitude length scales are $H \approx 10^3$ m and $L \approx 10^6$ m, implying $\alpha \approx 10^{-3}$. Hence, the small aspect ratio assumption is often made, eliminating the diffusion term in (4.15). While standard finite element techniques may be used to solve the Stokes problem with rotation, they become brittle under this approximation (e.g., Guillén-González and Rodríguez-Galván, 2015). To leverage established methods, we will therefore keep α larger than zero but small enough to capture the qualitative dynamics of the ocean. A similar approach was taken by Salmon (1986) for a PG model with Rayleigh drag. In section 4.3, we will explore the effects of an enhanced aspect ratio on the dynamics of our Fickian diffusion model.

The other parameters of the flow are free to be chosen to match the physical context. The rotation rate of the Earth is $\Omega \approx 10^{-4}$ s^{-1} and the stratification in the abyss is around $N \approx 10^{-3}$ s^{-1}, yielding a Burger number of $\varrho \approx 10^{-4}$. Over rough topography, one might expect strong turbulence associated with a turbulent diffusivity on the order of $\kappa_0 \approx 10^{-3}$ m^2 s^{-1} (e.g., Waterhouse et al., 2014). The magnitude of the turbulent viscosity depends on whether or not a parameterization of eddies is considered. Without eddies, it is reasonable to assume that, for weakly stratified abyssal waters, small-scale mixing of buoyancy would occur on similar scales to the mixing of momentum, implying that $\nu_0 \sim \kappa_0$, or $\mu \sim 1$ (e.g., Caulfield, 2021). An Eliassen–Palm flux equivalent to an eddy diffusivity of $K \approx 10^3$ m^2 s^{-1} (Gent and Mcwilliams, 1990), however, would require an enhanced viscosity of $\nu_0 \approx 10$ m^2 s^{-1}, or $\mu \approx 10^4$. This is consistent with previous studies that find $\mu \gg 1$ in the presence of submesoscale baroclinic eddies generated in abyssal mixing layers (e.g., Wenegrat et al., 2018; Callies, 2018). In the first case, where $\nu_0 \approx 10^{-3}$ m^2 s^{-1}, the Ekman number ε is on the order of 10^{-3}. In the eddy-parameterizing case of $\nu_0 \approx 10$ m^2 s^{-1}, on the other hand, it is enhanced to $\varepsilon \approx 10^{-1}$. Given that the nondimensional bottom Ekman layer thickness $\delta/L = \sqrt{2\nu_0/(\Omega_0 L^2)} = \sqrt{2}\,\alpha\varepsilon$, these differences are crucial in setting the minimum resolution required for numerical simulations. In the following, we apply the eddy parameterization with $\varepsilon = 2 \times 10^{-2}$ and $\mu = 10^4$ so that $\mu\varrho = 1$, which is both more realistic and reduces resolution constraints.

4.3 Numerical method

In this section, we describe the numerical scheme used in the νPGCM to solve the nondimensional PG equations (4.12)–(4.14). We discretize the domain using an unstructured mesh of tetrahedra, allowing considerable geometrical flexibility at the cost of requiring a more sophisticated numerical method than standard finite differences on a structured grid. The numerical solution satisfies the weak Galerkin form of the equations and lives in a specially chosen finite element space to guarantee stability. To obtain smooth solutions, we must artificially increase the aspect ratio α, introducing diffusion in the hydrostatic equation. The matrix equations for the PG inversion and evolution are solved separately using iterative solvers. We use Strang splitting to handle advection and diffusion as separate partial steps in the evolution equation.

4.3.1 Weak formulation

To derive the finite element formulation of the model equations, we first define the function spaces in which we would like our solutions to live. These spaces need not specify any

Neumann conditions such as in (4.6), (4.7), and (4.8), as those will be taken care of by boundary integrals in the weak formulation, as we will see below. The velocity, pressure, and buoyancy spaces are then

$$\mathcal{U} \equiv \left\{ \boldsymbol{u} \in [H^1(\mathcal{D})]^3 \,:\, \boldsymbol{u} = 0 \text{ on } \Gamma_{\mathrm{B}} \text{ and } u_i n_i = 0 \text{ on } \Gamma_{\mathrm{S}} \right\}, \tag{4.16}$$

$$\mathcal{P} \equiv \left\{ p \in L^2(\mathcal{D}) \,:\, \int_{\mathcal{D}} p \,\mathrm{d}\boldsymbol{x} = 0 \right\}, \tag{4.17}$$

$$\mathcal{B} \equiv L^2(\mathcal{D}) \quad \text{or} \quad \mathcal{B} \equiv \left\{ b \in L^2(\mathcal{D}) \,:\, b = b_0 \text{ on } \Gamma_{\mathrm{S}} \right\}, \tag{4.18}$$

respectively, where the buoyancy space depends on whether the Dirichlet or Neumann condition is chosen in (4.8). Here, $[H^1(\mathcal{D})]^3$ refers to the Sobolev space of all three-component vector functions that satisfy

$$\|\boldsymbol{u}\|_{H^1}^2 = \int_{\mathcal{D}} \left(u_i u_i + \frac{\partial u_i}{\partial x_j} \frac{\partial u_i}{\partial x_j} \right) \,\mathrm{d}\boldsymbol{x} < \infty, \tag{4.19}$$

and $L^2(\mathcal{D})$ refers to the Lebesgue space of all functions that are square integrable, i.e.,

$$\|p\|_{L^2}^2 = \int_{\mathcal{D}} p^2 \,\mathrm{d}\boldsymbol{x} < \infty. \tag{4.20}$$

Without the integral constraint in $\mathcal{P}$, the pressure may only be determined up to an additive constant.

The weak form of the PG inversion is obtained by dotting equations (4.12) and (4.13) with test functions $(\boldsymbol{v}, q) \in \mathcal{U} \times \mathcal{P}$, integrating over the domain, and performing integration by parts on the divergence of the strain rate, yielding

$$\int_{\mathcal{D}} \left[2e_{ijk}\Omega_j u_k v_i + \frac{\partial p}{\partial x_i} v_i + \frac{\partial u_i}{\partial x_i} q + \alpha^2 \varepsilon^2 \nu \sigma(\boldsymbol{u})_{ij} \sigma(\boldsymbol{v})_{ij} \right] \,\mathrm{d}\boldsymbol{x} = \int_{\mathcal{D}} \alpha^{-1} b z_i v_i \,\mathrm{d}\boldsymbol{x} + \int_{\Gamma_{\mathrm{S}}} \tau_{ij} n_j v_i \,\mathrm{d}\boldsymbol{x}. \tag{4.21}$$

This is known as a saddle-point problem (notice that the pressure p never multiplies its test function q). As we will see in the next section, this limits the discrete spaces on which we may stably represent the solution. Following the same steps for the buoyancy equation (4.14), this time multiplying by a test function $c \in \mathcal{B}$, yields the weak formulation

$$\int_{\mathcal{D}} \left[\frac{\partial b}{\partial t} c + u_i \frac{\partial b}{\partial x_i} c + \theta \kappa \frac{\partial b}{\partial x_i} \frac{\partial c}{\partial x_i} \right] \,\mathrm{d}\boldsymbol{x} = \theta \int_{\Gamma_{\mathrm{B}}} \mathcal{G} c \,\mathrm{d}\boldsymbol{x} + \theta \int_{\Gamma_{\mathrm{S}}} \mathcal{F} c \,\mathrm{d}\boldsymbol{x}, \tag{4.22}$$

where $\theta = \alpha^2 \varepsilon^2 / \mu \varrho$. In the Dirichlet boundary condition case, the last integral over Γ_{S} is removed .

4.3.2 Finite element discretization

To solve equations (4.21) and (4.22) numerically, we tesselate the domain into a mesh $\mathcal{T}_h$ of finite pieces (or "elements") with characteristic length scale h. In two dimensional space, each element $T_k \in \mathcal{T}_h$ is a triangle whereas in three dimensions we use tetrahedra (Fig. 4.2). In general, the quality of the mesh can have a significant impact on the accuracy of the solution. We use meshes generated by Gmsh (Geuzaine and Remacle, 2009), although there are many other meshing software packages available. We here show results for a parabolic bowl with

$$\Gamma_\mathrm{B} = \left\{ \boldsymbol{x} \in \mathbb{R}^3 \,:\, x_1^2 + x_2^2 \leq 1 \text{ and } x_3 = -\alpha(1 - x_1^2 - x_2^2) \right\}, \tag{4.23}$$

$$\Gamma_\mathrm{S} = \left\{ \boldsymbol{x} \in \mathbb{R}^3 \,:\, x_1^2 + x_2^2 \leq 1 \text{ and } x_3 = 0 \right\}, \tag{4.24}$$

though arbitrary geometries are possible with this method. In general, one now defines a subspace of the full solution space that can be spanned by a finite number of basis functions defined on the mesh, converting the continuous form of the weak formulation (4.16)–(4.22) into a discrete problem. A simple and common choice for this subspace is the set of continuous, piecewise-polynomial functions of degree n over the elements, $P_n(\mathcal{T}_h)$. Denoting each node in the mesh by $\boldsymbol{x}_i$, one can create a set of basis functions for this space $\{\varphi_i\}$ that satisfy

$$\varphi_i(\boldsymbol{x}_j) = \delta_{ij}, \tag{4.25}$$

where δ_{ij} is the Kronecker delta. For the linear space $P_1(\mathcal{T}_h)$, the element vertices supply enough nodes to span the space (orange crosses in Fig. 4.2a,c), but for higher-order spaces, more nodes are needed.

As discussed above, this formulation of the PG inversion is equivalent to the Stokes problem with rotation, allowing us to employ a standard mixed finite element scheme. Although not all discrete subspaces are stable for saddle-point problems such as (4.21), if they satisfy the so-called LBB condition, a unique solution that depends continuously on the forcing exists (e.g. Hughes, 1987; Elman et al., 2014). It is possible to choose a finite element basis that does not satisfy the LBB condition, but ad hoc stabilization schemes are necessary (e.g., Danilov et al., 2004). We instead choose the simple and accurate P_2–P_1 basis that is known to satisfy the LBB condition. In this basis, the velocities are quadratic while the pressure is linear, so that the discrete subspaces defined over the mesh are

$$\mathcal{U}_h \equiv [P_2(\mathcal{T}_h)]^3 \cap \mathcal{U} \quad \text{and} \quad \mathcal{P}_h \equiv P_1(\mathcal{T}_h) \cap \mathcal{P}. \tag{4.26}$$

The degrees of freedom for the velocity components therefore exist on both the midpoints and vertices of the elements while those of the pressure are just on the vertices (Fig. 4.2a,c). The added degrees of freedom from using second-order elements increases the computational demand of the PG inversion, but, as we will see in the next section, the convergence

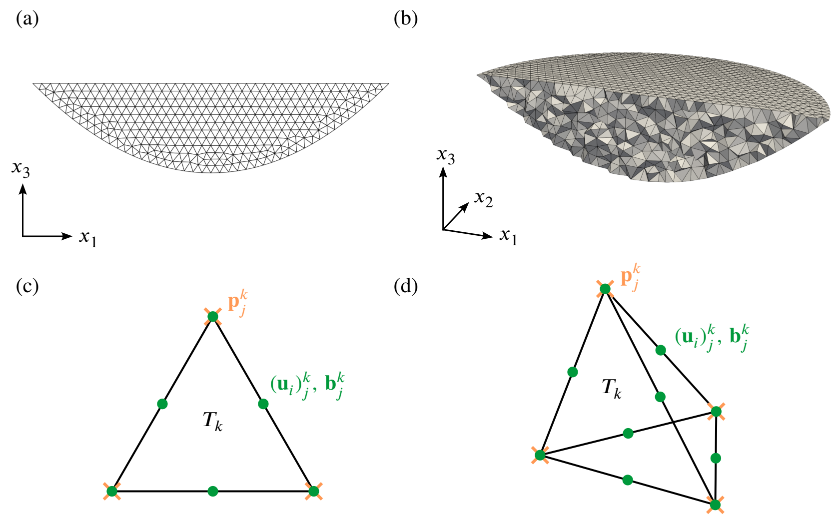

Figure 4.2: Meshes $\mathcal{T}_h$ of (a) two- and (b) three-dimensional basin domains and sketches of (c) triangular and (d) tetrahedral finite elements $T_k \in \mathcal{T}_h$. The meshes are generated for a parabolic basin with $\alpha = 1/2$ and a characteristic resolution of $h = 1/20$. In the mixed finite element method described in section 4.3.2, the pressure degrees of freedom $\mathbf{p}_j^k$ correspond to values on the vertices of each element while the velocity and buoyancy degrees of freedom $(\mathbf{u}_i)_j^k$ and $\mathbf{b}_j^k$ exist on both the vertices and midpoints. The superscripts indicate that these are the degrees of freedom on the local element T_k.

rate is rapid enough that resolution constraints are not as high. While not needed for stability, we represent buoyancy with quadratic, rather than linear, polynomials to ensure high accuracy:

$$\mathcal{B}_h \equiv P_2(\mathcal{T}_h) \cap \mathcal{B}. \tag{4.27}$$

With the discrete subspaces defined in (4.26) and (4.27), we can assemble the matrices needed to compute the PG inversion and evolve buoyancy in time. If $\{(\varphi_i)_j\}$, $\{\psi_j\}$, and $\{\varphi_i\}$ are the sets of basis vectors for $\mathcal{U}_h$, $\mathcal{P}_h$, and $\mathcal{B}_h$, respectively, then the solution to the weak formulation of the PG equations can be represented as linear combinations of these functions:

$$(u_i)_h(\boldsymbol{x}) = (\mathbf{u}_i)_j(\varphi_i)_j(\boldsymbol{x}), \quad p_h(\boldsymbol{x}) = \mathbf{p}_j\psi_j(\boldsymbol{x}), \quad b_h(\boldsymbol{x}) = \mathbf{b}_j\varphi_j(\boldsymbol{x}), \tag{4.28}$$

with $\mathbf{u}_i$, $\mathbf{p}$, and $\mathbf{b}$ being the vectors of projection coefficients. Note that, because the underlying basis vectors are continuously defined over the entire domain, so are the solutions. This is in contrast to typical finite difference methods where the solution is only defined on the grid. Conveniently, because of the choice of nodal basis functions defined by the property (4.25), the projection coefficients are equal to the values of these functions on the nodes of the mesh:

$$(u_i)_h(\boldsymbol{x}_k) = (\mathbf{u}_i)_k, \quad p_h(\boldsymbol{x}_k) = \mathbf{p}_k, \quad b_h(\boldsymbol{x}_k) = \mathbf{b}_k. \tag{4.29}$$

Given the buoyancy coefficients $\mathbf{b}$, the coefficients for the velocity and pressure $\mathbf{x} = [\mathbf{u_1}, \mathbf{u}_2,$

$\mathbf{u}_3, \mathbf{p}]^T$ can be determined by solving the matrix equation

$$\hat{\mathbf{K}}\mathbf{x} = \hat{\mathbf{M}}\mathbf{b} + \mathbf{s}, \tag{4.30}$$

where $\hat{\mathbf{K}}$, $\hat{\mathbf{M}}$, and $\mathbf{s}$ are computed by integrating the weak formulation of the inversion (4.21) for each basis function. For instance,

$$\hat{\mathbf{M}}_{ij} = \int_D \alpha^{-1}\varphi_j z_k(\varphi_k)_i \,\mathrm{d}\boldsymbol{x} \quad \text{and} \quad \mathbf{s}_i = \int_D \tau_{kj} n_j(\varphi_k)_i \,\mathrm{d}\boldsymbol{x}. \tag{4.31}$$

We use the Julia (Bezanson et al., 2017) package Gridap.jl to automate this step (Badia and Verdugo, 2020). A high-resolution three-dimensional inversion can easily contain millions of tetrahedra, making a direct solve of the matrix equation (4.30) impractical. Instead, we load $\hat{\mathbf{K}}$ onto a GPU using CUDA.jl (Besard et al., 2019) and solve the problem iteratively using Krylov.jl's (Montoison and Orban, 2023) implementation of the generalized minimum residual method (GMRES). In the following section, evaluate the error of this method.

4.3.3 Convergence rates for the PG inversion

As a test case to validate the accuracy and convergence rate of the numerical inversion, we solve for $(\boldsymbol{u}_h, p_h)$ given flat isopycnals in the parabolic bowl geometry: $b = \alpha^{-1}x_3$. The exact solution is

$$\boldsymbol{u} = 0 \quad \text{and} \quad p = \frac{x_3^2}{2\alpha^2} - C, \tag{4.32}$$

where C is a constant to satisfy the integral constraint equal to 4/35 for the two-dimensional bowl and 1/12 for the three-dimensional bowl. Deviations from this exact solution result from inaccuracies in representing horizontal pressure gradients, making it a useful test case. Since isopycnals are flat throughout much of the ocean, these pressure gradient errors can be detrimental for ocean models if they are not small relative to full flow. Such errors are ubiquitous in terrain-following coordinate models (e.g., Haney, 1991), prohibiting their use for global-scale problems. As we will see below, these errors are relatively modest in our model and, importantly, their magnitude rapidly decreases with increasing resolution.

From finite element theory (e.g., Hughes, 1987; Elman et al., 2014), the error in the so-called "energy norm" for the P_2–P_1 method scales as

$$\|\boldsymbol{u}_h\|_{H^1} + \|p - p_h\|_{L^2} \sim O(h^2), \tag{4.33}$$

where, again, h is the characteristic mesh resolution. This is indeed the case for a range of parameters in both two- and three-dimensional inversions (Fig. 4.3a,b). We also find that this error scales roughly like $O(\alpha^{-2}\varepsilon^{-2})$. This follows from the fact that the BL scale is proportional to $\alpha\varepsilon$ so that the effective resolution with respect to the BL $h_{\text{eff}} \sim h/(\alpha\varepsilon)$. Since the error tends to be concentrated near the boundary for this problem, it is not a surprise that the energy norm scales like h_{eff}^2.

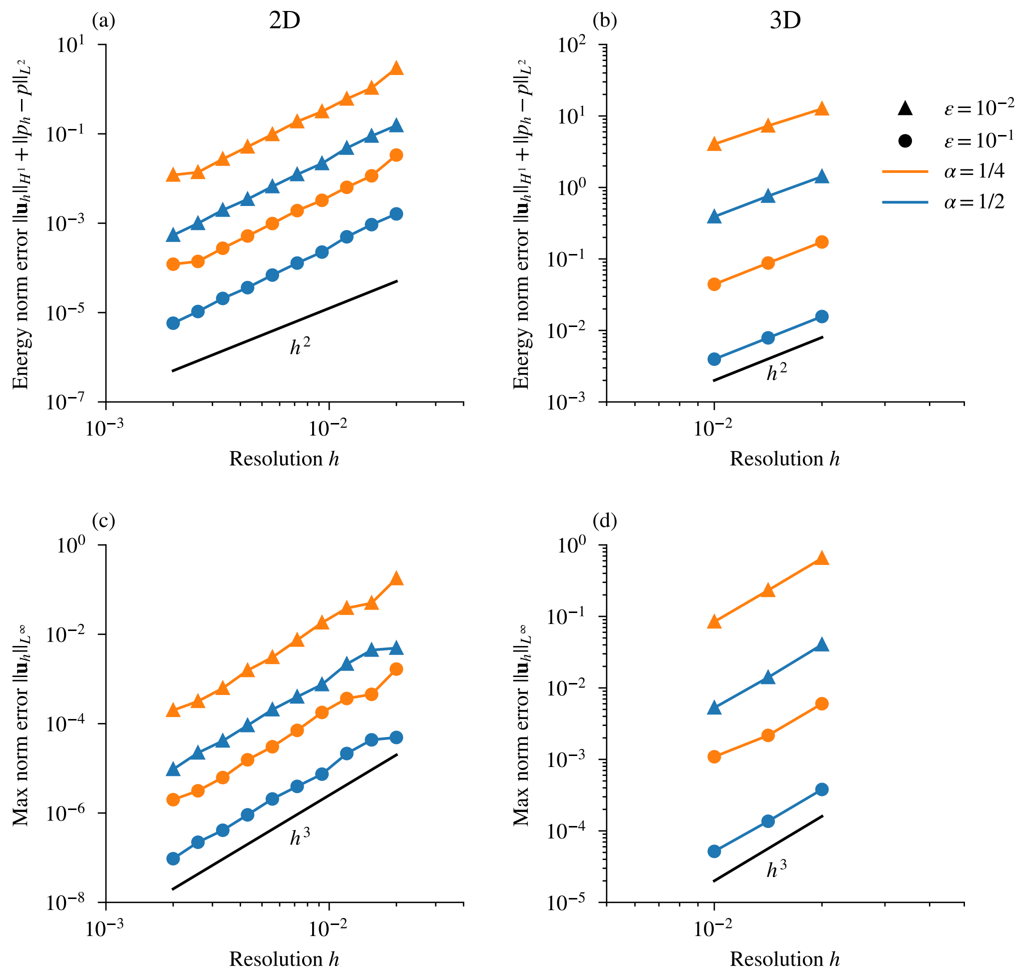

Figure 4.3: Convergence rates of the PG inversion with respect to resolution h, Ekman number ε, and aspect ratio α for the case of flat isopycnals in a parabolic bowl basin (see Fig. 4.2a,b) with true solution (4.32). (a) and (c) are for two-dimensional geometry and (b) and (d) show results for the three-dimensional inversion. The error scales like h^2 in the energy norm [(a) and (b)] and h^3 in the max norm [(c) and (d)].

While there is not a general theory for the scaling of the maximum error $\|\boldsymbol{u}_h\|_{L^\infty} \equiv \sup_D |\boldsymbol{u}_h|$, its value is more interpretable than that of the energy norm. We find that, for this particular test with flat isopycnals, the error empirically scales with h^3 (Fig. 4.3c,d). This rapid convergence rate in the maximum pressure gradient error is promising for the accuracy of large-scale ocean circulation simulated by this model. Next, we will couple the inversion to the evolution equation to simulate time-dependent flow.

4.3.4 Timestepping

Once the solution is projected onto the discrete finite element space described above, the weak form of the buoyancy evolution (4.22) becomes

$$\mathbf{M}\frac{\partial \mathbf{b}}{\partial t} + F(\mathbf{u}_i, \mathbf{b}) + \theta \mathbf{K}\mathbf{b} = \theta \mathbf{f}, \tag{4.34}$$

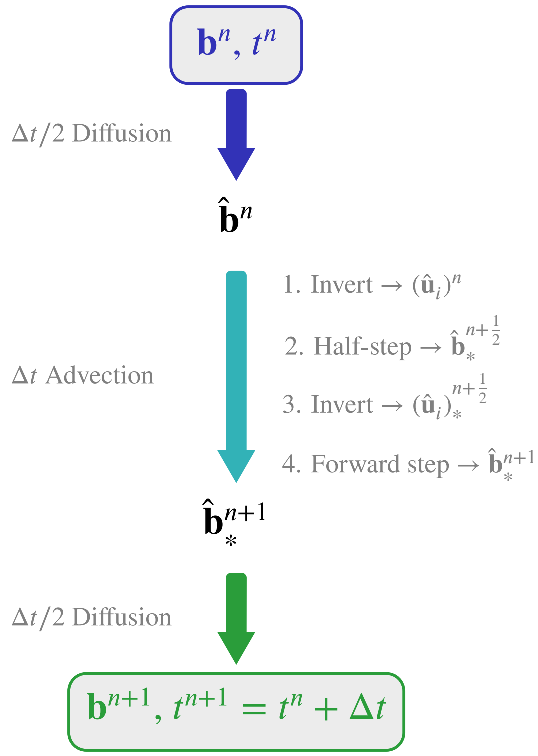

Figure 4.4: Flow chart of a single Strang-split timestep from t^n to $t^{n+1} = t^n + \Delta t$ in a simulation (see section 4.3.4 for details). "Invert" refers to solving the matrix equation (4.30) for the PG inversion. The half- and forward advection steps are described in equations (4.38) and (4.40), respectively, and the $\Delta t/2$ diffusion steps follow equation (4.41).

where

$$\mathbf{M}_{ij} = \int_D \varphi_i \varphi_j \, \mathrm{d}\boldsymbol{x} \quad \text{and} \quad \mathbf{K}_{ij} = \int_D \kappa \frac{\partial \varphi_i}{\partial x_k} \frac{\partial \varphi_j}{\partial x_k} \, \mathrm{d}\boldsymbol{x}, \tag{4.35}$$

are known as the "mass" and "stiffness" matrices in the finite element literature and the vector $\mathbf{f}$ is due to the forcing terms on the right-hand side of (4.22). The non-linear advection term takes the form

$$F(\mathbf{u}_i, \mathbf{b})_j = (\mathbf{u}_i)_k \mathbf{b}_l \int_D (\varphi_i)_k \frac{\partial \varphi_l}{\partial x_i} \varphi_j \, \mathrm{d}\boldsymbol{x}, \tag{4.36}$$

which must be explicitly re-computed as the solution evolves.

To simplify the treatment of both advection and diffusion, we employ Strang splitting (Strang, 1968) to handle each separately . Specifically, we split each timestep into (1) a half-step of diffusion, (2) a full-step of advection, and (3) a final half-step of diffusion (Fig. 4.4). For advection, we use a second-order explicit Runge–Kutta step (also known as the midpoint method):

$$\text{Step 1:} \quad \text{Solve (4.30) for } \mathbf{u}^n \text{ given } \mathbf{b}^n, \tag{4.37}$$

$$\text{Step 2:} \quad \mathbf{b}_*^{n+\frac{1}{2}} = \mathbf{b}^n - \frac{\Delta t}{2}\mathbf{M}^{-1}F(\mathbf{u}_i^n, \mathbf{b}^n), \tag{4.38}$$

$$\text{Step 3:} \quad \text{Solve (4.30) for } (\mathbf{u}_i)_*^{n+\frac{1}{2}} \text{ given } \mathbf{b}_*^{n+\frac{1}{2}}, \tag{4.39}$$

$$\text{Step 4:} \quad \mathbf{b}_*^{n+1} = \mathbf{b}^n - \Delta t\mathbf{M}^{-1}F\left((\mathbf{u}_i)_*^{n+\frac{1}{2}}, \mathbf{b}_*^{n+\frac{1}{2}}\right), \tag{4.40}$$

where Δt is the step size. The superscripts are a short-hand for $\mathbf{b}^n = \mathbf{b}(t^n)$ where $t^n = n\Delta t$ with $n = 0, 1, 2, \ldots$ and the the subscript $_*$ indicates that only an advection step has been performed. The matrix $\mathbf{M}^{-1}$ is not computed explicitly, but instead the linear system is iteratively solved on a GPU using the conjugate gradient (CG) method. Using a left preconditioner of $(\operatorname{diag}\mathbf{M})^{-1}$, this approach is extremely efficient, typically converging to a reasonable tolerance in less than 10 iterations. Note that this second-order method requires two updates of the velocity field (steps 1 and 3). For the diffusion half-steps, we use the second-order accurate, semi-implicit Crank–Nicolson method:

$$\left(\mathbf{M} + \theta\frac{\Delta t}{4}\mathbf{K}\right)\mathbf{b}^{n+1} = \left(\mathbf{M} - \theta\frac{\Delta t}{4}\mathbf{K}\right)\mathbf{b}_*^{n+1} + \theta\Delta t\mathbf{f}. \tag{4.41}$$

We again solve this linear system using the CG method preconditioned by the inverse of the diagonal of the matrix on the left-hand side.

A key advantage of solving the PG equations as opposed to the full Boussinesq system is that they filter out fast-timescale dynamics, allowing for large timesteps. For the results showcased in section 4.4, we use a uniform timestep of $\Delta t = 0.1$, which translates to a dimensional time of about $0.1/(\Omega\varrho) \approx 100$ days. This timestep, which is orders of magnitude larger that that of most global ocean models, enables us to relatively cheaply simulate large-scale ocean dynamics over long timescales. The basin simulations in the next section are run to a nondimensional time of $t = 25$ or about 80 years, with each taking only about 16 hours to complete on a single compute node with an H100 gpu. With some performance optimizations and parallelization, the νPGCM could therefore be used to investigate the millennial-timescale dynamics of the overturning circulation.

4.4 Results

With the methods laid out in the previous section, we now showcase some of the capabilities of the νPGCM. We begin by examining the effect of varying the aspect ratio α in a simple but representative example. Based on these results, we conclude that even $\alpha = 1/2$ qualitatively captures the same dynamics exhibited as $\alpha \to 0$. We then present results from a more complex simulation on a β-plane, which displays the model's ability to represent Rossby waves and complicated interior buoyancy evolution. While the formulation of the model allows for a general geometry, forcings, and nondimensional parameters, we here document results for the specific case of a parabolic bowl basin with no wind stress or buoyancy forcing.

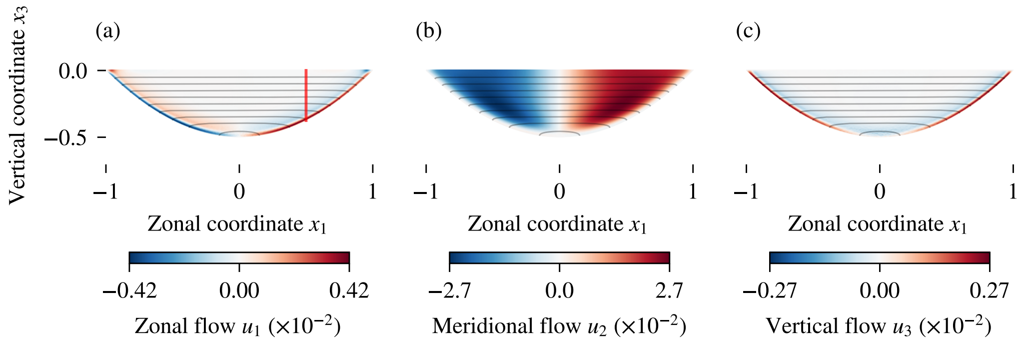

Figure 4.5: Snapshot of flow components (colors) and isopycnals (gray lines) at $x_2 = 0$ and nondimensional time $t = 25$ in a three-dimensional simulation of mixing-driven spin up on an f-plane ($\boldsymbol{\Omega} = \boldsymbol{e}_3$). The aspect ratio is $\alpha = 1/2$, Ekman number is $\varepsilon = 2 \times 10^{-2}$, and Prandtl times Burger number is $\mu\varrho = 1$. The vertical red line in (a) indicates location of profiles in Fig. 4.1.

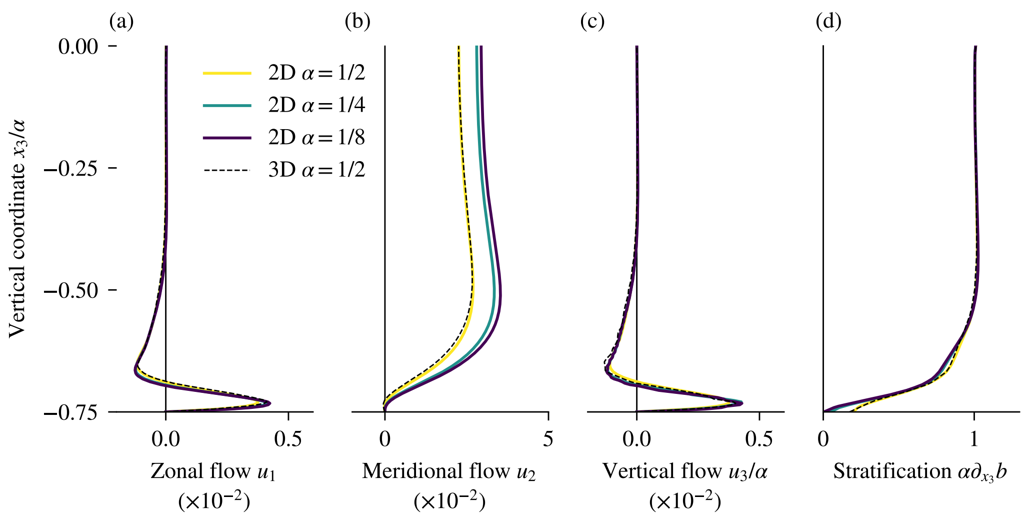

Figure 4.6: Vertical profiles taken at $x_1 = 0.5$ and $x_2 = 0$ in the bowl (red line in Fig. 4.5) at nondimensional time $t = 25$ for spin up on an f-plane ($\boldsymbol{\Omega} = \boldsymbol{e}_3$). The panels show the (a) zonal flow u_1, (b) meridional flow u_2, (c) vertical flow u_3/α, and (d) stratification $\alpha\partial_{x_3}b$, with solid lines for two-dimensional simulations and dashed lines for three-dimensional. Results are shown for an aspect ratio α of 1/2, 1/4, and 1/8, with the vertical coordinate scaled by $1/\alpha$ to allow for a direct comparison.

4.4.1 Aspect ratio effects

To examine the dynamical effect of an artificially increased aspect ratio, we run a set of simulations with $\alpha = 1/2$, 1/4, and 1/8 in the bowl on an f-plane, i.e., $\boldsymbol{\Omega} = \boldsymbol{e}_3 \equiv (0, 0, 1)^T$ in nondimensional coordinates. We choose a nondimensional turbulent diffusivity profile that decays exponentially with distance (in x_3) from the bottom $z_\mathrm{B}(\boldsymbol{x})$,

$$\kappa(\boldsymbol{x}) = 10^{-2} + \exp\left(-\frac{z_\mathrm{B}(\boldsymbol{x})}{\alpha/10}\right), \tag{4.42}$$

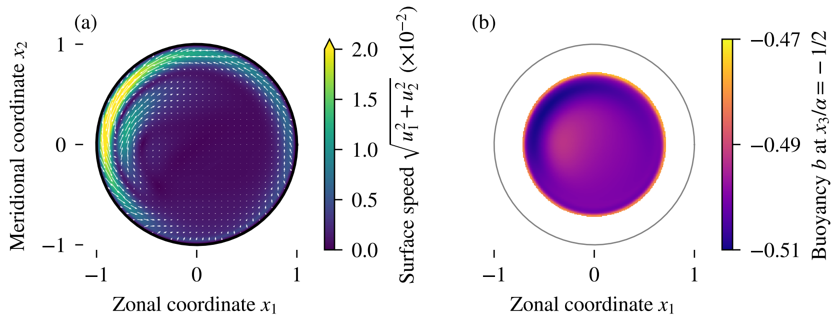

Figure 4.7: Snapshots at nondimensional time $t = 25$ of (a) velocity (arrows) and speed (colors) at the surface ($x_3 = 0$) and (b) buoyancy at $x_3/\alpha = 1/2$ in a three-dimensional simulation of mixing-driven spin up on an β-plane [$\mathbf{\Omega} = (1 + x_2)\boldsymbol{e}_3$]. The aspect ratio is $\alpha = 1/2$, Ekman number is $\varepsilon = 2 \times 10^{-2}$, and Prandtl times Burger number is $\mu\varrho = 1$. Gray circle in (b) represents the coastline at $x_3 = 0$.

qualitatively consistent with observations over rough topography (e.g., Polzin et al., 1997; Callies, 2018). Starting from flat isopycnals $b = x_3/\alpha$ and no flow, a weakly stratified layer near the bottom develops to satisfy the no-flux boundary condition, bending isopycnals into the slopes (gray lines in Fig. 4.5). The cross-slope buoyancy gradient within this layer generates strong upwelling in the bottom BL and weak downwelling aloft, characteristic of bottom-enhanced mixing (Fig. 4.5a,c). Due to the rotational symmetry of this geometry on an f-plane, the net transport of this secondary cross-slope circulation must be zero. By thermal wind balance, the horizontal buoyancy gradients also support substantial shear in the meridional flow near the bottom, leading to a strong circumbasin flow in the interior (Fig. 4.5b). This flow has little effect on the buoyancy evolution since along-slope buoyancy gradients are weak. The cross-slope BL upwelling, on the other hand, brings dense water up the slope, working against mixing to bolster the stratification near the bottom. Without any buoyancy forcing, however, the simulation tends towards a completely mixed state.

Because this geometry is axisymmetric on an f-plane, the dynamics are well-described by a two-dimensional model in polar coordinates with no variations in the azimuthal direction (Peterson and Callies, 2022, 2023). Even for a two-dimensional simulation in Cartesian coordinates, the flow and stratification are nearly identical to the three-dimensional bowl (compare solid to dashed lines in Fig. 4.6), providing a useful validation of the model. As the aspect ratio is decreased, some quantitative changes in the solution emerge, with the largest deviations occurring in the far-field along-slope flow (Fig. 4.6b) and the stratification near the bottom (Fig. 4.6d). The qualitative structure of the circulation, however, remains robust even for $\alpha = 1/2$. For the purposes of most idealized experiments, we therefore do not expect the artificially increased aspect ratio to affect qualitative conclusions. A more quantitative study of the overturning with realistic bathymetry and forcing, however, would warrant using an aspect ratio as small as computationally feasible.

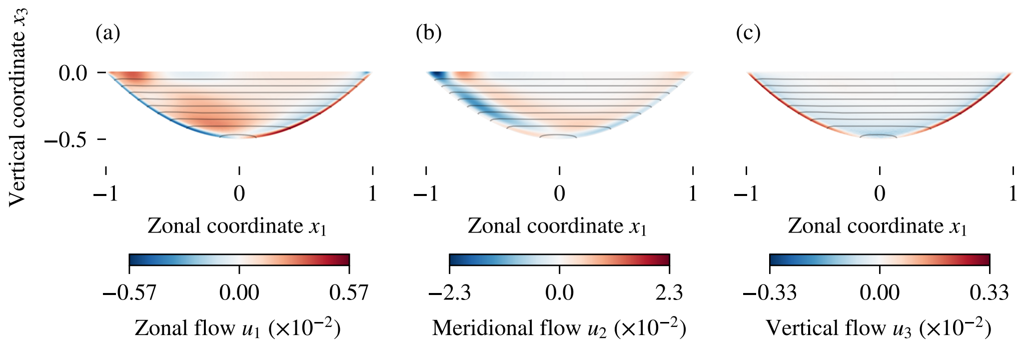

Figure 4.8: Snapshot of flow components (colors) and isopycnals (gray lines) at $x_2 = 0$ and nondimensional time $t = 25$ in a three-dimensional simulation of mixing-driven spin up on an β-plane [$\mathbf{\Omega} = (1 + x_2)\boldsymbol{e}_3$]. The aspect ratio is $\alpha = 1/2$, Ekman number is $\varepsilon = 2 \times 10^{-2}$, and Prandtl times Burger number is $\mu\varrho = 1$.

4.4.2 Circulation in a bowl basin on a β-plane

For a more dynamic showcase of the capabilities of the model, we solve for the dynamics on a β-plane, varying the rotation rate in the meridional direction such that $\mathbf{\Omega} = (1+x_2)\boldsymbol{e}_3$. This breaks the along-slope symmetry that was present in the f-plane setup, leading to a circulation that can no longer be described by two-dimensional physics. One particularly striking difference between the two simulations is the presence of Rossby waves on the β-plane (Figs. 4.7 and 4.8). The early evolution resembles the f-plane case, with mixing bending isopycnals into the slope, generating zonal buoyancy gradients that support a shear in the meridional flow by thermal wind balance. This initial perturbation in the meridional flow then excites Rossby waves that propagate westward along the planetary vorticity gradient. These waves eventually reach the western side of the basin, where they interact with the boundary and set up a western boundary current (e.g., Pedlosky et al., 1997). Other PG ocean models also set up western boundary currents (e.g., Callies and Ferrari, 2018), but Rayleigh drag tends to suppress Rossby waves more aggressively than the Fickian friction used here (Callies, personal communication).

4.5 Conclusions and Future Directions

The νPGCM represents a novel use of finite elements in a numerical model of the large-scale ocean circulation, allowing it to capture the complicated geometry of the ocean and accurately represent the near-bottom dynamics that are now understood to be a crucial component of the overturning. By making the PG approximation, which filters out fast, small-scale dynamics, the model can afford to take large timesteps needed to simulate the overturning on millennial timescales. This unique tool could therefore help answer many outstanding questions about the large-scale ocean circulation. For instance, this model could be used to explain how the overturning may have shifted during the Last Glacial Maximum to store more carbon (Curry and Oppo, 2005; Sigman et al., 2010; Lund et al., 2011; Ferrari et al., 2014;

Jansen, 2017). It could also be used to uncover the mechanisms behind and implications of the observed abyssal heat uptake in recent decades (Purkey and Johnson, 2010; Desbruyères et al., 2016; Lele et al., 2021; Johnson and Purkey, 2024). Ultimately, the νPGCM could even be coupled to ice, atmosphere, and land models to understand the full Earth system (e.g., Holden et al., 2016).

We also envision the numerical approaches developed here as potentially paving the way for the more general adoption of finite elements and unstructured grids in the field. The methods described in section 4.3 could naturally be extended to the full Boussinesq system by reformulating the inversion as an Oseen problem iteration. The aspect ratio trick could then be the key to leveraging standard mixed finite element methods in global ocean models without the need for complicated stabilization schemes.

Chapter 5

CONNECTING THE LOCAL RESPONSE TO ABYSSAL MIXING TO THE BASIN-SCALE CIRCULATION

5.1 Abstract

The circulation of the abyssal ocean is thought to be sustained by turbulence over a rough seafloor. Over sloping topography, this bottom-enhanced mixing produces diapycnal upwelling within a thin bottom boundary layer and downwelling aloft. Simplified theories have been developed to understand this local response to mixing, for example by assuming an along-slope symmetry and imposing a constraint on the cross-slope transport. Ultimately, the local response to mixing on slopes must be connected to the basin-scale circulation, however, and the barotropic transport must conserve potential vorticity. This coupling between the local response to mixing and the basin-scale circulation is studied here in the context of an idealized bowl-shaped basin. In the absence of wind forcing and the joint effect of baroclinicity and relief (JEBAR), the leading-order barotropic transport flows along f/H contours, where f is the Coriolis frequency and H is the depth. The local response to mixing is coupled to this barotropic circulation. It can be thought of as simultaneously constrained by the barotropic circulation and forcing it via a bottom stress curl. If f/H contours are closed, a strong barotropic circulation spins up along them as in simplified theories of the local response in the absence of along-slope variations. If these contours intersect the boundary, a case more typical in the real ocean, the barotropic transport is suppressed. This decouples the leading-order local response from the large-scale circulation and intensifies bottom boundary layer upwelling. Planetary geostrophic dynamics and boundary layer theory are used to describe this interplay between the local response to mixing and the basin-scale circulation, and numerical solution are presented to illustrate the flows and test the theory.

5.2 Introduction

After dense Antarctic Bottom Water fills the global abyssal ocean basins (e.g., Lumpkin and Speer, 2007; Talley, 2013), it must eventually undergo diapycnal transformation to return to the surface and close the overturning (e.g., Munk, 1966; Munk and Wunsch, 1998; Ferrari, 2014). This transformation is achieved by small-scale turbulent mixing, which we now understand to be bottom-enhanced over rough topography (e.g., Polzin et al., 1997; Ledwell et al., 2000; Waterhouse et al., 2014), where internal waves are prone to breaking (e.g., Garrett and Kunze, 2007; Nikurashin and Ferrari, 2011). Considering the one-dimensional balance between diapycnal advection and diffusion in the vertical, bottom-enhanced mixing must confine the upwelling needed to close the overturning to the bottom few meters of the water column (e.g., Ferrari et al., 2016; de Lavergne et al., 2016; McDougall and Ferrari,

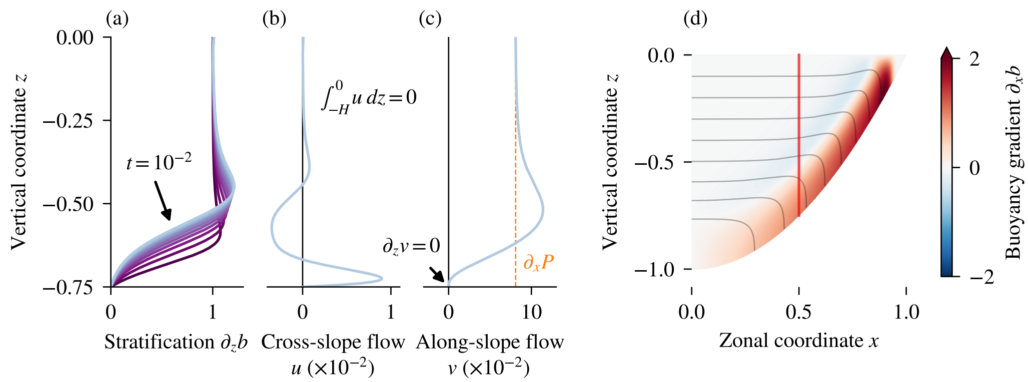

Figure 5.1: Illustration of buoyancy field generated from bottom-enhanced diffusion in the vertical and resulting flow predicted from the uniform slope model of PC22. For details of the dynamical equations and nondimensionalization, refer to section 5.3. (a) Vertical profiles of stratification $\partial_z b$ at a column depth of $H = 0.75$ corresponding to the red line in (d), with time ranging from $t = 10^{-3}$ (purple) to $t = 10^{-2}$ (light blue) at a spacing of 10^{-3}. For the remainder of the paper, we freeze the buoyancy field at $t = 10^{-2}$. (b) Cross-slope flow u and (c) along-slope flow v inferred from the uniform slope model at $t = 10^{-2}$. Parameters are as in section 5.4: an Ekman number of $\varepsilon = 2\times10^{-2}$, turbulent viscosity of $\nu = 1$, and nondimensional slope $\theta = \pi/4$ corresponding to the slope at the red line in (d). (d) Horizontal buoyancy gradient $\partial_x b$ (colors) and isopycnals (gray lines) at $t = 10^{-2}$ in a bowl geometry $H = 1 - x^2 - y^2$ for $0 \le x \le 1$ and $y = 0$.

2017). Recent observations from a canyon in the Rockall Trough agree with this prediction (Wynne-Cattanach et al., 2024). How this bottom-enhanced mixing on slopes shapes the hydrography and basin-scale circulation, however, remains poorly understood.

In some circumstances, it is possible to fully describe the local response of a water column to bottom-enhanced mixing using a one-dimensional model. Canonically, this model of a rotating and stratified fluid over a sloping seafloor assumes no cross- or along-slope variations of the flow, pressure, and buoyancy anomalies (e.g., Phillips, 1970; Wunsch, 1970; Thorpe, 1987; Garrett et al., 1993). It produces a peculiar steady-state solution, however, in which the vertically integrated cross-slope transport is set by the local slope and interior mixing strength, and it approaches this steady state diffusively over thousands of years for typical abyssal parameters (MacCready and Rhines, 1991; Thompson and Johnson, 1996). The inference that the local response dictates the net transport of the global circulation fails to consider that the coupling goes both ways. In Chapter 2 (hereafter PC22), we took a step toward accounting for the large-scale context in the local response to mixing. In the absence of along-slope variations, the vertically integrated cross-slope transport should vanish to satisfy volume conservation. The effects of this constraint are illustrated in Fig. 5.1 for a buoyancy field generated by bottom enhanced mixing of fluid with initially constant stratification over a uniform slope (panel a; see section 5.3 for details). The requirement that all the upwelling in the bottom boundary layer (BL) be returned in the interior above sets up a secondary cross-slope circulation (Fig. 5.1b). To allow for a transport constraint, the one-dimensional model must be modified to include a cross-slope barotropic pressure gra-

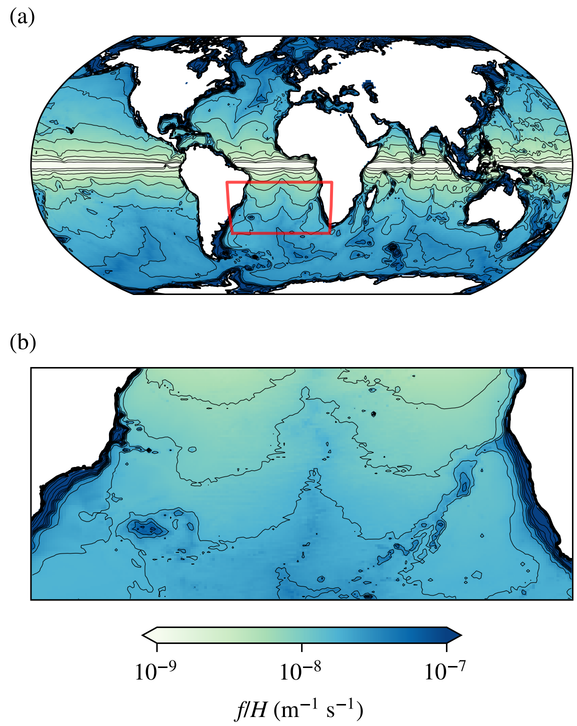

Figure 5.2: f/H contours for (a) the global ocean and (b) the south Brazil Basin region from 40°S to 10°S and 50°W to 20°E [red box in (a)]. Bathymetry data from Smith and Sandwell (1997, updated).

dient $\partial_x P$. As the cross-slope flow returns in the interior, it is turned in the along-slope direction by the Coriolis acceleration and put in geostrophic balance with the cross-slope pressure gradient (Fig. 5.1c). The interior along-slope flow is then enabled to spin up rapidly, rather than being controlled by diffusion. This transport-constrained model fully describes the spinup of mixing-generated flow in the absence of along-slope variations, capturing the flow spun up by bottom-enhanced mixing over an idealized ridge, for example (Ruan and Callies, 2020).

The PC22 model relies on symmetry in the along-slope direction to provide enough constraints to solve for the local response. This symmetry is broken if, for instance, meridional variations in the Coriolis parameter f are allowed. In general, the local response is coupled to the basin-scale potential-vorticity-conserving barotropic circulation. The net transport of the local response is constrained by the barotropic circulation, as in PC22 (though now in both directions). At the same time, the curl of the bottom stress due to the local response is itself a forcing in the barotropic problem. Classical models of the barotropic circulation (e.g., Stommel, 1948; Munk, 1950; Robinson, 1970; Rattray, 1982; Mertz and Wright, 1992) use a simple form of the bottom stress without considering buoyancy effects. In this work, we use standard Ekman BL theory (e.g., Pedlosky, 1979; Vallis, 2017) to derive explicit expressions for the bottom stress in terms of the barotropic transport, buoyancy field, and wind stress. This allows us to leverage intuition from textbook barotropic dynamics (e.g., Pedlosky, 1979; Vallis, 2017) to understand the connection between the local response to mixing and the basin-scale circulation.

To understand this coupling in a simple context, we study the flow produced by a prescribed buoyancy field, neglecting advective dynamics. In particular, for a buoyancy field dependent only on the depth of the fluid H (as in the purely mixing-generated field in Fig. 5.1), the joint effect of baroclinicity and relief (JEBAR) drops out of the barotropic vorticity equation. Furthermore, we find that the bottom-stress curl from Ekman BL theory is not a leading-order term in the barotropic vorticity budget in the interior of the basin. In the absence of a wind-stress curl, therefore, the leading-order barotropic flow in this case must follow f/H contours. These contours tend to be open and fairly longitudinal in the real ocean, but they can close around large enough topographic features (e.g., Dewar, 1998, cf. Fig. 5.2). These two different topological states of the f/H contours in an abyssal basin strongly alter the qualitative barotropic dynamics. Flow along closed contours is unencumbered in the inviscid equations of motion, allowing strong, resonant flows (e.g., Kawase, 1993; Thompson, 1995; Hallberg and Rhines, 1996). Open contours, on the other hand, intersect the boundary, thereby destroying the leading-order barotropic circulation. The first case only slightly modifies the circulation compared to the local response derived from the PC22 model, with the barotropic flow now directed along f/H contours rather than simply along-slope. These are one and the same on an f-plane, implying that the PC22 model would still apply (provided that the assumption of along-slope symmetry is still a good one). The second case, however, would require a modification of the local theory to include a constraint on both the cross- *and* along-slope transports, as we will see below.

In section 5.3 we begin by introducing the planetary geostrophic (PG) formulation and idealized abyssal basin that will serve as our testbed for the remainder of the paper. We then dive into the phenomenology of numerical solutions for the PG circulation within this basin in section 5.4. The hydrography is set by bottom-enhanced diffusion of buoyancy starting from flat isopycnals, and the resulting flow is computed on an f-plane and two β-planes, one with closed f/H contours and one with open ones. In section 5.5, we use intuition from these numerically-derived circulations to motivate a theoretical description of the connection between the local baroclinic response to mixing and the barotropic circulation. A discussion of the significance of these results and key conclusions are provided in sections 5.6 and 5.7, respectively.

5.3 A model problem for an abyssal basin

The goal of this study is to understand how the local response to bottom-enhanced mixing interacts with the basin-scale circulation. With this in mind, we will consider an idealized, closed basin to isolate this physics. We choose a bowl-shaped domain defined by a parabolic depth function, which sets a coastline along the unit circle centered at the origin

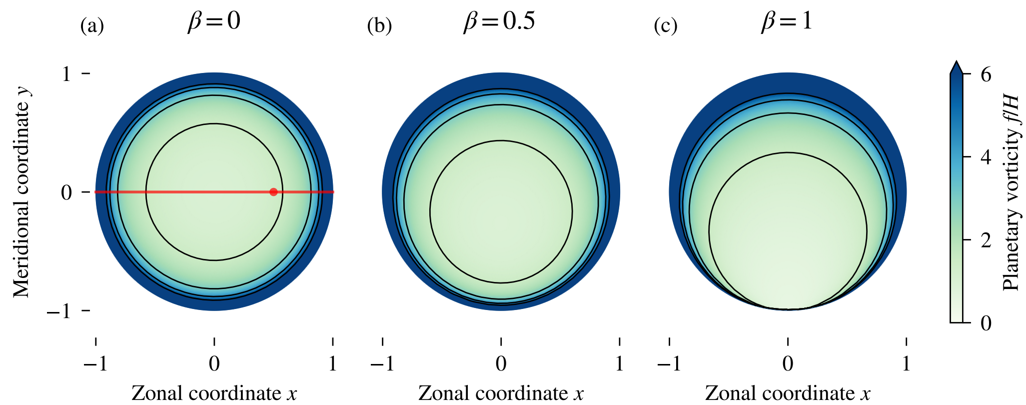

Figure 5.3: f/H contours in a circular mid-latitude basin for $H = 1 - x^2 - y^2$ and (a) $f = 1$, (b) $f = 1 + 0.5y$, (c) $f = 1 + y$. The red line and circle in (a) indicate where the zonal slices in Fig. 5.4 and the profiles in Fig. 5.5 are taken, respectively.

in the x–y plane (Fig. 5.3). The symmetry about the origin is the main reason for using this geometry as opposed to rectangular basin more often employed in idealized studies of the large-scale circulation (e.g., Ito and Marshall, 2008; Wolfe and Cessi, 2011; Nikurashin and Vallis, 2011; Callies and Ferrari, 2018; Jansen and Nadeau, 2019). By varying β in the the Coriolis parameter $f(y) = f_0 + \beta y$, we can examine the dynamics under different f/H contour topologies, with $f/H = (1 + \beta y)/(1 - x^2 - y^2)$ under the nondimensionalization defined below. On an f-plane ($\beta = 0$), this yields axisymmetric f/H contours (Fig. 5.3a), vastly simplifying the description of the coupling between the local and global dynamics, as we will see in the next section. As β is increased, the f/H contours shift southward (Fig. 5.3b,c), breaking this symmetry and demanding a more general treatment of the problem. Once $\beta \geq 1$, these contours open, perhaps more representative of most of the real ocean's f/H contours (Fig. 5.2). As anticipated in the introduction and explained in detail in the next section, the basin-scale dynamics are qualitatively different for open versus closed contours. In this way, the three cases considered here ($\beta = 0$, 0.5, 1) cover three key scenarios, allowing us to develop and test a general theory for the connection between the local response to mixing and the basin-wide abyssal circulation.

5.3.1 Planetary geostrophic equations

To put the focus on the mixing-generated abyssal circulation, we employ the planetary geostrophic (PG) approximation (e.g., Pedlosky, 1979; Vallis, 2017). The PG scaling assumes large horizontal scales and small Rossby numbers, removing the inertial terms in the momentum equations. This filters out fast-timescale dynamics such as small-scale turbulence, internal waves, and baroclinic eddies, but we interpret the PG flow as the residual flow after a thickness-weighted average over these transients, with their effects included as parameterized Eliassen–Palm and diapycnal fluxes (e.g., Young, 2012). The dimensional

PG equations in Cartesian space (x, y, z) are

$$-fv = -\frac{\partial p}{\partial x} + \frac{\partial}{\partial z}\left(\nu\frac{\partial u}{\partial z}\right), \tag{5.1}$$

$$fu = -\frac{\partial p}{\partial y} + \frac{\partial}{\partial z}\left(\nu\frac{\partial v}{\partial z}\right), \tag{5.2}$$

$$\frac{\partial p}{\partial z} = b, \tag{5.3}$$

$$\nabla \cdot \boldsymbol{u} = 0, \tag{5.4}$$

$$\frac{\partial b}{\partial t} + \boldsymbol{u} \cdot \nabla b = \frac{\partial}{\partial z}\left(\kappa\frac{\partial b}{\partial z}\right), \tag{5.5}$$

where $\boldsymbol{u} = (u, v, w)$ is the velocity vector, b is the buoyancy, and ν and κ are the turbulent viscosity and diffusivity, respectively. We apply no-slip ($\boldsymbol{u} = 0$) and no-flux ($\partial_z b = 0$) boundary conditions at the bottom that is located at $z = -H(x, y)$. At the surface ($z = 0$), we demand no normal flow ($w = 0$) with a wind stress forcing ($\nu\partial_z \boldsymbol{u}_\perp = \boldsymbol{\tau}$) and a fixed uniform buoyancy ($b = 0$). We here neglect horizontal turbulent fluxes, consistent with the assumption of a small aspect ratio if the turbulence is close to isotropic, though these terms are kept in the simulations for numerical stability (see section 5.4 and appendix A).

These PG dynamics can be viewed separately as an evolution equation for buoyancy (5.5) and an inversion statement for the flow (5.1) to (5.4). For this study, we aim to understand the inversion statement in isolation, leaving an analysis of the full PG system for future work. To consider a flow-field in the context of abyssal mixing, we apply the inversion statement to a buoyancy field generated by pure bottom-enhanced diffusion. We solve

$$\frac{\partial b}{\partial t} = \frac{\partial}{\partial z}\left(\kappa\frac{\partial b}{\partial z}\right) \tag{5.6}$$

with an initial condition of flat isopycnals, $b_0 = N^2 z$, where N^2 is the initial stratification. This setting is, of course, a major simplification of the dynamics; in reality, the ocean is thought to be in nearly steady state, with advection in balance with diffusion: $\boldsymbol{u} \cdot \nabla b = \partial_z(\kappa\partial_z b)$ (Munk, 1966). Instead, the buoyancy field satisfying (5.6) simply mixes towards $b = 0$, and the flow derived from the inversion statement has no impact on this evolution. As we will see in the following sections, however, the phenomenology the PG inversion alone is rich enough to warrant isolated study, and its understanding can be used as a stepping stone for studying the complete dynamics.

5.3.2 Nondimensionalization and parameters

To isolate key parameters in the problem, we will work with the nondimensional PG equations for the remainder of the paper. We define the characteristic scales for the horizontal and vertical coordinates, velocities, Coriolis parameter, and mixing coefficients such that

$$x, y \sim L, \quad z \sim H_0, \quad u, v \sim U_0, \quad w \sim \frac{U_0 H_0}{L}, \quad f \sim f_0, \quad \nu \sim \nu_0, \quad \kappa \sim \kappa_0. \tag{5.7}$$

Unlike in quasi-geostrophic theory, the PG equations do not impose an explicit background stratification. For the simple diffusion problem considered in (5.6), however, the initial condition sets a natural scaling for buoyancy of $b \sim N^2 H_0$. In general, a representative scale for N^2 in the abyssal ocean is not uniquely defined and will depend on the context. Finally, we assume that the horizontal pressure gradient terms in (5.1) and (5.2) scale with the Coriolis terms, that the buoyancy also scales with the pressure scale divided by H_0 from hydrostatic balance (5.3), and that time scales advectively:

$$p \sim f_0 U_0 L, \quad b \sim \frac{f_0 U_0 L}{H_0} = N^2 H_0, \quad t \sim \frac{L}{U_0}. \tag{5.8}$$

Applying these scales to equations (5.1) to (5.5) yields the following nondimensional PG equations:

$$-\tilde{f}\tilde{v} = -\frac{\partial \tilde{p}}{\partial \tilde{x}} + \varepsilon^2 \frac{\partial}{\partial \tilde{z}} \left(\tilde{\nu} \frac{\partial \tilde{u}}{\partial \tilde{z}} \right), \tag{5.9}$$

$$\tilde{f}\tilde{u} = -\frac{\partial \tilde{p}}{\partial \tilde{y}} + \varepsilon^2 \frac{\partial}{\partial \tilde{z}} \left(\tilde{\nu} \frac{\partial \tilde{v}}{\partial \tilde{z}} \right), \tag{5.10}$$

$$\frac{\partial \tilde{p}}{\partial \tilde{z}} = \tilde{b}, \tag{5.11}$$

$$\tilde{\nabla} \cdot \tilde{\boldsymbol{u}} = 0, \tag{5.12}$$

$$\mu \varrho \left(\frac{\partial \tilde{b}}{\partial \tilde{t}} + \tilde{\boldsymbol{u}} \cdot \tilde{\nabla} \tilde{b} \right) = \varepsilon^2 \frac{\partial}{\partial \tilde{z}} \left(\tilde{\kappa} \frac{\partial \tilde{b}}{\partial \tilde{z}} \right), \tag{5.13}$$

where $\varepsilon^2 = \nu_0 / f_0 H_0^2$ is the Ekman number, $\varrho = N^2 H_0^2 / f_0^2 L^2$ is the Burger number, and $\mu = \nu_0 / \kappa_0$ is the turbulent Prandtl number. The wind stress boundary condition at $\tilde{z} = 0$ is now $\varepsilon^2 \tilde{\nu} \partial_{\tilde{z}} \tilde{\boldsymbol{u}}_\perp = \tilde{\boldsymbol{\tau}}$. We will work in with nondimensional variables for the remainder of the paper, dropping the ˜ decoration for visual clarity.

Typical order-of-magnitude scales for an abyssal basin are

$$f_0 \approx 10^{-4}\ \mathrm{s}^{-1}, \quad H_0 \approx 10^3\ \mathrm{m}, \quad N \approx 10^{-3}\ \mathrm{s}^{-1}, \quad L \approx 10^6\ \mathrm{m}, \tag{5.14}$$

yielding a Burger number of $\varrho \approx 10^{-4}$. Over rough topography, one might expect strong turbulence associated with a turbulent diffusivity on the order of $\kappa_0 \approx 10^{-3}\ \mathrm{m}^2\,\mathrm{s}^{-1}$ (e.g., Waterhouse et al., 2014). Although the magnitude of the turbulent viscosity is less clear, it is reasonable to assume that, for weakly stratified abyssal waters, small-scale mixing of buoyancy would occur on similar scales to the mixing of momentum, implying that $\nu_0 \sim \kappa_0$, or $\mu \sim 1$ (e.g., Caulfield, 2021). Parameterizing the Eliassen–Palm flux of submesoscale baroclinic eddies generated in abyssal mixing layers would require $\mu \gg 1$ (e.g., Wenegrat et al., 2018; Callies, 2018), but we reserve a complete study of how eddy restratification affects the basin-scale circulation for future work. Taking $\nu_0 = \kappa_0 = 10^{-3}\ \mathrm{m}^2\,\mathrm{s}^{-1}$ then puts ε at about 3×10^{-3}. To properly resolve the BL in the numerical model described in the next section, we instead choose a magnified value of $\varepsilon = 2 \times 10^{-2}$, which thickens the BL and speeds up diffusion but does not qualitatively change the solutions.

For scales relevant to the basin-scale abyssal circulation, we therefore make the following assumptions:

$$\varepsilon \ll 1 \quad \text{and} \quad \mu\varrho \sim \varepsilon^2. \tag{5.15}$$

The first of these assumptions motivates the use of BL theory (section 5.5), as a typical ratio of the bottom Ekman layer thickness $\delta = \sqrt{2\nu_0/f_0}$ to the column depth H_0 is $\sqrt{2}\,\varepsilon \approx 2.8 \times 10^{-2}$ (this translates to a dimensional BL thickness of 28 m given $H_0 = 1$ km). According to the BL theory derived in Chapter 3 (hereafter PC23), the cross-isopycnal flow in the PC22 model is of $O(\varepsilon)$ in the BL and $O(\varepsilon^2)$ in the interior. Along with the second scaling assumption in (5.15), this would suggest that, in the absence of along-slope variations, advection of buoyancy in (5.13) is of higher order in ε than diffusion. While this may no longer be the case once along-slope variations are allowed, as we will show below, it further motivates our simplification of the buoyancy equation to pure diffusion (5.6) as a first look at the basin-scale dynamics. We therefore solve the nondimensional buoyancy diffusion equation in the vertical,

$$\mu\varrho\frac{\partial b}{\partial t} = \varepsilon^2\frac{\partial}{\partial z}\left(\kappa\frac{\partial b}{\partial z}\right), \tag{5.16}$$

with the initial condition $b = z$ and boundary conditions $\partial_z b = 0$ at $z = -H$ and $b = 0$ at $z = 0$.

5.4 Numerical inversions for the three-dimensional mixing-driven flow

Before developing a mathematical theory, in this section we will build intuition for the phenomenology of the mixing-generated circulation from numerical solutions of the idealized problem described above. We use the finite element method to integrate the diffusion equation (5.16) forward in time and solve a form of the PG inversion (5.9) to (5.12) with an artificially large aspect ratio for numerical stability (see appendix A). As expected, on an f-plane, the circulation in the bowl is axisymmetric, allowing us to describe the local dynamics using the theory from PC22 and PC23. The tilted isopycnals due to mixing rapidly spin up a far-field flow that circumnavigates the basin. On a β-plane, the along-slope symmetry is broken, and the barotropic circulation shifts southward following f/H contours. For open contours, the barotropic transport is nearly zero throughout the domain, constraining the vertical structure of the flow and leading to stronger BL transport.

5.4.1 Numerical approach

Despite the simplified form of the PG inversion (5.9) to (5.12) compared to the full Boussinesq system, solving the problem numerically in an arbitrary domain and with high resolution in the bottom BL can still prove challenging. The geometrically flexible finite element method is a natural choice for this problem, but the small aspect ratio of the ocean destabilizes standard techniques (e.g., Guillén-González and Rodríguez-Galván, 2015). To leverage the robustness of standard finite element techniques without altering the qualitative behavior of the circulation, we artificially increase the aspect ratio $\alpha = H_0/L$ to 1/2, re-introducing both diffusion in the vertical momentum equation and horizontal diffusion of momentum. This "aspect ratio trick" has been utilized in a number of other models (e.g., Kuang et al., 2005; Garner et al., 2007; Salmon, 2009). We consider the effects of the approximation in appendix A.

With horizontal diffusion terms included, the PG inversion is equivalent to rotating Stokes flow, which may be solved efficiently and accurately using textbook mixed finite element methods (e.g., Hughes, 1987; Elman et al., 2014). We choose the so-called P_2–P_1 method, where velocity and pressure are represented by quadratic and linear basis functions, respectively. For this method, the energy-normed error scales quadratically in mesh resolution. To resolve the BL scale, we discretize the domain using an unstructured tetrahedral mesh with a uniform resolution of 10^{-2} generated using Gmsh (Geuzaine and Remacle, 2009). We use the generalized minimum residual method (GMRES) to iteratively solve the resulting linear system for velocity and pressure given the buoyancy field. For simplicity, we do not specify a spatial structure in the nondimensional turbulent viscosity, setting $\nu = 1$ everywhere. The implementation in Julia (Bezanson et al., 2017), which makes use of Gridap.jl for finite elements (Badia and Verdugo, 2020), Krylov.jl for iterative solvers (Montoison and Orban, 2023), and CUDA.jl for GPU support (Besard et al., 2019), is hosted on GitHub (`https://github.com/hgpeterson/nuPGCM`).

As stated previously, we apply the PG inversion to a buoyancy field generated by bottom-enhanced diffusive mixing in the vertical (5.16). We choose a nondimensional turbulent diffusivity profile that decays exponentially with height above bottom,

$$\kappa(x, y, z) = 10^{-2} + \exp\left(-\frac{z + H(x, y)}{0.1}\right), \tag{5.17}$$

qualitatively consistent with observations over rough topography (e.g., Polzin et al., 1997; Callies, 2018). Equation (5.16) is then discretized using P_2 finite elements for buoyancy and integrated in time using the second-order semi-implicit Crank–Nicolson method. Starting from flat isopycnals $b = z$, a bottom mixing layer with $\partial_z b < 1$ instantaneously develops to satisfy the no-flux boundary condition (Fig. 5.1a). This mixing layer grows diffusively—first rapidly near the bottom where $\kappa \sim O(1)$, then more slowly once it reaches the interior where $\kappa \sim O(10^{-2})$—eroding the stratification in the column towards zero. When applied along the sloping bowl bathymetry, this vertical mixing bends isopycnals into the slopes, generating cross-slope buoyancy gradients (Fig. 5.1b). These buoyancy gradients, as we will see in the following sections, spin up a basin-scale circulation described by the PG inversion. We will analyze the PG inversion in the remainder of the paper for the buoyancy field at $t = 10^{-2}$ (light blue line in Fig. 5.1a). Using the scales defined above, this corresponds to a dimensional time of about $t^* = t/f_0\varrho \approx 10$ days. This short time reflects the artificially enhanced Ekman number, which accelerates the rate of diffusion by a factor of $\sim$100. We will now explore the phenomenology of the circulation set up by this buoyancy field for the three cases outlined in Fig. 5.3, starting with the simplest case of an f-plane.

5.4.2 Circulation on an f-plane

On an f-plane, by symmetry, the dynamics are equivalent for any slice through the origin. As discussed in the introduction, this along-slope invariance allows us to apply the theory built up in PC22 and PC23 to determine the local response. In particular, this means that the vertically integrated zonal velocity,

$$U \equiv \int_{-H}^{0} u \, \mathrm{d}z, \tag{5.18}$$

along a zonal section through $y = 0$ (red line in Fig. 5.3) must vanish. Along this zonal section, the flow field exhibits the BL upwelling and interior downwelling characteristic of bottom-enhanced mixing (Figs. 5.4a,g). The transport constraint, by the meridional momentum balance (5.10) and the along-slope symmetry, implies that the meridional (along-slope) shear at the bottom must vanish. This implies weak near-bottom flow, such that the thermal wind shear in the mixing layer leads to strong meridional flow in the interior (Fig. 5.4d). These dynamics are well-described by the local theory, as showcased in Fig. 5.5 for a particular profile taken at $x = 0.5$ and $y = 0$ (red dot in Fig. 5.3). In section 5.5, this local model will be described and generalized in detail, but for now the transport-constrained one-dimensional model from PC22 is a sufficient mental picture.

As we will make more explicit in section 5.5, the barotropic circulation must in general conserve potential vorticity, which depends on the geometry of the f/H contours, the vertically-integrated buoyancy field, and the wind-stress curl. For the symmetric buoyancy field considered here, and in the absence of a wind stress, this balance implies free leading-order barotropic flow along closed f/H contours. On an f-plane, this simply means that fluid columns must remain at a constant depth as they circumnavigate the basin. The barotropic streamfunction Ψ describing this circulation, defined such that

$$-\frac{\partial \Psi}{\partial y} = U \quad \text{and} \quad \frac{\partial \Psi}{\partial x} = V, \tag{5.19}$$

where $V \equiv \int_{-H}^{0} v \, \mathrm{d}z$, is therefore a function of H (Fig. 5.6). The strength of this along-slope barotropic circulation is set by the amount of thermal wind shear over the mixing layer (see section 5.5 and appendix C for details). Specifically, as we will see in equation (5.40), the magnitude of Ψ is linearly proportional to the thickness of the mixing layer, the strength of the cross-slope buoyancy gradient within it, and the depth of the fluid column.

5.4.3 Circulation on a β-plane

On a β-plane, the f/H contours shift southward, breaking the rotational symmetry that was present on the f-plane and therefore invalidating the model for the local response based on

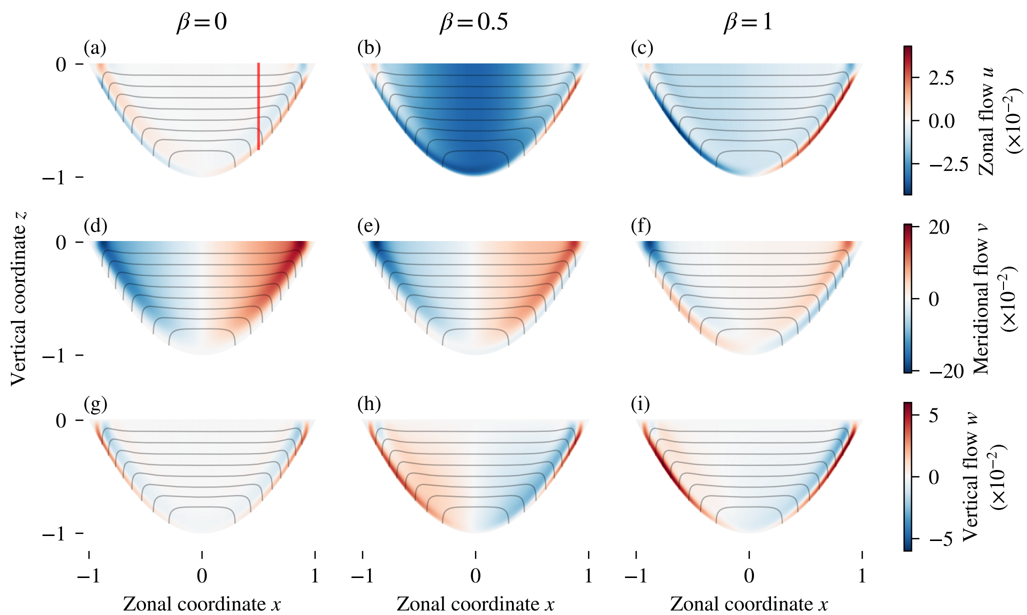

Figure 5.4: Zonal sections at $y = 0$ of velocity components (colors) and isopycnals (gray lines) at $t = 10^{-2}$ for (column 1; a, d, g) $\beta = 0$, (column 2; b, e, h) $\beta = 0.5$, and (column 3; c, f, i) $\beta = 1$. The velocity components are organized by row, with (row 1; a, b, c) zonal flow u at the top, (row 2; d, e, f) meridional flow v in the middle, and (row 3; g, h, i) vertical flow w at the bottom. Red line in (a) indicates location of profiles in Fig. 5.5.

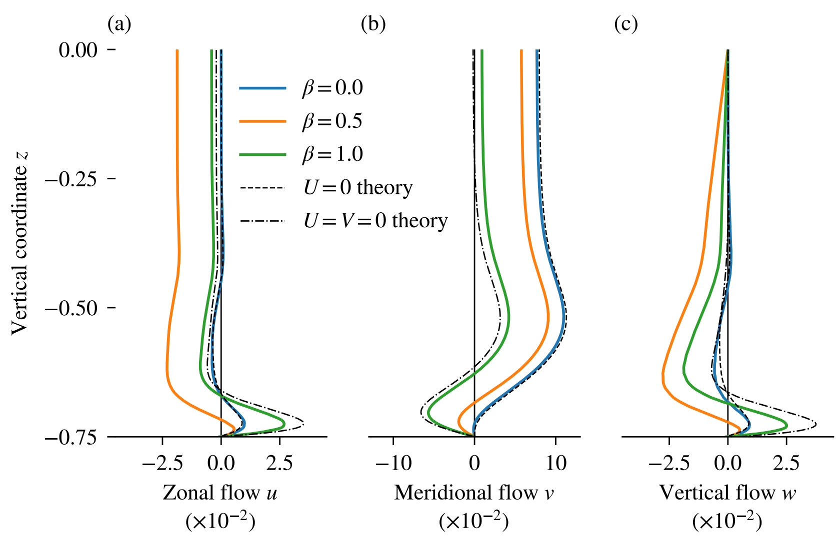

Figure 5.5: Vertical profiles of (a) zonal u, (b) meridional v, and (c) vertical w flow components from the 3D model inversion (solid) for $\beta = 0, 0.5, 1$ at $x = 0.5$, $y = 0$, and $t = 10^{-2}$. The second-order accurate local models for $U = 0$ and $U = V = 0$ (modified for an aspect ratio of 1/2, see appendices B and C) are shown in dashed and dashed-dotted lines, respectively.

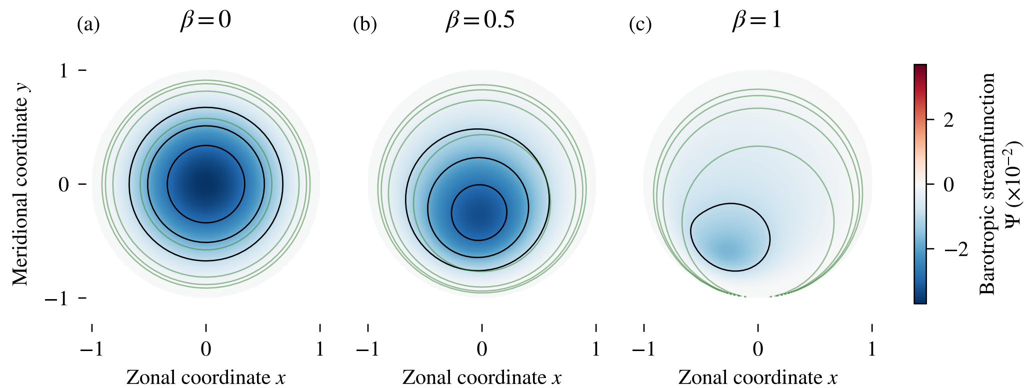

Figure 5.6: Barotropic streamfunction Ψ (colors and black lines) at $t = 10^{-2}$ for (a) $\beta = 0$, (b) $\beta = 0.5$, and (c) $\beta = 1$. Negative values imply counter-clockwise flow. For reference, the f/H contours from Fig. 5.3 are overlayed in green.

along-slope symmetry. We will consider two cases: $\beta = 0.5$ and $\beta = 1$, with the former having closed f/H contours and the latter having open contours (Fig. 5.3b,c). As alluded to in the introduction, these two cases lead to dramatically different barotropic circulations, which then shape the local response to mixing.

For closed f/H contours ($\beta = 0.5$), the magnitude of the barotropic circulation is comparable to that of the f-plane case (Fig. 5.6b). The streamfunction is very nearly a function of f/H, with a slight perturbation towards the western side of the basin. Looking again at a zonal section through $y = 0$, the interior meridional flow is similar to the f-plane case, with a slight barotropic shift toward zero in the interior (Fig. 5.4e). This is especially clear in the vertical profile at $x = 0.5$ and $y = 0$ (Fig. 5.5b). The zonal and vertical circulation in the interior of this section can best be understood by considering the stretching and squashing of fluid columns to conserve vorticity. Since f increases with y, fluid columns moving northward on the eastern side of the basin must stretch by moving towards deeper waters to the west in order to keep f/H constant. This explains the westward and downwelling flow on this side of the basin (Fig. 5.4b,h). On the other hand, fluid columns moving southward on the western side of the basin must squash by moving towards shallower waters, leading to westward and upwelling flow. The zonal flow in the interior is roughly barotropic, while the vertical component decays roughly linearly (Fig. 5.5a,c). This is consistent with vorticity conservation in the interior, given the nearly barotropic interior meridional flow. This zonal circulation in the interior is much stronger than that of the f-plane case, leading to enhanced shear in the BL.

The circulation completely changes once f/H contours open. As before, the leading order barotropic flow is directed along f/H contours, but this time these contours encounter the boundary, where the flow must be zero. The magnitude of the barotropic circulation is, therefore, considerably reduced (Fig. 5.6c). The near-zero transport throughout the domain provides a constraint that decouples the local response from the basin-wide circulation. Unlike the model for the local response in the f-plane case, here *both U and V* must vanish. This model for the local response, described in section 5.5 and appendix B, captures the qualitative vertical structure of the flow at $x = 0.5$ and $y = 0$, with quantitative errors to be expected given that the net transport is not exactly zero in the full inversion (Fig. 5.5). This constraint on the net transport has important implications for the vertical structure of the circulation. With the thermal wind shear unchanged, the meridional flow in the interior must shift to satisfy $V = 0$ (Figs. 5.4f and 5.5b). This generates a larger shear near the bottom, thereby enhancing the up-slope BL transport (Figs. 5.4c,i and 5.5a,c). If buoyancy advection was allowed, this stronger BL upwelling than the f-plane case would be more efficient at restratifying the mixing layer, as we will discuss further in section 5.6. To compensate for this BL transport and ensure that that $U \approx 0$, the zonal flow in the interior is weakly westward in balance with a barotropic meridional pressure gradient.

5.5 Theory for the flow inversion

The phenomenology exhibited in the previous section shows that, for a fixed buoyancy field, the circulation resulting from the PG inversion varies substantially depending on the underlying f/H contours. For open contours, the barotropic circulation vanishes at leading order, rendering the leading-order local response independent of any global context. For closed contours, on the other hand, a leading-order along-contour barotropic flow develops. This transport constrains the local response, whose bottom-stress curl then provides a sink of barotropic vorticity so that, in general, the two problems must be solved simultaneously. For the f-plane case, however, the along-slope symmetry provided enough of a constraint to allow us to describe the local response independently with the model derived in PC22. In this section, we will describe the mathematical formalism of these results, clarifying how the local and barotropic responses are coupled and deriving asymptotically accurate analytical expressions.

5.5.1 Barotropic vorticity conservation

Turbulent mixing of buoyancy in the abyss generates a local flow response that must recon with the basin-wide circulation. The barotropic circulation may be described by the barotropic vorticity equation, derived by integrating the horizontal momentum equations (5.9) and (5.10) over the water column and then cross-differentiating:

$$-\mathrm{J}\left(\frac{f}{H}, \Psi\right) = -\mathrm{J}\left(\frac{1}{H}, \gamma\right) + \boldsymbol{z} \cdot \left(\nabla \times \frac{\boldsymbol{\tau}}{H}\right) - \varepsilon^2 \boldsymbol{z} \cdot \nabla \times \left(\frac{\nu}{H} \frac{\partial \boldsymbol{u}}{\partial z}\Big|_{-H}\right), \tag{5.20}$$

where $\mathrm{J}(A, B) = \partial_x A\, \partial_y B - \partial_y A\, \partial_x B$ is the Jacobian operator. For a closed simply connected domain like the bowl considered in this study, the boundary condition is $\Psi = 0$. The first term on the right-hand side depends on both the topography and the three-dimensional structure of the buoyancy field through $\gamma = -\int_{-H}^{0} zb\, \mathrm{d}z$ and is therefore often called the joint-effect of baroclinicity and relief (JEBAR) term. For our simple diffusion case, $\gamma = \gamma(H)$, so that JEBAR is zero.

Equation (5.20) can be interpreted as a conservation equation for the "tracer" Ψ advected by the "flow" f/H and with "sources" and "sinks" on the right-hand side (e.g., Welander, 1968; Salmon, 1998; Vallis, 2017). This tracer analogy helps explain the qualitative difference between the open- and closed-contour inversions (Fig. 5.6). For closed f/H contours, the streamfunction can "flow" along a closed loop, gaining "concentration" from the "source" terms along the way. This is how the f-plane and $\beta = 0.5$ simulations could maintain such strong barotropic circulations (e.g., Hallberg and Rhines, 1996). For $\beta = 1$, however, the contours open, and any "concentration" acquired while "flowing" in the interior will be lost at the boundary. In the inversions shown above, the only "source" term is the bottom-stress curl, which is itself a part of the solution. For closed contours, this frictional term can become large outside a lateral boundary layer, whereas open contours produce lateral (western) boundary layers with friction remaining small in the interior.

A closed description requires an expression for the bottom-stress curl term in equation (5.20), where the barotropic circulation explicitly couples to the local response. In the classic Stommel (1948) model, the bottom stress is simply taken to be proportional to the vertically integrated transport; taking its curl then yields a term proportional to the horizontal Laplacian of Ψ, adding a lateral diffusion term to the tracer analogy. More physically, Ekman theory should be applied to the bottom boundary layer, such that the bottom stress depends on the near-bottom geostrophic flow. Because the near-bottom geostrophic flow depends on both the barotropic circulation and the baroclinic shear, this couples the barotropic problem to the local response to mixing. This theory is developed over the next two sections.

5.5.2 The local response to mixing

The local response can be determined by solving the frictional thermal wind relations, which arise from differentiating the momentum equations (5.9) and (5.10) in z and substituting hydrostatic balance (5.11):

$$-f\frac{\partial v}{\partial z} = -\frac{\partial b}{\partial x} + \varepsilon^2 \frac{\partial^2}{\partial z^2}\left(\nu\frac{\partial u}{\partial z}\right), \tag{5.21}$$

$$f\frac{\partial u}{\partial z} = -\frac{\partial b}{\partial y} + \varepsilon^2 \frac{\partial^2}{\partial z^2}\left(\nu\frac{\partial v}{\partial z}\right). \tag{5.22}$$

As a reminder, all variables (including f and ν) are nondimensional. Given the horizontal buoyancy gradients, equations (5.21) and (5.22) define a set of two coupled second-order ordinary differential equations in z for the shear of the horizontal flow $(\partial_z u, \partial_z v)$. The first set of boundary conditions are due to the wind stress ($\varepsilon^2\nu\partial_z u = \tau^x$ and $\varepsilon^2\nu\partial_z v = \tau^y$ at $z = 0$), while the second set arises from the barotropic transport constraint:

$$-\int_{-H}^{0} z\frac{\partial u}{\partial z}\,\mathrm{d}z = U \quad \text{and} \quad -\int_{-H}^{0} z\frac{\partial v}{\partial z}\,\mathrm{d}z = V, \tag{5.23}$$

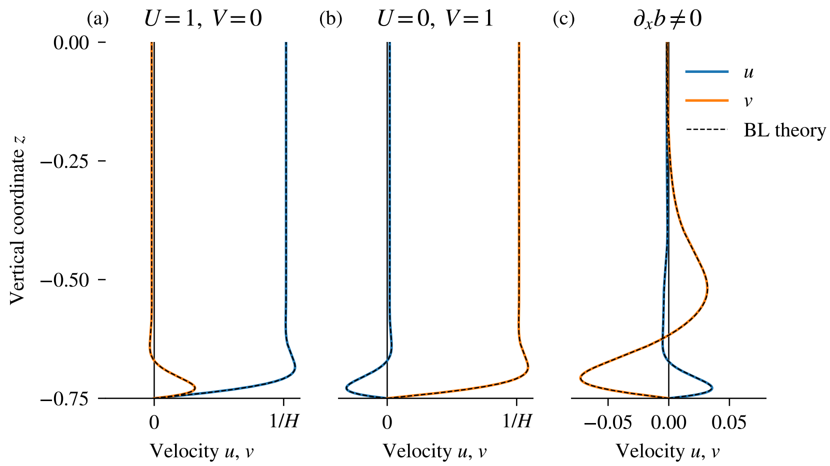

Figure 5.7: Solutions to the frictional thermal wind equations (5.21) and (5.22) for cases with (a) zonal transport only (b) meridional transport only, and (c) no transport with a zonal buoyancy gradient taken from the bowl simulation at $x = 0.5$, $y = 0$, and $t = 10^{-2}$ (see Fig. 5.1). Second-order accurate BL theory solutions (see appendix B) are shown in black dashed lines. Parameters are as in the full inversion at $x = 0.5$ and $y = 0$ ($\varepsilon = 2 \times 10^{-2}$, $f = 1$, $\nu = 1$, $H = 0.75$) with horizontal diffusion ignored.

coupling the problem to the barotropic vorticity equation (5.20). Since $\boldsymbol{u} = 0$ at $z = -H$, the horizontal flow can easily be determined from the shear by integrating upward: $u(z) = \int_{-H}^{z} \partial_z u \, \mathrm{d}z$ and $v(z) = \int_{-H}^{z} \partial_z v \, \mathrm{d}z$. The vertical flow can be determined by cross-differentiating the horizontal momentum equations (5.9) and (5.10) and applying continuity (5.12), which yields the frictional vorticity balance,

$$\beta v = f \frac{\partial w}{\partial z} + \varepsilon^2 \frac{\partial}{\partial z} \left(\nu \frac{\partial \zeta}{\partial z} \right), \tag{5.24}$$

where $\zeta = \partial_x v - \partial_y u$ is the relative vorticity. From this relation, it is clear that the local interior vertical velocity reflects the stretching or squashing needed to conserve potential vorticity of the fluid column as it moves across a meridional planetary vorticity gradient. Near the boundaries, where the friction term dominates, horizontal variations in the local response yield Ekman pumping and suction.

Solutions to the equations (5.21) to (5.22) are well-understood from standard Ekman theory (e.g., Ekman, 1905; Pedlosky, 1979; Vallis, 2017). For a purely zonal transport with no horizontal buoyancy gradients, the flow is constant in the interior with $u = U/H$ and $v = 0$, and both follow a classic Ekman spiral to zero in the bottom BL (Fig. 5.7a). For $f > 0$, the positive zonal transport spirals counter-clockwise, generating a small, positive meridional transport in the BL. Likewise, for a positive meridional transport, the constant interior flow $u = 0$ and $v = V/H$ spirals near the bottom such that a small, negative zonal BL transport is created (Fig. 5.7b). Finally, when no net transport is allowed but a buoyancy gradient in x is present due to turbulent mixing on a slope, the shear in the meridional flow satisfies thermal wind in the interior (Fig. 5.7c). The constraint that $V = 0$ then implies a non-zero interior flow at the top of the bottom BL, leading to an Ekman spiral with positive zonal transport in the BL.

These hypothetical profiles already shed light on the differences between the vertical structure of the flow from the inversions shown in the previous section. For each vertical column in the domain, linearity of the baroclinic equations (5.21) and (5.22) implies that the full flow is a linear combination of the solutions in Fig. 5.7. On an f-plane at $y = 0$ in the bowl, the zonal transport is zero, so that the full solution would be V times the response in Fig. 5.7b plus the response in Fig. 5.7c. The positive meridional transport at $(0.5, 0)$ in Fig. 5.6a then helps to explain the profiles in Fig. 5.5: the barotropic contribution in Fig. 5.7b shifts the dipole in the interior meridional flow in Fig. 5.7c up and reduces the up-slope BL transport. For $\beta = 0.5$, the meridional transport is reduced in magnitude and the zonal transport is slightly negative at this point, which explains the negative barotropic shifts in the interior flow. Finally, the $\beta = 1$ inversion has nearly zero barotropic transport throughout the domain due to the open f/H contours, leading to negligible contributions from the local responses due to transport. Thus, the profiles in the open-contour case mostly resembled the local baroclinic response to horizontal buoyancy gradients alone (Fig. 5.7c). By removing the response due to meridional transport, the up-slope transport is enhanced.

This formulation of the local problem is generally applicable, with the integral conditions (5.23) describing exactly how the local response is constrained by the barotropic problem (5.20). Similarly, when along-slope symmetry is present, such as in the f-plane case in the bowl geometry, the barotropic problem can be sufficiently simplified to enable an explicit calculation of the local response. Taking x and y to be the local cross- and along-slope directions, neglecting along-slope variations in the barotropic vorticity equation (5.20) implies

$$\frac{\partial}{\partial x}\left(\frac{\nu}{H}\frac{\partial v}{\partial z}\bigg|_{-H}\right) = 0. \tag{5.25}$$

Integrating in x from the center of the domain, where the flow must vanish by symmetry, this reduces to the requirement that the along-slope shear vanishes everywhere along the bottom:

$$\frac{\partial v}{\partial z} = 0 \quad \text{at} \quad y = 0, \quad z = -H. \tag{5.26}$$

The same conclusion can be reached by integrating the y-momentum equation from $z = -H$ to $z = 0$, assuming $\partial_y p = 0$ and $U = 0$ (PC22). The constraint in (5.26) then replaces the along-slope integral boundary condition in (5.23), and the cross-slope transport is set to zero by the symmetry described above. This local model is mathematically equivalent to the streamfunction formulation of the dynamics in the x–z plane from PC22, but it more naturally generalizes to the three-dimensional problem. If one assumes a uniform bottom slope θ, the horizontal buoyancy gradient becomes $\partial_x b = -\partial_z b \tan\theta$, and the vertical flow is simply $w = u \tan\theta$, as in the standard one-dimensional models (see appendices A and B).

5.5.3 Boundary layer theory

The barotropic and local problems outlined in the previous two sections form a complete description of the PG inversion. The two must be solved together, with the solution to the local problem feeding in to the bottom-stress curl "sink" term in the the barotropic vorticity equation (5.20) and the barotropic solution appearing in the integral constraint (5.23) of the local inversion (5.21) to (5.22). In this section we use standard Ekman BL theory (e.g., Pedlosky, 1979; Vallis, 2017) to arrive at an analytical expression for the bottom stress, allowing us to explicitly describe how the local response couples to the basin-wide dynamics. In the following, we here describe the salient results of the BL theory and leave the details in appendix B.

We split the flow into an interior contribution $\boldsymbol{u}_\mathrm{I}$, which varies slowly in z, and bottom and surface BL corrections $\boldsymbol{u}_\mathrm{B}$ and $\boldsymbol{u}_\mathrm{S}$, respectively, which ensure boundary conditions are satisfied and have appreciable magnitude in thin BLs only. The interior solution is then, to $O(\varepsilon)$, in thermal wind balance:

$$f\frac{\partial v_\mathrm{I}}{\partial z} = \frac{\partial b}{\partial x} \quad \text{and} \quad f\frac{\partial u_\mathrm{I}}{\partial z} = -\frac{\partial b}{\partial y}. \tag{5.27}$$

In the absence of a buoyancy gradient, the flow in the interior is constant, consistent with both profiles in Fig. 5.7a,b and u in Fig. 5.7c (where $\partial_y b = 0$). To satisfy the no-flow boundary condition at the bottom, this flow is brought to zero by friction in a classic Ekman spiral, with coefficients set by the (yet to be determined) interior flow at the top of the bottom BL:

$$u_\mathrm{B} = -e^{-q\bar{z}}\left(u_\mathrm{I}|_{-H}\cos q\bar{z} + v_\mathrm{I}|_{-H}\sin q\bar{z}\right), \tag{5.28}$$

$$v_\mathrm{B} = -e^{-q\bar{z}}\left(v_\mathrm{I}|_{-H}\cos q\bar{z} - u_\mathrm{I}|_{-H}\sin q\bar{z}\right). \tag{5.29}$$

The solution is written in terms of the stretched vertical coordinate $\bar{z} = (z+H)/\varepsilon$ and $q^{-1} = \sqrt{2\nu|_{-H}/f}$ is the bottom BL thickness in this coordinate. With $b = 0$ at $z = 0$, the shear of the interior velocities (5.27) is zero at the surface, automatically satisfying the surface boundary condition for no wind stress. If a non-zero wind stress is allowed, an $O(\varepsilon^{-1})$ Ekman spiral BL correction at the surface $\boldsymbol{u}_\mathrm{S}$ must be present as well.

The Ekman spiral in the bottom BL (5.28) and (5.29) generates considerable shear near the bottom, providing a frictional sink of barotropic vorticity. To derive an explicit formula for the curl of this bottom stress, we must first determine the interior flow at the top of the BL $u_\mathrm{I}|_{-H}$ and $v_\mathrm{I}|_{-H}$. This can be done by considering the contributions of the interior and BL components to the vertically-integrated transport:

$$U = U_\mathrm{I} + U_\mathrm{S} + \varepsilon U_\mathrm{B} \quad \text{and} \quad V = V_\mathrm{I} + V_\mathrm{S} + \varepsilon V_\mathrm{B}. \tag{5.30}$$

Due to the thinness of the surface and bottom BLs, their integrals pick up a factor of ε, but since the surface BL correction is of $O(\varepsilon^{-1})$, its integral contribution is of $O(1)$. Neglecting the $O(\varepsilon)$ contributions from the bottom BL in (5.30) and solving for the interior flow at the top of the bottom BL yields

$$u_{\mathrm{I}}|_{-H} = \frac{U}{H} - \frac{1}{fH}\int_{-H}^{0} z\frac{\partial b}{\partial y}\,\mathrm{d}z - \frac{\tau^y}{fH}, \tag{5.31}$$

$$v_{\mathrm{I}}|_{-H} = \frac{V}{H} + \frac{1}{fH}\int_{-H}^{0} z\frac{\partial b}{\partial x}\,\mathrm{d}z + \frac{\tau^x}{fH}. \tag{5.32}$$

With these constants determined, is now possible to write down the bottom stress due to the BL correction (5.28) and (5.29):

$$\left.\frac{\partial u_{\mathrm{B}}}{\partial z}\right|_{-H} = \frac{q}{\varepsilon}\left[\frac{U-V}{H} - \frac{1}{fH}\int_{-H}^{0} z\left(\frac{\partial b}{\partial x} + \frac{\partial b}{\partial y}\right)\,\mathrm{d}z - \frac{\tau^x+\tau^y}{fH}\right], \tag{5.33}$$

$$\left.\frac{\partial v_{\mathrm{B}}}{\partial z}\right|_{-H} = \frac{q}{\varepsilon}\left[\frac{U+V}{H} + \frac{1}{fH}\int_{-H}^{0} z\left(\frac{\partial b}{\partial x} - \frac{\partial b}{\partial y}\right)\,\mathrm{d}z + \frac{\tau^x-\tau^y}{fH}\right]. \tag{5.34}$$

This $O(\varepsilon^{-1})$ contribution is the dominant term in the full stress. Equations (5.33) and (5.34) explicitly separate the contributions to the bottom stress in terms of three physical sources: 1) the barotropic transports, 2) the full-column buoyancy gradients, and 3) the wind stress. The latter two terms are external forcings to the problem, while the barotropic transports couple the local flow to the basin-scale circulation.

Plugging these analytical expressions for the bottom stress into the barotropic vorticity equation (5.20) yields the following closed equation for the barotropic streamfunction:

$$\varepsilon\nabla_\perp\cdot\left(\frac{r}{H}\nabla_\perp\Psi\right) - \mathrm{J}\left(\frac{f+\varepsilon r}{H},\Psi\right) = -\mathrm{J}\left(\frac{1}{H},\gamma\right) + \boldsymbol{z}\cdot\left(\nabla\times\frac{\boldsymbol{\tau}}{H}\right) - \varepsilon\mathcal{B} - \varepsilon\mathcal{T}, \tag{5.35}$$

where $\nabla_\perp = (\partial_x, \partial_y)$ is the horizontal gradient operator,

$$\mathcal{B} = \frac{\partial}{\partial x}\left[\frac{r}{fH}\int_{-H}^{0} z\left(\frac{\partial b}{\partial x} - \frac{\partial b}{\partial y}\right)\,\mathrm{d}z\right] + \frac{\partial}{\partial y}\left[\frac{r}{fH}\int_{-H}^{0} z\left(\frac{\partial b}{\partial x} + \frac{\partial b}{\partial y}\right)\,\mathrm{d}z\right] \tag{5.36}$$

is the curl of the bottom stress due to baroclinicity, and

$$\mathcal{T} = \frac{\partial}{\partial x}\left(\frac{\tau^x+\tau^y}{fH}\right) - \frac{\partial}{\partial y}\left(\frac{\tau^y-\tau^x}{fH}\right), \tag{5.37}$$

is the curl of wind-induced bottom stress. Because the first terms in the equations for the bottom stresses (5.33) and (5.34) are proportional to U and V, a Laplacian term appears just as in the Stommel theory, with the diffusion coefficient $r/H = \nu|_{-H}q/H^2$ dependent on the thickness of the bottom BL. In contrast with the Stommel model, there is also a cross term $\varepsilon\,\mathrm{J}(r/H,\Psi)$, applying an $O(\varepsilon)$ modification to the "advection" term $\mathrm{J}(f/H,\Psi)$ (e.g., Rattray, 1982). The more important changes come from the the other two terms in the bottom stresses: the term due to the baroclinic buoyancy response and the term due to the bottom return flow from the wind stress forcing contribute $O(\varepsilon)$ "sources" to Ψ.

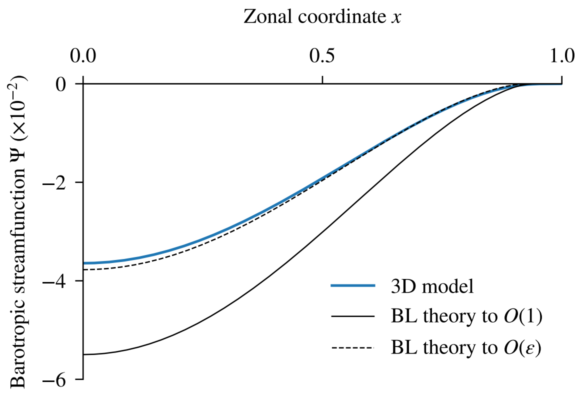

Figure 5.8: Comparison of the barotropic streamfunction Ψ at $t = 10^{-2}$ and $y = 0$ between the 3D f-plane inversion and the local model assuming along-slope symmetry (5.40). The modifications to the local model described in appendix C are applied to partially account for the added diffusion terms in the 3D model.

Making use of the fact that $\varepsilon \ll 1$, we can further describe the physics of the barotropic circulation in terms of its expansion in ε, defining $\Psi = \Psi_0 + \varepsilon\Psi_1 + \ldots$. The leading-order balance in (5.35) is then simply

$$-\mathrm{J}\left(\frac{f}{H}, \Psi_0\right) = -\mathrm{J}\left(\frac{1}{H}, \gamma\right) + \boldsymbol{z} \cdot \left(\nabla \times \frac{\boldsymbol{\tau}}{H}\right) = 0, \tag{5.38}$$

where the last equality is true in our inversions with no wind stress and $\gamma = \gamma(H)$. This confirms our intuition that the leading-order barotropic streamfunction is constant along f/H contours: $\Psi_0 = \Psi_0(f/H)$ (e.g., Rattray, 1982; Mertz and Wright, 1992). The source terms due to the curl of the bottom stress come into play at $O(\varepsilon)$:

$$\nabla_\perp \cdot \left(\frac{r}{H}\nabla_\perp \Psi_0\right) - \mathrm{J}\left(\frac{r}{H}, \Psi_0\right) - \mathrm{J}\left(\frac{f}{H}, \Psi_1\right) = \mathcal{B} + \mathcal{T}. \tag{5.39}$$

For open contours, $\Psi_0(f/H)$ must be identically zero due to the boundary condition $\Psi_0 = 0$ at the coast, explaining the destruction of the leading-order streamfunction for the $\beta = 1$ inversion (Fig. 5.6c). The strength of the circulation is then set at the next order by $\mathcal{B}$ and $\mathcal{T}$, with the addition of a lateral boundary layer to satisfy the boundary condition, as in the standard Stommel theory (Veronis, 1966). The theoretical profiles in Fig. 5.5, however, simply assume $U = V = 0$ to fully decouple the local response from the barotropic circulation. For closed contours, $\Psi_0(f/H)$ is non-zero and can, in general, be determined by integrating (5.39) along f/H contours to remove the Ψ_1 term. This leads to a second-order ODE for $\Psi_0(f/H)$ with a forcing due to the integral of $\mathcal{B} + \mathcal{T}$ on the RHS.

When along-slope symmetry is present, as in our f-plane case, the along-slope barotropic transport can be directly computed from the model for the local response described above and in appendix C. Applying the constraints $\partial_y b = 0$, $U = 0$, and $\partial_z v|_{-H} = 0$ and solving for V yields

$$\frac{\partial \Psi_0}{\partial x} = -\frac{1}{f}\int_{-H}^{0} z\frac{\partial b}{\partial x}\,\mathrm{d}z \quad \text{and} \quad \frac{\partial \Psi_1}{\partial x} = -\frac{H}{fq}\frac{\partial b}{\partial x}\bigg|_{-H}. \tag{5.40}$$

For a full derivation out to $O(\varepsilon^2)$, see appendix C. Physically, the leading-order term represents thermal-wind shear integrated over the column, suggesting that the along-slope transport scales with the horizontal buoyancy gradient over the mixing layer, the height of this layer, and the total depth of the column. The flow at the next order must be barotropic, setting up an $O(\varepsilon)$ Ekman layer at the bottom. Setting the $O(1)$ along-slope shear to zero then determines this $O(\varepsilon)$ correction to the barotropic transport, which plays an important quantitative role here due to the relative magnitudes of Ψ_0 and ε (Fig. 5.8). Similarly, to achieve quantitative agreement in Fig. 5.5, the profiles for the local responses are computed out to $O(\varepsilon^2)$ (see appendices B and C).

5.6 Discussion

The buoyancy distribution of the abyssal ocean in steady state is set by a balance between diapycnal advection and diapycnal mixing (Munk, 1966). The advecting flow is itself a function of this buoyancy field, and, in this work, we chose to focus our attention on this dependence in the context of the PG approximation. In the "strong diffusion regime," where $\mu\varrho \sim \varepsilon^2$, this yields a full description of the circulation: the buoyancy evolves according to simple diffusion and the flow passively varies according to the PG inversion of this field. Restricting ourselves to this very basic dynamics allowed us to make progress in understanding the generalizations of previous theories for the local response to mixing. It is worth noting that, assuming one somehow knew the steady-state buoyancy field from the advection–diffusion problem, the analysis presented here would apply to the steady-state flow field. Without a complete understanding of how this flow is determined, however, it would be impossible to know how the buoyancy field arrived at that steady state to begin with. This paper therefore represents one important step in developing a full theory for the abyssal circulation, with the next being to consider the feedback of this flow onto the buoyancy field.

Some speculation for how advection could shape the buoyancy field, given the flow inversions presented here, is possible. For instance, the enhanced BL upwelling for open f/H contours (Figs. 5.4i, 5.5c) could encounter a negative feedback once it is allowed to interact with the hydrography. This transport of dense water up the slope would work to restratify the BL, potentially alleviating the need for baroclinic eddies to maintain stratification in the abyss (Callies, 2018). This flattening of isopycnals will, in turn, reduce the thermal wind shear above the BL, weakening the BL transport. This negative feedback on the BL transport could be particularly relevant given the ubiquity of open f/H contours in the real ocean (Fig. 5.2). The larger interior vertical velocities for β-plane inversions (Figs. 5.4h,i, 5.5c) would also modify the interior stratification with advection allowed. The pattern of downwelling on the eastern side and upwelling on the western side of the basin for the zonal section at $y = 0$ would work to generate a negative zonal buoyancy gradient and hence equatorward shear in the interior meridional flow. This flow must, in turn, conserve vorticity, perturbing the vertical velocities and likely generating westward-propagating long Rossby waves. These Rossby waves would then allow for communication between the eastern and western sides of the basin, playing an important role in setting up a western boundary current in the early stages of spinup.

Ultimately, the goal will be to describe these dynamics in terms of BL–interior communication to better understand the role that bottom-enhanced mixing plays in shaping the abyssal circulation. The BL theory in PC23 builds a foundation for this theory by considering the case with along-slope symmetry. This theory illustrates how upslope BL transport supplies a downward flux of buoyancy that the interior feels as an effective bottom boundary condition. As the cross-slope stratification at the top of the BL evolves, so does the BL transport, providing an avenue for exchange. This description should carry over to the more general case, with the local response now coupled to the barotropic vorticity equation as discussed here. While the interior dynamics may evolve on a faster timescale, supporting Rossby waves, the BLs should remain quasi-steady, again setting an effective bottom boundary condition on the interior.

In this paper, we only show numerical inversions for the simple case of no wind stress and a symmetric buoyancy field in a simple basin geometry. The theory is general, however, allowing us to reason about how the circulation would change under different scenarios without explicitly computing the inversion. In general, the wind-stress curl and JEBAR terms provide leading-order sources/sinks of barotropic vorticity in equation (5.38). If these terms are nonzero, a leading-order barotropic circulation could be supported even in the open f/H contour case. The wind-forced circulation, however, should be largely confined to the thermocline, reducing its impact on the abyssal circulation, at least in subtropical regions (Luyten et al., 1983). We put our focus on the abyssal circulation powered by bottom-enhanced mixing, but its interplay with the wind-forced circulation, especially in subpolar regions, could be studied using the same framework.

As a final caveat, we note that the analytical theory presented in the main text of this work assumes no horizontal diffusion and no diffusion in the vertical momentum equation, while the numerical solutions to the PG equations do include these terms for stability. Over a uniform slope, these terms contribute a factor of $(1 + \alpha^2 \tan^2 \theta)^{3/4}$ modification the the BL scale q^{-1} (appendices A and C). While this leads to a slight quantitative modification to the flow, the qualitatively the physics remain unchanged. This correction is included in the BL solutions presented in Figures 5.5 and 5.8 to more directly compare with the three-dimensional model, although slight errors are still expected due to curvatures in the slope. The BL solutions in Figure 5.7 do not require this modification, as there the local response is computed directly from equations (5.21) and (5.22) without these diffusion terms.

5.7 Conclusions

Our understanding of how observed bottom-enhanced mixing shapes the global abyssal ocean circulation has been guided by theories focused on the local dynamics above slopes (e.g., Phillips et al., 1986; McDougall, 1989; Garrett, 1991; Dell and Pratt, 2015; Holmes et al., 2018; Callies and Ferrari, 2018; Drake et al., 2020). In this work, we explored how this local response couples to the basin-scale barotropic circulation for a fixed buoyancy field under the PG approximation. While barotropic dynamics have been well understood since Welander (1968), their connection to the baroclinic response to mixing over sloping topography is novel. We found that the bottom-stress curl of the local response forces the barotropic vorticity through three primary mechanisms: shear due to barotropic interior currents, baroclinicity of the buoyancy field, and bottom return flow due to the wind stress. These terms drop out at leading order away from the coastline, yielding the standard balance between "advection" of Ψ along f/H contours and "sources" from JEBAR and the wind-stress curl (e.g., Rattray, 1982; Mertz and Wright, 1992).

To focus on how baroclinicity of the local response shapes the barotropic circulation, we considered the flow field resulting from zero wind-stress and a buoyancy field that is a function of depth. The "sources" in the leading-order barotropic vorticity equations vanish in this case, implying that Ψ_0 must follow f/H contours. When these contours are closed, such as over large topographic features (e.g., Fig. 5.2b), a leading-order along-contour transport develops, with its magnitude set by the thermal wind shear over the mixing layer. On an f-plane, this corresponds to an along-*slope* transport, and, for axisymmetric bathymetry, the local response is completely determined by the one-dimensional model of PC22. For open f/H contours, in contrast, Ψ_0 must be zero, decoupling the leading-order local response from the large-scale context.

This second is case is more representative of the f/H contours in real ocean basins (Fig. 5.2a) and has important implications for the influence of the BL on the interior circulation. Constraining the net transport of the local response to zero enhances the along-slope shear at the top of the BL, promoting the BL upwelling from $O(\varepsilon)$ to $O(1)$ compared to the response in the case of along-slope symmetry. Once allowed to advect buoyancy, this BL flow would more efficiently transport dense water up the slope, supplying a stronger effective buoyancy flux at the bottom felt by the interior (cf. PC23). This could imply that baroclinic eddies are not required to maintain abyssal stratification (cf. Wenegrat et al., 2018; Callies, 2018).

5.8 Appendix A: The PG inversion with non-zero aspect ratio

The non-dimensional PG inversion as it is presented in equations (5.9) to (5.12) in the main text implicitly assumes a small aspect ratio and, hence, does not contain horizontal diffusion. This is an excellent assumption for the ocean, since, using the scales from section 5.35.3.2, the aspect ratio is around $H_0/L \sim 10^{-3}$. For numerical stability, however, we found it necessary to re-introduce these terms by artificially inflating the aspect ratio. This comes with the cost of quantitative errors, but the qualitative dynamics remain the same, as we hope to convince you of here.

The PG inversion that our numerical model ultimately solves reads

$$-fv = -\frac{\partial p}{\partial x} + \alpha^2\varepsilon^2\frac{\partial}{\partial x}\left(\nu\frac{\partial u}{\partial x}\right) + \alpha^2\varepsilon^2\frac{\partial}{\partial y}\left(\nu\frac{\partial u}{\partial y}\right) + \varepsilon^2\frac{\partial}{\partial z}\left(\nu\frac{\partial u}{\partial z}\right), \tag{5.41}$$

$$fu = -\frac{\partial p}{\partial y} + \alpha^2\varepsilon^2\frac{\partial}{\partial x}\left(\nu\frac{\partial v}{\partial x}\right) + \alpha^2\varepsilon^2\frac{\partial}{\partial y}\left(\nu\frac{\partial v}{\partial y}\right) + \varepsilon^2\frac{\partial}{\partial z}\left(\nu\frac{\partial v}{\partial z}\right), \tag{5.42}$$

$$\frac{\partial p}{\partial z} = b + \alpha^4\varepsilon^2\frac{\partial}{\partial x}\left(\nu\frac{\partial w}{\partial x}\right) + \alpha^4\varepsilon^2\frac{\partial}{\partial y}\left(\nu\frac{\partial w}{\partial y}\right) + \alpha^2\varepsilon^2\frac{\partial}{\partial z}\left(\nu\frac{\partial w}{\partial z}\right), \tag{5.43}$$

$$\nabla\cdot\boldsymbol{u} = 0, \tag{5.44}$$

where $\alpha = H_0/L$ is the squared aspect ratio. For $\alpha \neq 0$, horizontal diffusion terms are retained in the momentum equations. Crucially, hydrostatic balance is no longer exactly satisfied in equation (5.43). This allows us to use classical finite element techniques for Stokes flow, as described in the main text.

To quantify the impact that artificially increasing α has on the inversions considered here, we will consider the simple case of a uniform bottom slope in the x direction at an angle θ with the horizontal. We define the transformation from Cartesian to slope-following coordinates as

$$\xi = x, \quad \eta = y, \quad \zeta = z - x\tan\theta, \tag{5.45}$$

(see PC22, Fig. A1, for a sketch). The contravariant velocity components under this coordinate transformation are then

$$u^\xi = u, \quad u^\eta = v, \quad u^\zeta = w - u\tan\theta, \tag{5.46}$$

and the partial derivatives transform as

$$\frac{\partial}{\partial x} = \frac{\partial}{\partial\xi} - \tan\theta\frac{\partial}{\partial\zeta}, \quad \frac{\partial}{\partial y} = \frac{\partial}{\partial\eta}, \quad \frac{\partial}{\partial z} = \frac{\partial}{\partial\zeta}. \tag{5.47}$$

Neglecting variations in planes parallel to the slope (the ξ and η directions) while still allowing for a cross-slope barotropic pressure gradient $\partial_x P$, equations (5.41) to (5.44) become

$$-fu^\eta = -\frac{\partial P}{\partial x} + b'\tan\theta + \Gamma^2\varepsilon^2\frac{\partial}{\partial\zeta}\left(\nu\frac{\partial u^\xi}{\partial\zeta}\right), \tag{5.48}$$

$$fu^\xi = \Gamma\varepsilon^2\frac{\partial}{\partial\zeta}\left(\nu\frac{\partial u^\eta}{\partial\zeta}\right), \tag{5.49}$$

$$\int_{-H}^{0} u^\xi \,\mathrm{d}\zeta = 0, \tag{5.50}$$

where b' is the buoyancy perturbation from a background $b = z$. Equations (5.48) to (5.50) form the generalization of the (non-dimensional) transport-constrained 1D inversion for $\alpha \neq$

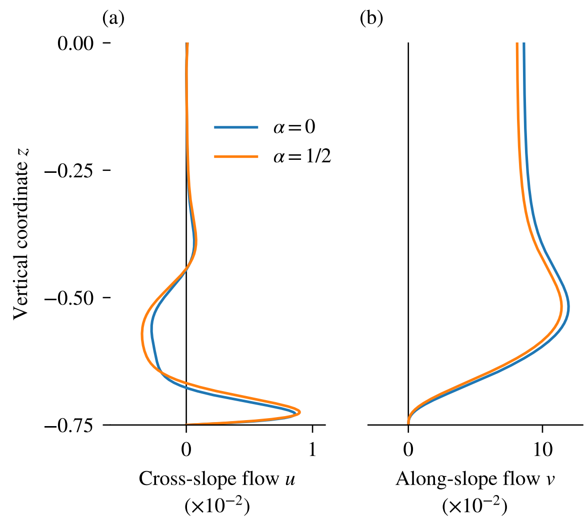

Figure 5.9: Snapshot of (a) cross-slope flow u and (b) along-slope flow v satisfying the transport-constrained 1D equations (5.48) to (5.50) for aspect ratios $\alpha = 0$ and 1/2 and the same mixing-driven buoyancy field at $t = 10^{-2}$ used in the main text. The column depth $H = 0.75$ and local slope $\theta = \pi/4$ corresponding to the point $x = 0.5$ and $y = 0$ on the bowl, as in Fig. 5.5. In this case, the vertical velocity is the same as the cross-slope flow since $w = u \tan\theta$.

0. The only differences to the $\alpha = 0$ model are the factors of $\Gamma = 1 + \alpha^2 \tan^2\theta$ multiplying the flux terms. Physically, these factors come from the projection of the horizontal fluxes in the direction of the slope, with an extra factor of Γ in the ξ-momentum equation due to the non-hydrostatic part of $\partial_\zeta p$.

Even for $\alpha = 0.5$, three orders of magnitude larger than that of the abyssal ocean, the 1D model solutions at $\theta = \pi/4$ (corresponding to $x = 0.5$ and $y = 0$ in the bowl, as in Fig. 5.5) are qualitatively similar to the $\alpha = 0$ case (Fig. 5.9). As expected, the factors of $\Gamma = 1.25$ on the friction terms lead to slight thickening of the BL (Fig. 5.9a). From BL theory, the new bottom Ekman layer thickness is $\delta = \Gamma^{4/3}\sqrt{2}\varepsilon$ (see appendix C). Somewhat more surprisingly, the interior along-slope flow is reduced for the $\alpha = 1/2$ case (Fig. 5.9b). This can be explained with BL theory, where we find that the asymptotic expansion of $\partial_x P \sim f v|_0$ in ε is

$$\frac{\partial P}{\partial x} = b'|_{-H} \tan\theta - \varepsilon\Gamma^{4/3}\sqrt{\frac{2\nu|_{-H}}{f}} \tan\theta + O(\varepsilon^2). \tag{5.51}$$

The first term comes from the transport constraint, which forces the interior along-slope flow to be zero at the top of the BL. The $O(\varepsilon)$ correction comes from the fact that the shear in the $O(1)$ interior along-slope flow must balance the shear from the $O(\varepsilon)$ BL correction. Since $\Gamma^{4/3} \approx 1.3$ for $\alpha = 1/2$, the change in $\partial_x P$ between the two cases is about 10^{-2}, consistent with the change in $v|_0$ in Fig. 5.9.

5.9 Appendix B: BL solution to the frictional thermal wind equations

This appendix contains the full derivation of the BL theory solution to the local inversion (5.21) and (5.22) described in section 5.5. As described in the main text, we split the flow into interior, surface BL, and bottom BL components $\boldsymbol{u}_\mathrm{I}$, $\boldsymbol{u}_\mathrm{S}$, and $\boldsymbol{u}_\mathrm{B}$, respectively. We further expand these components in ε so that $\boldsymbol{u}_\mathrm{I} = \boldsymbol{u}_{\mathrm{I}0} + \varepsilon \boldsymbol{u}_{\mathrm{I}1} + \varepsilon^2 \boldsymbol{u}_{\mathrm{I}2} + \dots$ and $\boldsymbol{u}_\mathrm{B} = \boldsymbol{u}_{\mathrm{B}0} + \varepsilon \boldsymbol{u}_{\mathrm{B}1} + \varepsilon^2 \boldsymbol{u}_{\mathrm{B}2} + \dots$. As we will see below, the surface boundary condition $\varepsilon^2 \nu \partial_z \boldsymbol{u}_\perp = \boldsymbol{\tau}$ requires that the leading-order surface BL correction be of $O(\varepsilon^{-1})$: $\boldsymbol{u}_\mathrm{S} = \varepsilon^{-1} \boldsymbol{u}_{\mathrm{S}-1} + \boldsymbol{u}_{\mathrm{S}0} + \varepsilon \boldsymbol{u}_{\mathrm{S}1} + \dots$. In what follows, we determine the solutions for each component up to $O(\varepsilon^2)$, applying matching conditions between them to satisfy the boundary conditions and transport constraints. In the last section, we briefly outline how the vertical flow may be determined.

5.9.1 Leading-order solution

Starting with the interior equations,

$$-f \frac{\partial v_\mathrm{I}}{\partial z} = -\frac{\partial b}{\partial x} + \varepsilon^2 \frac{\partial^2}{\partial z^2} \left(\nu \frac{\partial u_\mathrm{I}}{\partial z} \right), \tag{5.52}$$

$$f \frac{\partial u_\mathrm{I}}{\partial z} = -\frac{\partial b}{\partial y} + \varepsilon^2 \frac{\partial^2}{\partial z^2} \left(\nu \frac{\partial v_\mathrm{I}}{\partial z} \right), \tag{5.53}$$

we immediately find that, to leading-order, the horizontal flow is in thermal wind balance,

$$f \frac{\partial v_{\mathrm{I}0}}{\partial z} = \frac{\partial b}{\partial x} \quad \text{and} \quad f \frac{\partial u_{\mathrm{I}0}}{\partial z} = -\frac{\partial b}{\partial y}, \tag{5.54}$$

as shown in equation (5.27) in the main text. To ensure that the transport constraints (5.23) are satisfied at each order, we must keep track of the the vertically integrated transport due to each component of the flow. The transport due to this leading-order interior flow can be determined by integrating twice in the vertical:

$$\int_{-H}^{0} u_{\mathrm{I}0} \,\mathrm{d}z = H u_{\mathrm{I}0}|_{-H} + \frac{1}{f} \int_{-H}^{0} z \frac{\partial b}{\partial y} \,\mathrm{d}z \equiv U_{\mathrm{I}0}, \tag{5.55}$$

$$\int_{-H}^{0} v_{\mathrm{I}0} \,\mathrm{d}z = H v_{\mathrm{I}0}|_{-H} - \frac{1}{f} \int_{-H}^{0} z \frac{\partial b}{\partial x} \,\mathrm{d}z \equiv V_{\mathrm{I}0}, \tag{5.56}$$

where the leading-order interior flow at the top of the BL $\boldsymbol{u}_{\mathrm{I}0}|_{-H}$ is yet to be determined.

To determine the bottom BL correction, we transform equations (5.21) and (5.22) using the stretched vertical coordinate $z_\mathrm{B} = (z + H)/\varepsilon$ so that $\partial_z \to \varepsilon^{-1} \partial_{z_\mathrm{B}}$. The frictional terms are then promoted to $O(1)$ so, assuming the turbulent viscosity varies over a scale much larger than the bottom BL, the bottom BL flow satisfies

$$-f \frac{\partial v_\mathrm{B}}{\partial z_\mathrm{B}} = \nu|_{-H} \frac{\partial^3 u_\mathrm{B}}{\partial z_\mathrm{B}^3}, \tag{5.57}$$

$$f \frac{\partial u_\mathrm{B}}{\partial z_\mathrm{B}} = \nu|_{-H} \frac{\partial^3 v_\mathrm{B}}{\partial z_\mathrm{B}^3}. \tag{5.58}$$

Note that the buoyancy gradient terms are taken care of in the interior equations (5.52) and (5.53). Upon integration in the vertical (keeping in mind that $\boldsymbol{u}_\mathrm{B} \to 0$ as $z_\mathrm{B} \to \infty$) and substitution, equations (5.57) and (5.58) can be combined into a single, fourth-order ODE for u_B:

$$\frac{\partial^4 u_\mathrm{B}}{\partial z_\mathrm{B}^4} + 4q_\mathrm{B}^4 u_\mathrm{B} = 0, \tag{5.59}$$

where $q_\mathrm{B}^{-1} = \sqrt{2\nu|_{-H}/f}$ is the bottom BL thickness in z_B coordinates. Since there are no factors of ε in this equation, it is true for each order of u_B. The leading-order bottom BL correction is therefore a classic Ekman spiral with coefficients determined by the bottom boundary condition $\boldsymbol{u}_\mathrm{I0} = -\boldsymbol{u}_\mathrm{B0}$.

$$u_\mathrm{B0} = -e^{-q_\mathrm{B} z_\mathrm{B}} \left(u_\mathrm{I0}|_{-H} \cos q_\mathrm{B} z_\mathrm{B} + v_\mathrm{I0}|_{-H} \sin q_\mathrm{B} z_\mathrm{B} \right), \tag{5.60}$$

$$v_\mathrm{B0} = -e^{-q_\mathrm{B} z_\mathrm{B}} \left(v_\mathrm{I0}|_{-H} \cos q_\mathrm{B} z_\mathrm{B} - u_\mathrm{I0}|_{-H} \sin q_\mathrm{B} z_\mathrm{B} \right), \tag{5.61}$$

corresponding to equations (5.28) and (5.29) in the main text. The vertical integral of this leading-order bottom BL correction picks up a factor of ε due to the thinness of the layer:

$$\varepsilon \int_0^\infty u_\mathrm{B0}\, \mathrm{d}z_\mathrm{B} = -\varepsilon \frac{u_\mathrm{I0}|_{-H} + v_\mathrm{I0}|_{-H}}{2q_\mathrm{B}} \equiv \varepsilon U_\mathrm{B1}, \tag{5.62}$$

$$\varepsilon \int_0^\infty v_\mathrm{B0}\, \mathrm{d}z_\mathrm{B} = +\varepsilon \frac{u_\mathrm{I0}|_{-H} - v_\mathrm{I0}|_{-H}}{2q_\mathrm{B}} \equiv \varepsilon V_\mathrm{B1}. \tag{5.63}$$

If a non-zero buoyancy gradient and/or wind stress is present at the surface, a BL will form there as well. In the stretched vertical coordinate $z_\mathrm{S} = z/\varepsilon$, we again arrive at a fourth-order ODE for u_S,

$$\frac{\partial^4 u_\mathrm{S}}{\partial z_\mathrm{S}^4} + 4q_\mathrm{S}^4 u_\mathrm{S} = 0, \tag{5.64}$$

this time with $q_\mathrm{S}^{-1} = \sqrt{2\nu|_0/f}$. The surface stress boundary condition split between the interior and BL components is

$$\varepsilon\nu \frac{\partial u_\mathrm{S}}{\partial z_\mathrm{S}} = \tau^x - \varepsilon^2 \nu \frac{\partial u_\mathrm{I}}{\partial z} \quad \text{and} \quad \varepsilon\nu \frac{\partial v_\mathrm{S}}{\partial z_\mathrm{S}} = \tau^y - \varepsilon^2 \nu \frac{\partial v_\mathrm{I}}{\partial z} \tag{5.65}$$

at $z = 0$. As alluded to above, this shows explicitly that a surface BL correction of $O(\varepsilon^{-1})$ is needed to balance the $O(1)$ wind stress. This correction must again be of the form

$$u_{\mathrm{S}-1} = e^{q_\mathrm{S} z_\mathrm{S}} \left(c_1 \cos q_\mathrm{S} z_\mathrm{S} + c_2 \sin q_\mathrm{S} z_\mathrm{S} \right), \tag{5.66}$$

$$v_{\mathrm{S}-1} = e^{q_\mathrm{S} z_\mathrm{S}} \left(c_1 \sin q_\mathrm{S} z_\mathrm{S} - c_2 \cos q_\mathrm{S} z_\mathrm{S} \right), \tag{5.67}$$

where the coefficients can be determined from the $O(1)$ surface boundary condition (5.65), which yields

$$c_1 = \frac{\tau^x + \tau^y}{2\nu|_0 q_\mathrm{S}} \quad \text{and} \quad c_2 = \frac{\tau^x - \tau^y}{2\nu|_0 q_\mathrm{S}}. \tag{5.68}$$

The vertical integral of the surface BL correction again picks up a factor of ε due to the thinness of the layer, but this cancels with the order of the flow:

$$\varepsilon \int_{-\infty}^{0} \varepsilon^{-1} u_{\mathrm{S}-1} \, \mathrm{d}z_{\mathrm{S}} = +\frac{\tau^y}{f} \equiv U_{\mathrm{S}0}, \tag{5.69}$$

$$\varepsilon \int_{-\infty}^{0} \varepsilon^{-1} v_{\mathrm{S}-1} \, \mathrm{d}z_{\mathrm{S}} = -\frac{\tau^x}{f} \equiv V_{\mathrm{S}0}, \tag{5.70}$$

so this transport is ultimately of the same order as $\boldsymbol{U}_{\mathrm{I}0}$.

The leading-order solution to the local inversion is now fully characterized apart from the constants $u_{\mathrm{I}0}|_{-H}$ and $v_{\mathrm{I}0}|_{-H}$. These can be determined in terms of the barotropic transport $\boldsymbol{U}$ by combining the contributions from each of these components. Expanding the transport in ε so that $\boldsymbol{U} = \boldsymbol{U}_0 + \varepsilon \boldsymbol{U}_1 + \varepsilon^2 \boldsymbol{U}_2 + \ldots$, we have the $O(1)$ balance

$$\boldsymbol{U}_0 = \boldsymbol{U}_{\mathrm{I}0} + \boldsymbol{U}_{\mathrm{S}0}, \tag{5.71}$$

with $\boldsymbol{U}_{\mathrm{B}1}$ contributing at the next order. Substituting the results from equations (5.55), (5.56), (5.69), and (5.70) into (5.71) and solving for the interior velocities at the top of the bottom BL yields

$$u_{\mathrm{I}0}|_{-H} = \frac{U_0}{H} - \frac{1}{fH} \int_{-H}^{0} z \frac{\partial b}{\partial y} \, \mathrm{d}z - \frac{\tau^y}{fH}, \tag{5.72}$$

$$v_{\mathrm{I}0}|_{-H} = \frac{V_0}{H} + \frac{1}{fH} \int_{-H}^{0} z \frac{\partial b}{\partial x} \, \mathrm{d}z + \frac{\tau^x}{fH}, \tag{5.73}$$

as shown in equations (5.31) and (5.32) in the main text. The leading-order solution is now complete.

Apart from building intuition for the local response, this analytical solution can now also be used to explicitly couple the local response to the barotropic circulation via the bottom stress curl. By nature of the large vertical shear in the bottom BL correction, it dominates the bottom stress at leading order:

$$\left.\frac{\partial \boldsymbol{u}}{\partial z}\right|_{-H} = \left.\frac{\partial \boldsymbol{u}_{\mathrm{I}}}{\partial z}\right|_{-H} + \frac{1}{\varepsilon} \left.\frac{\partial \boldsymbol{u}_{\mathrm{B}}}{\partial z_{\mathrm{B}}}\right|_{0}. \tag{5.74}$$

The leading-order bottom stress is therefore of $O(\varepsilon^{-1})$ and, using $\boldsymbol{u}_{\mathrm{I}0}|_{-H}$ from (5.72) and (5.73), takes the form

$$\frac{1}{\varepsilon} \left.\frac{\partial u_{\mathrm{B}0}}{\partial z_{\mathrm{B}}}\right|_{0} = \frac{q_{\mathrm{B}}}{\varepsilon} \left[\frac{U_0 - V_0}{H} - \frac{1}{fH} \int_{-H}^{0} z \left(\frac{\partial b}{\partial x} + \frac{\partial b}{\partial y} \right) \mathrm{d}z - \frac{\tau^x + \tau^y}{fH} \right], \tag{5.75}$$

$$\frac{1}{\varepsilon} \left.\frac{\partial v_{\mathrm{B}0}}{\partial z_{\mathrm{B}}}\right|_{0} = \frac{q_{\mathrm{B}}}{\varepsilon} \left[\frac{U_0 + V_0}{H} + \frac{1}{fH} \int_{-H}^{0} z \left(\frac{\partial b}{\partial x} - \frac{\partial b}{\partial y} \right) \mathrm{d}z + \frac{\tau^x - \tau^y}{fH} \right], \tag{5.76}$$

corresponding to equations (5.33) and (5.34) in the main text.

5.9.2 $O(\varepsilon)$ solution

In the main text, only the leading-order solution is presented. It can be informative, however, to expand each component one more order in ε, particularly when the leading-order circulation set by thermal-wind shear is weak.

The interior equations (5.52) and (5.53) at $O(\varepsilon)$ are simply

$$\frac{\partial v_{\mathrm{I}1}}{\partial z} = 0 \quad \text{and} \quad \frac{\partial u_{\mathrm{I}1}}{\partial z} = 0, \tag{5.77}$$

implying that $u_{\mathrm{I}1}$ and $v_{\mathrm{I}1}$ are constants in z. The bottom BL equations (5.57) and (5.58) are the same at $O(\varepsilon)$, implying the same form of the second-order BL correction $\boldsymbol{u}_{\mathrm{B}1}$ as in (5.60) and (5.61), this time with the coefficients $\boldsymbol{u}_{\mathrm{I}0}|_{-H}$ replaced by $\boldsymbol{u}_{\mathrm{I}1}$. The integral will again pick up a factor of ε, yielding the $O(\varepsilon^2)$ contribution $\boldsymbol{U}_{\mathrm{B}2}$ to the total transport. The surface boundary condition (5.65) at $O(1)$ just becomes $\partial_{z_\mathrm{S}}\boldsymbol{u}_{\mathrm{S}0} = 0$, implying $\boldsymbol{u}_{\mathrm{S}0} = 0$, while at $O(\varepsilon)$ we have $\nu\partial_{z_\mathrm{S}}\boldsymbol{u}_{\mathrm{S}1} = -\nu\partial_z\boldsymbol{u}_{\mathrm{I}0}$ at $z = 0$. If a buoyancy gradient at the surface exists, this will lead to an $O(\varepsilon)$ surface BL correction of the same form as in (5.66) and (5.67) with coefficients of the same form as in (5.68) with $\boldsymbol{\tau}$ replaced by $-\nu\partial_z\boldsymbol{u}_{\mathrm{I}0}|_0$. This correction yields an $O(\varepsilon^2)$ contribution to the vertically integrated transport $\boldsymbol{U}_{\mathrm{S}2}$.

We again use the transport constraint to solve for $\boldsymbol{u}_{\mathrm{I}1}$ in terms of $\boldsymbol{U}_1$. The $O(\varepsilon)$ transport is determined by the first-order barotropic interior correction and the integral of the leading-order bottom BL correction:

$$\boldsymbol{U}_1 = H\boldsymbol{u}_{\mathrm{I}1} + \boldsymbol{U}_{\mathrm{B}1}. \tag{5.78}$$

Substituting the form of $\boldsymbol{U}_{\mathrm{B}1}$ from (5.62) and (5.63) and solving for $\boldsymbol{u}_{\mathrm{I}1}$ yields

$$u_{\mathrm{I}1} = \frac{U_1}{H} + \frac{u_{\mathrm{I}0}|_{-H} + v_{\mathrm{I}0}|_{-H}}{2Hq_\mathrm{B}}, \tag{5.79}$$

$$v_{\mathrm{I}1} = \frac{V_1}{H} - \frac{u_{\mathrm{I}0}|_{-H} - v_{\mathrm{I}0}|_{-H}}{2Hq_\mathrm{B}}, \tag{5.80}$$

where $\boldsymbol{u}_{\mathrm{I}0}|_{-H}$ can be read off from (5.72) and (5.73). The $O(1)$ bottom stress from (5.74), which comes in to the barotropic vorticity equation at $O(\varepsilon^2)$, is then

$$\left.\frac{\partial u_{\mathrm{I}0}}{\partial z}\right|_{-H} + \left.\frac{\partial u_{\mathrm{B}1}}{\partial z_\mathrm{B}}\right|_0 = -\frac{1}{f}\left.\frac{\partial b}{\partial y}\right|_{-H} + q_\mathrm{B}\left(u_{\mathrm{I}1} - v_{\mathrm{I}1}\right), \tag{5.81}$$

$$\left.\frac{\partial v_{\mathrm{I}0}}{\partial z}\right|_{-H} + \left.\frac{\partial v_{\mathrm{B}1}}{\partial z_\mathrm{B}}\right|_0 = +\frac{1}{f}\left.\frac{\partial b}{\partial x}\right|_{-H} + q_\mathrm{B}\left(u_{\mathrm{I}1} + v_{\mathrm{I}1}\right). \tag{5.82}$$

5.9.3 $O(\varepsilon^2)$ solution

Finally, we here present the results for the $O(\varepsilon^2)$ solution for completeness, which are not needed to understand the leading-order physics but are used to compute the solutions shown in Figs. 5.5 and 5.7 for quantitative comparison. The most important modification comes from the interior equations (5.52) and (5.53) at $O(\varepsilon^2)$,

$$-f\frac{\partial v_{\mathrm{I}2}}{\partial z} = \frac{\partial^2}{\partial z^2}\left(\nu\frac{\partial u_{\mathrm{I}0}}{\partial z}\right) \quad \text{and} \quad f\frac{\partial u_{\mathrm{I}2}}{\partial z} = \frac{\partial^2}{\partial z^2}\left(\nu\frac{\partial v_{\mathrm{I}0}}{\partial z}\right), \tag{5.83}$$

or, after plugging in the leading-order solution (5.54),

$$f^2 \frac{\partial v_{\mathrm{I2}}}{\partial z} = \frac{\partial^2}{\partial z^2}\left(\nu \frac{\partial b}{\partial y}\right) \quad \text{and} \quad f^2 \frac{\partial u_{\mathrm{I2}}}{\partial z} = \frac{\partial^2}{\partial z^2}\left(\nu \frac{\partial b}{\partial x}\right). \tag{5.84}$$

The thermal wind shear therefore contributes a second-order correction to the flow, which can again be directly determined upon integration,

$$u_{\mathrm{I2}} = u_{\mathrm{I2}}|_{-H} + \frac{1}{f^2}\frac{\partial}{\partial z}\left(\nu \frac{\partial b}{\partial x}\right) - \frac{1}{f^2}\frac{\partial}{\partial z}\left(\nu \frac{\partial b}{\partial x}\right)\bigg|_{-H}, \tag{5.85}$$

$$v_{\mathrm{I2}} = v_{\mathrm{I2}}|_{-H} + \frac{1}{f^2}\frac{\partial}{\partial z}\left(\nu \frac{\partial b}{\partial y}\right) - \frac{1}{f^2}\frac{\partial}{\partial z}\left(\nu \frac{\partial b}{\partial y}\right)\bigg|_{-H}, \tag{5.86}$$

where again $u_{\mathrm{I2}}|_{-H}$ and $v_{\mathrm{I2}}|_{-H}$ are constants to be determined by the matching conditions. Integration over the column then yields a second-order contribution to the barotropic transport:

$$\int_{-H}^{0} u_{\mathrm{I2}}\,\mathrm{d}z = H u_{\mathrm{I2}}|_{-H} + \frac{\nu}{f^2}\frac{\partial b}{\partial x}\bigg|_{0} - \frac{\nu}{f^2}\frac{\partial b}{\partial x}\bigg|_{-H} - \frac{H}{f^2}\frac{\partial}{\partial z}\left(\nu \frac{\partial b}{\partial x}\right)\bigg|_{-H} \equiv U_{\mathrm{I2}}, \tag{5.87}$$

$$\int_{-H}^{0} v_{\mathrm{I2}}\,\mathrm{d}z = H v_{\mathrm{I2}}|_{-H} + \frac{\nu}{f^2}\frac{\partial b}{\partial y}\bigg|_{0} - \frac{\nu}{f^2}\frac{\partial b}{\partial y}\bigg|_{-H} - \frac{H}{f^2}\frac{\partial}{\partial z}\left(\nu \frac{\partial b}{\partial y}\right)\bigg|_{-H} \equiv V_{\mathrm{I2}}. \tag{5.88}$$

As at $O(\varepsilon)$, the $O(\varepsilon^2)$ bottom BL takes on the same form as (5.60) and (5.61), now with coefficients $u_{\mathrm{I2}}|_{-H}$ and $v_{\mathrm{I2}}|_{-H}$. This correction only modifies the transport by $O(\varepsilon^3)$. There is no surface BL correction at $O(\varepsilon^2)$ since the surface boundary condition (5.65) at this order is simply $\partial_{z_{\mathrm{S}}} \boldsymbol{u}_{\mathrm{S2}} = 0$. As before, the coefficients for the second-order flow at the top of the bottom BL can be determined by writing the second-order transport in terms of its interior and BL contributions, $\boldsymbol{U}_2 = \boldsymbol{U}_{\mathrm{I2}} + \boldsymbol{U}_{\mathrm{B2}} + \boldsymbol{U}_{\mathrm{S2}}$, which becomes

$$U_2 = H u_{\mathrm{I2}}|_{-H} - \frac{\nu}{f^2}\frac{\partial b}{\partial x}\bigg|_{-H} - \frac{H}{f^2}\frac{\partial}{\partial z}\left(\nu \frac{\partial b}{\partial x}\right)\bigg|_{-H} - \frac{u_{\mathrm{I1}} + v_{\mathrm{I1}}}{2q_{\mathrm{B}}}, \tag{5.89}$$

$$V_2 = H v_{\mathrm{I2}}|_{-H} - \frac{\nu}{f^2}\frac{\partial b}{\partial y}\bigg|_{-H} - \frac{H}{f^2}\frac{\partial}{\partial z}\left(\nu \frac{\partial b}{\partial y}\right)\bigg|_{-H} + \frac{u_{\mathrm{I1}} - v_{\mathrm{I1}}}{2q_{\mathrm{B}}}, \tag{5.90}$$

where u_{I1} and v_{I1} are determined above. Note that the surface terms in (5.87) and (5.88) cancel with those that appear from the surface BL correction $\boldsymbol{U}_{\mathrm{S2}}$.

5.9.4 Vertical flow

As described in the main text, the vertical flow can be determined from the horizontal flow by the frictional vorticity balance (5.24). In general, this will require knowledge of how the horizontal flow varies in x and y due to the ζ term. For the special local responses shown in Fig. 5.5, however, a consistent local solution up to $O(\varepsilon)$ can be determined. The $O(1)$ and $O(\varepsilon)$ balances in the interior for (5.24) are

$$\beta v_{\mathrm{I0}} = f \frac{\partial w_{\mathrm{I0}}}{\partial z} \quad \text{and} \quad \beta v_{\mathrm{I1}} = f \frac{\partial w_{\mathrm{I1}}}{\partial z}. \tag{5.91}$$

Using v_{I0} and v_{I1} from the previous sections, these can then be integrated from $z = 0$ to determine w_{I0} and w_{I1}. The constants of integration $w_{\mathrm{I0}}|_0$ and $w_{\mathrm{I1}}|_0$ are the zeroth- and first-order contributions to the Ekman pumping velocities, respectively. For the profiles in Fig. 5.5, these are zero. Due the ζ term in (5.24), a rigorous treatment of the bottom BL correction as above is not possible. Instead, we make the simplifying assumption that, in the bottom BL, the flow is aligned with the slope:

$$w_{\mathrm{B0}} = -H_x u_{\mathrm{B0}} - H_y v_{\mathrm{B0}} \quad \text{and} \quad w_{\mathrm{B1}} = -H_x u_{\mathrm{B1}} - H_y v_{\mathrm{B2}}. \tag{5.92}$$

In general, the matching conditions for w_0 and w_1 may not be satisfied with this assumption. For the simple cases of either along-slope symmetry or $U = V = 0$, however, the boundary condition is satisfied.

5.10 Appendix C: Models for the local response to mixing

The BL theory in appendix B is presented in terms of general expansions for the transports U and V and fully neglects the terms that arise when the aspect ratio is increased (appendix A). For the open-contour case, the local model simply sets $U = V = 0$, but the local model in the absence of along-slope variations instead assumes $U = 0$ and $\partial_z v|_{-H} = 0$. We here outline how one can solve for the expansions of V in the latter case and clarify how the BL theory can be modified to account for the added diffusion terms used in the numerical model. The models for the local response shown in Figs. 5.5 and 5.8 use these modifications.

5.10.1 Modification for $\alpha \neq 0$

Following appendix A, for $\partial_y b = 0$ and $H_y = 0$ (as is the case at $y = 0$ in the bowl), the frictional thermal wind equations (5.21) and (5.22) for an increased aspect ratio are approximately

$$-f\frac{\partial v}{\partial z} = -\frac{\partial b}{\partial x} + \Gamma^2\varepsilon^2\frac{\partial^2}{\partial z^2}\left(\nu\frac{\partial u}{\partial z}\right), \tag{5.93}$$

$$f\frac{\partial u}{\partial z} = \Gamma\varepsilon^2\frac{\partial^2}{\partial z^2}\left(\nu\frac{\partial v}{\partial z}\right), \tag{5.94}$$

where $\Gamma = 1+\alpha^2 H_x^2$. This modification does not account for curvature in H. The BL theory for these equations follows the same procedure as in appendix B, now with $\partial_y b = 0$ and the added Γ terms. The most notable modification is in the BL equations, which become

$$-f v_{\mathrm{B}} = \Gamma^2 \nu|_{-H}\frac{\partial^2 u_{\mathrm{B}}}{\partial z_{\mathrm{B}}^2}, \tag{5.95}$$

$$f u_{\mathrm{B}} = \Gamma \nu|_{-H}\frac{\partial^2 v_{\mathrm{B}}}{\partial z_{\mathrm{B}}^2}, \tag{5.96}$$

at the bottom and similarly for the surface. At $O(1)$, this leads to a modified bottom BL correction compared to (5.60) and (5.61) of the form

$$u_{B0} = -e^{-q_B z_B}\left(u_{I0}|_{-H}\cos q_B z_B + \Gamma^{-1/2} v_{I0}|_{-H}\sin q_B z_B\right), \tag{5.97}$$

$$v_{B0} = -e^{-q_B z_B}\left(v_{I0}|_{-H}\cos q_B z_B - \Gamma^{+1/2} u_{I0}|_{-H}\sin q_B z_B\right), \tag{5.98}$$

where now $q_B^{-1} = \Gamma^{3/4}\sqrt{2\nu|_{-H}/f}$. The BL solutions at other orders follow the same pattern. Thus, the added terms due to increasing the aspect ratio lead to a thicker BL by a factor of $\Gamma^{3/4}$ and a slightly asymmetrical Ekman spiral. The $O(1)$ and $O(\varepsilon)$ interior solutions are unchanged, but an extra factor of Γ does appear at $O(\varepsilon^2)$ compared to (**??**):

$$f^2\frac{\partial u_{I2}}{\partial z} = \Gamma\frac{\partial^2}{\partial z^2}\left(\nu\frac{\partial b}{\partial x}\right). \tag{5.99}$$

5.10.2 Assuming along-slope symmetry

We now turn specifically to the local model in the case of along-slope symmetry. From (5.54), the leading-order interior cross-slope flow u_{I0} must be a constant since $\partial_y b = 0$. The transport constraint $U = 0$ then implies that this constant is zero so that $U_0 = H u_{I0}|_{-H} = 0$. Setting the leading-order along-slope bottom stress from (5.76) to zero implies that

$$V_0 = -\frac{1}{f}\int_{-H}^{0} z\frac{\partial b}{\partial x}\,\mathrm{d}z, \tag{5.100}$$

as in (5.40) in the main text. From (5.56), this implies that $v_{I0}|_{-H} = 0$ as noted in PC23. Since the leading-order interior flow in both directions vanishes at the bottom, there is no leading-order BL correction: $\boldsymbol{u}_{B0} = 0$. Consequently, there is no $O(\varepsilon)$ contribution to the net transport from the cross-slope BL correction, and thus equations (5.79) and (5.80) imply that $u_{I1} = 0$ and $v_{I1} = V_1/H$. We can determine v_{I1} from setting the second-order along-slope bottom stress (5.82) to zero, which yields

$$V_1 = -\frac{H}{f q_B}\frac{\partial b}{\partial x}\bigg|_{-H}, \tag{5.101}$$

as in (5.40) in the main text. Note that q_B is modified for $\alpha \neq 0$ as described in the previous section. At the next order, we find that v_{I2} is a constant from equation (5.86) and $U_2 = 0$ implies that

$$u_{I2}|_{-H} = \frac{\Gamma}{f^2}\frac{\partial}{\partial z}\left(\nu\frac{\partial b}{\partial x}\right)\bigg|_{-H}, \tag{5.102}$$

from (5.89), modified for the $\alpha \neq 0$ case. This yields

$$u_{I2} = \frac{\Gamma}{f^2}\frac{\partial}{\partial z}\left(\nu\frac{\partial b}{\partial x}\right), \tag{5.103}$$

from (5.99). As usual, these lead to an $O(\varepsilon^2)$ BL correction that contributes an $O(\varepsilon^3)$ term to the net transport. Setting the along-slope bottom stress from this correction to zero yields

$$v_{I2} = -u_{I2}|_{-H} = -\frac{\Gamma}{f^2}\frac{\partial}{\partial z}\left(\nu\frac{\partial b}{\partial x}\right)\bigg|_{-H}, \tag{5.104}$$

so that

$$V_2 = -\frac{\Gamma H}{f^2}\frac{\partial}{\partial z}\left(\nu\frac{\partial b}{\partial x}\right)\bigg|_{-H} + \frac{1}{2fq_{\mathrm{B}}^2}\frac{\partial b}{\partial x}\bigg|_{-H}, \tag{5.105}$$

following (5.90).

Chapter 6

CONCLUSIONS AND FUTURE DIRECTIONS

6.1 Conclusions

A beautiful (and sometimes frustrating) quality of the ocean is that the spatial and temporal scales of its flows span multiple orders of magnitude, with the global-scale overturning depending on centimeter-scale diapycnal mixing to return dense waters to the surface (Munk, 1966). Observations of this turbulent mixing show that it is bottom-enhanced over rough topography (e.g., Polzin et al., 1997; Ledwell et al., 2000; Waterhouse et al., 2014), putting a recent spotlight on the dynamics of thin bottom BLs of upwelling (e.g., Ferrari et al., 2016; de Lavergne et al., 2017; McDougall and Ferrari, 2017; Holmes et al., 2018). The theory and numerical simulations presented in this thesis aim to understand the implications of this heterogeneous mixing for the circulation of the abyssal ocean. To that end, we focused mainly on PG dynamics driven by mixing modeled by an idealized turbulent diffusivity profile.

We began by examining the local dynamics over a uniform bottom slope, which we showed must include a transport constraint and barotropic pressure gradient to account for the large-scale context (Chapter 2). With these added physics, this local theory predicts a rapid spin up of strong along-slope flow. BL theory can then be employed to elucidate how the BL communicates with the interior in the absence of along-slope variations (Chapter 3). We found that the upslope BL transport, which itself depends on the interior evolution, generates a downward flux of buoyancy that acts as an effective bottom boundary condition on the interior. This two-way coupling between the BL and interior then provides an avenue for exchange as the transport varies across the slope.

Lifting the along-slope symmetry assumption made in Chapters 2 and 3 requires consideration of the coupling between local and basin-scale PG dynamics. To aid in the study of this interaction and work toward a more realistic description of the abyssal circulation, we developed the νPGCM, a finite element model of the three-dimensional PG equations (Chapter 4). Facilitated by simulations in an idealized bowl-shaped basin, we developed a theory for the PG inversion that describes how the local response to mixing connects to the barotropic circulation (Chapter 5). In this theory, which generalizes the transport constraint applied in Chapter 2, the local response is constrained by the barotropic circulation while simultaneously forcing it via a bottom stress curl. The barotropic flow must conserve vorticity, implying that the character of f/H contours, which are open throughout most of the real ocean, can shape the abyssal response to mixing. In the absence of wind forcing and JEBAR, the leading-order barotropic circulation must vanish for open f/H contours. This enhances the along-slope shear near the bottom, strengthening BL upwelling compared to the case with along-slope symmetry. This suggests that the upwelling in bottom BLs could be more efficient at restratifying the abyss than previously thought, potentially alleviating the need for eddy restratification (cf. Callies, 2018).

6.2 Future Directions

The theory for the dynamics of the abyssal ocean has come a long way since the flat bottom, uniform upwelling models pioneered by Stommel and Arons (1959a) and Munk (1966). While it has recently become clear that observed bottom-enhanced mixing limits abyssal upwelling to thin bottom BLs over slopes, it remains to be seen precisely how these dynamics modify our existing understanding of the overturning. With the theory and numerical model developed in this thesis, it should now be possible to directly probe this question.

In the real ocean, as discussed in Chapter 1, the abyssal overturning is largely diabatic while the mid-depth overturning is quasi-adiabatic, relying on buoyancy and wind forcing in the Southern Ocean to upwell. These qualitative pathways can be captured using a simple ocean geometry consisting of a single basin connected to a re-entrant channel, which has served as a testbed for understanding scalings for the abyssal overturning (e.g., Ito and Marshall, 2008; Nikurashin and Vallis, 2011; Mashayek et al., 2015; Jansen and Nadeau, 2016). Previously, however, this geometry has been represented as a "shoebox" with a flat bottom and vertical sidewalls, leading to unphysical water mass transformations. Using the the νPGCM (Chapter 4), this problem can be revisited in a more realistic setup with bottom-enhanced mixing and sloping bathymetry (e.g., Fig. 6.1). In this more realistic configuration, we expect most of the modifications to the abyssal stratification to occur in mixing layers near the bottom, with the interior stratification set by the balance between wind stress forcing and eddy restratification in the channel. This may invalidate previous theories based on the horizontal average diffusivity acting on the horizontal average stratification at a particular depth (e.g., Mashayek et al., 2015; Jansen and Nadeau, 2019). Based on the simple case with along-slope symmetry (Chapter 3), the cross-slope stratification at the top of the BL is likely to play an important role in setting the strength of BL upwelling and, hence, the overturning. We therefore envision a stronger abyssal overturning compared to previous theories, consistent with some global ocean model simulations with bottom-enhanced mixing (e.g., Saenko and Merryfield, 2005; Jayne, 2009; Melet et al., 2016).

The large timesteps afforded by employing the PG approximation allow the νPGCM to be used as a powerful tool to investigating the ocean's role in shaping past, present, and future climate. Simulations with a forcing equivalent to that of the Last Glacial Maximum could explain how the overturning may have shifted to store more carbon (Curry and Oppo, 2005; Sigman et al., 2010; Lund et al., 2011; Ferrari et al., 2014; Jansen, 2017). A modern-day forcing, on the other hand, could be used to uncover the mechanisms behind and implications of the observed abyssal heat uptake in recent decades (Purkey and Johnson, 2010; Desbruyères et al., 2016; Lele et al., 2021; Johnson and Purkey, 2024). Even the controversial human-

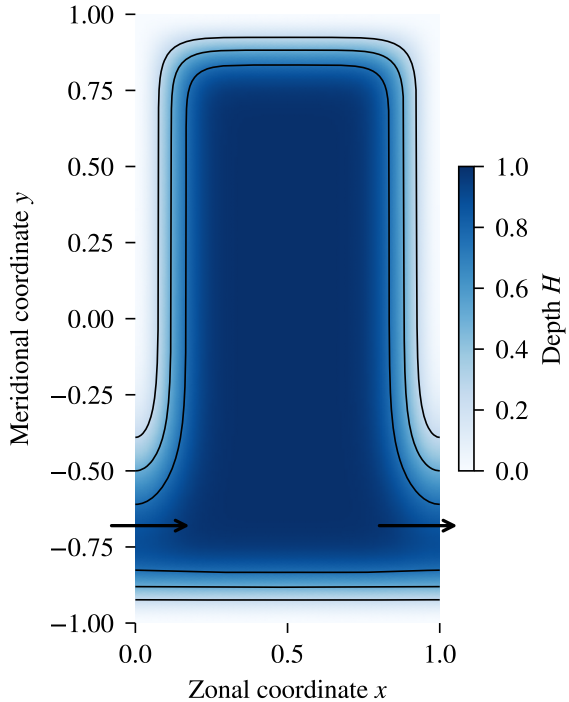

Figure 6.1: Sketch of potential channel–basin geometry with sloping topography, which could be used in the νPGCM in idealized studies of the overturning circulation. The nondimensional depth smoothly goes to zero along the coast except in the southern part of the domain, meant to represent the Southern Ocean, where it is re-entrant (arrows).

driven "AMOC slowdown" hypothesis (e.g., Gregory et al., 2005; Rahmstorf et al., 2015; Jackson et al., 2015; Weijer et al., 2020; Baker et al., 2023) could be studied within this framework. Even with decades of model development and computational scaling, the large spread in mean overturning strengths between the global ocean models commonly used to explore each of these climate states has not changed (e.g., Schmittner et al., 2005; Nayak et al., 2024). Based on the discussion above, this could be due to the prevailing failure of all global models to accurately represent BL upwelling. Given the strong control of the background stratification on the efficiency of ocean heat uptake (Newsom et al., 2023), properly representing this mean overturning is crucial for understanding the circulation response to various climate forcings. The νPGCM could therefore shed light on this problem and, in the long-term, be coupled to idealized ice, atmosphere, and land models with realistic bathymetry to understand the role of the overturning in the full Earth system (cf. Holden et al., 2016).

Alongside these numerical experiments, efforts to develop a complete theory for the abyssal ocean's response to bottom enhanced mixing will help build our intuition for these problems. An important next step would be to extend the BL theory in Chapter 5 to include the full buoyancy evolution, as was done for the simplified case of along-slope symmetry in Chapter 3. Such a theory would help make explicit the effects that bottom BLs of upwelling would have on the basin-scale circulation, allowing us to pinpoint how previous overturning theories will be altered once this physics is properly resolved. The simulations presented at the end of Chapter 4 provide a first look at the rich phenomenology of these full dynamics. While the interior evolution is far more complex with buoyancy advection, the quasi-equilibrium assumption for the BLs still holds. This bodes well for BL theory, with the BL again supplying an effective bottom boundary condition on the interior. The interplay of long Rossby waves in the interior with this BL transport will likely contribute to the story, though we still know little about what processes excite these waves, what determines the character of their propagation, and how they will modify abyssal upwelling. We hypothesize that the initial mixing-driven along-slope shear could provide the initial excitation. An eigenmode decomposition of the linearized PG equations for general bathymetry would be key in understanding how this perturbation projects onto the natural wave modes of the system and subsequently evolves. This could be accomplished within the same numerical framework as the νPGCM.

The theory and numerical model developed in this thesis aim to take key steps toward a complete understanding of the mixing-driven abyssal ocean circulation over sloping topography. They will hopefully pave the way for a fresh perspective on the overturning as they are applied to more realistic problems in the future.

References

Adcroft, A., C. Hill, and J. Marshall, 1997: Representation of topography by shaved cells in a height coordinate ocean model. *Monthly Weather Review*, **125 (9)**, 2293–2315, doi:10.1175/1520-0493(1997)125<2293:ROTBSC>2.0.CO;2.

Arakawa, A., and V. R. Lamb, 1981: A potential enstrophy and energy conserving scheme for the shallow water equations. *Monthly Weather Review*, **109 (1)**, 18–36, doi:10.1175/1520-0493(1981)109<0018:APEAEC>2.0.CO;2.

Badia, S., and F. Verdugo, 2020: Gridap: An extensible Finite Element toolbox in Julia. *Journal of Open Source Software*, **5 (52)**, 2520, doi:10.21105/joss.02520.

Baker, J. A., M. J. Bell, L. C. Jackson, R. Renshaw, G. K. Vallis, A. J. Watson, and R. A. Wood, 2023: Overturning pathways control AMOC weakening in CMIP6 models. *Geophysical Research Letters*, **50 (14)**, e2023GL103 381, doi:10.1029/2023GL103381.

Bender, C. M., and S. A. Orszag, 1999: *Advanced Mathematical Methods for Scientists and Engineers I*. Springer-Verlag, New York.

Benthuysen, J., and L. N. Thomas, 2012: Friction and diapycnal mixing at a slope: Boundary control of potential vorticity. *Journal of Physical Oceanography*, **42 (9)**, 1509–1523, doi:10.1175/JPO-D-11-0130.1.

Besard, T., C. Foket, and B. De Sutter, 2019: Effective extensible programming: Unleashing Julia on GPUs. *IEEE Transactions on Parallel and Distributed Systems*, **30 (4)**, 827–841, doi:10.1109/TPDS.2018.2872064.

Bezanson, J., A. Edelman, S. Karpinski, and V. B. Shah, 2017: Julia: A fresh approach to numerical computing. *SIAM Review*, **59 (1)**, 65–98, doi:10.1137/141000671.

Brink, K. H., and S. J. Lentz, 2010: Buoyancy arrest and bottom Ekman transport. Part I: Steady flow. *Journal of Physical Oceanography*, **40 (4)**, 621–635, doi:10.1175/2009JPO4266.1.

Callies, J., 2018: Restratification of abyssal mixing layers by submesoscale baroclinic eddies. *Journal of Physical Oceanography*, **48 (9)**, 1995–2010, doi:10.1175/JPO-D-18-0082.1.

Callies, J., and R. Ferrari, 2018: Dynamics of an abyssal circulation driven by bottom-intensified mixing on slopes. *Journal of Physical Oceanography*, **48 (6)**, 1257–1282, doi:10.1175/JPO-D-17-0125.1.

Carpenter, W. B., 1874: Lenz's doctrine of ocean circulation. *Nature*, **10 (244)**, 170–171, doi:10.1038/010170a0.

Caulfield, C., 2021: Layering, instabilities, and mixing in turbulent stratified flows. *Annual Review of Fluid Mechanics*, **53 (1)**, 113–145, doi:10.1146/annurev-fluid-042320-100458.

Chang, H., 2007: *Advanced Analytic Methods in Applied Mathematics, Science and Engineering*. LuBan Press, Boston.

Chapman, D. C., 2002: Deceleration of a finite-width, stratified current over a sloping bottom: Frictional spindown or buoyancy shutdown? *Journal of Physical Oceanography*, **32 (1)**, 336–352, doi:10.1175/1520-0485(2002)032<0336:DOAFWS>2.0.CO;2.

Colin de Verdière, A., 1986: On mean flow instabilities within the planetary geostrophic equations. *Journal of Physical Oceanography*, **16 (11)**, 1981–1984, doi:10.1175/1520-0485(1986)016<1981:OMFIWT>2.0.CO;2.

Colin de Verdière, A., 1988: Buoyancy driven planetary flows. *Journal of Marine Research*, **46 (2)**, 215–265, doi:10.1357/002224088785113667.

Curry, W. B., and D. W. Oppo, 2005: Glacial water mass geometry and the distribution of δ^{13}C of ΣCO_2 in the western Atlantic Ocean. *Paleoceanography*, **20 (1)**, PA1017, doi:10.1029/2004PA001021.

Danilov, S., G. Kivman, and J. Schröter, 2004: A finite-element ocean model: principles and evaluation. *Ocean Modelling*, **6 (2)**, 125–150, doi:10.1016/S1463-5003(02)00063-X.

de Lavergne, C., G. Madec, F. Roquet, R. M. Holmes, and T. J. McDougall, 2017: Abyssal ocean overturning shaped by seafloor distribution. *Nature*, **551 (7679)**, 181–186, doi:10.1038/nature24472.

de Lavergne, C., G. Madec, J. L. Sommer, A. J. G. Nurser, and A. C. N. Garabato, 2016: On the consumption of Antarctic Bottom Water in the abyssal ocean. *Journal of Physical Oceanography*, **46 (2)**, 635–661, doi:10.1175/JPO-D-14-0201.1.

Dell, R., and L. Pratt, 2015: Diffusive boundary layers over varying topography. *Journal of Fluid Mechanics*, **769**, 635–653, doi:10.1017/jfm.2015.88.

Desbruyères, D. G., S. G. Purkey, E. L. McDonagh, G. C. Johnson, and B. A. King, 2016: Deep and abyssal ocean warming from 35 years of repeat hydrography. *Geophysical Research Letters*, **43 (19)**, 10,356–10,365, doi:10.1002/2016GL070413.

Dewar, W. K., 1998: Topography and barotropic transport control by bottom friction. *Journal of Marine Research*, **56 (2)**, 295–328, doi:10.1357/002224098321822320.

Drake, H. F., R. Ferrari, and J. Callies, 2020: Abyssal circulation driven by near-boundary mixing: Water mass transformations and interior stratification. *Journal of Physical Oceanography*, **50 (8)**, 2203–2226, doi:10.1175/JPO-D-19-0313.1.

ECCO Consortium, I. Fukumori, O. Wang, I. Fenty, G. Forget, P. Heimbach, and R. M. Ponte, 2021: Synopsis of the ECCO central production global ocean and sea-ice state estimate, version 4 release 4. Tech. rep., Zenodo.

Edwards, N. R., A. J. Willmott, and P. D. Killworth, 1998: On the role of topography and wind stress on the stability of the thermohaline circulation. *Journal of Physical Oceanography*, **28 (5)**, 756–778, doi:10.1175/1520-0485(1998)028<0756:OTROTA>2.0.CO;2.

Ekman, V. W., 1905: On the influence of the Earth's rotation on ocean currents. *Arkiv för Matematik, Astronomi och Fysik.*, **2 (11)**, 1–53.

Elman, H. C., D. J. Silvester, and A. J. Wathen, 2014: *Finite elements and fast iterative solvers: with applications in incompressible fluid dynamics*. 2nd ed., Numerical mathematics and scientific computation, Oxford university press, Oxford.

Emile-Geay, J., and G. Madec, 2009: Geothermal heating, diapycnal mixing and the abyssal circulation. *Ocean Science*, **5 (2)**, 203–217, doi:10.5194/os-5-203-2009.

Ferrari, R., 2014: What goes down must come up. *Nature*, **513 (7517)**, 179–180, doi:10.1038/513179a.

Ferrari, R., M. F. Jansen, J. F. Adkins, A. Burke, A. L. Stewart, and A. F. Thompson, 2014: Antarctic sea ice control on ocean circulation in present and glacial climates. *Proceedings of the National Academy of Sciences*, **111 (24)**, 8753–8758, doi:10.1073/pnas.1323922111.

Ferrari, R., A. Mashayek, T. J. McDougall, M. Nikurashin, and J.-M. Campin, 2016: Turning ocean mixing upside down. *Journal of Physical Oceanography*, **46 (7)**, 2239–2261, doi:10.1175/JPO-D-15-0244.1.

Fox-Kemper, B., and Coauthors, 2019: Challenges and prospects in ocean circulation models. *Frontiers in Marine Science*, **6**, 65, doi:10.3389/fmars.2019.00065.

Fox-Kemper, B., and Coauthors, 2021: Ocean, Cryosphere and Sea Level Change. *Climate Change 2021: The Physical Science Basis. Contribution of Working Group I to the Sixth Assessment Report of the Intergovernmental Panel on Climate Change*, V. Masson-Delmotte, P. Zhai, A. Pirani, S. Connors, C. Péan, S. Berger, N. Caud, Y. Chen, L. Goldfarb, M. Gomis, M. Huang, K. Leitzell, E. Lonnoy, J. Matthews, T. Maycock, T. Waterfield, O. Yelekçi, R. Yu, and B. Zhou, Eds., Cambridge University Press, Cambridge, United Kingdom and New York, NY, USA, 1211–1362.

Garner, S. T., D. M. W. Frierson, I. M. Held, O. Pauluis, and G. K. Vallis, 2007: Resolving convection in a global hypohydrostatic model. *Journal of the Atmospheric Sciences*, **64 (6)**, 2061–2075, doi:10.1175/JAS3929.1.

Garrett, C., 1982: On spindown in the ocean interior. *Journal of Physical Oceanography*, **12**, 989–993, doi:10.1175/1520-0485(1982)012<0989:OSITOI>2.0.CO;2.

Garrett, C., 1990: The role of secondary circulation in boundary mixing. *Journal of Geophysical Research: Oceans*, **95 (C3)**, 3181–3188, doi:10.1029/JC095iC03p03181.

Garrett, C., 1991: Marginal mixing theories. *Atmosphere-Ocean*, **29 (2)**, 313–339, doi:10.1080/07055900.1991.9649407.

Garrett, C., 2001: An isopycnal view of near-boundary mixing and associated flows. *Journal of Physical Oceanography*, **31 (1)**, 138–142, doi:10.1175/1520-0485(2001)031<0138:AIVONB>2.0.CO;2.

Garrett, C., and E. Kunze, 2007: Internal tide generation in the deep ocean. *Annual Review of Fluid Mechanics*, **39 (1)**, 57–87, doi:10.1146/annurev.fluid.39.050905.110227.

Garrett, C., P. MacCready, and P. Rhines, 1993: Boundary mixing and arrested Ekman layers: Rotating stratified flow near a sloping boundary. *Annual Review of Fluid Mechanics*, **25**, 291–323, doi:10.1146/annurev.fl.25.010193.001451.

Garrett, C. J. R., and J. W. Loder, 1981: Dynamical aspects of shallow sea fronts. *Philosophical Transactions of the Royal Society of London. Series A, Mathematical and Physical Sciences*, **302 (1472)**, 563–581, doi:10.1098/rsta.1981.0183.

Gent, P. R., and J. C. Mcwilliams, 1990: Isopycnal mixing in ocean circulation models. *Journal of Physical Oceanography*, **20 (1)**, 150–155, doi:10.1175/1520-0485(1990)020<0150:IMIOCM>2.0.CO;2.

Geuzaine, C., and J.-F. Remacle, 2009: Gmsh: A 3-D finite element mesh generator with built-in pre- and post-processing facilities. *International Journal for Numerical Methods in Engineering*, **79 (11)**, 1309–1331, doi:10.1002/nme.2579.

Gill, A. E., 1981: Homogeneous intrusions in a rotating stratified fluid. *Journal of Fluid Mechanics*, **103**, 275–295, doi:10.1017/S0022112081001341.

Greatbatch, R. J., and K. G. Lamb, 1990: On parameterizing vertical mixing of momentum in non-eddy resolving ocean models. *Journal of Physical Oceanography*, **20 (10)**, 1634–1637, doi:10.1175/1520-0485(1990)020<1634:OPVMOM>2.0.CO;2.

Gregg, M. C., 1989: Scaling turbulent dissipation in the thermocline. *Journal of Geophysical Research: Oceans*, **94 (C7)**, 9686–9698, doi:10.1029/JC094iC07p09686.

Gregory, J. M., and Coauthors, 2005: A model intercomparison of changes in the Atlantic thermohaline circulation in response to increasing atmospheric CO2 concentration. *Geophysical Research Letters*, **32 (12)**, doi:10.1029/2005GL023209.

Griffies, S., and Coauthors, 2009: Problems and prospects in large-scale ocean circulation models. *Proceedings of OceanObs'09*, J. Hall, D. Harrison, and D. Stammer, Eds., ESA Publication WPP-306, Venice, WPP-306, Vol. 2, doi:10.5270/OceanObs09.cwp.38.

Guillén-González, F., and J. R. Rodríguez-Galván, 2015: Analysis of the hydrostatic Stokes problem and finite-element approximation in unstructured meshes. *Numerische Mathematik*, **130 (2)**, 225–256, doi:10.1007/s00211-014-0663-8.

Hallberg, R., and P. Rhines, 1996: Buoyancy-driven circulation in an ocean basin with isopycnals intersecting the sloping boundary. *Journal of Physical Oceanography*, **26 (6)**, 913–940, doi:10.1175/1520-0485(1996)026<0913:BDCIAO>2.0.CO;2.

Haney, R. L., 1991: On the pressure gradient force over steep topography in sigma coordinate ocean models. *Journal of Physical Oceanography*, **21 (4)**, 610–619, doi:10.1175/1520-0485(1991)021<0610:OTPGFO>2.0.CO;2.

He, J., M. Winton, G. Vecchi, L. Jia, and M. Rugenstein, 2017: Transient climate sensitivity depends on base climate ocean circulation. *Journal of Climate*, **30 (4)**, 1493–1504, doi:10.1175/JCLI-D-16-0581.1.

Holden, P. B., N. R. Edwards, K. Fraedrich, E. Kirk, F. Lunkeit, and X. Zhu, 2016: PLASIM–GENIE v1.0: a new intermediate complexity AOGCM. *Geoscientific Model Development*, **9 (9)**, 3347–3361, doi:10.5194/gmd-9-3347-2016.

Holmes, R. M., C. de Lavergne, and T. J. McDougall, 2019: Tracer transport within abyssal mixing layers. *Journal of Physical Oceanography*, **49 (10)**, 2669–2695, doi:10.1175/JPO-D-19-0006.1.

Holmes, R. M., C. d. Lavergne, and T. J. McDougall, 2018: Ridges, seamounts, troughs, and bowls: Topographic control of the dianeutral circulation in the abyssal ocean. *Journal of Physical Oceanography*, **48 (4)**, 861–882, doi:10.1175/JPO-D-17-0141.1.

Holton, J. R., 1965: The influence of viscous boundary layers on transient motions in a stratified rotating fluid: Part I. *Journal of the Atmospheric Sciences*, **22 (4)**, 402–411, doi:10.1175/1520-0469(1965)022<0402:TIOVBL>2.0.CO;2.

Hughes, T. J. R., 1987: *The finite element method: linear static and dynamic finite element analysis*. Dover Publications, Mineola, NY.

Ito, T., and J. Marshall, 2008: Control of lower-limb overturning circulation in the Southern Ocean by diapycnal mixing and mesoscale eddy transfer. *Journal of Physical Oceanography*, **38 (12)**, 2832–2845, doi:10.1175/2008JPO3878.1.

Jackson, L. C., R. Kahana, T. Graham, M. A. Ringer, T. Woollings, J. V. Mecking, and R. A. Wood, 2015: Global and European climate impacts of a slowdown of the AMOC in a high resolution GCM. *Climate Dynamics*, **45 (11)**, 3299–3316, doi:10.1007/s00382-015-2540-2.

Jansen, M. F., 2017: Glacial ocean circulation and stratification explained by reduced atmospheric temperature. *Proceedings of the National Academy of Sciences*, **114 (1)**, 45–50, doi:10.1073/pnas.1610438113.

Jansen, M. F., A. Adcroft, S. M. Griffies, and I. Grooms, 2024: The averaged hydrostatic Boussinesq ocean equations in generalized vertical coordinates. *Journal of Advances in Modeling Earth Systems*, **16 (12)**, e2024MS004 506, doi:10.1029/2024MS004506.

Jansen, M. F., and L.-P. Nadeau, 2016: The effect of Southern Ocean surface buoyancy loss on the deep-ocean circulation and stratification. *Journal of Physical Oceanography*, **46 (11)**, 3455–3470, doi:10.1175/JPO-D-16-0084.1.

Jansen, M. F., and L.-P. Nadeau, 2019: A toy model for the response of the residual overturning circulation to surface warming. *Journal of Physical Oceanography*, **49 (5)**, 1249–1268, doi:10.1175/JPO-D-18-0187.1.

Jansen, M. F., L.-P. Nadeau, and T. M. Merlis, 2018: Transient versus equilibrium response of the ocean's overturning circulation to warming. *Journal of Climate*, **31 (13)**, 5147–5163, doi:10.1175/JCLI-D-17-0797.1.

Jayne, S. R., 2009: The impact of abyssal mixing parameterizations in an ocean general circulation model. *Journal of Physical Oceanography*, **39 (7)**, 1756–1775, doi:10.1175/2009JPO4085.1.

Jeffreys, H., 1925: On fluid motions produced by differences of temperature and humidity. *Quarterly Journal of the Royal Meteorological Society*, **51 (216)**, 347–356, doi:10.1002/qj.49705121604.

Johnson, G. C., and S. G. Purkey, 2024: Refined estimates of global ocean deep and abyssal decadal warming trends. *Geophysical Research Letters*, **51 (18)**, e2024GL111 229, doi:10.1029/2024GL111229.

Kageyama, M., J. Mignot, D. Swingedouw, C. Marzin, R. Alkama, and O. Marti, 2009: Glacial climate sensitivity to different states of the Atlantic Meridional Overturning Circulation: results from the IPSL model. *Clim. Past*, **5**, 551–570.

Kawase, M., 1993: Effects of a concave bottom geometry on the upwelling-driven circulation in an abyssal ocean basin. *Journal of Physical Oceanography*, **23 (2)**, 400–405, doi:10.1175/1520-0485(1993)023<0400:EOACBG>2.0.CO;2.

Kuang, Z., P. N. Blossey, and C. S. Bretherton, 2005: A new approach for 3D cloud-resolving simulations of large-scale atmospheric circulation. *Geophysical Research Letters*, **32 (2)**, doi:10.1029/2004GL021024.

Kunze, E., C. MacKay, E. E. McPhee-Shaw, K. Morrice, J. B. Girton, and S. R. Terker, 2012: Turbulent mixing and exchange with interior waters on sloping boundaries. *Journal of Physical Oceanography*, **42 (6)**, 910–927, doi:10.1175/JPO-D-11-075.1.

Large, W. G., J. C. McWilliams, and S. C. Doney, 1994: Oceanic vertical mixing: A review and a model with a nonlocal boundary layer parameterization. *Reviews of Geophysics*, **32 (4)**, 363–403, doi:10.1029/94RG01872.

Ledwell, J. R., 2018: Comment on “Abyssal upwelling and downwelling driven by near-boundary mixing”. *Journal of Physical Oceanography*, **48 (3)**, 739–748, doi:10.1175/JPO-D-17-0089.1.

Ledwell, J. R., L. C. S. Laurent, J. B. Girton, and J. M. Toole, 2011: Diapycnal mixing in the Antarctic Circumpolar Current. *Journal of Physical Oceanography*, **41 (1)**, 241–246, doi:10.1175/2010JPO4557.1.

Ledwell, J. R., E. T. Montgomery, K. L. Polzin, L. C. S. Laurent, R. W. Schmitt, and J. M. Toole, 2000: Evidence for enhanced mixing over rough topography in the abyssal ocean. *Nature*, **403 (6766)**, 179–182, doi:10.1038/35003164.

Ledwell, J. R., A. J. Watson, and C. S. Law, 1993: Evidence for slow mixing across the pycnocline from an open-ocean tracer-release experiment. *Nature*, **364 (6439)**, 701–703, doi:10.1038/364701a0.

Lele, R., and Coauthors, 2021: Abyssal Heat Budget in the Southwest Pacific Basin. *Journal of Physical Oceanography*, **51 (11)**, 3317–3333, doi:10.1175/JPO-D-21-0045.1.

Liu, Z., and Coauthors, 2009: Transient simulation of last deglaciation with a new mechanism for Bølling-Allerød warming. *Science*, **325 (5938)**, 310–314, doi:10.1126/science.1171041.

Lumpkin, R., and K. Speer, 2007: Global ocean meridional overturning. *Journal of Physical Oceanography*, **37 (10)**, 2550–2562, doi:10.1175/JPO3130.1.

Lund, D. C., J. F. Adkins, and R. Ferrari, 2011: Abyssal Atlantic circulation during the Last Glacial Maximum: Constraining the ratio between transport and vertical mixing. *Paleoceanography*, **26 (1)**, doi:10.1029/2010PA001938.

Luyten, J. R., J. Pedlosky, and H. Stommel, 1983: The ventilated thermocline. *Journal of Physical Oceanography*, **13 (2)**, 292–309, doi:10.1175/1520-0485(1983)013<0292:TVT>2.0.CO;2.

MacCready, P., and P. B. Rhines, 1991: Buoyant inhibition of Ekman transport on a slope and its effect on stratified spin-up. *Journal of Fluid Mechanics*, **223 (-1)**, 631, doi:10.1017/S0022112091001581.

MacCready, P., and P. B. Rhines, 1993: Slippery bottom boundary layers on a slope. *Journal of Physical Oceanography*, **23 (1)**, 5–22, doi:10.1175/1520-0485(1993)023<0005:SBBLOA>2.0.CO;2.

Marshall, J., and K. Speer, 2012: Closure of the meridional overturning circulation through Southern Ocean upwelling. *Nature Geoscience*, **5 (3)**, 171–180, doi:10.1038/ngeo1391.

Marshall, J. C., and A. J. G. Nurser, 1992: Fluid dynamics of oceanic thermocline ventilation. *Journal of Physical Oceanography*, **22 (6)**, 583–595, doi:10.1175/1520-0485(1992)022<0583:FDOOTV>2.0.CO;2.

Mashayek, A., R. Ferrari, M. Nikurashin, and W. R. Peltier, 2015: Influence of enhanced abyssal diapycnal mixing on stratification and the ocean overturning circulation. *Journal of Physical Oceanography*, **45 (10)**, 2580–2597, doi:10.1175/JPO-D-15-0039.1.

McDougall, T. J., 1989: Dianeutral advection. *Proc. Fifth 'Aha Huliko'a Hawaiian Winter Workshop on Parameterization of Small-Scale Processes*, Hawaii Institute of Geophysics, Honolulu, 289–315.

McDougall, T. J., and R. Ferrari, 2017: Abyssal upwelling and downwelling driven by near-boundary mixing. *Journal of Physical Oceanography*, **47 (2)**, 261–283, doi:10.1175/JPO-D-16-0082.1.

Melet, A., S. Legg, and R. Hallberg, 2016: Climatic impacts of parameterized local and remote tidal mixing. *Journal of Climate*, **29 (10)**, 3473–3500, doi:10.1175/JCLI-D-15-0153.1.

Mertz, G., and D. G. Wright, 1992: Interpretations of the JEBAR term. *Journal of Physical Oceanography*, **22 (3)**, 301–305, doi:10.1175/1520-0485(1992)022<0301:IOTJT>2.0.CO;2.

Montoison, A., and D. Orban, 2023: Krylov.jl: A Julia basket of hand-picked Krylov methods. *Journal of Open Source Software*, **8 (89)**, 5187, doi:10.21105/joss.05187, URL https://joss.theoj.org/papers/10.21105/joss.05187.

Munk, W., and C. Wunsch, 1998: Abyssal recipes II: Energetics of tidal and wind mixing. *Deep Sea Research Part I: Oceanographic Research Papers*, **45 (12)**, 1977–2010, doi:10.1016/S0967-0637(98)00070-3.

Munk, W. H., 1950: On the wind-driven ocean circulation. *Journal of the Atmospheric Sciences*, **7 (2)**, 80–93, doi:10.1175/1520-0469(1950)007<0080:OTWDOC>2.0.CO;2.

Munk, W. H., 1966: Abyssal recipes. *Deep Sea Research and Oceanographic Abstracts*, **13 (4)**, 707–730, doi:10.1016/0011-7471(66)90602-4.

Nayak, M. S., D. B. Bonan, E. R. Newsom, and A. F. Thompson, 2024: Controls on the strength and structure of the Atlantic meridional overturning circulation in climate models. *Geophysical Research Letters*, **51 (11)**, e2024GL109 055, doi:10.1029/2024GL109055.

Newsom, E., L. Zanna, and J. Gregory, 2023: Background pycnocline depth constrains future ocean heat uptake efficiency. *Geophysical Research Letters*, **50 (22)**, e2023GL105 673, doi:10.1029/2023GL105673.

Nikurashin, M., and R. Ferrari, 2011: Global energy conversion rate from geostrophic flows into internal lee waves in the deep ocean. *Geophysical Research Letters*, **38 (8)**, L08 610, doi:10.1029/2011GL046576.

Nikurashin, M., and S. Legg, 2011: A mechanism for local dissipation of internal tides generated at rough topography. *Journal of Physical Oceanography*, **41 (2)**, 378–395, doi:10.1175/2010JPO4522.1.

Nikurashin, M., and G. Vallis, 2011: A theory of deep stratification and overturning circulation in the ocean. *Journal of Physical Oceanography*, **41 (3)**, 485–502, doi:10.1175/2010JPO4529.1.

Osborn, T. R., and C. S. Cox, 1972: Oceanic fine structure. *Geophysical Fluid Dynamics*, **3 (4)**, 321–345, doi:10.1080/03091927208236085.

Pedlosky, J., 1979: *Geophysical Fluid Dynamics*. Springer-Verlag, New York.

Pedlosky, J., 1998: *Ocean Circulation Theory*. Springer Berlin Heidelberg, Berlin, Heidelberg, doi:10.1007/978-3-662-03204-6.

Pedlosky, J., L. J. Pratt, M. A. Spall, and K. R. Helfrich, 1997: Circulation around islands and ridges. *Journal of Marine Research*, **55 (6)**, 1199–1251, doi:10.1357/0022240973224085.

Peterson, H. G., and J. Callies, 2022: Rapid spinup and spindown of flow along slopes. *Journal of Physical Oceanography*, **52 (4)**, 579–596, doi:10.1175/JPO-D-21-0173.1.

Peterson, H. G., and J. Callies, 2023: Coupling between abyssal boundary layers and the interior ocean in the absence of along-slope variations. *Journal of Physical Oceanography*, **53 (1)**, 307–322, doi:10.1175/JPO-D-22-0082.1.

Phillips, O. M., 1970: On flows induced by diffusion in a stably stratified fluid. *Deep Sea Research and Oceanographic Abstracts*, **17 (3)**, 435–443, doi:10.1016/0011-7471(70)90058-6.

Phillips, O. M., J.-H. Shyu, and H. Salmun, 1986: An experiment on boundary mixing: Mean circulation and transport rates. *Journal of Fluid Mechanics*, **173**, 473–499, doi:10.1017/S0022112086001234.

Polzin, K. L., J. M. Toole, J. R. Ledwell, and R. W. Schmitt, 1997: Spatial variability of turbulent mixing in the abyssal ocean. *Science*, **276 (5309)**, 93–96, doi:10.1126/science.276.5309.93.

Purkey, S. G., and G. C. Johnson, 2010: Warming of global abyssal and deep Southern Ocean waters between the 1990s and 2000s: Contributions to global heat and sea level rise budgets. *Journal of Climate*, **23 (23)**, 6336–6351, doi:10.1175/2010JCLI3682.1.

Rahmstorf, S., J. E. Box, G. Feulner, M. E. Mann, A. Robinson, S. Rutherford, and E. J. Schaffernicht, 2015: Exceptional twentieth-century slowdown in Atlantic Ocean overturning circulation. *Nature Climate Change*, **5 (5)**, 475–480, doi:10.1038/nclimate2554.

Rattray, M., 1982: A simple exact treatment of the baroclinicity-bathymetry interaction in a frictional, iterative, diagnostic ocean model. *Journal of Physical Oceanography*, **12 (10)**, 997–1003, doi:10.1175/1520-0485(1982)012<0997:ASETOT>2.0.CO;2.

Redi, M. H., 1982: Oceanic isopycnal mixing by coordinate rotation. *Journal of Physical Oceanography*, **12 (10)**, 1154–1158, doi:10.1175/1520-0485(1982)012<1154:OIMBCR>2.0.CO;2.

Rhines, P. B., and P. MacCready, 1989: Boundary control over the large-scale circulation. *Proc. Fifth 'Aha Huliko'a Hawaiian Winter Workshop on Parameterization of Small-Scale Processes*, Hawaii Institute of Geophysics, Honolulu, 75–97.

Rhines, P. B., and W. R. Young, 1982: Homogenization of potential vorticity in planetary gyres. *Journal of Fluid Mechanics*, **122**, 347–367, doi:10.1017/S0022112082002250.

Robinson, A., and H. Stommel, 1959: The oceanic thermocline and the associated thermohaline circulation. *Tellus*, **11 (3)**, 295–308, doi:10.1111/j.2153-3490.1959.tb00035.x.

Robinson, A. R., 1970: Boundary layers in ocean circulation models. *Annual Review of Fluid Mechanics*, **2 (1)**, 293–312, doi:10.1146/annurev.fl.02.010170.001453.

Rousselet, L., P. Cessi, and G. Forget, 2021: Coupling of the mid-depth and abyssal components of the global overturning circulation according to a state estimate. *Science Advances*, **7 (21)**, eabf5478, doi:10.1126/sciadv.abf5478.

Ruan, X., and J. Callies, 2020: Mixing-driven mean flows and submesoscale eddies over mid-ocean ridge flanks and fracture zone canyons. *Journal of Physical Oceanography*, **50 (1)**, 175–195, doi:10.1175/JPO-D-19-0174.1.

Ruan, X., A. F. Thompson, and J. R. Taylor, 2019: The evolution and arrest of a turbulent stratified oceanic bottom boundary layer over a slope: Downslope regime. *Journal of Physical Oceanography*, **49 (2)**, 469–487, doi:10.1175/JPO-D-18-0079.1.

Ruan, X., A. F. Thompson, and J. R. Taylor, 2021: The evolution and arrest of a turbulent stratified oceanic bottom boundary layer over a slope: Upslope regime and PV dynamics. *Journal of Physical Oceanography*, **51 (4)**, 1077–1089, doi:10.1175/JPO-D-20-0168.1.

Rugenstein, M., and Coauthors, 2019: LongRunMIP: Motivation and design for a large collection of millennial-length AOGCM simulations. *Bulletin of the American Meteorological Society*, **100 (12)**, 2551–2570, doi:10.1175/BAMS-D-19-0068.1.

Saenko, O. A., and W. J. Merryfield, 2005: On the effect of topographically enhanced mixing on the global ocean circulation. *Journal of Physical Oceanography*, **35 (5)**, 826–834, doi:10.1175/JPO2722.1.

Salmon, R., 1986: A simplified linear ocean circulation theory. *Journal of Marine Research*, **44 (4)**, 695–711, doi:10.1357/002224086788401602.

Salmon, R., 1998: *Lectures on geophysical fluid dynamics*. Oxford University Press, New York.

Salmon, R., 2009: An ocean circulation model based on operator-splitting, Hamiltonian brackets, and the inclusion of sound waves. *Journal of Physical Oceanography*, **39 (7)**, 1615–1633, doi:10.1175/2009JPO4134.1.

Salmun, H., P. D. Killworth, and J. R. Blundell, 1991: A two-dimensional model of boundary mixing. *Journal of Geophysical Research: Oceans*, **96 (C10)**, 18 447–18 474, doi:10.1029/91JC01917.

Samelson, R. M., and G. K. Vallis, 1997a: Large-scale circulation with small diapycnal diffusion: The two-thermocline limit. *Journal of Marine Research*, **55 (2)**, 223–275, doi:10.1357/0022240973224382.

Samelson, R. M., and G. K. Vallis, 1997b: A simple friction and diffusion scheme for planetary geostrophic basin models. *Journal of Physical Oceanography*, **27 (1)**, 186–194, doi:10.1175/1520-0485(1997)027<0186:ASFADS>2.0.CO;2.

Sandström, J., 1908: Dynamicsche Versuche mit Meerwasser. *Ann. Hydrogr. Martimen Meteorol.*, **36**, 6–23.

Sarmiento, J. L., and N. Gruber, 2006: *Ocean Biogeochemical Dynamics*. Princeton University Press.

Sarmiento, J. L., and J. R. Toggweiler, 1984: A new model for the role of the oceans in determining atmospheric pCO_2. *Nature*, **308 (5960)**, 621–624, doi:10.1038/308621a0.

Schmittner, A., M. Latif, and B. Schneider, 2005: Model projections of the North Atlantic thermohaline circulation for the 21st century assessed by observations. *Geophysical Research Letters*, **32 (23)**, doi:10.1029/2005GL024368.

Sigman, D. M., M. P. Hain, and G. H. Haug, 2010: The polar ocean and glacial cycles in atmospheric CO2 concentration. *Nature*, **466 (7302)**, 47–55, doi:10.1038/nature09149.

Sloyan, B. M., and S. R. Rintoul, 2001: The Southern Ocean limb of the global deep overturning circulation. *Journal of Physical Oceanography*, **31 (1)**, 143–173, doi:10.1175/1520-0485(2001)031<0143:TSOLOT>2.0.CO;2.

Smith, W. H. F., and D. T. Sandwell, 1997: Global sea floor topography from satellite altimetry and ship depth soundings. *Science*, **277 (5334)**, 1956–1962, doi:10.1126/science.277.5334.1956.

Stommel, H., 1948: The westward intensification of wind-driven ocean currents. *Eos, Transactions American Geophysical Union*, **29 (2)**, 202–206, doi:10.1029/TR029i002p00202.

Stommel, H., and A. B. Arons, 1959a: On the abyssal circulation of the world ocean—I. Stationary planetary flow patterns on a sphere. *Deep Sea Research (1953)*, **6**, 140–154, doi:10.1016/0146-6313(59)90065-6.

Stommel, H., and A. B. Arons, 1959b: On the abyssal circulation of the world ocean—II. An idealized model of the circulation pattern and amplitude in oceanic basins. *Deep Sea Research (1953)*, **6**, 217–233, doi:10.1016/0146-6313(59)90075-9.

Strang, G., 1968: On the construction and comparison of difference schemes. *SIAM Journal on Numerical Analysis*, **5 (3)**, 506–517, doi:10.1137/0705041.

Talley, L., 2013: Closure of the global overturning circulation through the Indian, Pacific, and Southern Oceans: Schematics and transports. *Oceanography*, **26 (1)**, 80–97, doi:10.5670/oceanog.2013.07.

Thomas, L. N., and C. M. Lee, 2005: Intensification of ocean fronts by down-front winds. *Journal of Physical Oceanography*, **35 (6)**, 1086–1102, doi:10.1175/JPO2737.1.

Thompson, L., 1995: The effect of continental rises on the wind-driven ocean circulation. *Journal of Physical Oceanography*, **25 (6)**, 1296–1316, doi:10.1175/1520-0485(1995)025<1296:TEOCRO>2.0.CO;2.

Thompson, L., and G. C. Johnson, 1996: Abyssal currents generated by diffusion and geothermal heating over rises. *Deep Sea Research Part I: Oceanographic Research Papers*, **43 (2)**, 193–211, doi:10.1016/0967-0637(96)00095-7.

Thorpe, S. A., 1987: Current and temperature variability on the continental slope. *Philosophical Transactions of the Royal Society A: Mathematical, Physical and Engineering Sciences*, **323 (1574)**, 471–517, doi:10.1098/rsta.1987.0100.

Trowbridge, J. H., and S. J. Lentz, 1991: Asymmetric behavior of an oceanic boundary layer above a sloping bottom. *Journal of Physical Oceanography*, **21 (8)**, 1171–1185, doi:10.1175/1520-0485(1991)021<1171:ABOAOB>2.0.CO;2.

Vallis, G. K., 2017: *Atmospheric and Oceanic Fluid Dynamics: Fundamentals and Large-Scale Circulation*. 2nd ed., Cambridge University Press.

Veronis, G., 1966: Wind-driven ocean circulation—Part 1. Linear theory and perturbation analysis. *Deep Sea Research and Oceanographic Abstracts*, **13 (1)**, 17–29, doi:10.1016/0011-7471(66)90003-9.

Warren, B. A., and C. Wunsch, Eds., 1981: *Evolution of physical oceanography: Scientific surveys in honor of Henry Stommel*. MIT Press, Cambridge, Mass.

Waterhouse, A. F., and Coauthors, 2014: Global patterns of diapycnal mixing from measurements of the turbulent dissipation rate. *Journal of Physical Oceanography*, **44 (7)**, 1854–1872, doi:10.1175/JPO-D-13-0104.1.

Weijer, W., W. Cheng, O. A. Garuba, A. Hu, and B. T. Nadiga, 2020: CMIP6 models predict significant 21st century decline of the Atlantic meridional overturning circulation. *Geophysical Research Letters*, **47 (12)**, e2019GL086 075, doi:10.1029/2019GL086075.

Welander, P., 1959: An advective model of the ocean thermocline. *Tellus*, **11 (3)**, 309–318, doi:10.1111/j.2153-3490.1959.tb00036.x.

Welander, P., 1968: Wind-driven circulation in one- and two-layer oceans of variable depth. *Tellus*, **20 (1)**, 1–16, doi:10.1111/j.2153-3490.1968.tb00347.x.

Wenegrat, J. O., J. Callies, and L. N. Thomas, 2018: Submesoscale baroclinic instability in the bottom boundary layer. *Journal of Physical Oceanography*, **48 (11)**, 2571–2592, doi:10.1175/JPO-D-17-0264.1.

Wenegrat, J. O., and L. N. Thomas, 2020: Centrifugal and symmetric instability during Ekman adjustment of the bottom boundary layer. *Journal of Physical Oceanography*, **50 (6)**, 1793–1812, doi:10.1175/JPO-D-20-0027.1.

Whalen, C. B., C. de Lavergne, A. C. Naveira Garabato, J. M. Klymak, J. A. MacKinnon, and K. L. Sheen, 2020: Internal wave-driven mixing: Governing processes and consequences for climate. *Nature Reviews Earth & Environment*, **1 (11)**, 606–621, doi:10.1038/s43017-020-0097-z.

Winton, M., W. G. Anderson, T. L. Delworth, S. M. Griffies, W. J. Hurlin, and A. Rosati, 2014: Has coarse ocean resolution biased simulations of transient climate sensitivity? *Geophysical Research Letters*, **41 (23)**, 8522–8529, doi:10.1002/2014GL061523.

Wolfe, C. L., and P. Cessi, 2011: The adiabatic pole-to-pole overturning circulation. *Journal of Physical Oceanography*, **41 (9)**, 1795–1810, doi:10.1175/2011JPO4570.1.

Woods, A. W., 1991: Boundary-driven mixing. *Journal of Fluid Mechanics*, **226**, 625–654, doi:10.1017/S0022112091002549.

Wunsch, C., 1970: On oceanic boundary mixing. *Deep Sea Research and Oceanographic Abstracts*, **17 (2)**, 293–301, doi:10.1016/0011-7471(70)90022-7.

Wunsch, C., and P. Heimbach, 2008: How long to oceanic tracer and proxy equilibrium? *Quaternary Science Reviews*, **27 (7)**, 637–651, doi:10.1016/j.quascirev.2008.01.006.

Wynne-Cattanach, B. L., and Coauthors, 2024: Observations of diapycnal upwelling within a sloping submarine canyon. *Nature*, **630 (8018)**, 884–890, doi:10.1038/s41586-024-07411-2.

Young, W. R., 2012: An exact thickness-weighted average formulation of the Boussinesq equations. *Journal of Physical Oceanography*, **42 (5)**, 692–707, doi:10.1175/JPO-D-11-0102.1.

Zhang, X., G. Lohmann, G. Knorr, and X. Xu, 2013: Different ocean states and transient characteristics in Last Glacial Maximum simulations and implications for deglaciation. *Climate of the Past*, **9 (5)**, 2319–2333, doi:10.5194/cp-9-2319-2013.